Numerical simulation of magma ascent by dykes and crust formation at spreading centres

Dissertation
zur Erlangung des Doktorgrades
der Naturwissenschaften im Fachbereich
Geowissenschaften
der Universität Hamburg

vorgelegt von

Daniela Kerstin Kühn

aus
Berlin Steglitz

Hamburg
2005

Als Dissertation angenommen vom Fachbereich Geowissenschaften der Universität Hamburg

aufgrund der Gutachten von	Prof. Dr. Torsten Dahm
und	Prof. Dr. Frank Roth

Hamburg, den 10. Mai 2005

Professor Dr. H. Schleicher
(Dekan des Fachbereichs Geowissenschaften)

Contents

List of Figures

Notation

Variable[1]	**Meaning**	**Dimension**[2]
Latin		
A_0, A_1	fracture area	m^2
$A^{ij}; A^{ij}_{nn}, A^{ij}_{ss}, A^{ij}_{ns}, A^{ij}_{sn}$	boundary influence coeff. for stress	Pa/m
$B^{ij}; B^{ij}_{nn}, B^{ij}_{ss}, B^{ij}_{ns}, B^{ij}_{sn}$	boundary influence coeff. for displacement	none
B	dislocation density function	none
a	vertical fracture half length	m
a_c	critical fracture half length	m
a_g	grain size	m
$\mathcal{C}$	boundary of region of interest	m
c	specific heat	kJ/kg K
D	displacement	m
$D_i; D_x, D_z; D_n, D_s$	displacement discontinuity	m
d	cross section	m
E	Young's modulus	Pa
$\vec{e_x},\ \vec{e_y},\ \vec{e_z}$	unit vectors in Cartesian coordinate system	none
$\vec{F}, F_i$	body force	N
f	function of specified variable	
$\mathcal{G}$	Griffith force	Pa m^3
$\vec{g}, g$	gravity acceleration	m/s^2
h	depth	m
i, j	counter	
K	bulk modulus	Pa
K_I, K_{II}, K_{III}	stress intensity factors	$\mathrm{N}/\sqrt{m^3}$
K_c	critical stress intensity factor	$\mathrm{N}/\sqrt{m^3}$
K_{Ic}	plane strain fracture toughness	$\mathrm{N}/\sqrt{m^3}$
$\mathbf{K}$	permeability tensor	m^2
k	permeability	m^2
k_0	permeability at porosity ϕ_0	m^2
k_{aa}, k_{bb}	principal permeabilities	m^2

---

[1] Names of variables are the same for all chapters. As far as possible, I tried to avoid using the same symbol with different meanings; in the few cases I failed to do so, the meaning of the variable is clear from the context.

[2] Please note that dimensions are given in 3-D

k_t	thermal conductivity	W/m K
L	latent heat of fusion	kJ/K
L_d	characteristic length in porous melt flow models	m
l	length	m
l	horizontal fracture length	m
N	number of boundary elements	none
$\vec{n}$	unit vector normal to surface element	none
P, p	pressure	Pa
P_f, P_s	lithostatic pressure caused by fluid/solid	Pa
p_0	constant pressure	Pa
$\mathcal{P}$	dynamic pressure	Pa
Q	heat	W
q	heat flux	W/m^2
$\mathcal{R}$	region of interest	m^2
$r, \vec{e_r}$	radial distance (polar coordinates)	m
S	surface energy	J
T	extensional stress	Pa
T	temperature	K
T_0	temperature at time t=0	K
T_b	temperature at dyke-rock boundary	K
T_m	melt temperature	K
T_s	surface temperature	K
t	time	s
t_s	solidification time	s
$\vec{t}$	traction	Pa
U	strain energy	J
U_{ex}	work energy of external load	J
U_e	elastic energy	J
V	volume	m^3
$\vec{u}, u_i; u_x, u_y, u_z, u_n, u_s$	displacement	m
$\vec{u}, u_i$	particle motion	m
$\vec{v}, v_i$	velocity	m/s
v_D	Darcy velocity	m/s
v_f, v_s	velocity of fluid/solid	m/s
v_x, v_y	velocity in direction of Cartesian coordinates x, y	m/s
v_r, v_θ	velocity in radial/angular direction	m/s
w	fracture width	m
w_0	separation velocity between melt and matrix	m/s
$\vec{x}, x_i; x, y, z$	Cartesian coordinates	m
x_m	time-dependent position of solidification boundary	m
z_0	depth of asthenosphere	m

GREEK

α, α'	wedge angle, complementary wedge angle	°
Γ	melting function	kg/m^3 s
γ_s	specific surface energy	N/m
Δ	difference	none
δ_{ij}	Kronecker's symbol	none
ε	strain	none
$\varepsilon_{xx}, \varepsilon_{yy}, \varepsilon_{zz}$	normal strain in Cartesian coordinate system	none
$\varepsilon_{xy}, \varepsilon_{xz}, \varepsilon_{yz}$	shear strain in Cartesian coordinate system	none
ζ	matrix bulk viscosity	Pa s
η	dynamic shear viscosity	Pa s
η_f, η_s	dynamic shear viscosity of fluid/solid	Pa s
Θ	dimensionless temperature	none
$\theta, \vec{e_\theta}$	angle (polar coordinates)	°
κ	thermal diffusivity	m^2/s
λ	thermodynamic similarity variable	none
λ_2	dimensionless position of solidification boundary	none
μ	shear modulus	Pa
ν	Poisson's ratio	none
π	Ludolph's constant	none
ρ	density	kg/m^3
ρ_f, ρ_s	density of fluid/solid	kg/m^3
ρ_{melt}, ρ_{rock}	density of melt/rock	kg/m^3
σ	stress	Pa
σ_d	stress resulting from dislocation distribution	Pa
σ_{ex}	external load	Pa
σ_m	mean stress	Pa
σ_n, σ_s	normal/shear stress	Pa
$\sigma_{rr}, \sigma_{\theta\theta}$	normal stress in radial/angular direction	Pa
$\sigma_{r\theta}$	shear stress parallel in radial/angular direction	Pa
$\sigma_{xx}, \sigma_{yy}, \sigma_{zz}$	normal stress in Cartesian coordinate system	Pa
$\sigma_{xy}, \sigma_{xz}, \sigma_{yz}$	shear stress in Cartesian coordinate system	Pa
$\sigma_1, \sigma_2, \sigma_3$	principal stresses	Pa
τ	viscoelastic relaxation time	s
ϕ, ϕ_0	porosity, characteristic porosity	none
ψ	stream function	m^2/s
ψ_f, ψ_s	stream function of fluid/solid	m^2/s

MISCELLANEOUS

$\bigtriangledown$	Laplacian operator
$\frac{D}{Dt}$	total differential
∂	partial derivative
erf	errorfunction
erfc	complementary errorfunction

ABBREVIATIONS

AMC	axial magma chamber
BE	boundary element (method)
EPR	East-Pacific Rise
FD	finite-difference (method)
FE	finite-element (method)
LNB	level of neutral buoyancy
LREE	light rare earth element
MAR	Mid-Atlantic Ridge
Mg #	Mg-number, Mg/(Mg+Fe^{2+})
MOR	mid-ocean ridge
MORB	mid-ocean ridge basalt
REE	rare earth element

Abstract

Mid-ocean ridges are common topographic features found in all major ocean basins and represent the most productive sites of magma generation worldwide. Both the processes of oceanic crust formation and volcanism at divergent plate boundaries are fundamental to plate tectonics and therefore important to understand. Magma dykes are an essential element in building oceanic crust, most prominent in sheeted dyke complexes in the upper crust. In this work, the interaction of magma chambers and dykes and their stress fields is used to analyse the formation of oceanic crust and in particular sheeted dyke complexes. Because of the sparseness of available data and the inability of analytical models to deal with inhomogeneous media and heterogeneous stress fields, numerical modelling is a vital tool to gain further insight. A boundary element method is used to simulate the ascent of dykes as fluid-filled, propagating fractures.

A model for magma ascent in the mantle should take into account the fast transport velocity of magma, the prevention of chemical re-equilibration by the separation of melt and rock and the focussing of magma from a broad melting zone at depth towards a narrow extrusion area at the spreading axis. Magma transport by fractures has been simulated and compared with models of porous melt flow and melt flow through dunite channels. The convective mantle flow was modelled by corner flow. Dynamic pressure and deviatoric stress fields arise from mantle rock deformation. Unfortunately, the deviatoric stress field prevents the focussing of fractures. Widespread models of porous melt flow lead to focussing, but satisfy neither the requirement of fast ascent velocity nor of separation of melt and mantle rock. Furthermore, they neglect the existence of the deviatoric stress field. Since there are indications that porous melt flow and dykes react in a similar manner to external stress fields, I conclude that models of porous melt flow including a deviatoric stress field in addition to a dynamic pressure gradient would not achieve a focussing of melt towards the spreading axis in analogy to the melt transport in fluid-filled fractures.

Since dykes alter the magnitude and orientation of the local stress field, they cannot be treated as passive infillings of extensional fractures. The parallelity of dykes in the sheeted dyke complex is surprising, since the dyke-induced stress fields lead to focussing and crossing of dykes. In this work, a combination of dyke propagation and dyke interaction algorithms is used. Dyke interaction is represented by the reaction of ascending dykes on the stress field caused by previous fractures arrested in the crust. The composition of mature oceanic crust is relatively uniform, although it emerges from spreading centres with different spreading rates exhibiting various characteristics in topography and

location of magma chambers. This phenomenon is analysed.
A model is developed, where the low to non-existent extensional stress field at fast-spreading ridges causes the formation of a crustal magma chamber in addition to the magma reservoir at the crust-mantle boundary due to focussing of dykes. Since the ascent path from the crustal magma chamber to the level of neutral buoyancy is only short, further focussing is inhibited and dykes are aligned parallel and vertical. The regional, extensional stress field at slow-spreading ridges impedes the formation of an additional crustal magma chamber, but causes the vertical ascent of dykes from the reservoir at the crust-mantle boundary to the level of neutral buoyancy, resulting in a sheeted dyke complex.

To my knowledge, neither magma ascent in the mantle nor in the crust beneath mid-ocean ridges has previously been studied in such complexity for melt ascent by fluid-filled dykes.

Zusammenfassung

Mittelozeanische Rücken finden sich in allen größeren Ozeanbecken der Erde. Sie besitzen die weltweit höchste Produktionsrate an Extrusiv- und Intrusivgesteinen. Bildung ozeanischer Kruste und Vulkanismus an divergenten Plattengrenzen sind fundamentale Prozesse, deren Grundverständnis wichtig ist. Magmatische Dykes bauen einen Großteil ozeanischer Kruste auf. Ihr Vorkommen ist besonders augenfällig im sogenannten Sheeted-Dyke-Komplex der oberen Kruste. In dieser Arbeit wird die Wechselwirkung zwischen Magmakammern und Dykes aufgrund von Spannungsfeldern untersucht. Die Ergebnisse werden zur Analyse ozeanischer Krustenbildung im allgemeinen und des Sheeted-Dyke-Komplexes im besonderen benutzt.
Da nur wenig Daten über die Geologie mittelozeanischer Rücken und den Verlauf magmatischer Prozesse verfügbar sind und analytische Modelle zumeist an der Berücksichtigung inhomogener Medien und heterogener Spannungsfelder scheitern, stellen numerische Modelle ein wichtiges Werkzeug zur weiteren Erforschung dieser Abläufe dar. Um den Aufstieg von Dykes als Fortbewegung fluidgefüllter Risse zu berechnen, wurde eine Randelementmethode verwendet.

Modelle für den Magmaaufstieg im Mantel müssen sowohl die hohen Transportgeschwindigkeiten als auch die Trennung von Schmelze und Mantelgestein zur Verhinderung chemischer Ausgleichsreaktionen und die Fokussierung des Magmas von der breiten Schmelzzone in der Tiefe zur schmalen Austrittszone an der Rückenachse leisten. In dieser Arbeit wurde der Magmatransport in Dykes simuliert und mit Modellen für Schmelzfluß im Porenraum des Mantelgesteins und in Dunitröhren verglichen. Die Mantelkonvektion wurde durch einen sogenannten "corner flow" dargestellt. Dieser führt zur Ausbildung eines dynamischen Drucks sowie eines deviatorischen Spannungsfeldes, die neben den Auftriebskräften auf die fluidgefüllten Risse einwirken. Es stellte sich heraus, daß das deviatorische Spannungsfeld die geforderte Fokussierung der Schmelze verhindert. Die weithin bekannten Modelle für porösen Schmelzfluß sind in der Lage, diese Fokussierung nachzubilden. Sie erfüllen aber weder die Forderung nach hohen Transportgeschwindigkeiten noch der Trennung von Schmelze und Mantelgestein und vernachlässigen die Existenz des deviatorischen Spannungsfeldes völlig. Da Hinweise existieren, wonach poröser Schmelzfluß und Dykes in ähnlicher Weise auf äußere Spannungsfelder reagieren, stelle ich die Behauptung auf, daß in den Modellen für porösen Schmelzfluß die Fokussierung der Schmelze durch den Einbau des deviatorischen Spannungsfeldes ebenso unterbunden würde wie in meinem Modell für den Magmatransport in Dykes.

Da Dykes Stärke und Orientierung vorhandener Spannungsfelder lokal verändern, können sie nicht als passives Füllmaterial von Dehnungsrissen betrachtet werden. Die Parallelität der Dykes innerhalb des Sheeted-Dyke-Komplexes ist angesichts ihres Eigenspannungsfeldes, das zu einer Fokussierung und Überlagerung von Dykes führt, erstaunlich hoch. In dieser Arbeit wird erstmals eine Kombination aus Dykeaufstieg und -interaktion vor dem geologischen Hintergrund eines mittelozeanischen Rückens und seiner Kruste untersucht. Die Reaktion propagierender Risse auf das Spannungsfeld bereits aufgestiegener und in der Kruste erstarrter Dykes wird erforscht. Hierbei wird besonders auf die auffällige Einheitlichkeit des ozeanischen Krustenaufbaus an divergenten Plattengrenzen unterschiedlicher Spreizungsgeschwindigkeit, und daher verschiedener Charakteristika die Topographie und Lage von Magmakammern betreffend, eingegangen.
Ich schlage ein Modell vor, bei dem die Ursache für die Parallelität der Dykes im Sheeted-Dyke-Komplex an schnell und langsam spreizenden Rücken unterschiedlich ist, die grundsätzlichen magmatischen Prozesse aber dieselben bleiben. An schnell spreizenden Rücken bildet sich zusätzlich zum Magmareservoir an der Kruste-Mantel-Grenze eine krustale Magmakammer aus, da die schwache oder fehlende Extensionsspannung die Fokussierung und Anhäufung von Dykes begünstigt. Der Aufstiegspfad von dieser krustalen Magmakammer zum endgültigen Erstarrungssniveau der Dykes – das Niveau neutralen Auftriebs (engl. *level of neutral buoyancy*) – ist kurz und verhindert somit eine weitere Fokussierung. Die Dykes verbleiben senkrecht und parallel zueinander. An langsam spreizenden Rücken verhindert die herrschende regionale Extensionsspannung die Bildung einer krustalen Magmakammer, sorgt aber gleichzeitig für einen vertikalen Aufstieg der Dykes vom Reservoir an der Kruste-Mantel-Grenze bis zum Niveau neutralen Auftriebs. Somit sind auch hier die Voraussetzungen für die Ausbildung eines Sheeted-Dyke-Komplexes gegeben.

Meines Wissens wurde der Aufstieg von Magma in Dykes in Kruste und Mantel an mittelozeanischen Rücken noch nie zuvor in solcher Komplexität analysiert.

Chapter 1

Introduction

Motivation

Mid-ocean ridges are present in all major ocean basins and have a combined length of more than 60 000 km. On average, they extend 1000–3000 m above the ocean floor. According to plate tectonic theory, mid-ocean ridges are constructive plate margins, where new oceanic lithosphere is formed. They represent volumetrically the most important sites of magma generation at present time, with an extrusion rate of 3 km^3/a and an intrusion rate of 18 km^3/a, compared with a global total production rate of 3.7–4.1 km^3/a of volcanic rocks and 22.1–29.5 km^3/a of plutonic rocks (Wilson, 1989). Because of this high productivity and the basic character of processes, the understanding of crust formation and volcanism at divergent boundaries is of great importance and of use for volcanic hazard assessment worldwide.

Magma dykes are among the most important structural elements of oceanic crust (Gudmundsson, 1990b). Surface volcanism takes place in a few distinct regions at the spreading axis itself, but the bulk of magma solidifies in the form of sheeted dykes and intrusions at greater depths (Wilson, 1989). The upper part of the oceanic crust consists of a thin sedimentary layer covering pillow lavas generated by magma penetrating the surface. A sheeted dyke complex is situated underneath, which is composed of vertical, parallel dykes. This is underlain by a gabbro layer, which may include sheeted sills, and the upper mantle consisting of peridotites and dunites.
An unique opportunity to study dyke emplacement at divergent boundaries is offered on Iceland, which represents the only subaerial part of a mid-ocean ridge. It matches the volcano-tectonic structure of oceanic ridges very well and at the same time is the most prominent example for ridge-hot spot interaction (Gudmundsson, 1990a, 2000).

In this work, the aim is to study the interaction between magma chambers, dykes and stresses, which will aid understanding of oceanic crust formation. I will focus in particular on the sheeted dyke complex, as well as the origin of crustal magma chambers and their role in crust accretion. In most models of oceanic crust formation, dykes and crustal magma chambers act as key factors. However, few authors combine these two features into a coherent tectonic model (Gudmundsson, 1990b). Repeated dyke injections are fed from both shallow and deep-seated reservoirs. Most probably, both the interaction among dykes and between existing shallow reservoirs and dykes has an impact on crust formation. Curewitz and Karson (1998) point out that dyke intrusions cannot be treated as passive infillings of tensile fractures as is often done. Since the dyke emplacement alters the magnitude and orientation of the local stress field, changes in the structure of the crust can be expected from diking on all time scales. Dyke propagation may also be of importance for melt migration in the mantle beneath spreading centres, though this is a point of contention.

Present knowledge

Although the process of fracturing of materials exposed to external loading is a common occurrence, the process is not yet fully explained mathematically.
The investigation of fracture mechanics begins with Griffith (1921), who carried out experiments on brittle material and develops an energy balance approach as a criterion for brittle fracturing. Westergaard (1939) and Sneddon (1946) consider a 1-D crack in an infinite solid to derive analytical solutions for the asymptotic behaviour of the stress field near its tip. Irwin (1948) and Orowan (1952) include properties of less brittle material into the energy balance and Irwin (1948) combines the energy balance method with an approach including a critical stress intensity factor. Exact solutions of elastic problems exist only for idealised implementations in infinite or semi-infinite regions. The method of complex stress functions originates from Kolosov (1909). Muskhelishvili (1953) gives a general solution for boundary value problems in a slitted plane.

A number of authors develop simplified analytical expressions for the propagation of dykes as fluid-filled fractures (e.g. Weertman, 1971). Although they take into account buoyancy forces, finite fluid volume, fluid viscosity, fracture strength and elastic forces, they neglect certain aspects of the complex process for the sake of mathematical simplicity, which restricts the solutions to specific problems (Dahm, 2000b). Weertman (1971) is the first to look at fracture propagation in detail. He implements a dislocation problem to calculate the behaviour of a liquid-filled crack. The fracture grows until it reaches a critical length and then rises upwards because of its buoyancy. It opens at the tip whilst it closes at the base, such that it maintains its length.

Analytical models of upward fracture migration are not able to deal with inhomogeneous media and heterogeneous stress fields (Dahm, 2000a). The emplacement of dykes and sills leads to stress field inhomogeneities. Until now, most models have been qualitative and neglected these self-induced stress fields. A numerical approach is well suited to deal with such heterogeneous stress fields.
Crouch (1976b) and Crouch and Starfield (1983) apply a boundary value method to solve elastostatic problems numerically. In this thesis, a quasistatic version of the method is used to compute the growth and wholesale propagation of a fluid-filled fracture to describe magma transport in dykes. The necessary alterations to change the code from static to quasi-static were performed by Dahm (1996, 2000a, 2000b).

While numerical calculations of static fracture mechanics are more common (e.g. Crouch and Starfield, 1983; Bonafede and Rivalta, 1999b, 1999a), few authors deal with magma transport by propagating dykes (Rubin, 1998; Dahm, 2000a, 2000b) and only Ito and Martel (2002) have compared their models with the magmatic processes at mid-ocean ridges. Very few authors consider the interaction of dykes, which is a related problem (Wei and De Bremaecker, 1995; Ito and Martel, 2002).

Further insight into crack propagation has been obtained from laboratory experiments on dyke propagation (Takada, 1990; Heimpel and Olson, 1994; Ito and Martel, 2002; Rivalta *et al.*, 2005).
Geoscientific experiments at mid-ocean ridges include dredging, deep-sea drilling and marine geophysics, e.g. reflection and refraction seismic surveys, seismology, electrics, magnetics and gravimetry. Recently, submersibles have been used to recover samples and take photographs near spreading centres (Auzende *et al.*, 1989). Ophiolites, which represent obducted ancient oceanic crust are another possibility to study the structure of oceanic crust (Nicolas and Jackson, 1982; Nicolas, 1986; Lippard *et al.*, 1986; Ceuleneer *et al.*, 1988; Kelemen *et al.*, 1995, 1997).

Objectives

Geophysical experiments conducted at mid-ocean ridges, e.g. the MELT experiment (Forsyth *et al.*, 1998a), are able to differ between distinct geological units, but not to observe the fine structure of the sheeted dyke complex in detail. Dredging allows no stratigraphic control. In most cases, deep-sea drilling reaches only the upper crustal layers; so far, merely one borehole penetrated the sheeted dyke complex with a maximum penetration depth of 2111 mbsf (Hole 504B, Leg 148, Alt *et al.*, 1993). Most methods provide only snapshots from which no solid conclusions on the temporal development can be drawn.

Because of the sparseness of available data in geological structure and magmatic processes at mid-ocean ridges, numerical modelling is a vital tool to gain further insight into crust forming processes. At the same time, verification and interpretation of the numerical models is difficult.
Some significant modifications were made by Dahm (1996, 2000a, 2000b) to the boundary element method developed by Crouch and Starfield (1983). Among other things, the fluid volume enclosed in the fracture is considered and a transition from a static to a quasi-static code is performed where the direction of fracture propagation is determined by a maximum strain energy release-rate criterion. During modelling, every single dyke and its movement is calculated, i.e. its position, equilibrium shape, thickness and length.
The numerical approach considers fluid buoyancy, heterogeneous stress fields and fracture mechanics and has to my knowledge never been used to study crust formation beneath spreading centres before.

Focussing of magma supply in the mantle

The general mechanism of oceanic crust formation is well known. Material from the deep mantle ascends and partial melting occurs due to adiabatic decompression. Magma may be stored temporarily in shallow magma chambers beneath the spreading axis and intrudes into the rift, where it solidifies. The melt zone in the mantle extends up to several hundred of kilometres laterally, whereas the extrusion area at the spreading axis is confined to a narrow belt, only 2–3 km in width. The mechanism of focussing and melt extraction from the mantle is still poorly understood, despite the important role of the process for oceanic crust formation and plate tectonics.

Two different kinds of models for the flow regime of magma and solid rock beneath mid-ocean ridges exist: spreading-induced passive mantle flow or buoyancy-induced active upwelling of hot mantle material. Geochemical experiments at the East Pacific Rise show a good agreement with the passive flow model (Spiegelman and Reynolds, 1999).

A widespread mode of magma transport in the mantle is the porous flow of melt through the pore space of the mantle rock towards the spreading axis due to pressure gradients (Spiegelman and McKenzie, 1987; Phipps Morgan, 1987; Müller, 2003). Ghods and Arkani-Hamed (2000) include matrix compaction and decompaction due to melt removal and accumulation in the porous flow model. If the lithosphere acts as an impermeable barrier, a decompacting layer with a high melt content forms at the top of the asthenospheric layer. The melt flux is strongly decoupled from the matrix flow and moves toward the spreading axis. Kelemen *et al.* (1995) state that petrological arguments disagree with the porous flow of melt through the mantle rock, since mid-ocean ridge basalts are not in equilibrium with the residual mantle peridotite. Porous flow is slow and encourages chemical reactions because of the close contact between melt and rock. A transport process is required to hinder the re-equilibration between ascending melt and surrounding peridotite. Another constraint on melt flux is the transport velocity. Kelemen *et al.* (1995) model an initial porous flow of magma separated by dunite channels from the mantle matrix, which Kelemen *et al.* (1997) identify as dissolution channels. They explain the development of dunite conduits during fluid flow in porous media, but do not account for the initial focussing of channels toward the spreading axis.

Weertman (1971) deals with upward dyke propagation due to pseudo-Archimedian buoyancy forces by solving a dislocation problem. Nicolas and Jackson (1982) and Nicolas (1986) give geological evidence of dykes in ophiolites in general and in the Oman ophiolite in particular. Nicolas and Jackson (1982) consider brittle failure of rock possible at any depth if the fluid pressure is high enough. Nicolas (1986) suggests a network of hydrofractures, which acts as a conduit for melt between the mantle and the ridge. Sleep (1988) describes the formation of dykes from magma-filled veins. Porous influx of magma into a crack and subsequent vertical channel flow, fracturing the overlying rock, is proposed by Rubin (1998). Dahm (2000a) identifies the propagation of fluid-filled fractures and magma-filled dykes as an important mechanism for fluid transport through the lithosphere and possibly the asthenosphere. Among others, Nicolas and Jackson (1982), Nicolas (1986), Sleep (1988) and Phipps Morgan (1987) hold the view that dykes propagate in direction of maximum compressive stress. Dahm (2000a) shows that the buoyancy forces as well as the effects of the finite fluid volume enclosed in the fracture may force the dykes to stray

from this propagation direction.
More elaborate models incorporate the 3-dimensionality of the mid-ocean ridge. Sparks *et al.* (1993) refer to local-buoyancy sources that cause the 3-D structure. If viscosity and spreading rate are low, a time-dependent flow pattern develops and plumelike upwellings migrate along and across the spreading axis, forming axis-parallel convection cells. Rabinowicz *et al.* (1993) obtain a strong localised downwelling beneath transform faults by using thermal buoyancy and layered viscosity.

Porous melt flow, favoured during the last years as model of melt extraction from the mantle beneath mid-ocean ridges, has difficulties explaining the fast ascent velocities and hinder re-equilibration between mid-ocean ridge basalt and mantle rocks. Channelling and diking is being discussed as an alternative or complementary mechanism for fast and efficient melt transport. Magma transport in dykes in the mantle beneath mid-ocean ridges has rarely been simulated numerically except for Ito and Martel (2002), who refrain from including external stress fields that arise from mantle convection.
This thesis analyses if the simple corner flow model together with a rigorous study of dyke ascent paths can fit the observed convergence of melt from a broad melting to a narrow extrusion zone. I present a numerical model of melt ascent in the mantle by wholesale propagation of fluid-filled fractures. This model includes the separation of melt and rock required from petrological arguments as well as the high ascent velocity. I study dyke ascent paths under different stress conditions. In particular, this includes the deviatoric stress, which is neglected in the models of porous melt flow, but possesses a high influence on melt propagation. Buoyancy and enclosed finite fluid volume are considered in contrast to early models of dyke movement. With a similar model, Dahm (2000a) is able to reconstruct magma transport at subduction zones.
To my knowledge, the ascent of magma-filled dykes has never before analysed in such complexity at mid-ocean ridge settings.

Modelling of sheeted dyke complex formation

Most authors dealing with oceanic crust formation restrict themselves to the origin of the eruptive layer (Macdonald, 1982; Gràcia and Escartín, 1999; Smith and Cann, 1999) or the gabbro layer (Henstock *et al.*, 1993; Morgan and Chen, 1993; Boudier *et al.*, 1996; Lissenberg *et al.*, 2004). The location and the influence of magma chambers has been analysed (Macdonald, 1982; Sempere and Macdonald, 1987; Gudmundsson, 1990b; Gràcia and Escartín, 1999). The topic of dyke emplacement (Gudmundsson, 1990a, 1990b) or the origin of the sheeted dyke complex (Weertman, 1971, 1973) have rarely been covered and never the astonishing parallelity of dykes within the complex has been analysed. The nature of influencing factors is unclear. Until now, most models have been qualitative and neglected the stress field caused by dyke emplacement and openings, although locally, it may be more significant than regional stress fields. This self-induced stress field leads to dyke focussing and thus hinders the parallelity required to construct the sheeted dyke complex. In this work, heterogeneities of the stress field are treated quantitatively.

A paradox exists between different characteristics of spreading centres at variable spreading rates and the high uniformity of mature oceanic crust regarding geophysical, petrological and geochemical properties (Henstock *et al.*, 1993). A striking difference between slow- and fast-spreading ridges is the lack of a central rift valley and smoother topography at fast-spreading ridges (Wilson, 1989). At slow-spreading ridges, an axial magma chamber exists only at the crust-mantle boundary, whereas fast-spreading ridges feature also a permanent crustal magma chamber (Macdonald, 1982; Sempere and Macdonald, 1987; Morgan and Chen, 1993; Gràcia and Escartín, 1999; Lissenberg *et al.*, 2004). Gràcia and Escartín (1999) state that oceanic crust at slow-spreading ridges exhibits a higher variability; peridotites and gabbros may be dredged at the end of ridge segments, either due to tectonic extension or more heterogeneous crustal composition. Although the magma supply may be different for these ridge types, the mature oceanic crust principally looks the same (Henstock *et al.*, 1993), and always includes a sheeted dyke complex, the formation of which is the main focus of this thesis. Igneous processes may be similar across a range of spreading rates. The pattern of fine scale crustal structure and tectonics appears to be largely independent of the spreading rate (Macdonald, 1982).

I present a unique combination of dyke propagation and dyke interaction algorithms applied at mid-ocean ridge settings. The most important issues are the sheeted dyke complex formation, the dependence of crust formation processes on the spreading rate, and the development of crustal magma chambers. The difficulty in modelling the generation of the sheeted dyke complex arises from the high parallelity of dykes, which conflicts with their self-induced stress fields. The existence of the sheeted dyke complex is proven at slow- and fast-spreading ridges without knowing if similar or different magmatic processes are involved in its formation. The storage and solidification of dykes enclosing hot magma in the crust heats the surrounding area and can lead to the generation of a small magma reservoir.
Hitherto, few authors have tackled the interaction between dykes although it constitutes an immensely important process in the formation of the sheeted dyke complex. Neighbouring dykes influence each other's behaviour, e.g. two fractures ascending simultaneously attract one another (Ito and Martel, 2002). In this work, the reaction of ascending cracks on the stress field produced by previous fractures is analysed. The assumption is made that previous dykes are completely solidified before the ascent of the next dyke, but their stress field is maintained. Thus, the time span of solidification is shorter than the recurrence time of dyke ascent, which in turn is shorter than the viscoelastic relaxation time of the stress field.

My thesis is laid out as follows.
The ascent of magma-filled dykes beneath mid-ocean ridges is analysed. The surrounding rock is assumed to be linear elastic, at least on the time scale of dyke propagation. The theoretical background is presented in chapter 2.
Since the concepts of stress and strain in solids are well known, only a short overview is given. In contrast, the theory of fracturing is not established commonly and is explained in more detail. It is subdivided to describe the general features of stable and unstable crack growth, before proceeding to the subject of wholesale fracture movement by a combination of crack tip opening and closing.

The boundary element method is suitable for computing fracture growth and propagation. Since only the crack surfaces have to be discretised, the method saves time and memory compared with the discretisation of the whole model area. Additionally, stress and displacement fields at arbitrary points outside the fracture can be calculated accurately after solving the main problem. The boundary element method is introduced in chapter 3, alongside with a description of how the program code is adjusted to deal with the objectives of this thesis.

Chapters 4 and 5 contain separated applications of magma transport by fluid-filled dykes. In chapter 4, the propagation of dykes in the mantle is analysed. The corner flow model is used to represent mantle convection. It results in two kinds of stress fields, a dynamic pressure and a deviatoric stress field. Their influence on fracture movement is discussed, together with a critical review of other theories for magma ascent.

Chapter 5 deals with the modelling of oceanic crust formation, especially the sheeted dyke complex. Interaction between dykes proves to be important and is analysed accurately. Starting from the interaction of two dykes, the model is refined to compute the stress field of all previously ascended dykes and their impact on the propagation of successive dykes.

Chapter 6 attempts to draw the conclusions and to give an integrated review of the magmatic processes at mid-ocean ridges.

Chapter 2

Elasticity and fracturing

In this thesis, the ascent of magma-filled dykes beneath mid-ocean ridges is analysed. Crust and mantle are assigned a linear elastic behaviour, at least on the short time scale of dyke propagation. Dykes are considered as brittle fractures and their wholesale[1] movement is modelled through a combination of crack tip opening and closing.
Since the concepts of stress and strain in solids are for the most part well known, they are introduced only briefly in section 2.1. Special cases of plane stress, plane strain, simple and pure shear which are commonly used to simplify present conditions are shown separately. The numerical model is 2-D and uses the plane strain state to describe the situation at the spreading axis, since little variation is expected in axial direction of the ridge.
In contrast, the theory of fracturing is not assumed to be well established. It is therefore described in more detail in section 2.2 (pp. 20).

2.1 Linear elasticity

”Elastic” means that strains are recovered when stresses are removed. As a consequence, a certain stress corresponds to a particular strain and vice versa, irrespective of the history of loading. Linear elastic behaviour signifies in addition that each stress component can be expressed as a linear combination of all strain components. Only infinitesimal strains which are negligible compared to unity are treated. Therefore, products of two or more strains can be neglected and it is not necessary to distinguish between deformed and undeformed shapes of bodies when defining strain components. Strains produced at any point in a body by one system of stress can be added to those produced by another system, the final result being independent of the order in which stresses are added up. Constants connecting components of stress and strain specify the elastic properties of a certain body. If those properties are independent of position and orientation within a body, that body is said to be homogeneous and isotropic (Crouch and Starfield, 1983).

Almost all solid materials, including rocks at relatively low temperatures and pressures, act elastically if the applied forces are not too large. Moreover, elastic strain of many

---

[1] ”Wholesale” refers to the fracture being self-contained and no longer connected to its place of origin. The fluid volume enclosed in the fracture is constant, no liquid is left behind in its trail.

rocks is linearly proportional to applied stress. Usually, the isotropic approximation is satisfactory for the earth's crust and mantle, which simplifies the equations to be applied. The lithosphere is assumed to be elastic on geological time scales (Turcotte and Schubert, 1982).

Stress

Stress, being a surface force, acts on surface areas bounding a volume element (Turcotte and Schubert, 1982). The magnitude of surface forces is directly proportional to the area of surface on which it acts and depends on surface orientation.

In most cases, stress needs to be described in three dimensions. Therefore, a vector of traction $\vec{t}$ is defined (Zabaras, 2001). For any type of Cartesian coordinate system with $\vec{n} = n_1\vec{e_x} + n_2\vec{e_y} + n_3\vec{e_z}$, tractions are calculated from

$$\left\{ \begin{array}{c} t_{nx} \\ t_{ny} \\ t_{nz} \end{array} \right\} = \begin{bmatrix} \sigma_{xx} & \sigma_{xy} & \sigma_{xz} \\ \sigma_{yx} & \sigma_{yy} & \sigma_{yz} \\ \sigma_{zx} & \sigma_{zy} & \sigma_{zz} \end{bmatrix} \left\{ \begin{array}{c} n_1 \\ n_2 \\ n_3 \end{array} \right\} \tag{2.1}$$

where $\vec{n}$ is the unit vector normal to the surface affected by external force and $\vec{e_x}$, $\vec{e_y}$, $\vec{e_z}$ are unit vectors in direction of x, y and z axis. The first subscript of σ denotes the direction of the normal to the surface where the stress is applied, and the second subscript describes the direction in which the stress is targeted. (Direction of stresses are depicted in appendix A.1, Fig. A.1 on p. 142.) Thus σ_{xx}, σ_{yy} and σ_{zz} describe normal stresses, whereas σ_{xy}, σ_{xz}, etc. denote shear stresses. Because of equilibrium conditions, $\sigma_{xy} = \sigma_{yx}$, $\sigma_{yz} = \sigma_{zy}$ and $\sigma_{xz} = \sigma_{zx}$. Hence, only six out of nine components are independent.

Normal and shear stresses can be specified as σ_n and σ_s with respect to local coordinates (Crouch and Starfield, 1983). They can be calculated from the traction components by simple means of trigonometry.

Since an orthogonal transformation exists for every symmetric tensor such that the tensor is converted into a diagonal matrix (Bronstein *et al.*, 1995), a system of principal stress directions σ_1, σ_2 and σ_3 can be found.

By convention, σ_1 denotes the maximum and σ_3 the minimum principle stress. The idea is that for any arbitrary state of stress it is possible to find a surface oriented in such a manner that there are no shear forces exerted on it. The direction of principal axes of stress is given by the eigenvectors of the stress tensor, which are orthogonal to each other. It further holds that $\sigma_{xx} + \sigma_{yy} + \sigma_{zz} = \sigma_1 + \sigma_2 + \sigma_3$ (Turcotte and Schubert, 1982).

Hydrostatic state of stress is defined by the three principal stresses being equal, that means the state of stress is isotropic. Any set of orthogonal axes qualifies as principal axis coordinate system and stresses are equivalent to the pressure P (Turcotte and Schubert, 1982). If the stress increases proportionally with depth at a rate depending on the density of material, the state of stress is called lithostatic. In the case of unequal principal stresses, pressure is defined as mean stress $\sigma_m = \frac{1}{3}(\sigma_1+\sigma_2+\sigma_3)$. Some examples for stress conditions including uniaxial tension, biaxial tension, hydrostatic pressure and triaxial tension are explained in appendix A.1, Fig. A.2 on p. 143.

Usually, the stress matrix is split into two parts (Zabaras, 2001): the first consists of the hydrostatic and the second of the deviatoric stress. The hydrostatic stress is defined as

$$\sigma = \begin{bmatrix} \sigma_m & 0 & 0 \\ 0 & \sigma_m & 0 \\ 0 & 0 & \sigma_m \end{bmatrix} \quad . \tag{2.2}$$

Deviatoric stress is the difference between total and hydrostatic stress, which is

$$\sigma = \begin{bmatrix} \sigma_1 - \sigma_m & 0 & 0 \\ 0 & \sigma_2 - \sigma_m & 0 \\ 0 & 0 & \sigma_3 - \sigma_m \end{bmatrix} = \begin{bmatrix} \frac{2\sigma_1 - \sigma_2 - \sigma_3}{3} & 0 & 0 \\ 0 & \frac{-\sigma_1 + 2\sigma_2 - \sigma_3}{3} & 0 \\ 0 & 0 & \frac{-\sigma_1 - \sigma_2 + 2\sigma_3}{3} \end{bmatrix} \tag{2.3}$$

in terms of principal stresses. The relevance of the decomposition lies within the hydrostatic part describing change of volume during deformation, whereas the deviatoric stress indicates induced distortion.

Considerations on the equilibrium of stress lead to the following equations

$$\frac{\partial \sigma_{xx}}{\partial x} + \frac{\partial \sigma_{yx}}{\partial y} + \frac{\partial \sigma_{zx}}{\partial z} + F_x = 0 \tag{2.4}$$

$$\frac{\partial \sigma_{xy}}{\partial x} + \frac{\partial \sigma_{yy}}{\partial y} + \frac{\partial \sigma_{zy}}{\partial z} + F_y = 0 \tag{2.5}$$

$$\frac{\partial \sigma_{xz}}{\partial x} + \frac{\partial \sigma_{yz}}{\partial y} + \frac{\partial \sigma_{zz}}{\partial z} + F_z = 0 \ , \tag{2.6}$$

where F_x, F_y and F_z are body forces with dimensions of force per volume. Since this is not enough to calculate the six independent components of the stress tensor (Crouch and Starfield, 1983), additional equations arising from deformations associated with the stresses are required.

Strain

The concept of strain is used to specify the way in which a solid, continuous body deforms when it is subjected to stress. Deformations consist of a change in geometry and occur when various points in the body are displaced relative to each other. A change in length of a small line element is characterised by normal strain, whereas change in angle between two small line elements is represented by shear strain. Since changes are specified relatively, normal and shear strain are dimensionless (Crouch and Starfield, 1983).

When the initial stress is small, strain is reversible and proportional to stress (Hooke's law in 1-D, e.g. Berckhemer, 1990)

$$\varepsilon = \frac{1}{E}\sigma \quad . \tag{2.7}$$

The constant of proportionality E is called the **Young's modulus** and is a measure of the material's resistance to elastic deformation (stiffness).
At the same time a material of original length l is shortened by Δl if an applied uniaxial stress is positive, the cross section d is enlarged by Δd. The ratio

$$\nu = \frac{\Delta d}{d} / \frac{\Delta l}{l} \tag{2.8}$$

is called **Poisson's ratio**. Hydrostatic pressure P leads to a volumetric change ΔV in the specimen without deformation, which can be described by

$$\frac{\Delta V}{V} = -\frac{1}{K}P \quad , \tag{2.9}$$

where K is the **bulk modulus**, the reciprocal to the compressibility (Turcotte and Schubert, 1982). A tangential shear stress σ_s leads to deformation without volumetric change with the angle of shear γ being dependent on the **shear modulus** μ

$$\gamma = \frac{1}{\mu}\sigma_s \quad . \tag{2.10}$$

If the observed medium is homogeneous, isotropic and elastic, only two of the moduli are independent. Relations are given in Table 2.1. The elastic moduli are further explained by Fig. A.3 in appendix A.1, p. 143.

K	E	μ
–	$3K(1-2\nu)$	$\frac{3}{2}K\frac{1-2\nu}{1+\nu}$
$E\frac{1}{3(1-2\nu)}$	–	$E\frac{1}{2(1+\nu)}$
$\frac{2}{3}\mu\frac{1+\nu}{1-2\nu}$	$2\mu(1+\nu)$	–

Table 2.1: Relations between elastic moduli; partly gathered from e.g. Berckhemer (1990) or Stacey (1969)

A generalised Hooke's law for stress-strain relations in 3-D can be written

$$\begin{aligned}
\varepsilon_{xx} &= \frac{1}{E}\left[\sigma_{xx} - \nu(\sigma_{yy} + \sigma_{zz})\right] && (2.11)\\
\varepsilon_{yy} &= \frac{1}{E}\left[\sigma_{yy} - \nu(\sigma_{xx} + \sigma_{zz})\right] && (2.12)\\
\varepsilon_{zz} &= \frac{1}{E}\left[\sigma_{zz} - \nu(\sigma_{xx} + \sigma_{yy})\right] && (2.13)\\
\varepsilon_{xy} &= \varepsilon_{yx} = \frac{1}{2\mu}\sigma_{xy} && (2.14)\\
\varepsilon_{xz} &= \varepsilon_{zx} = \frac{1}{2\mu}\sigma_{yz} && (2.15)\\
\varepsilon_{yz} &= \varepsilon_{zy} = \frac{1}{2\mu}\sigma_{xz} && (2.16)
\end{aligned}$$

which indicates that shear stresses and strains are all independent of each other. Furthermore, the first three equations show that normal stresses cause no shear strain and the last three that shear stresses generate no normal strain (Crouch and Starfield, 1983).

Strain components can also be defined by means of a displacement field assumed to consist of the displacements in $x,\ y$ and z direction $u_x,\ u_y$ and u_z (Crouch and Starfield, 1983)

$$\begin{aligned}
\varepsilon_{xx} &= \frac{\partial u_x}{\partial x} && (2.17)\\
\varepsilon_{yy} &= \frac{\partial u_y}{\partial y} && (2.18)\\
\varepsilon_{zz} &= \frac{\partial u_z}{\partial z} && (2.19)\\
\varepsilon_{xy} &= \varepsilon_{yx} = \frac{1}{2}(\frac{\partial u_x}{\partial x} + \frac{\partial u_y}{\partial y}) && (2.20)\\
\varepsilon_{xz} &= \varepsilon_{zx} = \frac{1}{2}(\frac{\partial u_x}{\partial x} + \frac{\partial u_z}{\partial z}) && (2.21)\\
\varepsilon_{yz} &= \varepsilon_{zy} = \frac{1}{2}(\frac{\partial u_y}{\partial y} + \frac{\partial u_x}{\partial z})\ , && (2.22)
\end{aligned}$$

where $\varepsilon_{xx},\ \varepsilon_{yy},\ \varepsilon_{zz}$ are normal strains indicating changes of length per unit length of infinitesimal line elements in $x,\ y$ and z directions. The other components are shear components representing the change in angle between two infinitesimal line elements originally parallel to the appropriate axes of coordinate system.

Since the strain matrix is symmetric, it can also be transformed in a principal axis coordinate system (corresponding to a rotation of the specimen into an orientation where the shear strain components vanish). For isotropic and linear elastic material, the principal strain directions are the same as the principal stress directions.

Since solving of elasticity problems often involves finding stress and displacement distributions in an elastic body subject to a known set of boundary conditions, in the general 3-D case six independent stress components and three displacements as a function of position in the body are searched. Equilibrium equations Eqs. (2.4)–(2.6) combined with stress-strain relations Eqs. (2.11)–(2.16) give nine equations for these nine unknowns. Displacement and strain are connected via Eqs. (2.17)–(2.22).

Similar to stress which can be divided into a hydrostatic and a deviatoric part, strain can be split up into a dilatational and a distortional part. Dilatational strain results in volume change without distortion, whereas distortional strain produces distortion without change of volume.

Special cases

The case of plane strain is applied for the calculations of fracture propagation beneath mid-ocean ridges. It is assumed that geometry and regional stress field do not change in the axial direction of the ridge. Simple and pure shear are important simplifications of complex shear stresses. The state of plane stress is quoted for the sake of completeness.

- **Plane strain**
  An illustration for a situation involving plane strain is shown in Fig. 2.1. Since the block is fixed in one direction (here assumed to be direction of y coordinate), no extension or contraction parallel to its length may occur.
  It is assumed to be an appropriate approximation for thick plates where geometry

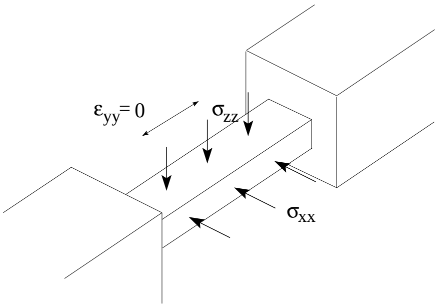

Figure 2.1: Plane strain state; no strain can occur in direction of the y coordinate; sketch after Turcotte and Schubert (1982)

and loading does not vary significantly in one of the coordinate directions (Aliabadi and Rooke, 1991). The displacement in direction u_y is zero at every cross section through the plate and thus, the strain components ε_{yy}, ε_{xy}, ε_{yz} vanishes.

Three strain components are defined in terms of two displacements. Thus, the strain components cannot be specified independently from one another, in fact, they are connected by the compatibility condition (Crouch and Starfield, 1983)

$$\frac{\partial^2 \varepsilon_{xx}}{\partial z^2} + \frac{\partial^2 \varepsilon_{zz}}{\partial x^2} = \frac{2\partial^2 \varepsilon_{xz}}{\partial x \partial z} \quad . \tag{2.23}$$

- **Plane stress**
  Plane stress is a state in which one of the three principal stresses (e.g. y coordinate) is zero and the remaining two are nonzero as is the case for a thin sheet stressed in its own plane (Fig. 2.2). For thin plates, the stresses including the y coordinate direction (σ_{yy}, σ_{xy}, σ_{yz}) are zero on both sides of the plate and are assumed to be so within the plate as well. The non-zero components of stress are averaged over the thickness and are independent of the y coordinate. The strain components ε_{xy}, ε_{yz} vanish on the surfaces (Aliabadi and Rooke, 1991). The equilibrium equations Eqs. (2.4)–(2.6) reduce to

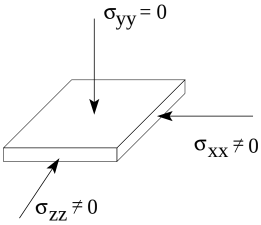

Figure 2.2: Plane stress state, no stress acts in direction of the y coordinate

$$\frac{\partial \sigma_{xx}}{\partial x} + \frac{\partial \sigma_{zx}}{\partial z} + F_x = 0 \tag{2.24}$$

$$\frac{\partial \sigma_{xz}}{\partial x} + \frac{\partial \sigma_{zz}}{\partial z} + F_z = 0 \quad . \tag{2.25}$$

The stress tensor has three independent components remaining, the equilibrium equations give two equations for these three unknowns (Crouch and Starfield, 1983).

- **Simple and pure shear**
  One of the simplest forms of shear imaginable is the shear along a fault plane where the two sides move in opposite directions (Fig. 2.3, left). It is therefore called simple shear (Dutch, 2002). On the right, the directions of stress causing pure shear are indicated. Shear occurs whenever an object is deformed. In Fig. 2.4, both types of deformation are shown for a specimen. At the top, a block being deformed by simple shear is depicted. The change in angle α, β is indicated by $\alpha + \gamma$, $\beta - \gamma$. In the case of simple shear, one direction remains constant and everything is rotated relative to it. t the bottom, a block undergoing pure shear is displayed; even if the impression is of deformation involving only compression and extension, shear stress is visible in change in angle between the diagonals of the block. The directions of compression and extension as well as the direction of the major and minor axes of the deforming ellipse remain constant, while all other inner lines rotate (Dutch, 2002).
  If the amount of shear is equal, the change in angles is the same for both simple and pure shear. In addition, the shape of the plotted ellipse is the same.

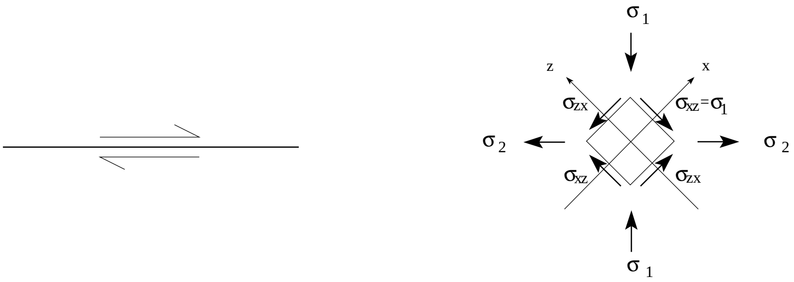

Figure 2.3: Left: fault undergoing simple shear, right: direction of stresses in case of pure shear; sketch after Turcotte and Schubert (1982)

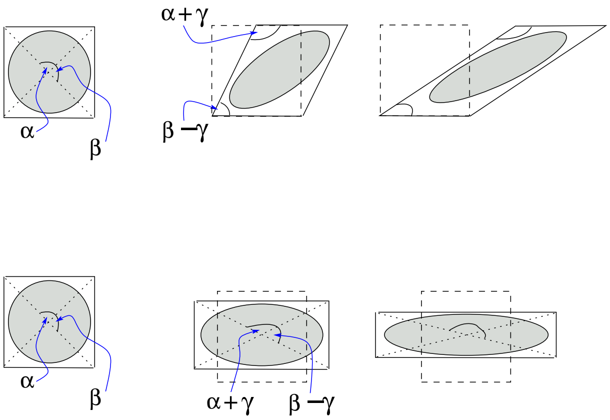

Figure 2.4: Comparison of blocks undergoing simple shear (at the top) and pure shear (at the bottom); sketch after Dutch (2002)

2.2 Fracturing

Fracturing of material exposed to external loading is a common occurrence. Nevertheless, the phenomenon is not yet fully explained mathematically.

As portrayed by Aliabadi and Rooke (1991), Griffith (1921) carried out experiments on brittle material and stated the existence of crack-like failures which could increase in size under the influence of external loading. He described the growth of cracks as controlled by an energy balance between the available strain energy and the energy required to form new crack surfaces. Westergaard (1939) gave equations for a penny-shaped 1-D crack in an infinite solid and the asymptotic behaviour of the stress field near its tip. Those were further developed by Sneddon (1946) for the case of a 2-D crack, where the controlling parameters differed from Westergaard (1939) by a simple multiplicative factor. Irwin (1948) and Orowan (1952) changed the energy balance given by Griffith (1921) to include the behaviour of less brittle materials by supplementing the surface energy with the work done in plastic deformation. Irwin (1948) showed that the functional dependence of the stress field near the crack tip on spatial coordinates is determined by a single parameter, the stress intensity factor. Furthermore, he related the energy balance approach to the critical stress intensity factor approach.

In section 2.2.1, I give some general remarks on fracturing before proceeding to the Griffith theory of brittle fracturing and the wholesale propagation of fractures, which may occur in particular situations once their growth process is finished. The terms of "crack" and "fracture" are employed synonymously. Please note that for the 2-D case discussed here, variables are meant to be defined per unit length with respect to the third dimension. Parameter units thus may differ from those given in the table of notations.

2.2.1 Crack growth

Two main types of fracturing are brittle and ductile fracturing. Brittle fracturing is displayed mainly by nonmetals which possess a larger compressive than tensile strength, but are very sensitive to flaws and imperfections. Little or no deformation precedes the fracturing. Procedures of treatment are based on the theory of elasticity (Hahn, 1976, this and following comments, if not stated otherwise).

Ductile fracturing is typically preceded by plastic deformation and is characteristic for metals. The precise manner of crack growth depends on the material itself, shape and dimension of the body, loading, temperature and the state of stress and strain.

Fracturing is a heterogeneous process; it does not occur by a contemporaneous demolition of all lattice bindings, but begins where uncoupling is found locally. Crack initiation takes place where plastic deformation (e.g. by dislocation creep) is locally blocked by an obstacle, e.g. impurities or grain boundaries. Up to 1000 dislocations may accumulate at such a barrier and finally, the high stress concentration leads to microfracturing.

If a fracture comes into existence, its length increases subcritically and thus slowly with a velocity of approximately cm/min or less (stable crack growth). The crack ceases to grow if the external load is held constant, until the burden is increased again. After a critical length is reached, the fracture grows critically without need for a further enhancement of the external load; the velocity increases up to several hundreds or thousands of m/s (unstable crack growth), although this velocity may be smaller if a fluid is entrained in

the crack.
Fractures can be described by a superposition of three principal modes, which are displayed in Fig. 2.5: tension (mode I, resulting in opening of the fracture), in-plane shear (mode II, resulting in sliding) and out-of-plane shear (mode III, resulting in tearing).

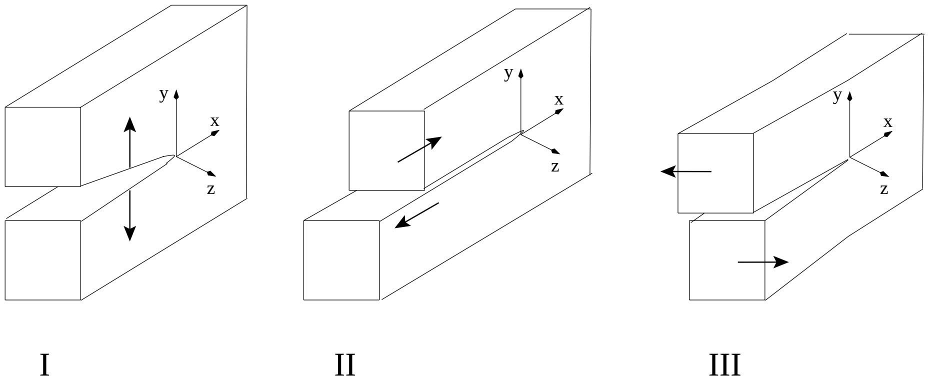

Figure 2.5: Three principal modes of fracturing; left: tension (mode I), middle: in-plane shear (mode II), right: out-of-plane shear (mode III)

In most cases, exact solutions of elastic problems can only be found if problems are idealised to represent limiting cases of infinite or semi-infinite regions. Only a small number of solutions for bodies of finite dimensions are known, since the exact fulfilment of boundary conditions often poses insurmountable difficulties. Hahn (1976) refers to Kolosov (1909) as an originator of the method of complex stress functions and to Muskhelishvili (1953) as having established a general solution for boundary value problems in a slitted plane by means of complex analysis theorems dealing with analytical continuation of complex stress functions. In general, stresses in the surroundings of one or several cracks with simple geometry can be traced back to the solution of a so-called Hilbert Problem. However, such calculations are immensely complicated and exceed the theory required for the comprehension of this thesis. Instead, the critical stress intensity factor criterion for fracturing is presented. A derivation is not provided.

A simple crack model, to which more complex problems are frequently reduced, is known as Griffith crack. It originates from the problem of an elliptical opening in a loaded disk (Fig, 2.6, left) if the length of the semi-minor ellipse axis shrinks to zero (right).

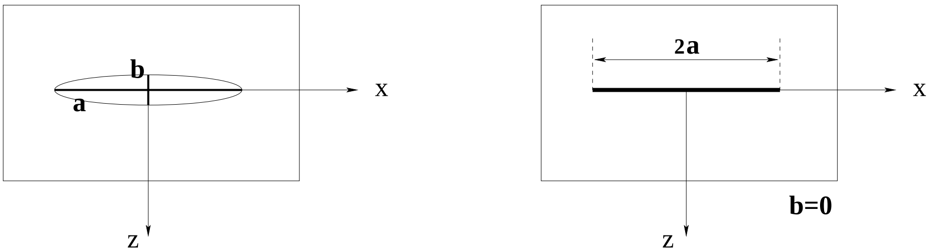

Figure 2.6: Griffith crack (on the right) originating from the problem of an elliptical opening in a loaded disk (on the left); sketch partially after Hahn (1976)

The asymptotic behaviour of the stress field at the crack tip can be approximated by

$$\sigma_{ij} = \frac{1}{\sqrt{2\pi r}} \left[K_I f_{ij}^{I}(\theta) + K_{II} f_{ij}^{II}(\theta) + K_{III} f_{ij}^{III}(\theta) \right] \quad , \tag{2.26}$$

where r and θ are polar coordinates. Eq. (2.26) is exact if the distance from the crack tip r approaches zero and is a good approximation for regions where r is small compared with fracture length. It is characteristic for crack problem solutions in homogeneous, isotropic materials with linear elasticity. The dimensionless functions $f_{ij}^{I}, f_{ij}^{II}, f_{ij}^{III}$ give the dependence of the stress field on the angle θ, whereas the parameters K_I, K_{II}, K_{III} are called stress intensity factors. They indicate the strength of the stress field singularity and include the geometry of the problem as well as the external load. If elasticity is assumed to be linear, stress intensity factors of combined loadings can be obtained by summing of contributions.

The stress intensity factor K_I for the Griffith crack in opening mode is

$$K_I = \sigma_{ex}\sqrt{\pi a} \tag{2.27}$$

with σ_{ex} being the amount of external load and a being the fracture half length.
Since stress intensity factors can be calculated without knowing the exact stress distribution, one can avoid fully solving difficult elastic boundary value problems.

Griffith theory of brittle fracturing

In the Griffith theory of brittle fracturing, the resistance to crack growth coexists with a driving force for crack extension. The resistance is associated with the demand of surface energy for the newly formed crack surfaces, whereas the driving force results from the release of strain energy. Griffith used an energy balance approach which leads to a critical condition for fracturing (Kanninen and Popelar, 1985).
The energy contributions to a fractured sample under external load are as follows:

1. The strain energy U which is stored in the material and generated by an external load U_{ex} and the presence of a crack which disturbs the stress distribution and decreases the elastic energy U_e.
2. The surface energy S of the fracture.

Bueckner (1958) discovered the equivalence of stress intensity factors resulting from external loading on a body and those generated by internal tractions on the crack surfaces. Thus, U_{ex} and U_e are not independent, rather $U_{ex} = -2U_e$ in case of linear elastic material, such that $U = -U_e$.
In this thesis, fractures propagate through mantle and crust; the external load results from the lithostatic gradient as well as from deviatoric stresses of the regional stress field. Additionally, a loading of fracture surfaces is induced by an inner pressure caused by an enclosed fluid mass.

In the case of fracture growth, strain energy is released, but surface energy increases. A premise for unstable fracture growth is that the total potential energy $(U + S)$ must be reduced which means that the elastic energy released during the growth process must exceed the required surface energy. This leads to

$$\begin{aligned} \frac{d}{da}(U+S) &> 0 \quad \text{for a stable crack and} \qquad (2.28)\\ \frac{d}{da}(U+S) &\leq 0 \quad \text{for an unstable crack.} \qquad (2.29) \end{aligned}$$

In the case of a fracture of the length $2a$ contained in an infinite disc loaded by σ_{ex}, the amount of released strain energy is

$$\begin{aligned} U &= -\frac{\pi\sigma_{ex}^2 a^2}{E} \quad \text{for plane stress and} \qquad (2.30)\\ U &= -\frac{\pi\sigma_{ex}^2 a^2(1-\nu^2)}{E} \quad \text{for plane strain.} \qquad (2.31) \end{aligned}$$

The derivation is rather complex, but the meaning is that the homogeneous stress field with an amplitude of σ_{ex} around the fracture is disturbed approximately in a circular region with radius a. In the following, only the case of plane strain is considered.
Since the surface energy in a finite body is $S = 4a\gamma_s$ with γ_s being the specific surface energy, it follows that at the point of instability

$$\frac{d(U+S)}{da} = -\frac{2\pi\sigma_{ex}^2 a(1-\nu^2)}{E} + 4\gamma_s = 0 \qquad (2.32)$$

and hence, the critical parameters are

$$\begin{aligned} \sigma_c &= \sqrt{\frac{2E\gamma_s}{\pi a(1-\nu^2)}} \quad \text{for critical stress and} \qquad (2.33)\\ a_c &= \frac{2E\gamma_s}{\pi(1-\nu^2)\sigma_{ex}^2} \quad \text{for critical half length,} \qquad (2.34) \end{aligned}$$

see also Fig. 2.7. The critical stress σ_c is the maximum safe operating stress in presence of a given crack-size and the critical half length a_c is the maximum safe crack-size at a given stress level (Aliabadi and Rooke, 1991). To test his hypothesis, Griffith carried out laboratory experiments with glass spheres and found a critical fracture length of about 10^{-4} cm as well as a critical stress value of 170 MPa, although the theoretical tensile

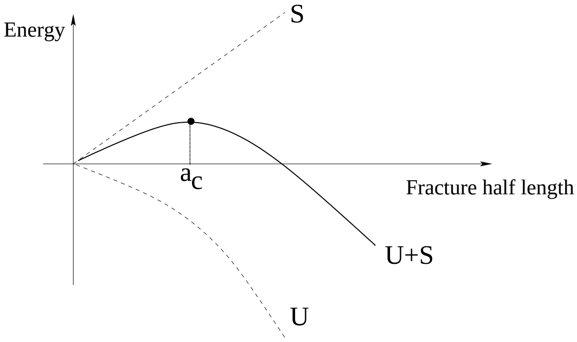

Figure 2.7: In case of fracture growth, strain energy U is released, but surface energy S increases; above critical fracture length $2a_c$, instable crack growth occurs; sketch after Hahn (1976)

strength was significantly higher, that is 2.4 GPa. Differences between theoretical and experimental tensile strengths of materials are caused by macroscopic defects, so-called "Griffith flaws". Therefore, experimental tensile strength depends on sample size and age among other things. Nevertheless in many textbooks, the tensile strengths of rocks is still illustrated as material constant.

Irwin (1948) interpreted Griffith's fracture criterion as local condition which must be fulfilled at the crack tip. Hence, fracture half length a is replaced by infinitesimal length change ∂a. The Griffith fracture criterion becomes

$$-\frac{\partial U}{\partial a} \geq 4\gamma_s \tag{2.35}$$

or

$$\mathcal{G} \geq 2\gamma_s \tag{2.36}$$

with the Griffith force $\mathcal{G}^2$ defined by the change of strain energy with crack length

$$\mathcal{G} = -\frac{1}{2}\frac{\partial U}{\partial a} \quad . \tag{2.37}$$

The crack force satisfies the total energy demands for fracture growth. Unstable crack growth occurs at a critical value of crack force $\mathcal{G}_c$ or stress intensity factor K_c. $\mathcal{G}_c$ and K_c are linked by

$$\mathcal{G}_c = \frac{1}{2}\frac{\pi\sigma_{ex}^2 a(1-\nu^2)}{2\mu(1+\nu)} = K_c^2\,\frac{1-\nu}{4\mu} \quad . \tag{2.38}$$

For a certain material, experimental values for K_c approach a minimum called plane strain fracture toughness K_{Ic} with increasing sample thickness. It is a material parameter which depends strongly on temperature and loading velocity. Standard rules for the determinations of the plane strain fracture toughness are prescribed by the American Society for Testing and Materials (ASTM).

2.2.2 Wholesale propagation of fractures

Fluid-filled cracks may propagate through a medium because of their quasi-buoyancy[3]. Weertman (1971) gives simple estimates of displacements for 2-D cracks, assuming the fractures to have reached a certain length and thus neglecting the surface energy effects which are important in the Griffith theory.

In his view, an open crack can be seen as an array of infinitesimal edge dislocations. The opening is caused by a net displacement D across the plane of the crack. The displacement is linked to the infinitesimal dislocations within the crack by the dislocation density function B

$$B(z) = -\frac{dD(z)}{dz} \qquad \text{and} \tag{2.39}$$

$$D(z) = \int_z^a B(z)dz, \qquad \text{respectively} \tag{2.40}$$

---

[2] The definition of the Griffith force seems to differ by the one from Hahn (1976) given here in some papers such that $\mathcal{G} = -\frac{\partial U}{\partial a}$

[3] The definition of Archimedian buoyancy is limited to the case of a solid body floating in a fluid. Here, it is dealt with a fluid moving through a solid body because of stress gradients. In the strict sense, it is not permitted to speak of "buoyancy", although both terms are equal in magnitude. Nevertheless, it is commonly used.

in case of a crack extending from $-a$ to a with its plane parallel to the z axis. The stress σ_d normal to the plane passing through the crack resulting from the dislocation distribution is

$$\sigma_d(z) = \frac{\mu}{2\pi(1-\nu)} \int_{-a}^{a} \frac{B(z')}{(z-z')} dz' \tag{2.41}$$

and must fulfil the condition

$$\int_{-a}^{a} \frac{\sigma_d(z)}{\sqrt{a^2-z^2}} dz = 0 \tag{2.42}$$

to guarantee a disappearance of stress at infinity.

In Fig. 2.8, a fluid-filled fracture is displayed oriented vertically on the z plane of a plate at a depth of h beneath a surface and being centred at $z = x = 0$. A constant horizontal extensional stress field T exists within the plate. At $z = 0$, the lithostatic pressure is $P_s = \rho_s g h$, elsewhere it is $P_s + \rho_s g z$, where ρ_s is the density of the solid and g is the gravitational acceleration. The lithostatic pressure within the liquid is P_f at $z = 0$ and $P_f + \rho_f g z$ elsewhere, ρ_f being the density of the fluid. It is assumed that $\rho_f < \rho_s$. For $-a < z < a$ it applies that

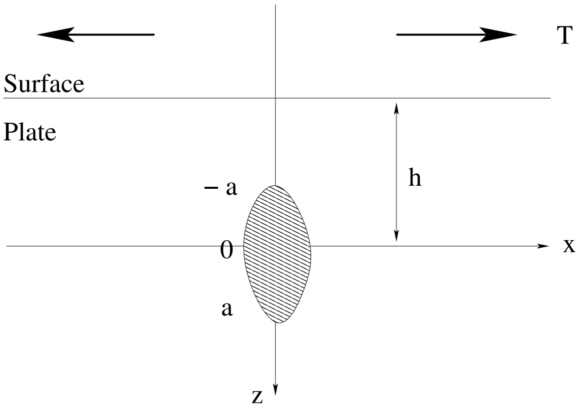

Figure 2.8: Fluid-filled fracture positioned within a plate at depth h beneath the surface and extending from $-a$ to a with its plane parallel to the z axis

$$\sigma_d(z) = -T + P_s - P_f - (\rho_f - \rho_s) g z \tag{2.43}$$

which means that the sum of the stress produced by the dislocations σ_d plus the external stress $T - (P_s + \rho_s g z)$ has to match the normal stress $-(P_f + \rho_f g z)$ exerted by the fluid on the crack surfaces. The displacement of the fracture surfaces is

$$\begin{aligned} D(z) &= \frac{1-\nu}{\mu}\sqrt{a^2-z^2}\,\left[2(T - P_s + P_f) + (\rho_f - \rho_s) g z\right] \quad \text{or} \\ &= \sqrt{a^2-z^2}\,\left[\frac{2V}{\pi a^2} + (\rho_f - \rho_s)\frac{(1-\nu) g z}{\mu}\right] \end{aligned} \tag{2.44}$$

if the volume of the enclosed fluid is taken as

$$V = \int_{-a}^{a} D(z) dz = \frac{(1-\nu)\pi a^2}{\mu}(T - P_s + P_f) \quad . \tag{2.45}$$

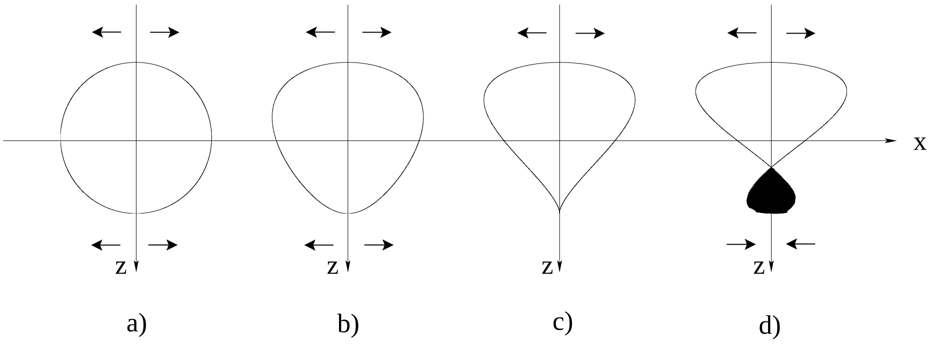

Figure 2.9: Displacements of cracks with half length a increasing from left to right, arrows indicating infinite tensile and compressive stress ahead of crack tip; a), b): $a < a_c$, crack is still growing at both tips, c): crack has reached critical half length, d) crack cannot exist since negative displacement in area shown in black is not allowed physically; horizontal scale greatly exaggerated

If the extensional stress T is constant, the fluid pressure P_f decreases when the fracture grows in length. In Fig. 2.9, displacements are shown for fractures with their half lengths increasing from left to right. A critical half length a_c exists, which the fracture cannot exceed. Only if the fracture length satisfies the inequality

$$a < \sqrt[3]{\frac{2V\mu}{\pi(1-\nu)g(\rho_f - \rho_s)}} \quad , \tag{2.46}$$

the displacement is positive. A negative displacement is not allowed physically. Thus, crack (d) cannot exist since displacement is negative in the area shown in black.

Consider again the fracture depicted in Fig. 2.8. As z approaches $-a$, an infinite tensile stress is generated immediately above the upper crack tip, which breaks the rock ahead of the fracture. The fracture grows in length, the upper crack tip possesses a blunt shape. As z approaches a and $a < a_c$, the infinite tensile stress just below the crack tip breaks the rock to also increase the fracture length. As soon as $a = a_c$, this stress becomes zero; but because the upper crack tip grows continuously, an infinite compressive stress is built up below the lower tip, which closes the fracture and leads to a pointed tail. Thus, the fracture ascends towards the surface in a "tadpole" shape. Weertman (1971) calls this a "break-open, heal-shut, rise-up" behaviour. In order for a non-preexisting fracture to nucleate at the bottom of a plate, a tensile stress is required.

In terms of the stress intensity factor, upper and lower crack tip possess different factors K_I^+ and K_I^-

$$K_I^{\pm} = (P_f \pm P_f \; g \; \frac{a}{2})\sqrt{\pi a} \quad . \tag{2.47}$$

If $P_f = P_f \; g \; \frac{a}{2}$, K_I^- is zero and the crack tip closes (Torsten Dahm, University of Hamburg, personal communication).

Chapter 3

Numerical method

The numerical simulations concerning ascent of magma-filled fractures, both in the mantle (chapter 4, pp. 47) and in the crust (chapter 5, pp. 81), are calculated using a numerical approach based on the boundary element method. The theory, which is described in detail in section 3.1 (pp. 29) was originally constructed to solve elastostatic problems (Crouch, 1976b; Crouch and Starfield, 1983).

Dahm (1996, 2000a, 2000b) developed the boundary element method in several ways. Modifications are described section 3.3 (pp. 35). In this thesis, a quasi-static version was used to simulate the growth and wholesale propagation of fluid-filled fractures to model magma transport (section 3.3.2, pp. 41). Finally, I take into account the interaction between subsequently ascending dykes (section 3.3.3, pp. 43).

The following explanation of the boundary element method is taken from Crouch and Starfield (1983), unless otherwise stated. Boundary value problems can be found in many scientific and engineering areas such as heat and mass transfer, fluid flow, electrostatics and solid mechanics. They are characterised by a region of interest $\mathcal{R}$ limited by a boundary $\mathcal{C}$. The physics of the problem in $\mathcal{R}$ is governed by a partial differential equation which has to be solved including certain constraints or conditions defined on the boundary. Since in this thesis modelling is two-dimensional, $\mathcal{R}$ is a plane region and $\mathcal{C}$ is a bounding contour. Only a few of the relevant parameters are defined at the boundary, others are obtained as a part of the solution of the boundary value problem.

In the case of a homogeneous region of interest $\mathcal{R}$, regular model geometry, simple boundary conditions and linear partial differential equations, the solution to the problem can be achieved analytically. Many singular solutions exist for the case of a point disturbance in an infinite homogeneous region. They can be summed to derive solutions for problems with more than one point disturbance. However, for the most part no such ideal conditions are present and numerical methods must be used to approximate the solution.

Numerical methods for solving boundary value problems can be divided into two classes: those that require approximations to be made throughout the whole region of modelling and those that require approximations to be made only on the boundary of the considered object. Both methods are illustrated in Fig. 3.1.

The first class of problems is often modelled by finite-difference (FD) and finite-element (FE) methods. The whole region of interest $\mathcal{R}$ is subdivided into a network of elements.

Figure 3.1: Difference between finite-difference/finite-element method and boundary element method; left: in FD/FE methods, whole region $\mathcal{R}$ is subdivided into a network of elements; right: in BE method, only the boundary $\mathcal{C}$ is subdivided

Unknown parameters, the nodal values in $\mathcal{R}$, are expressed in terms of known nodal values at the mesh points on the boundary $\mathcal{C}$. Solutions are calculated at the interior mesh points and are approximated between them. This results in a large, but sparse system of equations.

The second class can be modelled by the boundary element method. The idea is that characteristics of a source-free region can be determined from their values on a boundary $\mathcal{C}$. The numerical solution is constructed from the known analytical solutions for simple singular problems such that the specified boundary conditions on $\mathcal{C}$ are approximated. Since each of the singular solutions satisfies the governing partial differential equations in $\mathcal{R}$, there is no need to subdivide the whole region; only the boundary $\mathcal{C}$ is discretised into elements. This results in a small, but dense system of equations.

A boundary value problem is solved in the following manner. First, the boundary $\mathcal{C}$ is subdivided into N elements. An approximate solution is required which satisfies the applied conditions on $\mathcal{C}$ at the midpoints of the elements. Accordingly, N singular solutions are required whose superposition fits the constraints at the midpoint of each element. The "strength" of a single singularity is not known, only the combined effect via the boundary conditions on $\mathcal{C}$. A system of linear algebraic equations can be formed in which the unknowns are the strengths of the singularities. Once these equations are solved, the solution at any point in the region of interest can be constructed. Thus, the points at which the solution is to be computed can be chosen arbitrarily, in contrast to finite-difference or finite-element methods, where results are generated automatically at a number of fixed locations.

In addition, the system of algebraic equations is smaller than in the case of finite-difference or finite-element methods, because fewer nodal values are involved. The resulting matrix is no longer sparse, since each singularity plays a part in every equation. Due to the use of analytically derived solutions which are valid throughout the region $\mathcal{R}$, the boundary element method is potentially more accurate than finite-difference or finite-element methods, where approximations are made in every subdivision of $\mathcal{R}$.

More details about the boundary element method and the variety used in this thesis are revealed in the following section.

3.1 Boundary element method

The boundary element method can be divided into two separate problems: the interior problem, where the region of interest is the finite region inside the boundary $\mathcal{C}$ and the exterior problem, where the region of interest is the infinite region outside the boundary. The interior and the exterior problem are depicted in Fig. 3.2.

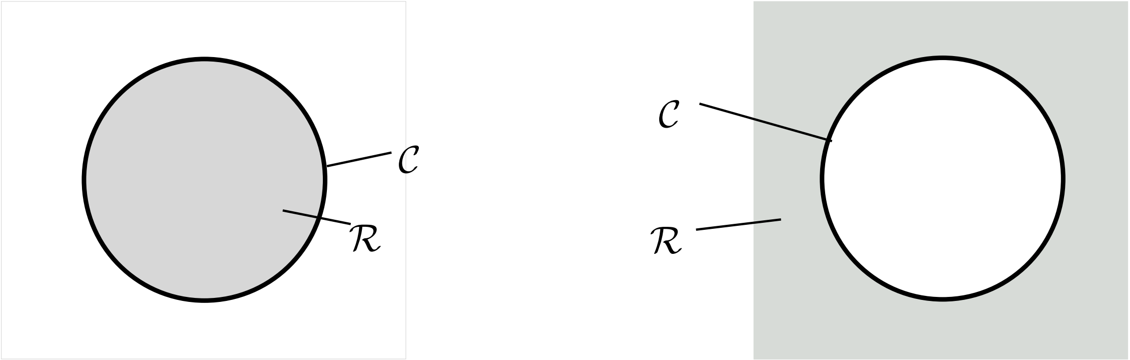

Figure 3.2: Boundary element method; left: interior problem, the region of interest $\mathcal{R}$ lies within boundary $\mathcal{C}$; right: exterior problem, the region of interest $\mathcal{R}$ is the infinite region outside boundary $\mathcal{C}$

Boundary element methods can be further divided into indirect and direct methods. In the case of the indirect method as applied here, the system of equations is solved first for singularities that meet the required boundary conditions. The rest of the boundary parameters, which are not subjected to any constraints, are subsequently computed in terms of these singular solutions. With the direct boundary element method, fundamental integral theorems are used to eliminate the intermediate step; unknown parameters are linked directly to the specified parameters at each segment by the system of algebraic equations.

Exterior problems can be easily used to address the question of a cavity enclosed in an infinite body, where $\mathcal{C}$ describes the cavity walls. This approach is used here to deal with fluid-filled fractures propagating through the host rock. Thus, the circular boundary of the exterior problem shown above on the right is deformed into a crack-like boundary where two surfaces, which coincide at the first instance, obtain a displacement relative to each other which is called displacement discontinuity.

The displacement discontinuity method is based on the analytical solution to the problem of a constant discontinuity in displacement over a finite line segment in the x, z plane of an infinite, elastic solid (see Fig. 3.3 for explanation). The line segment is chosen to lie on the x axis such that $z = 0$. The length of the crack is taken to be $2a$. The crack has two surfaces, one defined to be positive (denoted by $z = 0_+$) and the second to be negative (denoted by $z = 0_-$). When crossing the line segment, the displacements change by a constant value of displacement discontinuity $D_i = (D_x, D_z)$:

$$D_x = u_x(x, 0_-) - u_x(x, 0_+) \tag{3.1}$$

$$D_z = u_z(x, 0_-) - u_z(x, 0_+) \quad , \tag{3.2}$$

where u_x and u_z are absolute displacements in direction of the x and z axes. The displacements u_x, u_z are continuous for $|x| > a$ on $z = 0$, but have constant discontinuities

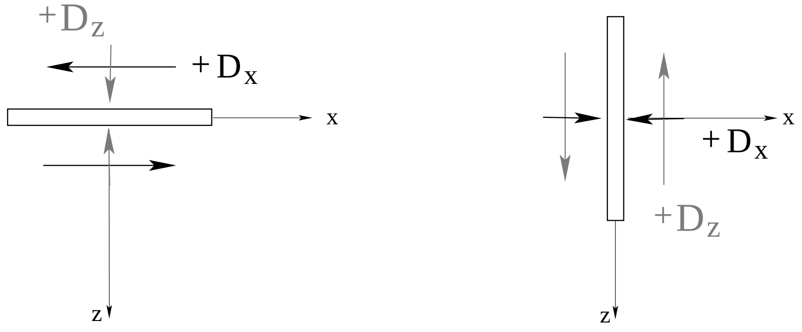

Figure 3.3: Displacement discontinuities D_x indicated in black and D_z marked in grey for horizontal (left) and vertical (right) orientation of fracture; indicated are the displacement directions which result in positive values for discontinuities

D_x, D_z for $|x| < a$. The orientation of positive displacement discontinuities resulting from the above formulas is displayed in Fig. 3.3. A positive value of D_z stands for overlapping surfaces of the crack, which is physically but not mathematically impossible. The analytical solution to the problem of a horizontal crack is given by Crouch (1976a, 1976b) for displacements u_x, u_z

$$\begin{aligned} u_x &= D_x\ [2(1-\nu)f_{,z} - zf_{,xx}] + D_z\ [-(1-2\nu)f_{,x} - zf_{,xz}] \qquad (3.3)\\ u_z &= D_x\ [(1-2\nu)f_{,x} - zf_{,xz}] + D_z\ [2(1-\nu)f_{,z} - zf_{,zz}] \qquad (3.4)\end{aligned}$$

and stresses σ_{xx}, σ_{zz} and σ_{xz}

$$\begin{aligned} \sigma_{xx} &= 2\mu D_x\ [+2f_{,xz} + zf_{,xzz}] + 2GD_z\ [f_{,zz} + zf_{,zzz}] \qquad (3.5)\\ \sigma_{zz} &= 2\mu D_x\ [-zf_{,xzz}] + 2GD_z\ [f_{,zz} - zf_{,zzz}] \qquad (3.6)\\ \sigma_{xz} &= 2\mu D_x\ [f_{,zz} + zf_{,zzz}] + 2GD_z\ [-zf_{,xzz}] \qquad (3.7)\end{aligned}$$

with ν being Poisson's constant and μ being the shear modulus. The function $f(x, z)$ is given by

$$\begin{aligned} f(x,z) = \quad & \frac{1}{4\pi(1-\nu)}\Big[\ z\ (\arctan\frac{z}{x-a} - \arctan\frac{z}{x+a} \\ & -(x-a)\ \ln\sqrt{[(x-a)^2+z^2]} + (x+a)\ \ln\sqrt{[(x+a)^2+z^2]}\ \Big] \qquad (3.8)\end{aligned}$$

and its derivatives can be found in appendix A.2.

Normal stresses σ_{xx} and σ_{zz} depend only on the normal component of the discontinuity displacement D_z, whereas the shear stress σ_{xz} is only connected with the transverse component D_x. Stresses are finite and continuous everywhere except for $x = \pm a$, where they are singular and discontinuous. The solution for the case of displacements situated on the line $z = 0$ is given in appendix A.2, Eqs. (A.18)–(A.26).

In order to use the analytical solutions to numerically derive properties of a fracture situated in a host rock, the fracture is segmented into N so-called boundary elements, each of which represents an elemental displacement discontinuity (Fig. 3.4). The analytical solution of the problem of an elemental displacement discontinuity is used to approximate

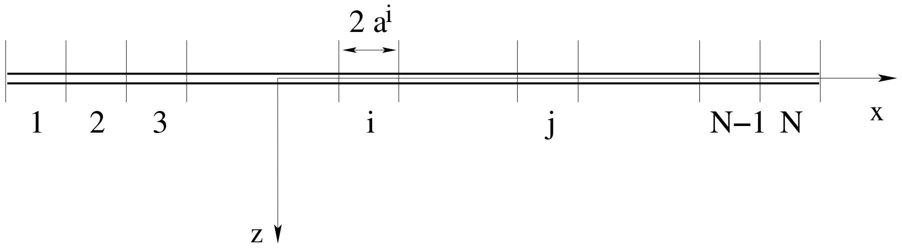

Figure 3.4: Segmentation of a fracture into N boundary elements; x, z denote the global coordinate system

the boundary conditions at the midpoint of each segment. In my work, mostly stress or pressure components at the fracture surface are used to formulate boundary conditions. The displacement discontinuities are the unknowns. Each of the boundary elements i is influenced by all other elements j and influences the behaviour of all other elements.

3.1.1 The problem of a pressurised line crack

I now consider the problem of a pressurised line crack in an infinite body, for which all displacements and stresses are zero at infinity. Fig. 3.3 (left) shows the special case of an horizontal elemental line crack located at $z = 0$ with the length $2a$. Because of the pressure applied inside, e.g. due to an enclosed fluid volume, the fracture opens; thus, only the normal displacement D_z is involved. Compressional pressure is assumed to be positive and extensional negative. The problem is defined by the following conditions:

$$\begin{aligned} \sigma_{xz} &= 0 \qquad -\infty < x < \infty, z = 0 \\ \sigma_{zz} &= P \qquad |x| < a, z = 0 \\ u_z &= 0 \qquad |x| \geq a, z = 0 \quad . \end{aligned}$$

The analytical solution is described by (cp. Eq. A.25, appendix A.2)

$$\sigma_{zz}(x,0) = \frac{-a\ \mu}{\pi(1-\nu)}\ D_z\ \frac{1}{x^2 - a^2} = P \quad .$$

The stress on the fracture surface which corresponds to the normal stress σ_{zz} at the positions $(x, 0)$ is defined to be P. This pressure induces a displacement D_z which in turn causes a stress field to build up in the infinite region around the crack because of elastic deformation of the rock outside the fracture. This stress field is in equilibrium with the pressure applied to the crack surface.

The fracture is segmented into N boundary elements (indices i, j as stated above, q.v. description of Fig. 3.4)

$$\sigma_{zz}(x^i,0) = \frac{-a^j\ \mu}{\pi(1-\nu)}\ D_z^j\ \frac{1}{(x^i - x^j)^2 - (a^j)^2} \tag{3.9}$$

with the length $2a^j$, centred at $x = x^j$. $\sigma_{zz}(x^i, 0)$ is the stress at the midpoint of the ith element due to the displacement at the jth element. The stress at the midpoint of the ith element because of the displacements at all other elements is obtained by the sum

$$\sigma_{zz}(x^i,0) \equiv \sigma_{zz}^i = \sum_{j=1}^{N} A^{ij} D_z^j \tag{3.10}$$

in which the boundary influence coefficients

$$A^{ij} = \frac{-a^j \ \mu}{\pi(1-\nu)} \ \frac{1}{(x^i - x^j)^2 - (a^j)^2} \tag{3.11}$$

are defined. That means a system of N simultaneous linear equations with N unknowns (namely D_z^i from $i = 1$ to N) has to be solved

$$\sigma_{zz}^i = P = \sum_{j=1}^{N} A^{ij} D_z^j, \quad i = 1, \cdots, N \ . \tag{3.12}$$

The singular solution used to construct these equations automatically satisfies the required conditions, e.g. zero displacements at infinity.

Because of arbitrary fracture orientation and possible curvature, a transformation from the global coordinate system in the x, z plane to a local coordinate system with normal and shear components n, s is fulfilled (see Fig. 3.5). It is assumed that the fracture can be approximated with sufficient accuracy by N straight line segments. This leads to two components of stress at the midpoint of the ith element in terms of the displacement discontinuities at the jth element

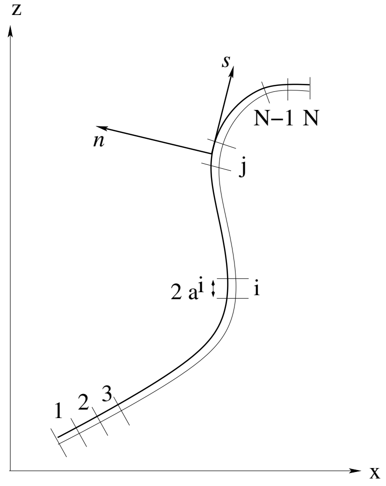

Figure 3.5: Segmentation of a fracture with arbitrary orientation into N boundary elements; x, z denote the global coordinate system, n, s show the local coordinate system

$$\left.\begin{array}{rcl} \sigma_s^i &=& A_{ss}^{ij} D_s^j + A_{sn}^{ij} D_n^j \\ \sigma_n^i &=& A_{ns}^{ij} D_s^j + A_{nn}^{ij} D_n^j \end{array}\right\} i = 1, \cdots, N \tag{3.13}$$

or

$$\left.\begin{array}{rcl} \sigma_s^i &=& \sum_{j=1}^N A_{ss}^{ij} D_s^j + \sum_{j=1}^N A_{sn}^{ij} D_n^j \\ \sigma_n^i &=& \sum_{j=1}^N A_{ns}^{ij} D_s^j + \sum_{j=1}^N A_{nn}^{ij} D_n^j \end{array}\right\} i = 1, \cdots, N \tag{3.14}$$

for shear and normal stresses at the midpoint of the ith element due to the displacement discontinuities at all other elements, which is identical to

$$\begin{pmatrix} \sigma_s^i \\ \sigma_n^i \end{pmatrix} = \begin{pmatrix} A_{ss}^{ij} & A_{sn}^{ij} \\ A_{ns}^{ij} & A_{nn}^{ij} \end{pmatrix} \begin{pmatrix} D_s^j \\ D_n^j \end{pmatrix}, \quad i = 1, \cdots, N \ , \tag{3.15}$$

that is a system of $2N$ simultaneous linear equations with $2N$ unknowns (namely D_n^i and D_s^i from $i = 1$ to N).

Components for normal stress σ_n^i and shear stress σ_s^i are defined for each element (e.g. isotropic pressure as before). Displacement discontinuities along the crack which correspond to the assigned stresses are wanted. The influence coefficients $A_{ss}^{ij}, A_{sn}^{ij}, A_{ns}^{ij}, A_{nn}^{ij}$ can be calculated from model geometry. For example, A_{ns}^{ij} represents the normal stress σ_n^i at the midpoint of the ith element because of a constant unit shear displacement discontinuity $D_s^j = 1$ over the jth element. Matrix inversion gives the remaining unknown normal and shear displacement discontinuities D_n^j, D_s^j at each element.

From those, stress and displacement fields at arbitrary points can be calculated. The displacements along the crack are given by

$$\left.\begin{array}{rcl} u_s^i & = & \sum_{j=1}^N B_{ss}^{ij} D_s^j + \sum_{j=1}^N B_{sn}^{ij} D_n^j \\ u_n^i & = & \sum_{j=1}^N B_{ns}^{ij} D_s^j + \sum_{j=1}^N B_{nn}^{ij} D_n^j \end{array}\right\} i = 1, \cdots, N \ , \tag{3.16}$$

where $B_{ss}^{ij}, B_{sn}^{ij}, B_{ns}^{ij}, B_{nn}^{ij}$ are boundary influence coefficients for displacements. The advantage of the boundary element method is that stress and dislocation fields can be determined at arbitrary points for the infinite region outside the fracture without the restrictions of a predefined model area.

Instead of defining normal and shear stresses for each element, normal and shear displacements on one side of the crack surface can be assigned. It is then searched for normal and shear stresses that must be applied to the ith element to produce the applied displacements. It is even possible to work with mixed boundary conditions in which either u_s^i and σ_n^i or u_n^i and σ_s^i are defined.

Coordinate transformations

Boundary elements are oriented arbitrarily with respect to the global coordinate system and with respect to other boundary elements. The regional stress field as well as geometric parameters (midpoint coordinates of elements, angles of element orientation) are defined in global coordinates, whereas boundary conditions for normal and shear stress are established in local coordinates for each segment. Therefore, coordinate transformations from local to global coordinates and back are required. In the boundary element code used in this thesis, equations for 2-D coordinate transformations are extracted from Crouch and Starfield (1983). In general, such equations can be derived from trigonometrical observations. The transformation from global to local coordinates is depicted in Fig. 3.6. The line segment is situated at $|\bar{x}| \leq a$ and $\bar{z}$=0. A coordinate transformation is performed by rotating and/or translating the coordinate system (e.g. Bronstein *et al.*, 1995); in this case, a rotation by angle β from global (x, z) to local coordinates $(\bar{x}, \bar{z})$ is performed. Local coordinates are described in general and not in the special case of normal and shear components. Fig. A.4 describes the corresponding coordinate transformation of displacements

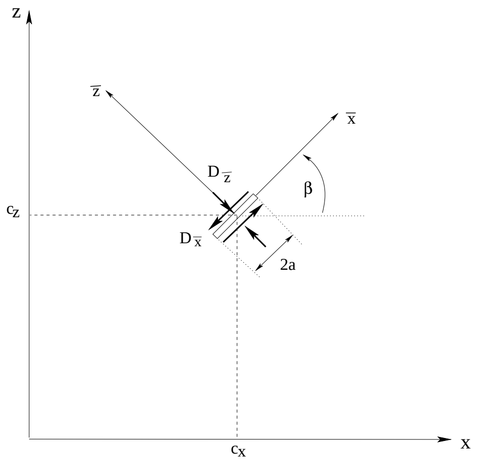

Figure 3.6: Since every boundary element is oriented arbitrarily with respect to the global coordinate system and the other boundary elements, a coordinate transformation from global (x, z) to local coordinates $(\bar{x}, \bar{z})$ is required; sketch after Crouch and Starfield (1983).

and stresses, the corresponding equations are given in appendix A.2.
For an infinite body containing N line segments, which possess an arbitrary orientation with respect to each other, an angle γ can be introduced

$$\gamma = \beta^i - \beta^j \tag{3.17}$$

which gives the inclination of the ith element with respect to the jth element. This can be used to transfer boundary element coefficients directly from the local coordinate system $(\bar{x}^i, \bar{z}^i)$ at the ith element to the local coordinate system $(\bar{x}^j, \bar{z}^j)$ at the jth element.

3.2 Combination of theories

The above-mentioned theories are now implemented in the numerical model. In particular, the energy approach of the Griffith theory of brittle fracturing is combined with the boundary element method. The aim is the analysis of the behaviour of magma-filled fractures ascending through the earth's mantle and crust beneath mid-ocean ridges.

The basis is formed by the theory of linear elastic fracture mechanics and calculations are performed in 2-D. The plane strain case is assumed, which means that dyke extension parallel to the spreading axis is mathematically infinite. In reality, the horizontal dyke is roughly several kilometres in length, but large compared to dyke opening perpendicular to the ridge axis, which is in the order of decimetres to metres.
The energy balance of the crack is computed according to the Griffith theory of brittle fracturing (Griffith, 1921) and the formulation of Irwin (1948). The two crack surfaces are made of boundary elements which are free to open, close or remain unchanged during each iteration. The "break-up, heal-shut, rise-up behaviour" described by Weertman (1971) is established by means of a density difference between the fluid enclosed in the fracture and the surrounding rock. Fracture segments are added in the direction of the maximum strain energy release-rate (also called Griffith force). If an additional amount of energy is

required to keep them open, they are removed. A rock fracture toughness can be defined, but was left out during the calculations done in this thesis.

Some significant modifications were made by Dahm (1996, 2000a, 2000b) to the boundary element method developed by Crouch and Starfield (1983). A more detailed description is available in section 3.3.

- The impact of the fluid mass enclosed in the fracture is considered.
- Opening and closing of crack surface segments are determined by a maximum strain energy release-rate criterion.
- The mathematically possible, but physically meaningless overlapping of fracture surfaces is prevented.
- A transition from a static to a quasi-static code is performed.

The core of the program code for static and quasi-static modelling of fluid-filled fractures is identical. Growth and quasi-static propagation of fluid-filled fractures in regions with inhomogeneous and deviatoric stresses are calculated in two steps. First, the boundary value problem for predefined stresses on the fracture surfaces is solved and afterwards, the resulting surface dislocations are used to evaluate stresses and displacements at arbitrary points in the studied area (Dahm, 2000a). The program flow is as follows:

1. Definition of coordinates of boundary elements and specification of the boundary conditions, which in my case are components of normal traction caused by the magma enclosed in the fracture
2. Calculation of boundary influence coefficients; setup of the system of linear equations in the form of matrices and vectors
3. Solving the problem by matrix inversion, calculation of the unknown variables, i.e. displacements on the fracture surfaces
4. Calculation of boundary influence coefficients and hence the stress and displacement field at arbitrary points

Flow charts can be found in sections 3.3.1 and 3.3.2. The special case of dyke interaction, which constitutes a major task of this thesis, is described in section 3.3.3. To introduce dyke interaction in the analysis of oceanic crust formation, I included additionally in the code

- the influence of stress fields of dykes already ascended and solidified on the propagation path of subsequent dykes.

3.3 Modifications to boundary element approach

In the program code employed in this thesis, the boundary element approach was modified to include the effect of the enclosed fluid mass (e.g. Dahm, 1996, 2000a).

In addition to the elastic deformation of the rock due to the opening of the fracture, the enclosed fluid mass, which is constant during calculation, gives an additional contribution to pressure because of its expansion caused by its compressibility. During fracture ascent, the lithostatic pressure drops from P_0 to $P_1 < P_0$ (see Fig. 3.7 for explanation). The

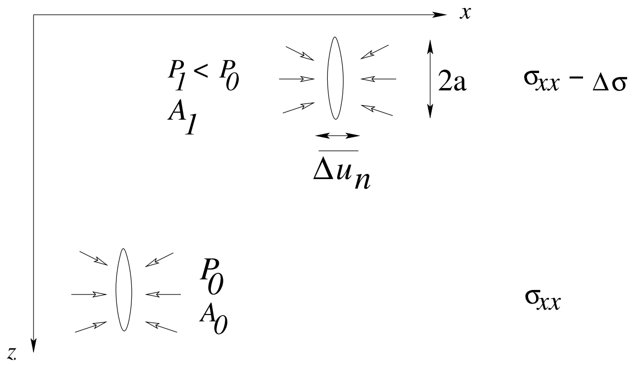

Figure 3.7: During fracture ascent, the lithostatic pressure drops from P_0 to $P_1 < P_0$ and the fracture can open an additional amount Δu_n which in turn increases the fracture surface area from A_0 to A_1

fracture is able to open an additional amount Δu_n which in turn increases the fracture surface area from A_0 to A_1. The pressure difference and the change in area are related by the bulk modulus K which can be expressed in terms of the additional amount of opening Δu_n

$$\Delta P = -K\frac{A_1 - A_0}{A_0} = -K\frac{A_1}{A_0} + K = -K\frac{2a}{A_0}\overline{\Delta u_n} + K \quad . \tag{3.18}$$

The matrix equation (3.15) is extended in its normal component to include the bulk modulus and the term related to the amount of opening

$$\begin{pmatrix} \sigma_s^i \\ \sigma_n^i - K \end{pmatrix} = \begin{pmatrix} A_{ss}^{ij} & A_{sn}^{ij} \\ A_{ns}^{ij} & (A_{nn}^{ij} - K\frac{2a}{A_0}) \end{pmatrix} \begin{pmatrix} D_s^j \\ D_n^j \end{pmatrix} \quad . \tag{3.19}$$

Another important modification of the boundary element approach is the opening and closing of fracture segments to account for the growth or healing of fractures. That means during each iteration, the fracture may open or close or remain unchanged by adding or removing a fluid-filled segment at the tip or end of the fracture. Figure 3.8 shows schematically the outline of a fracture discretised by segments of length δa. Fracture growth occurs at a critical value of crack force $\mathcal{G}_c$ or stress intensity factor K_c (Hahn, 1976). During modelling, a maximum strain energy release-rate criterion determines whether a segment is added or not. If the difference between the strain energy released by the boundary element

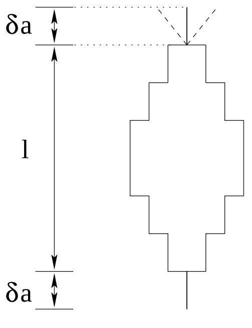

Figure 3.8: Fracture discretised by segments of length δa; segments may open, close or remain unchanged during each iteration

configuration including the newly added tip segment and the previous boundary element configuration is larger than a critical value linked to the rock's fracture toughness, the tip segment is added. If it is zero or even negative, the last tip segment is deleted. The possible orientation of a new boundary element is determined by parabolic interpolation (Press *et al.*, 1989) of the strain energy release about a specified angular range (e.g. ± 10°, since a strong change in propagation direction is unlikely). A wholesale migration of the fractures occurs due to continuous opening at one end and closing at the other. Propagation is controlled by the apparent buoyancy force due to the density difference between magma and surrounding rock and the lithostatic gradient, as well as pressure and stress gradients resulting from the regional stress field. No indication of the propagation velocity is obtainable since the calculation is quasi-static and contains no time variable.

The overlapping of crack surfaces corresponding to a positive value of the displacement discontinuity normal to the surfaces is mathematically possible, but physically meaningless. Dahm (2000a) introduced a positivity constraint by using the non-negative least square method (NNLS) developed by Lawson and Hanson (1974). Eq. (3.19) is solved with the inequality constraint $-D_n^j \geq 0$ as a side condition such that negative normal displacements corresponding to positive displacement discontinuities are not allowed (see also Fig. 3.3). Hence, situations as in Fig. 2.9 (d) (section 2.2.2, p. 26) are avoided automatically.

3.3.1 Fluid-filled fracture growth

The FORTRAN program code to calculate both the behaviour of static and propagating fractures by the method of boundary elements was provided by Dahm (1996, 2000a, 2000b). I adapted the routines to different geological situations. All variations are based upon the static program code named *"bem2d.f"*, which is explained by means of a simplified flow chart in Fig. 3.15 on p. 44 at the end of this chapter.

First, the input file is read. It contains parameters of rock properties (e.g. Poisson's ratio, shear modulus, regional stress field), magma properties (e.g. compressibility) as well as boundary conditions (e.g. traction on crack surfaces) and geometry of the problem (e.g. location of endpoints of boundary segments, surface area of fracture; for details, see input file in appendix B.1). Subsequently, the location of boundary elements is defined. Tail and tip of segments are converted in midpoint coordinates and the angle between local and global coordinate systems is calculated. New boundary conditions are formed which contain the regional stress field including horizontal and vertical gradients. During my calculations, mostly vertical gradients are used to imply lithostatic gradients. Boundary conditions are expressed in normal and shear components.

Boundary influence coefficients are computed in several steps. Segments are subdivided into two groups: boundary elements forming interfaces and boundary elements located within layers. Since layered media are not considered in my model, no boundary elements are used to describe interfaces. If layer interfaces are required, e.g. as level of neutral buoyancy, density layering is introduced which manifests itself only in a change of slope of the lithostatic gradient.

The calculation of the boundary coefficients comprises computation of Green's functions u_x, u_z, σ_{xx}, σ_{xz}, σ_{zz} and the rotation of the coefficients by the angle γ (Eq. 3.17). The system of algebraic equations is laid out in form of matrices and vectors. The first matrix contains the boundary influence coefficients $A^{ij}_{s,n}$ (Eqs. 3.11, 3.14), whereas the vector holds the boundary conditions (in this case, normal and shear traction on crack surfaces). A second matrix contains boundary influence coefficients $B^{ij}_{s,n}$ (Eq. 3.16). After balancing and preconditioning, the first matrix is inverted. Routines used are common Fortran *LAPACK*-libraries (LAPACK, 1994) and are not described in detail. Afterwards, unknown variables – the displacements at the crack surfaces – are calculated from the solution with the help of the second matrix.

In Fig. 3.9, normal and shear displacements at "left" and "right" crack surfaces are depicted. The crack starts at 9 km depth and finishes at 11 km depth. It is subdivided into 20 boundary elements. Fluid density is assumed to be 2700 kg/m^3, which is realistic for basaltic melts. If normal traction is defined at the boundary elements (top row), normal displacement occurs which naturally is largest in the middle of the fracture. Simultaneously, a shear displacement takes place which should not be interpreted in terms of a "real" movement between the two sides of the fracture, but which is the same for both surfaces and is caused by contraction of the crack perpendicular to the opening direction. In the case of shear traction defined at the boundary elements (bottom row), a shear displacement occurs, that means the "left" side of the fracture moves down whereas the "right" side of the fracture moves up. Both surfaces of the crack feature the same apparent normal displacement which is generated by a slight rotation of the fracture (fracture tail moves to the left, fracture tip to the right).

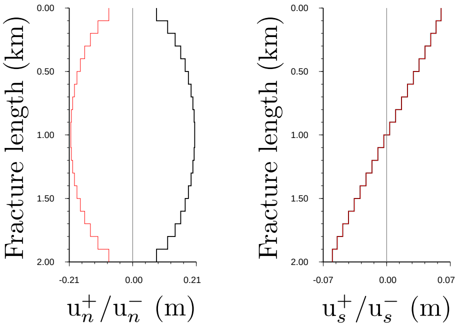

Normal traction defined at boundary elements

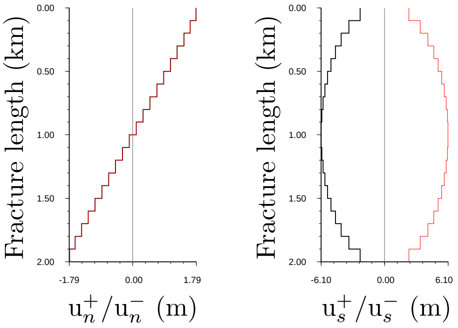

Shear traction defined at boundary elements

Figure 3.9: Normal and shear displacements at crack surfaces; black and red line refer to "left" and "right" surface of fracture; left: normal displacement; right: shear displacement; top: normal traction at boundary elements is defined, bottom: shear displacement is assigned

Because of the vertical extension of the crack, a gradient in the fluid pressure develops, which is depicted in Fig. 3.10 (top). The fracture opening is wider at its base due to the higher inner pressure. This corresponds to a fracture lying above the level of neutral buoyancy, where the lithostatic gradient is smaller than the gradient of inner hydrostatic pressure. Further, a lithostatic gradient is introduced because of the overlying rock; this is demonstrated shown in Fig. 3.10 (bottom), where an additional lithostatic gradient is applied, which corresponds to a rock density of 3000 kg/m^3. The opening of the fracture is broader at its top, where the ratio of inner and outer pressure is more advantageous than at its base. In the middle row of Fig. 3.10, a fracture is placed at its level of neutral buoyancy (created by a rock density change from 2400 kg/m^3 in the upper layer to 3000 kg/m^3 in the lower halfspace). The result is very similar to a fracture with a constant inner pressure (cp. Fig. 3.9, top), but normal displacements are slightly asymmetric and

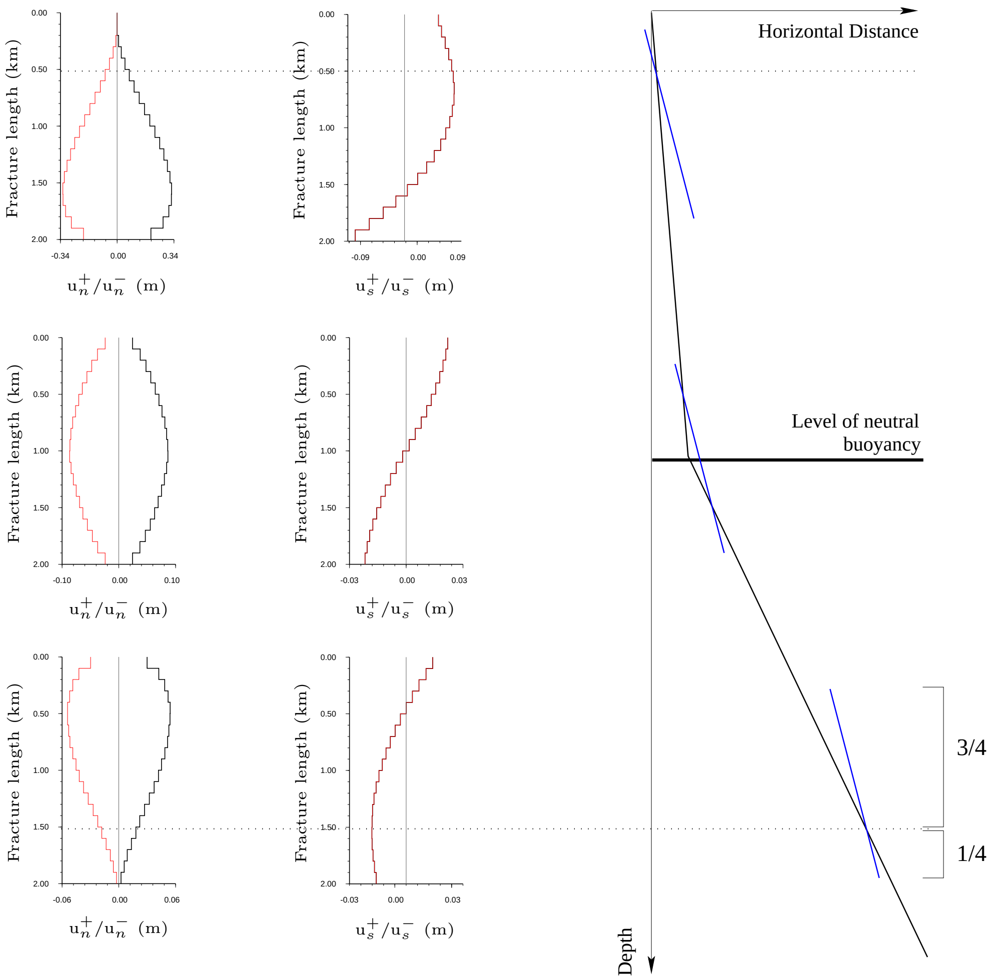

Figure 3.10: Normal and shear displacements at crack surfaces under influence of lithostatic and hydrostatic pressure gradients; left: normal displacement, middle: shear displacement, right: sketch of appropriate geological situation, lithostatic gradient in black, hydrostatic pressure in the fracture shown in blue; top row: only fluid pressure gradient introduced, middle row: fluid pressure and lithostatic gradient applied, fracture is situated at level of neutral buoyancy, bottom row: lithostatic gradient and fluid pressure adopted, fracture located below level of neutral buoyancy

shear displacements cease to be entirely linear. Lithostatic gradient as well as hydrostatic gradient are shown on the right. The fracture length ratio of 3/4 : 1/4 above and beneath the intersection of pressure gradients is derived from Dahm (2000b).
If desired, displacement and stress fields can be calculated at arbitrary points in the infinite area outside the fracture. Appropriate boundary influence coefficients for relative positions of chosen points and fracture segments have to be computed. In Fig. 3.11, the displacement and stress fields are shown for the case of normal traction defined at the boundary elements according to the conditions of Fig. 3.9, top row. Displacement and stress have their highest magnitude near the fracture and decay with distance. Displacement is largest in the horizontal plane through the midpoint of the crack. The above-mentioned contraction is clearly visible above and below the fracture. The stress field is presented in the principle axis system and is largest at the crack tips. To the left and right of the fracture, compressive stress is horizontal because of the opening, whereas above and below the crack, extensional stress is horizontal.

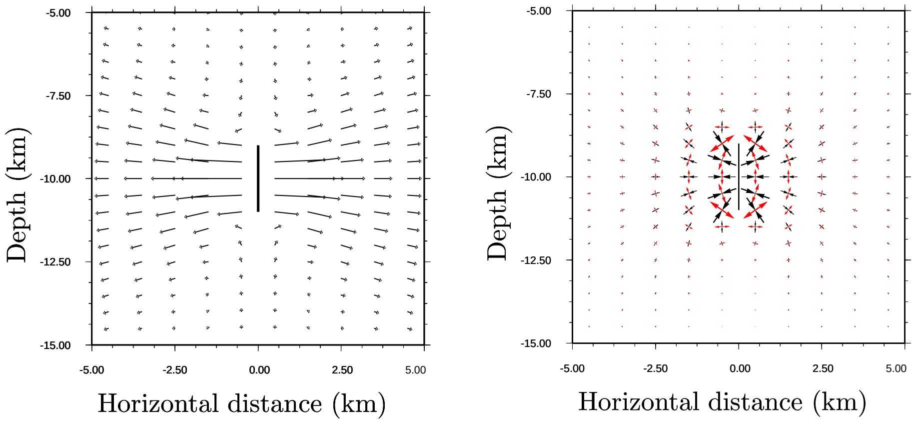

Figure 3.11: Displacement and stress field at arbitrary points outside the fracture caused by normal traction defined at boundary elements; left: displacement field, amount and orientation of displacement indicated by arrows; right: stress field, principal axis of compression indicated by black, principal axis of extension shown by red arrows

In Fig. 3.12, the displacement and stress fields are shown for the case of shear traction defined at the boundary elements (cp. Fig. 3.9, bottom row). The displacement of both fracture sides down- and upwards is clearly visible as well as the above mentioned rotation. The stress field displays shearing alongside the fracture, where principal axis of compression and extension are oriented 45° to the horizontal axis. Because of the rotation, large values of compression are visible left of the fracture tail and right of the fracture tip, whereas right of the fracture tail and left of the fracture tip, high extension can be found. In these diagrams, crack openings are not shown, since they are much smaller than the length.
Laboratory experiments can further help the understanding of dyke propagation (Takada, 1990; Heimpel and Olson, 1994; Ito and Martel, 2002; Rivalta *et al.*, 2005). In Fig. 3.13, taken from laboratory experiments carried out by Rivalta *et al.* (2005), the physical dimensions of an air-filled dyke ascending in gelatine can be observed. The width, the vertical length and the horizontal length of the fracture are indicated by w, $2a$ and l respectively. The fracture openings displayed e.g. in Fig. 3.9 corresponds to w and represent cross-

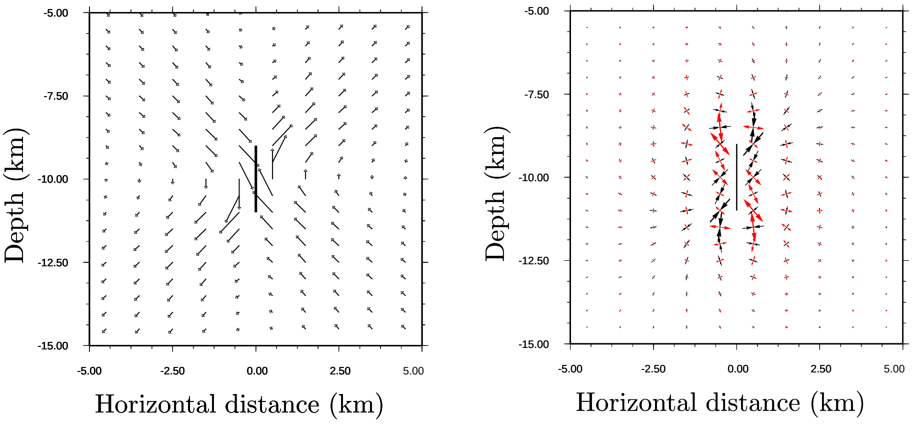

Figure 3.12: Displacement and stress field at arbitrary points outside the fracture caused by shear traction defined at boundary elements; left: displacement field, right: stress field

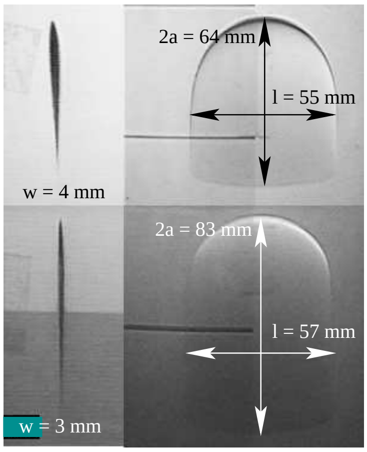

Figure 3.13: Shape of air-filled dyke in gelatine; width as well as vertical and horizontal length of the fracture are indicated by $w, 2a$ and l; laboratory experiments conducted by Rivalta *et al.* (2005)

sections through the dyke. Note that fractures extend to a much larger distance along the spreading axis (equivalent to l). Horizontal fracture length l is assumed to be infinite in my modelling such that the plane strain state can be adopted, since it extends parallel to the spreading axis of the mid-ocean ridge. Dimensions can not be scaled directly to a magma-filled dyke in the crust, since the elastic moduli are different.

3.3.2 Fluid-filled fracture propagation

The static simulation of fluid-filled fractures can be helpful to visualise the effect of a fracture getting stuck in its surroundings, for example at the level of neutral buoyancy. For "observation" of fracture propagation through the mantle and crust, a quasi-static simulation is required. The necessary changes to the afore mentioned program code are illustrated in the flow chart 3.16 on p. 45.

Obviously, an iteration mechanism is needed. It is not introduced in the main code, but into an external script such that the main code is processed iteratively. In order to simulate focussing of fractures in the mantle (see chapter 4, pp. 47), a number of maximum iterations is carried out independent of fracture position. Later, when an arrest of fractures at a level of neutral buoyancy is imposed to study fracture ascent in the crust (see chapter 5, pp. 81), iterations are stopped when fractures cease to change position (see flow chart 3.17). The next dyke starts to rise automatically.

As mentioned in section 3.3, a wholesale migration of fractures occurs due to continuous opening of new fracture tip segments and simultaneous closing at the tail. The direction of appended fracture segments is derived from a maximum strain-energy release-rate criterion; the maximum is found by using a parabolic interpolation across a pre-set angular range and is imbedded in the main program. The stress field is calculated only at required points, this means the current tip positions. They can be calculated for every single dyke position and the whole area of modelling after computation of the fracture ascent path is completed. Position and boundary conditions for the new tip segment are inserted in the input file by an auxiliary routine. Fig. 3.14 shows the ascent path of a fracture depicted by a black line. The initial position of the crack is indicated by a blue line, the end position at the level of neutral buoyancy by a red line. In the model, an initial fracture area (equivalent to a crack volume in 2-D) instead of its length is defined. The actual length results from this area, the ratio between inner and outer pressure and the magma's bulk modulus. If no external stress field exists, the fracture ascent is vertical due to the buoyancy of the enclosed fluid, whose density in general is smaller than the density of the surrounding rock.

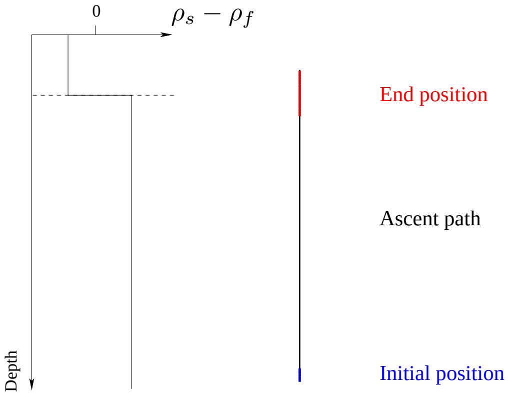

Figure 3.14: Example of fracture propagation path finishing at the LNB; black: ascent path, blue: initial position in depth, red: end position

In both instances of fracture ascent studied in this thesis, the background stress field plays an important role. In the case of ascent in the mantle, the stress field results from rock deformation because of convection. Fractures act independently of each other. In the case of propagation in the crust, the stress field is generated by previously ascended fractures. In most figures displayed in the following chapters, fracture ascent paths and stress fields are depicted.

3.3.3 Simulation of dyke interaction

Dykes which are close together influence each others behaviour. Even in static simulations, fractures are no longer able to open freely if the distance between them becomes too small. Instead, their opening depends on the stress field caused by the opening of other cracks and vice versa. As in the case of two vertical, parallel fractures, their "inner" surfaces experience a minor amount of displacement compared to the "outer" surfaces.
Two fractures ascending simultaneously attract each other, the smaller joining the larger (Ito and Martel, 2002). In chapter 5, the reaction of ascending cracks to the stress field produced by fractures risen previously is analysed. As long as no regional stress field is present, they tend to focus towards one another. The assumption is made that the first dyke solidifies completely before the ascent of the next dyke, but that its stress field is maintained. That means that the time span of solidification is much shorter than the recurrence time of dyke ascent, and this in turn falls below the time of viscoelastic relaxation. In section 5.1 (pp. 84), the tenability of this premise is demonstrated. The solidification of a dyke occurs in a period of time ranging from days to months. The recurrence time is in the range of a few years to a century at most, whereas the viscoelastic decay of a stress field takes place on a time scale of centuries or even millennia, depending on the viscosity of the rock. A freezing of the dyke on its way to the surface is omitted as well, since dykes can reach ascent velocities in the order of m/s. Estimates about ascent times from volcanological observations are given in chapter 4.

To examine dyke interaction, the stress field of the dyke which has ascended previously and arrested at the level of neutral buoyancy has to be preserved. The influence of the solidification process on the magnitude of the stress field is neglected. An advantage of the boundary element method is that not the whole modelling region is discretised, but only the fracture surfaces. Stress and displacement fields can be computed with high accuracy at any point outside the fracture. I made the most out of it by developing a method not storing the stress field directly. This approach has the major advantage that a heterogeneous stress field must not be gridded and afterwards interpolated to intergrid points, which would introduce further approximations. Only the geometry of segments (midpoint coordinates, angle to global coordinate system, segment length) as well as the normal and shear displacement discontinuities are saved to a file. At the time of the next dyke ascent, the main program reads these parameters in and computes the stress field generated by displacements at boundary elements of previously ascended dykes at the required point, e.g. the crack tip of currently ascending dyke. This stress field is added to the background stress field which consists of the lithostatic gradient and may contain a regional stress field additionally. Since the equations involved in stress field computation are linear, a stress field generated by the opening of several dykes being situated at the level of neutral buoyancy can be easily calculated by summation of the individual parts. The arbitrary heterogeneous stress field resulting from the presence of one up to a multitude of previously ascended dykes can thus be calculated precisely at every point with the precision of the boundary element initialisation. Computation time and storage requirements are reduced by recording only a few parameters at the boundary element positions compared to saving the whole stress field at prefixed locations.

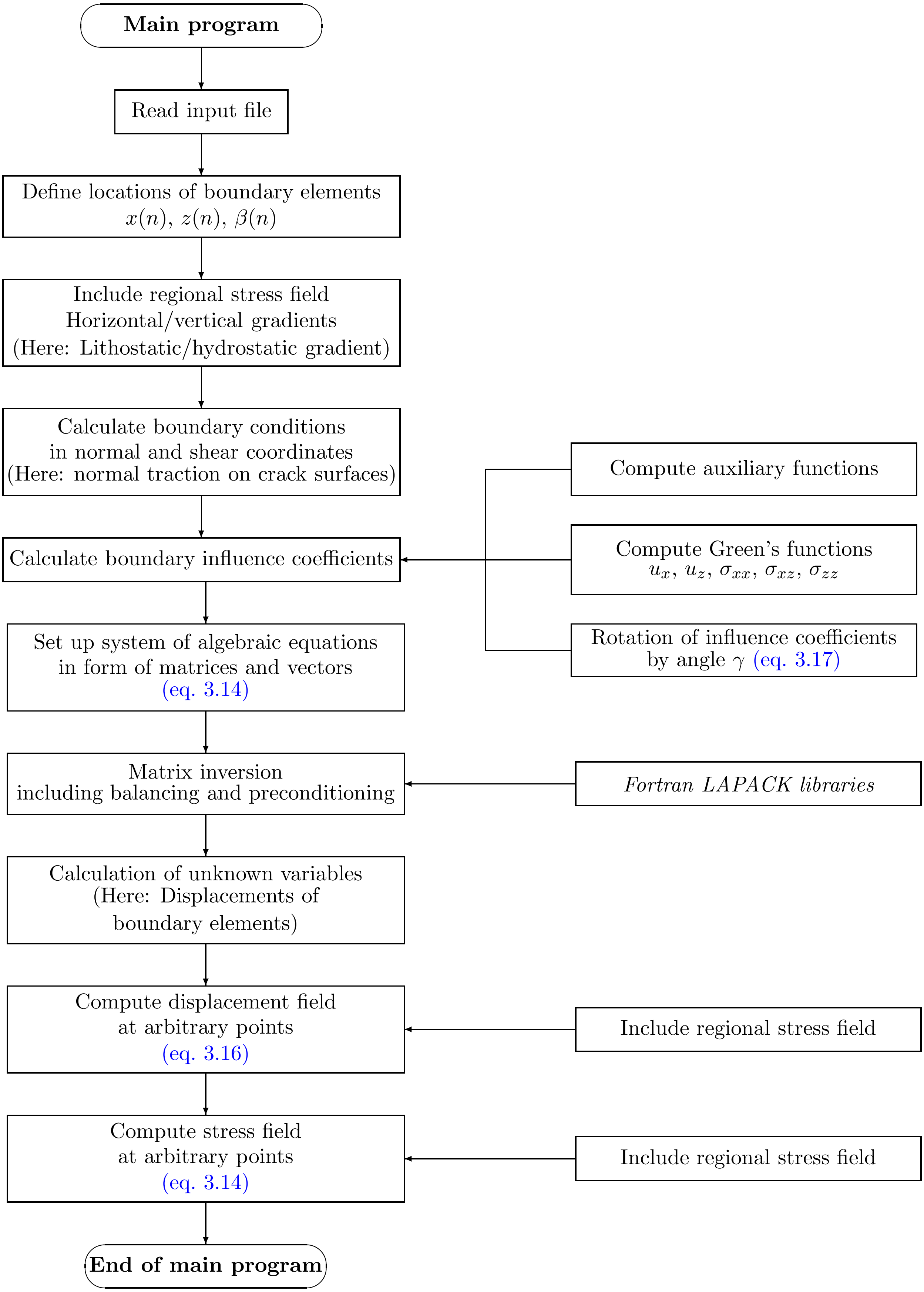

Figure 3.15: Program flow chart for static simulations of fluid-filled fractures with Fortran program **bem2d.f**

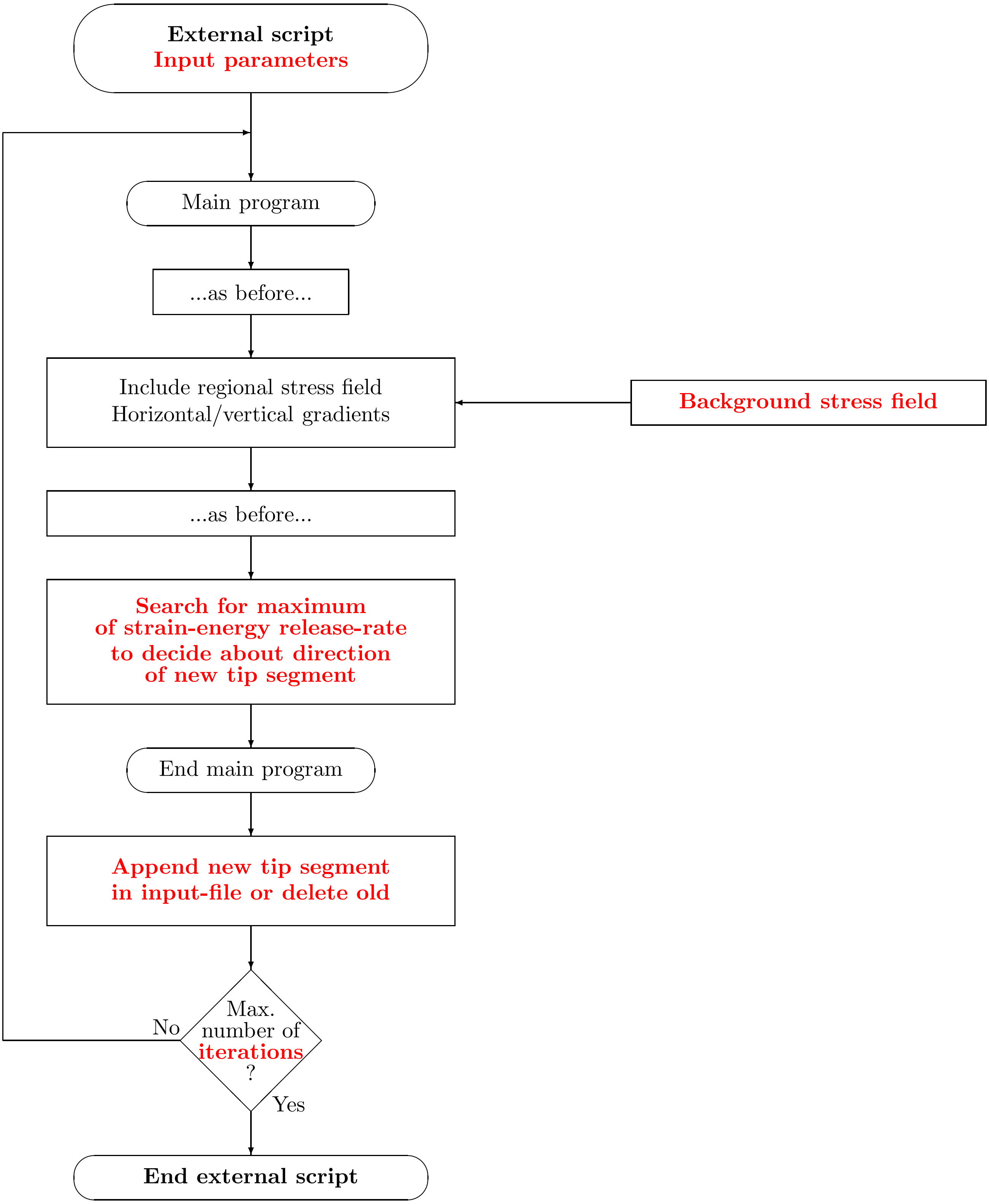

Figure 3.16: Program flow chart for quasi-static simulations of fluid-filled fractures with Fortran program **bem2dgrow.f**

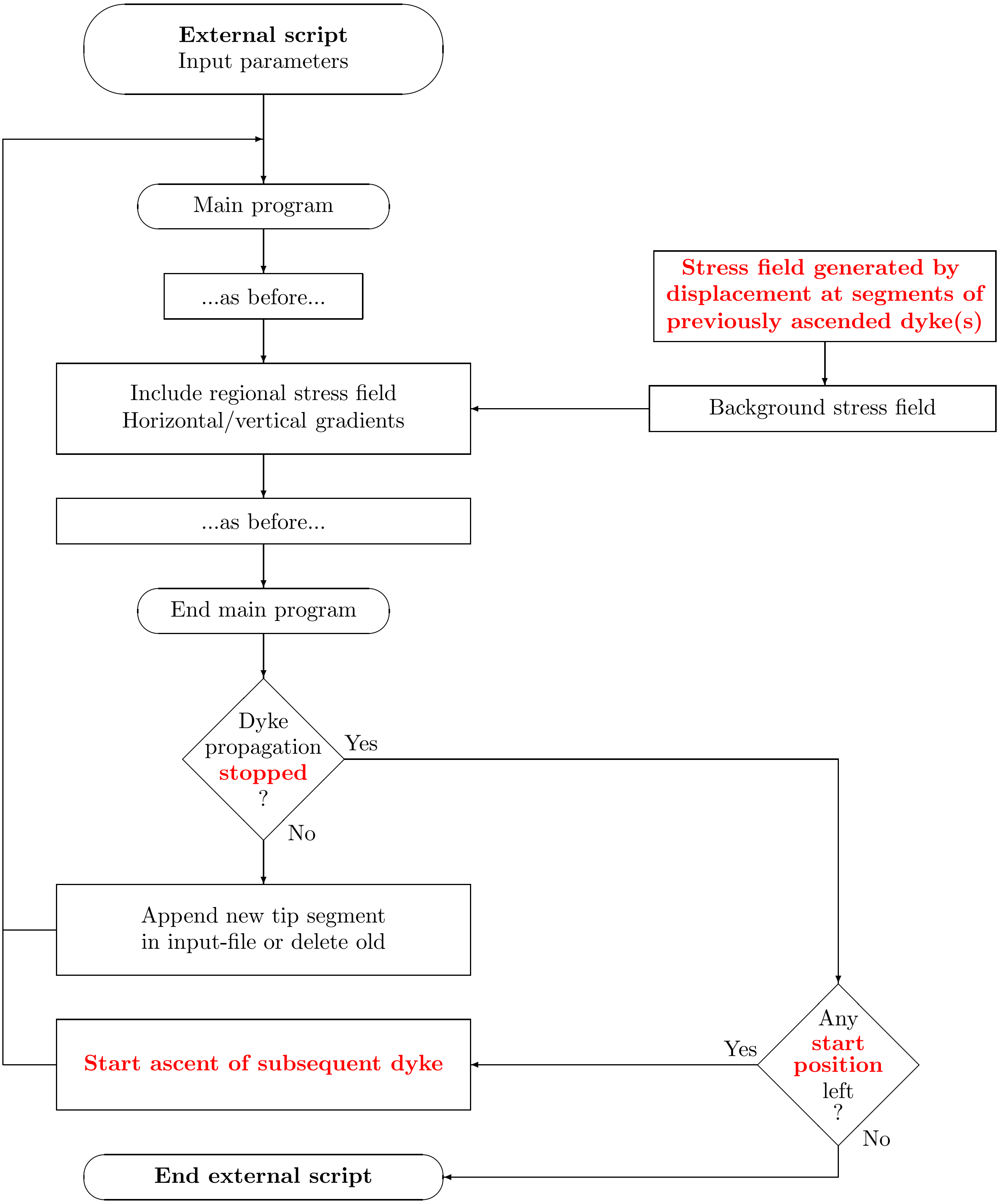

Figure 3.17: Program flow chart for dyke interaction with Fortran program **bem2ddyke.f**

Chapter 4

Magma ascent in the mantle

This chapter concentrates on the simulation of the magma ascent in the earth's mantle beneath oceanic spreading centres. The general mechanism of the formation of oceanic crust is well known and is related to the separation of plates at mid-ocean ridges. Mantle material ascends and partial melting occurs due to adiabatic decompression of the mantle rock. Magma may be stored temporarily in high-level magma chambers beneath the ridge axis, thereby intruding into the rift between the plates and solidifying. These are thought to be non-permanent and extremely small beneath slow-spreading ridges, and permanent and large beneath fast-spreading ridges.
Although the melting zone at depth extends up to several hundreds of kilometres laterally, the extrusion area at the spreading axis is confined to a narrow belt, only two to three kilometres in width. The mechanism of melt focussing and extraction from the mantle beneath mid-ocean ridges is still poorly understood, despite the important role of the process for the formation of crust and for plate tectonics.
Using numerical simulations, I study the ascent paths of magma-filled dykes under various stress conditions. In contrast to previous models, I consider effects of stress and pressure gradients, buoyancy and enclosed finite fluid mass. With a similar model, Dahm (2000a) simulates the propagation paths of magma at subduction zones. The passive motion of the mantle due to plate spreading is modelled assuming an isothermal 2-D corner flow. An isotropic dynamic pressure is produced as well as a deviatoric stress field. To my knowledge, the ascent of fluid-filled fractures at mid-ocean ridges has not been studied before in such complexity.

In the first section, geological, geophysical and geochemical observations at mid-ocean ridges are introduced and the theoretical background of mantle corner flow is explained. The melt ascent models presented here follow the idea of a mantle corner flow, that means a passive motion of the mantle driven by the spreading of oceanic plates at the mid-ocean ridge. This motion is responsible for the formation of pressure and stress gradients which in turn control the magma transport.
Section 4.3 deals with the magma ascent models. The first assumes magma migration by the propagation of fluid-filled fractures (section 4.3.1, pp. 61). Evidence of fracturing in the mantle is supported by examinations of the Oman ophiolite. Hydrostatic fracturing has previously been proposed as a model of melt extraction from the mantle rocks (Nicolas

and Jackson, 1982; Nicolas, 1986; Sleep, 1988; Rubin, 1998), but these models mostly fail to include the effects of the fluid pressure of the magma enclosed in the fracture.
The fluid-filled fracture model is compared with the model of porous melt flow from Spiegelman and McKenzie (1987) and Phipps Morgan (1987) in section 4.3.2 on pp. 65, where the partial melt is moving through the connected pore space of the mantle rock. The theory of focussed flow of melt in dunite channels of Kelemen *et al.* (1995, 1997) is based on examinations of the Oman ophiolite and is addressed in section 4.3.3 on pp. 72. The chapter ends with a discussion of the advantages and disadvantages of the individual models comprising extended approaches.

4.1 Observations and constraints

Geoscientific experiments are conducted at mid-ocean ridges to gain further insight into the processes occurring in the mantle and the crust. Investigations involve dredging which has the disadvantage that no stratigraphic control is exercised and that rock is frequently gathered from anomalous areas such as fault scarps. In most cases, deep-sea drilling involves only the upper crustal layers. A variety of marine geophysical data are acquired such as reflection and refraction seismics, electric, magnetic and gravimetry. In recent times, expeditions using manned submersibles have been launched. Ophiolites, representing obducted ancient oceanic crust are yet another possibility to study crustal structure and crust-forming mechanisms.

Geological background

Oceanic crust forms at mid-ocean ridges. Mid-ocean ridge basalts (MORB) represent the largest volume of eruptive rocks on the earth (Wilson, 1989). A geological model of the oceanic crust is given in Fig. 4.1. The uppermost layer (layer 1) consists of abyssal sediments. Layer 2 contains basalts; the lava extruding at the seafloor solidifies in pillow formations whereas the magma intruding between the separating plates consolidates in the form of vertical dykes (sheeted dyke complex). These dykes extend parallel to the ridge axis and have a thickness of several decimetres to several metres perpendicular to the axis. The magma beneath cools down and forms a gabbroic layer (layer 3). The undermost layer – separated from the gabbro layer by the Moho – is composed of ultrabasic peridotites which represent residual mantle rock.

Magma dykes are among the most important structural elements of the oceanic crust. Surface volcanism takes place at a few distinct regions at the spreading axis itself, but the bulk of magma solidifies in the form of sheeted dykes and intrusions at greater depth in the crust (Wilson, 1989). The role of dykes and diking at mantle depth is still unclear. Geophysical observations are not possible, because dyke propagation generates no seismic signal during the ascent in the mantle and the effects of dyke emplacement are too small to produce measurable ocean-floor deformation.
The majority of the oceanic crust is formed at a distance less than 2 km away from the ridge axis with an average thickness of about 6 km. Plank *et al.* (1995) describe the extent of partial melting in the mantle beneath mid-ocean ridges as a fundamental

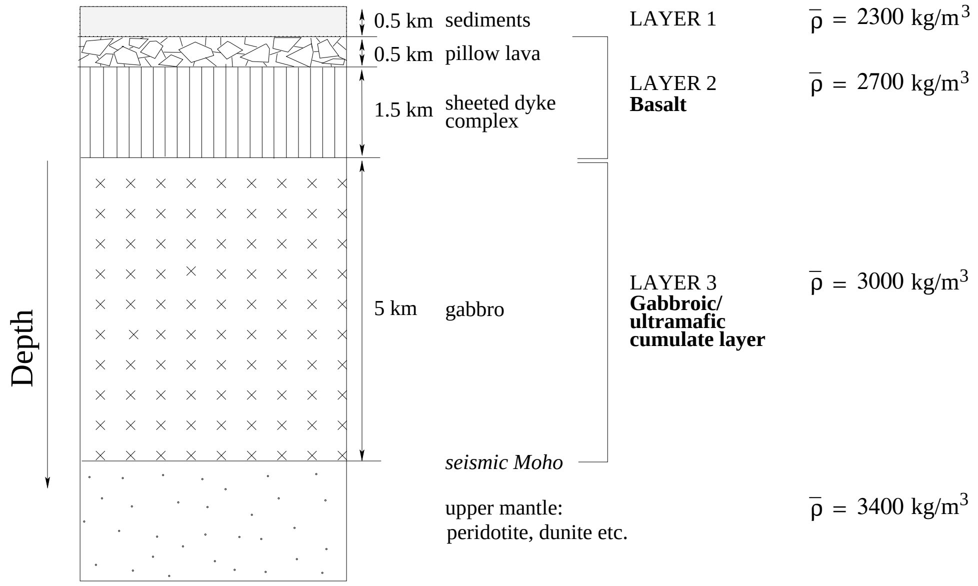

Figure 4.1: Distinct layers of a typical oceanic crust (after Wilson, 1989)

parameter for both the composition of the mid-ocean ridge basalts and the thickness of the crust. This parameter is not easy to derive, since the mantle undergoes partial melting to different degrees at different depths throughout a large melting region. Furthermore, the mean extent of melting depends on the type of the melting model (e.g. passive/active upwelling, fractional/batch melting, complete/incomplete focussing, depth at which the melting ceases below the crust). As a rule of thumb, the crustal thickness is the product of the bulk degree of melting times the depth of the solidus (in general unknown) measured from the base of the crust as long as no melt is retained in the mantle (Plank *et al.*, 1995).

Geophysical work

The Mantle Electromagnetic and Tomography (MELT) Experiment (Forsyth *et al.*, 1998a) was conducted at the East Pacific Rise to explore magma flow beneath mid-ocean ridges, and in particular to distinguish between passive and active flow models. Passive flow is driven by plate spreading which brings about a broad zone of upwelling and melt production. The melt migrates at right angles to the ridge axis. Active flow is driven by buoyancy. The density reduction induced by melt extraction from the mantle as well as the decrease in viscosity in the upwelling zone may lead to focussed upwelling and melting in a narrow zone. The melt is transported mainly vertically and the convective pattern is likely to be 3-D with distinct upwelling centres. Further investigations have been concerned with the extent in depth of the melting zone and its geometry. Preliminary results (Fig. 4.2) show an asymmetry across the ridge, where the Pacific plate to the west has twice the spreading velocity of the Nazca plate to the east. However, this asymmetry is not included in my modelling; only the general results from the various seismic techniques are considered to deduce values for the modelling parameters.

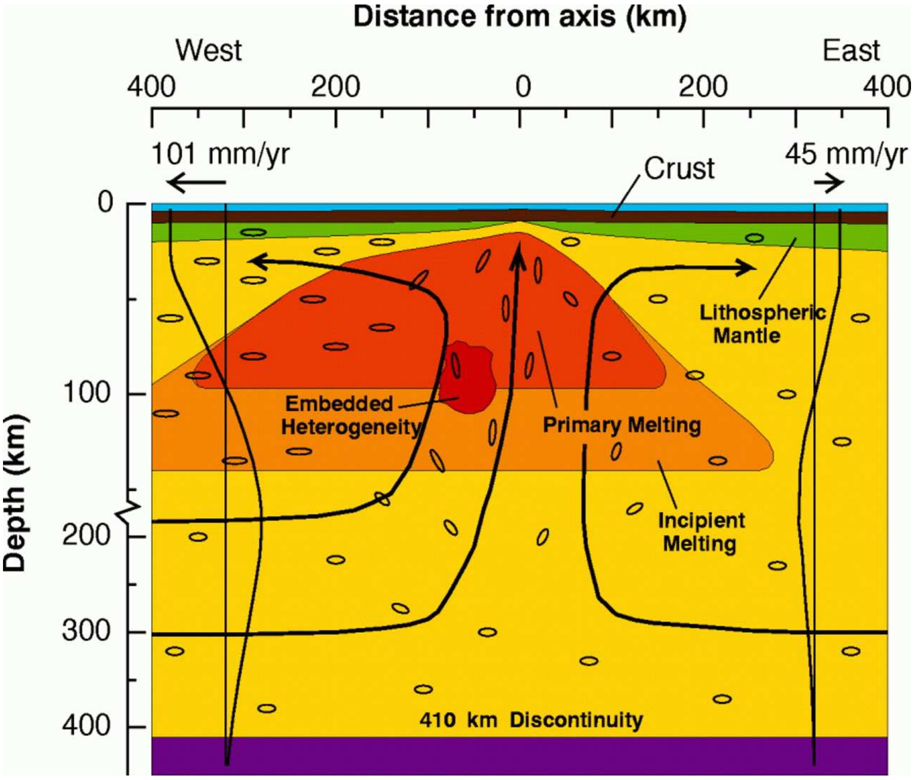

Figure 4.2: Schematic cross-section of the East Pacific Rise; regions of primary and incipient melting indicated, mantle flow lines are shown; the plate spreading velocities are asymmetric across the ridge, solid lines beneath velocity arrows specify possible vertical profiles of horizontal velocities away from the ridge axis; ellipses display direction of preferred alignment of olivine a axes, the faster motion of the pacific plate is assumed to produce greater shear stress; figure taken from Forsyth *et al.* (1998a)

Maps of large phase velocity changes of Rayleigh waves indicate melt in the depth range of 15–70 km. The results of the waveform inversion of regional events (Webb and Forsyth, 1998) show the presence of a low-velocity zone extending to depths greater than 100 km. Melting may either taper off at about 180 km or finish sharply at depths between 130–160 km. The velocity decrease corresponds to a melt fraction of about 1–5 %. An extension of the melting zone to depths greater than 100 km would also be required to fit results from tomographic experiments modelling P and S wave delays.

Receiver functions from teleseismic body waves are used to examine the structure of the 410- and 660-km phase boundaries (representing the exothermic transition from α- to β-phase and the endothermic transition to γ-phase olivine respectively). The depths of both transitions are temperature dependent, an excess in temperature at either boundary leads to the reduction in the thickness of the enclosed layer. Since the average transition zone thickness at the ridge corresponds to the global average, no excess in temperature exists due to deep mantle upwelling beneath the ridge indicating that the ridge is a shallow feature with passive upwelling decoupled from the flow in the deep mantle.

Rayleigh waves with a period of 25 s constrain the lateral distribution of melt at depths between 20–70 km where their sensitivity to the shear wave velocity is highest (Forsyth *et al.*, 1998b). Even at this depth, the width of the melting zone seems to extend to a

lateral distance of more than 400 km from the ridge axis. Such a broad melting region is inconsistent with models of active mantle upwelling which would result in a narrow melting zone.
Scheirer *et al.* (1998) used multibeam, swath measurements of bathymetry and sea-floor reflectivity to map the distributions of seamounts and recent lava-flows. They point out that, in contrast to the broad melting region in the mantle, 98–99 % of the crust is generated within 1–2 km of the ridge axis. Seamounts and low-relief lava flows can be found off-axis. Most seamounts are formed 5–50 km away from the axis and none on the axis itself. Most off-axis lava flows emerge within 60 km of the ridge axis (some up to 100 km). Off-axis seamounts and lava flows can be generated by either narrow mantle upwelling or focussed melt flow, as well as by off-axis melting of small-volume mantle heterogeneities.

Geochemical findings

The following comments on mid-ocean ridge geochemistry are taken from Wilson (1989). The chemical composition of magma depends predominantly on the composition and mineralogy of the source, and the degree of partial melting of the source. The mechanism of partial melting, depth of magma segregation, extent of fractional crystallisation and magma mixing processes during the storage of magma in high-level sub-axial magma chambers play secondary roles. Magma chambers are more likely to occur beneath fast-spreading ridges with their size growing as the spreading velocity increases. The size of the reservoir controls the resulting processes. Small reservoirs beneath slow-spreading ridges undergo a closed-system fractional crystallisation with extensive differentiation, therefore generating a wide compositional range of magmas, whereas large reservoirs support an open-system fractionation combined with an efficient magma mixing, hence producing a compositionally uniform magma.

Mid-ocean ridge basalts are mostly sub-alkaline (low content of Na_20 and K_20) and tholeiitic (relative high content of FeO and Fe_2O_3) with a narrow range of major element composition between ridges indicating a relative constancy of the source and the involved processes. As far as the major elements are concerned, the composition of the MORB is comparable to oceanic island tholeiites, island-arc tholeiites and continental flood tholeiites. With respect to the trace element compositions, two varieties of basalt are erupted. The N-type (normal) basalt is depleted in light rare earth elements (LREE) and incompatible elements. Its source is found in the depleted asthenosphere of the upper mantle. The P-type (plume) basalt is erupted at topographic highs related to hot spots along the ridges and is less depleted in LREE and incompatible elements. It is derived from a more enriched source.
Basalt with a very primitive composition has been observed and typifies primary mantle melts. However, most basalts are more evolved which requires more enhanced mixing and fractionation processes presumably in sub-axial magma chambers. The primary magmas are generated by polybaric partial melting processes in ascending mantle diapirs starting at depths around 60 km. The Mg-rich, more evolved MORB saturated with olivine, clinopyroxene and orthopyroxene at pressures in excess of 8–10 kbar correspond to a minimum segregation depth from the mantle of 25–30 km.

The flow regimes of magma and solid mantle beneath mid-ocean ridges are still to be investigated. The outcome is vital for the understanding of plate dynamics and the formation of oceanic crust. Two endmembers of flow schemes are imaginable: passive flow of mantle induced by plate spreading and active upwelling of hot mantle material due to buoyancy driven small-scale convection. These flow fields seem to possess distinctive geochemical features as shown by Spiegelman (1996) with the aid of 2-D transport models. The reason lies in the different course of melt and solid stream lines (see Fig. 4.3) and in the fact that incompatible elements are released first in the melting process. In the case of passive flow driving convergent melt flow (left), only a small amount of solid has melted near the axis, but a large amount of incompatible trace elements from off-axis is added due to the focussing of melt trajectories towards the ridge axis. Off-axis melts are derived from shallow, mostly depleted residues. Therefore, an enrichment of incompatible elements at the axis is obtained which decreases with distance from the mid-ocean ridge within the crustal accretion zone (marked by the black arrows). During active flow (Fig. 4.3, right), the solid looses incompatible elements to off-axis melt trajectories before it reaches the region of maximum melt production in the narrow upwelling zone. Any further melting now adds to the dilution of incompatible elements. Convergent solid flow leads to depletion of incompatible trace elements at the axis and the concentration of incompatible elements will increase with distance.

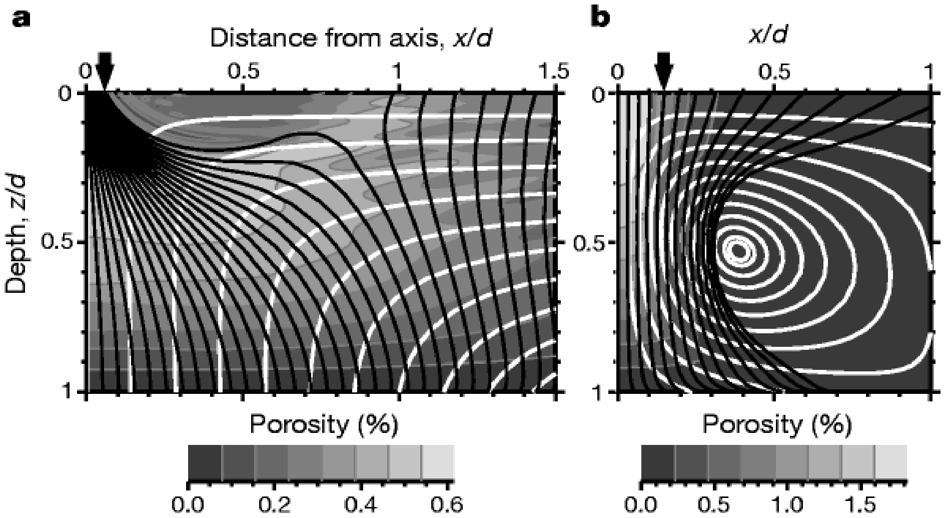

Figure 4.3: Distinction between different flow regimes beneath mid-ocean ridges, distances scaled to depth of melting (80–100 km); black curves: melt flow, white curves: solid flow, black arrows: crustal accretion zone; left: passive, plate driven flow, right: active, buoyancy driven flow; figure taken from Spiegelman and Reynolds (1999)

Spiegelman and Reynolds (1999) apply those models to geochemical measurements at the East Pacific rise. They found that the off-axis melts were more depleted in incompatible trace elements than the axial melts across a range of elements. Both the overall shapes of patterns and the off-axis distances were in good agreement with the model of passive mantle flow. Thus, the geochemical signatures were interpreted as evidence for lateral melt migration, though it was not possible to distinguish between models of equilibrium and disequilibrium transport or different mechanisms for convergent melt flow.

In this work, I compare mainly models of melt transport in fluid-filled fractures with models of porous melt flow. Petrological arguments mostly disagree with porous flow of melt through the mantle rock. Kelemen *et al.* (1995) argue that mid-ocean ridge basalt is not in equilibrium with the residual mantle peridotites (harzburgite and lherzolite). For example, MORB is saturated with orthopyroxene at pressures corresponding to a depth of 25–30 km, but MORB is not saturated with orthopyroxen at Moho pressures whereas orthopyroxen is a major constituent of the residual peridotites. Furthermore, there is no trace-element equilibrium. Hence, MORB is considered to have been in equilibrium with mantle peridotite at pressures much higher than the pressure at the base of the crust, namely the melting site, whereas harzburgite represents the upwelling mantle beneath the spreading centre. A transport process is required which hinders re-equilibration between the ascending melt (MORB) and the surrounding peridotite. The diffuse porous flow of melt from the source to the crust would afford an opportunity for chemical reactions between melt and matrix.
Another constraint of melt flux models is the required transport velocity. Freshly deposited MORB contain excesses of radioactive isotopes. In comparison with the half lives of the isotopes, a rapid transport from the source to the extrusion area is necessary. If an origin of the isotopes from the garnet stability field at 75 km depth is supposed, transport velocities of 1 m/a and 50 m/a are required, since ^{230}Th has a half life of approximately 75 000 years and ^{226}Ra of 1600 years. Although the disequilibrium of ^{226}Ra is no strong constraint because it may form at shallower depths, the model of intensified melt ascent in Iceland as a consequence of deglaciation and subsequent decompression calls likewise for melt transport velocities of 50 m/a, assuming a depth of the melting region of about 100 km and a rising time of 2000 years. Melt transport by porous flow is considerably slower than the ascent of melt-filled fractures. It can satisfy the velocity constraint of 1 m/a, but cannot afford melt velocities of 50 m/a without including unreasonable large grain sizes in the model (Kelemen *et al.*, 1997). Magma dykes may reach velocities in the range of 0.1–1 m/s as indicated by numerical studies of Dahm (2000b). Observations from volcanic areas suggest dyke ascent velocities from 0.025 m/s (Piton de la Fournaise, Réunion, Indian Ocean; Battaglia, 2001) up to 1.2 m/s (Krafla, Iceland; Brandsdóttir and Einarsson, 1979). Mantle xenolithes provide another evidence for the existence of a fast transport mechanism of mantle magma to the surface.

Conclusions

The model must fulfil several requirements. The results of various seismic techniques suggest that zones containing melt fractions could extend to depths starting with at least 70 km–180 km. The lateral melt distribution at depths of about 20–70 km stretches across several hundred kilometres up to 400 km perpendicular to the ridge axis. Bathymetry and seafloor reflectivity indicate that 98–99 % of the crust is generated within 1–2 km of the ridge axis. These dimensions imply a broad region of melting and a narrow extrusion zone, and point to a passive flow model for the dynamic regime of the mid-ocean ridge. The occurrence of incompatible elements at the ridge axis, which decreases with distance, is another indicator for a passive flow model. Since MORB is not in equilibrium with the residual peridotites at Moho pressures, a melt transport process is required which prevents re-equilibration between ascending melt and surrounding rocks.

4.2 Theory

Two models will be explained in detail: the model of melt ascent by fluid-filled fractures and the porous flow model. The mathematical background is explained in this section in order to allow further comparison between the models.
Both models share the concept of pressures and stresses generated by the convective mantle motion. Following the previous discussion, the mantle flow is assumed to be passive, and therefore results solely from plate spreading at the mid-ocean ridge. An appropriate description of such a motion is provided by the corner flow model. The passive transport of melt along the stream lines of the mantle flow would not result in the observed focussing of magma from the broad melting region to the narrow extrusion zone at the ridge. Thus, the melt flow must be separated from the mantle flow, which is achieved by pressure and stress gradients as a consequence of mantle rock deformation. Section 4.2.1 (pp. 54) describes the calculation of the corner flow stream lines, section 4.2.2 (p. 57) derives a so-called "dynamic pressure gradient" and section 4.2.3 (pp. 58) demonstrates the generation of a deviatoric stress field.

4.2.1 Corner flow

The passive motion of the mantle beneath mid-ocean ridges can be described by the model of the corner flow (e.g. Batchelor, 1967). It is used by various authors to describe mantle flow beneath spreading axes (McKenzie, 1969, 1979; Spiegelman and McKenzie, 1987; Phipps Morgan, 1987). A similar model is applied successfully by Dahm (2000a) to simulate the fluid ascent in the mantle wedge above a subducting slab. However, the boundary conditions for the corner flow at mid-ocean ridges are different from the boundary conditions necessary to model the flow at subduction zones. In the following, the equation of motion will be developed and the stream function will be calculated.
According to McKenzie (1969), the corner flow model neglects certain aspects as e.g. dependence of viscosity on temperature; otherwise non-linear terms dominate the solution and no analytical solution can be obtained. The analytical solution allows the determination of the stress field produced by the mantle motion at every point in the modelling region.

After (Batchelor, 1967), the Navier-Stokes equation, which represents the most general form of an equation of motion for a moving fluid, can be written as

$$\rho \frac{Dv_i}{Dt} = \rho F_i - \frac{\partial p}{\partial x_i} + \frac{\partial}{\partial x_i}[2\eta(\varepsilon_{ij} - \frac{1}{3}\varepsilon_{ii}\ \delta_{ij})] \quad , \tag{4.1}$$

where

$$\varepsilon_{ij} = \frac{1}{2}\left(\frac{\partial v_i}{\partial x_j} + \frac{\partial v_j}{\partial x_i}\right), \ j = 1, 2, 3 \quad . \tag{4.2}$$

$\frac{D}{Dt}$ denotes the total differential, ρ is density of the material, v_i velocity, F_i body force, p pressure, η dynamic shear viscosity, ε_{ij} strain and δ_{ij} Kronecker's symbol. If temperature differences are small enough for the viscosity to be considered uniform over the fluid ($\eta(x_i) = \eta =$ constant) and the fluid is incompressible ($\bigtriangledown \cdot \vec{v} = 0$), Eq. (4.1) becomes

$$\rho \frac{D\vec{v}}{Dt} = \rho\vec{F} - \bigtriangledown p + \eta \bigtriangledown^2 \vec{v} \quad . \tag{4.3}$$

For a stationary fluid motion, $\frac{D\vec{v}}{Dt} = \vec{0}$. The body force is assumed to consist only of the gravity force. A "modified pressure" p may be applied (Batchelor, 1967) using

$$p = p_0 + \rho\vec{g} \cdot \vec{x} + \mathcal{P} \quad , \tag{4.4}$$

where p_0 is a constant and $p_0 + \rho\vec{g} \cdot \vec{x}$ denotes the pressure which would exist in the same fluid at rest. $\mathcal{P}$ is the pressure that arises solely from the effect of fluid motion

$$\vec{0} = - \bigtriangledown \mathcal{P} + \eta \bigtriangledown^2 \vec{v} \quad , \tag{4.5}$$

which can be written for a 2-D flow with coordinates x, y

$$0 = -\frac{\partial \mathcal{P}}{\partial x} + \eta \left(\frac{\partial^2 v_x}{\partial x^2} + \frac{\partial^2 v_x}{\partial y^2} \right) \tag{4.6}$$

$$0 = -\frac{\partial \mathcal{P}}{\partial y} + \eta \left(\frac{\partial^2 v_y}{\partial x^2} + \frac{\partial^2 v_y}{\partial y^2} \right) \quad . \tag{4.7}$$

To satisfy the continuity equation in 2-D, it is possible to define a stream function ψ (Turcotte and Schubert, 1982) such that

$$v_x = -\frac{\partial \psi}{\partial y} \tag{4.8}$$

$$v_y = \frac{\partial \psi}{\partial x} \quad . \tag{4.9}$$

Stream lines are often used to visualise flow motion. The stream function is constant along a stream line (Batchelor, 1967), which means that the distance between the stream lines is proportional to the magnitude of the fluid velocity (narrow intervals between stream lines expressing high velocities). Additionally, stream lines are tangential to the direction of particle motion at every point in the fluid. Quantitatively, the integral of $\delta\psi$ between two points equals the volumetric flow rate between the points and the difference between the values of the stream function at two points gives the volumetric flow rate across any line drawn between those points (Turcotte and Schubert, 1982), whereas the absolute value of the stream function is arbitrary.

Substitution of Eqs. (4.8) and (4.9) in Eqs. (4.6) and (4.7) yields

$$0 = \frac{\partial \mathcal{P}}{\partial x} + \eta \left(\frac{\partial^3 \psi}{\partial x^2 \partial y} + \frac{\partial^3 \psi}{\partial y^3} \right) \tag{4.10}$$

$$0 = -\frac{\partial \mathcal{P}}{\partial y} + \eta \left(\frac{\partial^3 \psi}{\partial x^3} + \frac{\partial^3 \psi}{\partial y^2 \partial x} \right) \quad . \tag{4.11}$$

The pressure can be eliminated by taking the partial derivatives and adding them subsequently

$$0 = \frac{\partial^4 \psi}{\partial x^4} + 2\frac{\partial^4 \psi}{\partial x^2 \partial y^2} + \frac{\partial^4 \psi}{\partial y^4} \quad , \tag{4.12}$$

which is the biharmonic equation

$$\nabla^2(\nabla^2 \psi) = \nabla^4 \psi = 0 \quad , \tag{4.13}$$

written in terms of the Laplacian operator. This equation of motion is used to compute the stream function. The flow field is denoted as "corner flow" (Batchelor, 1967) and is calculated in the following using polar coordinates.
The stream function depends on distance r and angle θ (measured from beneath the mid-ocean ridge, see small sketch at Fig. 4.4)

$$\psi(r, \theta) = r f(\theta) \tag{4.14}$$

with the general solution of the differential equation

$$\psi(r, \theta) = r(A \sin\theta + B\cos\theta + C\theta\sin\theta + D\theta\cos\theta) \quad , \tag{4.15}$$

where A, B, C and D represent constant coefficients according to the specific boundary conditions. As boundary conditions, I assume that the shear stress $\sigma_{r\theta}$ is zero directly beneath the ridge, the plate is moving away from the ridge with a constant velocity v corresponding to the half spreading velocity and that the flow field is symmetric to both sides of the ridge (McKenzie, 1979, see also Fig. 4.4, left).

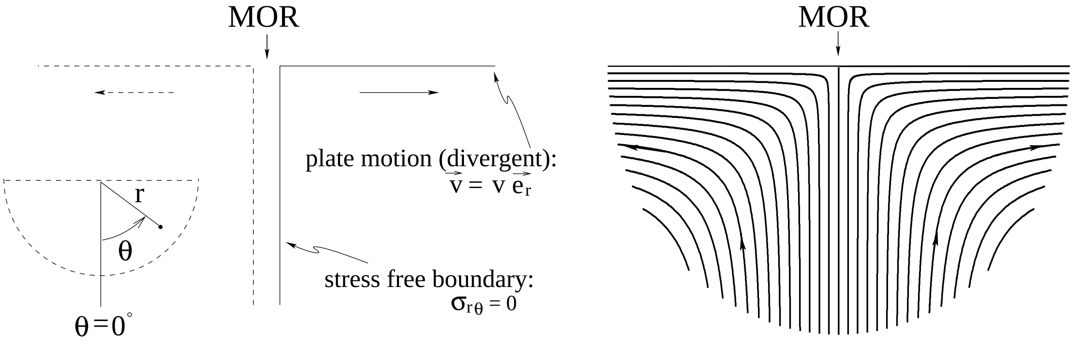

Figure 4.4: Left: geometry of the corner flow model, indication of boundary conditions: at $\theta = 0 \Rightarrow \sigma_{r\theta} = 0$, the boundary is stress free and at $\theta = \pi/2 \Rightarrow \vec{v} = v\ \vec{e_r}$, the plate is moving with a constant half spreading velocity v; right: resulting stream lines

This leads to coefficients of

$$\begin{aligned} A &= \frac{2v\cos\alpha^2}{2\alpha - \sin 2\alpha} \\ D &= -\frac{2v}{2\alpha - \sin 2\alpha} \end{aligned}$$

and

$$B = C = 0 \ .$$

α denotes the so-called “wedge angle“, i.e. the angle between the ridge axis and the bottom side of the plate which is assumed to be 90° in the following. The resulting formula for the stream function is

$$\psi = \frac{-2vr}{\pi}\theta\cos\theta \quad . \tag{4.16}$$

The magnitude depends on spreading velocity v, distance r and angle θ. The associated stream lines are depicted in Fig. 4.4 (right). Because of the deformation of mantle material, the flow field causes an isotropic stress called “dynamic pressure“ and a deviatoric stress field. Both components are treated separately and in more detail in the following sections. They are computed by the Fortran subroutine ”cornerflow” (see appendix B.2 and B.3, pp. 158).

4.2.2 Dynamic pressure

For incompressible flow as assumed here, the dynamic pressure is derived from the gradient due to volume conserving shear deformation of the mantle rock (Spiegelman and McKenzie, 1987, cp. also Eq. 4.5)

$$\triangledown\mathcal{P} = \eta\,\triangledown^2\,\vec{v} \quad . \tag{4.17}$$

This can be expressed in polar coordinates as follows

$$\begin{pmatrix} \dfrac{\partial\mathcal{P}}{\partial r} \\ \dfrac{1}{r}\dfrac{\partial\mathcal{P}}{\partial\theta} \end{pmatrix} = \eta \begin{pmatrix} \dfrac{\partial^2 v_r}{\partial r^2} + \dfrac{1}{r^2}\dfrac{\partial^2 v_r}{\partial\theta^2} + \dfrac{1}{r}\dfrac{\partial v_r}{\partial r} - \dfrac{2}{r^2}\dfrac{\partial v_\theta}{\partial\theta} - \dfrac{v_r}{r^2} \\ \dfrac{\partial^2 v_\theta}{\partial r^2} + \dfrac{1}{r^2}\dfrac{\partial^2 v_\theta}{\partial\theta^2} + \dfrac{1}{r}\dfrac{\partial v_\theta}{\partial r} - \dfrac{2}{r^2}\dfrac{\partial v_r}{\partial\theta} - \dfrac{v_\theta}{r^2} \end{pmatrix} \quad , \tag{4.18}$$

where v_r and v_θ are the radial and angular velocities

$$v_r = \frac{1}{r}\frac{\partial\psi}{\partial\theta} \tag{4.19}$$

$$v_\theta = -\frac{\partial\psi}{\partial r} \tag{4.20}$$

which gives

$$\mathcal{P} = -\frac{4\eta v}{r\pi}\cos\theta \quad . \tag{4.21}$$

In Fig. 4.5, the dynamic pressure contour lines are illustrated. Although depth is displayed with negative coordinates, z is considered to be positive downwards during computation. The contour lines are scaled to the depth of the asthenosphere z_0, assumed to be 200 km, to gain a non-dimensionalisation and to make them comparable to the results of various authors (e.g. Spiegelman and McKenzie, 1987). The values of dynamic pressure are scaled by $(\eta v/z_0)^{-1}$ to reveal dynamical similarities.

Dynamic pressure possesses a minimum at zero distance due to a singularity in Eq. (4.21) and grows with increasing depth and distance from the ridge axis in which the increase with depth is slower than with distance. For large distances, the dynamic pressure approaches zero ($r \to \infty \Rightarrow \mathcal{P} \to 0$).

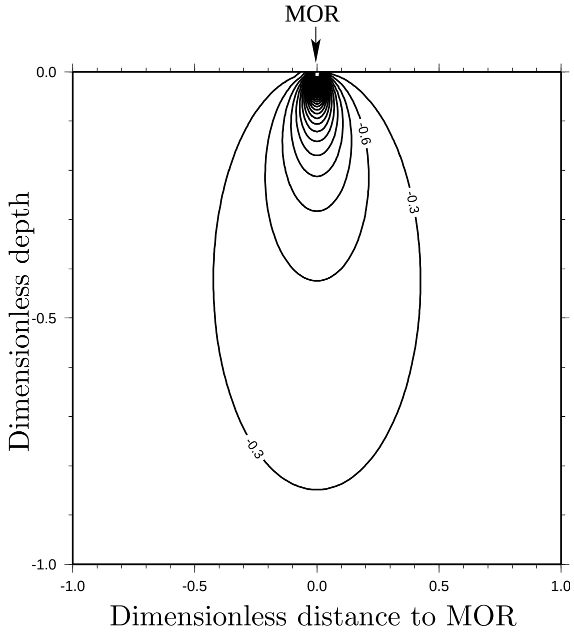

Figure 4.5: Dynamic pressure contour lines (normalised by $(\eta v/z_0)^{-1}$); mid-ocean ridge axis indicated (MOR), dimensionless sketch

4.2.3 Deviatoric stress field

In addition to the dynamic pressure gradient, a deviatoric stress field is generated by the fluid motion of the corner flow. The stress field can be calculated from the stream function using following expressions

$$\sigma_{rr} = 2\eta \frac{\partial v_r}{\partial r} = 0 \tag{4.22}$$

$$\sigma_{\theta\theta} = 2\eta \left(\frac{1}{r}\frac{\partial v_\theta}{\partial \theta}\right) = 0 \tag{4.23}$$

$$\sigma_{r\theta} = 2\left(\frac{1}{r}\frac{\partial v_r}{\partial \theta} + \frac{\partial v_\theta}{\partial r} - \frac{v_\theta}{r}\right) = \frac{4\eta v}{r\pi}\sin\theta \ . \tag{4.24}$$

The normal stresses σ_{rr} and $\sigma_{\theta\theta}$ are zero, only the shear stress $\sigma_{r\theta}$ contributes. The resulting stress field is displayed in Fig. 4.6 in terms of the principal axis coordinate system. Once again, the plot is dimensionless. The compressive axis (denoted by σ_1) is indicated by black arrows and the extensional axis (denoted by σ_3) by red arrows. The figure displays only the mantle section, not the crust, and matches a depth of 50 km and a distance of 75 km to the mid-ocean ridge axis. The stresses directly beneath the spreading axis and at the crust-mantle interface are much higher than elsewhere, therefore the arrows do not reflect stress magnitudes, but are plotted with uniform length. The position of the mid-ocean ridge axis is indicated by a dotted line. Thin lines represent the direction of maximum compressive stress.

The derivation of this principal stress field is best shown graphically. Fig. 4.7 (top) rep-

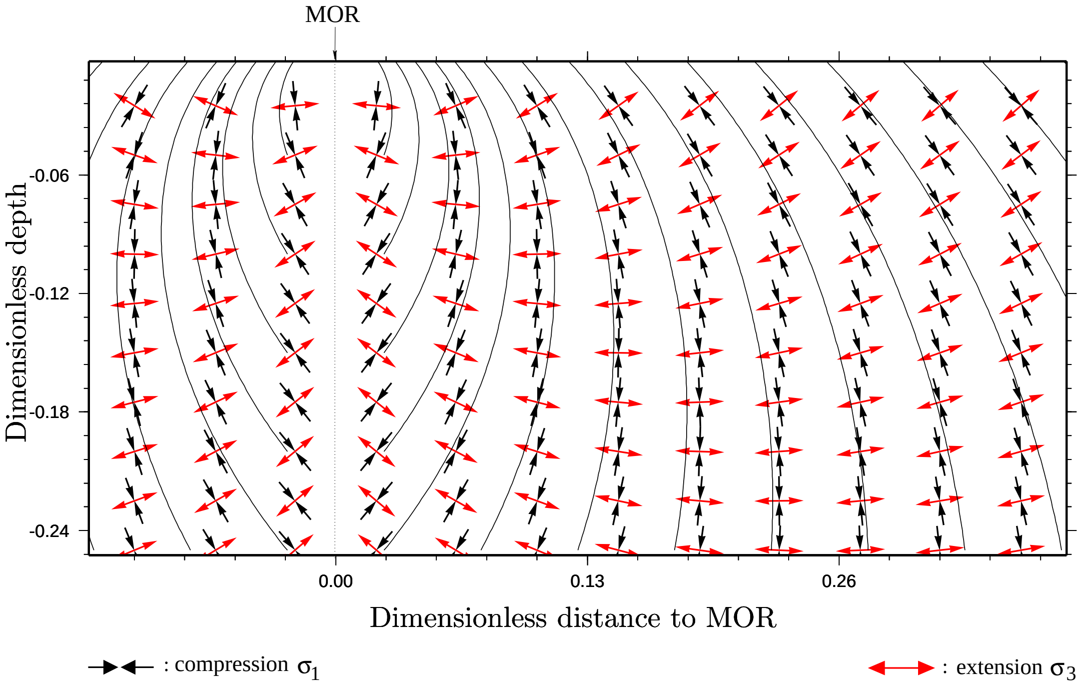

Figure 4.6: Deviatoric stress field showing compressive principal axis denoted by σ_1 (black arrows) and extensional principal axis denoted by σ_3 (red arrows)

resents the initial state of a rectangular grid at the time $t = 0$. Each corner of a grid cell can be considered to be the position of a particle. Fig. 4.7 (bottom) shows the state of deformation at a certain time $t^{'} = \Delta t$. The new positions of the corners of each grid cell are calculated from the distance moved by the particle (denoted by grey velocity vectors). The amount of deformation depends on the velocity, but the direction of the deformation is independent of flow speed. The principal axes of stress are found by the comparison of the resulting grid cells with their initial state (black arrows). Directly beneath the ridge axis, the shear stress is zero by definition. The extensional stress at the spreading axis is at an angle of approximately 45°. This angle is measured from the vertical and the principal axis of compressive stress is oriented perpendicular to the principal axis of extensional stress. Extensional stress is aligned horizontally at $\theta \approx 45°$, and rotates to be -45° along the surface of the mantle section. The greatest amount of deformation occurs at the spreading axis itself and decreases rapidly with horizontal distance and depth.
The influence of the dynamic pressure and the deviatoric stress field on the propagation of fluid-filled fractures will be investigated in the next section.

4.3 Models

This section deals with models of magma transport in the mantle. It is divided into three parts. First, some general ideas about hydrofracturing in the mantle will be introduced. Then, the model of magma transport in the mantle by the migration of fluid-filled fractures is considered in detail and compared to the model of porous melt flow. Finally, melt transport in dunite channels is presented.

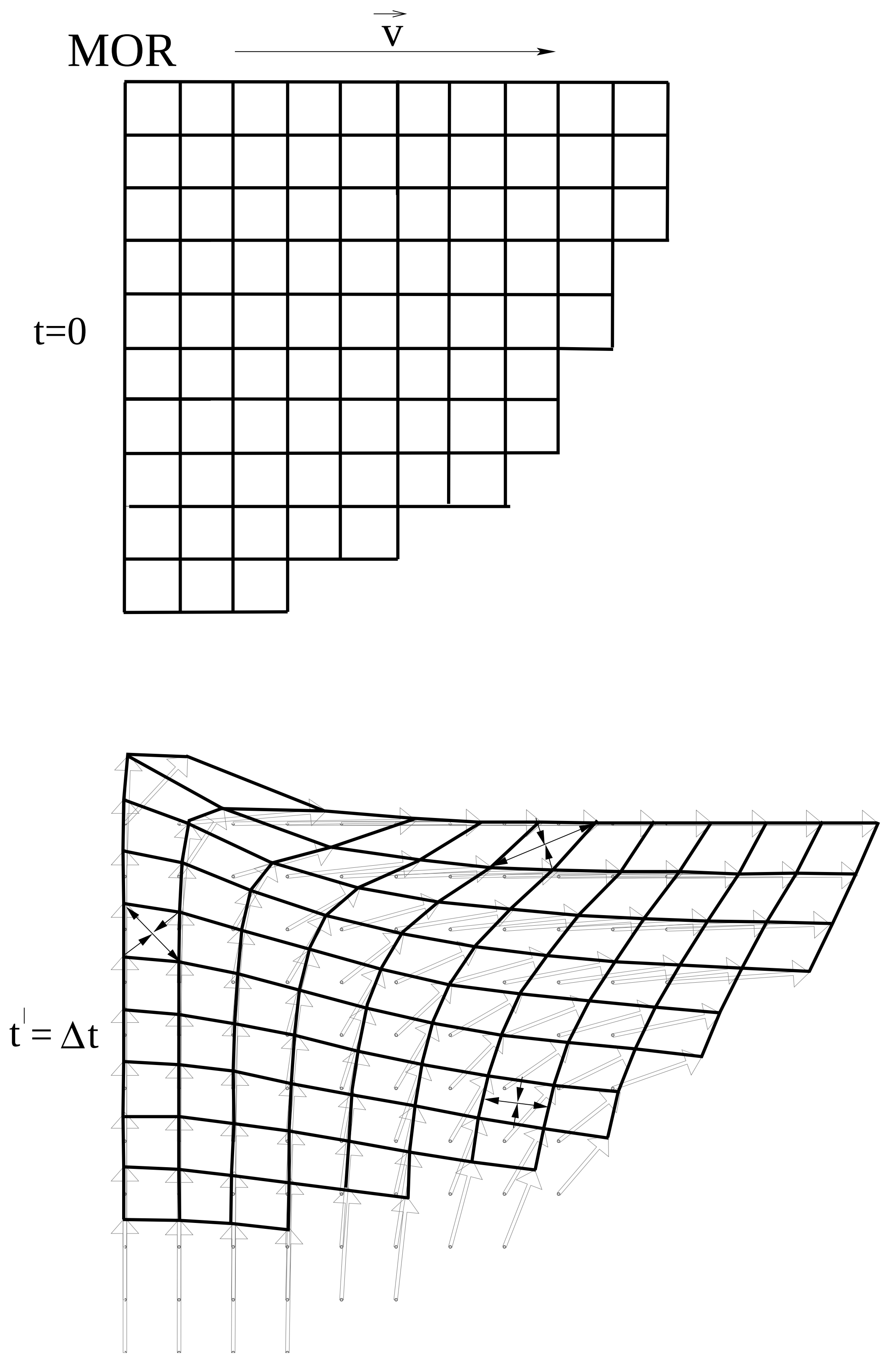

Figure 4.7: Derivation of the principal stress field; top: initial state at time $t = 0$; bottom: total deformation at time $t^{'} = \Delta t$; grey arrows: velocity vectors, black arrows: principal axes of compression and extension

4.3.1 Fracturing of the mantle

During the partial melting of peridotites, a partial fluid pressure arises due to volume increase. Nicolas and Jackson (1982) argue that brittle failure of rock may occur at any depth if the fluid pressure is high enough, because the presence of a partial fluid pressure reduces the deviatoric stress needed to fracture the rock. They studied the orientation of high temperature dykes with respect to the plastic flow foliation and lineation of peridotites in several massifs. Two main fracture regimes exist, both of which are caused by magma pressure during partial melting. In regions of low deviatoric stress, tension fractures will develop, since fluid pressure can build up at initial melting sites. High deviatoric stress assists fracturing; the fluids are expelled before a fluid pressure builds up, leading to shear fracturing.

Nicolas (1986) develops a model of melt extraction by dykes from a rising diapir by studying five lherzolite massifs. He describes the melt extraction process from observation in the Lanzo massif (western Alps). The first sign of melt segregation is indicated by feldspathic gashes encircled by a feldspar free zone a few centimetres in width. They represent fractures created under high fluid pressures in a shear stress regime. Subsequently, these shear gashes coalesce into so-called "indigenous gabbro dykelets". They too are enclosed by a depleted zone. Gabbro dykes develop by further depletion of the environment which produces dunitic walls over 10–100 cm for a dyke with a width of 10 cm. Since transitions exist between ubiquitous indigenous pyroxenite dykes with dunite walls to dunite veins of every size, Nicolas and Jackson (1982) interpret dunite bodies in the ophiolitic harzburgite massifs as residual of mafic dykes. Additionally, intrusive dykes exist which crosscut the lherzolite, forming sharp contacts with the wall rocks.

The model of melt extraction of Nicolas (1986), which describes the dyke formation in a mantle diapir, consists of a zone of first melting at approximately 75 km depth and the creation of an interconnected network of melt veins during the adiabatic uprise of mantle rock due to increased partial melting (Fig. 4.8). At a critical point ($\approx$ 50 km depth), hydraulic fracturing of the overlaying rocks occurs and a fracture propagates rapidly towards the surface. The propagation path is defined by the direction of maximum principal stress which does not need to be vertical as indicated here. When the fracture reaches the surface, it drains the melt network at its root and along its propagation path which is then closed by the rock pressure. This leads to depletion of the surrounding peridotites. In this model the melt extraction process is discontinuous, reflecting the nature of the dyke swarms in the oceanic crust where each dyke represents a single extraction event. This episodicity is translated into a continuous spreading motion due to the elastic behaviour of the upper crust.

Sleep (1988) considers also the tapping of melt by veins and dykes. In contrast to Nicolas (1986), he does not assume that the fractures extend uninterrupted from the melting zone to the surface. His model starts with the growth of veins in a deforming viscous mush through porous flow of melt into veins with locally reduced pressure. This reduced pressure is maintained by further opening of the vein fracturing rock at its ends due to interaction between the melt pressure in the vein and the most tensile principal stress. The extent of the opening is maximised when the melt pressure in the vein equals the regional melt pressure of the surroundings. The rate of porous flow into the vein and the

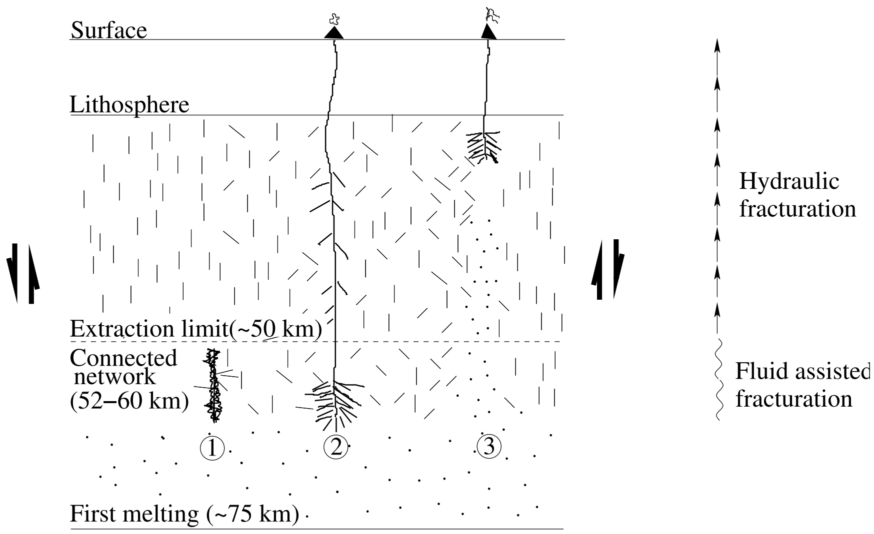

Figure 4.8: Melt extraction cycle in a mantle diapir by hydraulic fracturing, dots: isolated melt, dashes: melt veins; 1) creation of interconnected network of melt veins, 2) hydraulic fracturing of overlaying rock, 3) melt network is drained along propagation path and closed by the rock pressure; figure after Nicolas (1986)

rate of vein opening depends on the compaction and the permeability of the matrix. If several veins intersect, the larger veins drain the smaller ones because of their higher fluid pressure. Due to the density difference between the melt in the veins and the ambient rock, large veins tend to propagate upwards as dykes. The fluid pressure outweighs the least principal stress at the dyke's top causing it to open. At the base of the dyke, the situation is reversed; hence, the dyke closes and migrates upwards in a wholesale movement. This results in a cyclic process: Initially, veins are filled by porous flow which leads to opening. When a dyke forms, it absorbs the veins in its surrounding. Melt is injected in veins above the dyke when the dyke approaches and is extracted after the centre of the dyke has bypassed them. The veins are closed afterwards; the reduced pressure drives porous flow towards the vein which refills. According to Sleep (1988), competing processes with magma migration in dykes are filter pressing and porous flow. Porous flow is important near the ridge axis, where the deviatoric strain and strain rate are low whereas the importance of vein and dyke growth increases away from the ridge axis due to enhanced deviatoric stress, neglecting mechanism of filter pressing.

Weertman (1971) was the first to look at the fracture propagation process in detail. He used a dislocation problem to describe the behaviour of a liquid-filled crack in a horizontal elastic plate subjected to tensile stress. He derived the dislocation density distribution, the net displacement of the crack walls and the fracture volume respectively for a defined tension and hydrostatic pressure within the plate as well as the hydrostatic pressure within the liquid. The fracture grows steadily until it reaches a critical length at which it develops a typical tadpole shaped geometry now known as a Weertman crack. Due to the gravity field, it rises upwards by opening at its upper tip whilst closing at its lower tip because of evolving compressive stress. In this way, its length is maintained (see also chapter 2, section 2.2.2). Weertman (1971) reproduces only the ascent of magma-filled fractures in the lithosphere. However, if the movement of the fracture through the rock is fast enough to neglect creep deformations, it is applicable also to the ascent of fractures in the mantle.

Another model of wholesale dyke ascent in partially molten rock is provided by Rubin (1998). In his model, the stress intensity factor at the crack tip is also considered and fracture propagation occurs if the stress intensity factor outweighs the fracture toughness of the rock. The author differentiates between two types of flow: the vertical channel flow of magma within the dyke, which is driven by the magma buoyancy, and the porous flow of melt across the crack wall into the dyke, which is driven by the pore fluid pressure exceeding the least compressive stress and the melt pressure in the dyke.
The dyke thickness seems to be insensitive to its vertical length. Because of the effectiveness of channel flow compared with porous flow, the resulting dykes are very thin, only in the range of a few millimetres for dykes of several kilometres in length. This means they would freeze rapidly once entering the cool lithosphere. Rubin (1998) states that crustal dykes must possess additional sources of magma instead of partial melts. Although not modelled, the author thinks it to be possible due to a residual porosity at greater depth to enable the dyke walls to close and leave behind dunite channels as observed for example in the Oman ophiolite.

Nicolas and Jackson (1982) and Nicolas (1986) give geological evidence for the existence of dykes in ophiolites in general and beneath the ancient spreading centre of the Oman ophiolite in particular. Sleep (1988) discusses the formation of dykes out of magma filled veins and quantifies the relative importance of dyke growth and porous flow beneath mid-ocean ridges. Weertman (1971) models the upward dyke propagation due to a pseudo-Archimedian buoyancy in the gravity field using a dislocation problem calculation. Rubin (1998) simulates the dyke propagation in terms of porous influx of magma into the crack and vertical channel flow, fracturing the overlying rock.
It seems clear to the groups mentioned previously that dyke propagation will occur in the direction of the least tensile and maximum compressive stress. However, the direction of maximum compressive stress would not focus dyke propagation towards the mid-ocean ridge (see Phipps Morgan, 1987, and Fig. 4.6 on p. 59, direction of maximum compressive stress due to the deviatoric stress field). As Dahm (2000a) shows, the influence of buoyancy forces and effects of the finite fluid volume contained in the fracture which may extend or compress due to a changing outer pressure may force the fractures to diverge from the direction of the maximum compressive stress.

Propagation of magma-filled fractures modelled by the boundary element code

I present a numerical model for melt ascent in the mantle by the wholesale propagation of fluid-filled fractures. The transport of melt in fluid-filled fractures fulfils the condition of the separation of melt and mantle rock which is required by petrological arguments.
The corner flow model is applied to simulate the impact of the plate spreading. The flow generates two stress fields: a dynamic pressure as well as a deviatoric stress field. Both fields will be taken into account separately. First, the propagation paths of fluid-filled fractures in a deviatoric stress field are illustrated. These paths will then be compared with the influence of the dynamic pressure. The results will be compared with the flow

lines of porous melt flow in section 4.3.2.
The propagation paths for fluid-filled fractures are calculated using the program of Dahm (2000a) which is described in chapter 3 (section 3.3.2, pp. 41).

The effect of the deviatoric stress field resulting from the corner flow on fracture propagation is studied simultaneously with the effect of buoyancy while the effect of dynamic pressure is ignored in the first instance. Fig. 4.9 displays various propagation paths of fluid-filled fractures for two initial fracture positions which are examples of different kinds of behaviour. The figure possesses the same dimensions as Fig. 4.6. The strength of the stress field is proportional to the product of viscosity and velocity whereas the strength of the buoyancy force is proportional to the lithostatic gradient and the density difference between magma and surrounding rock. The results for the lithostatic pressure σ_m and the deviatoric stress field $\sigma_{r\theta}$ are scaled by $\eta v/z_0$. The principal axis of compression is indicated by black arrows, the principal axis of extension by red arrows. The produced deviatoric stress has a minimum of 0.05 MPa ($\eta = 10^{18}$ Pa s, $v = 1$ cm/a) and a maximum of roughly 5300 MPa ($\eta = 10^{22}$ Pa s, $v = 10$ cm/a). The density of magma and mantle rock is assumed to be 2700 kg/m^3 and 3300 kg/m^3 respectively, resulting in a lithostatic gradient of about 32.37 MPa/m and a maximum buoyancy force of roughly 290 MPa at 50 km depth. However, the general pattern is reproducible using different ratios of densities as well as viscosities and velocities. The bright coloured lines show the propagation paths for a small product of $\eta \cdot v$; the effect of buoyancy is stronger than the influence of the deviatoric stress field and leads to an almost vertical ascent of the fractures. The dark coloured lines represent the propagation paths for a large product of $\eta \cdot v$; the effect of the deviatoric stress is stronger than the influence of buoyancy force and the fracture

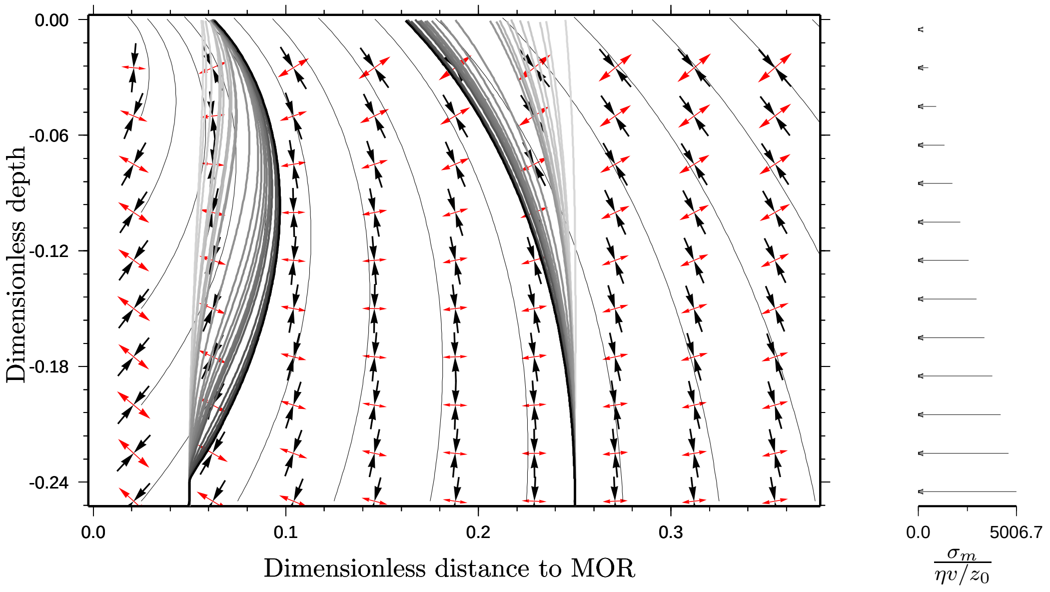

Figure 4.9: Effect of deviatoric stress field on fracture propagation in contrast to the effect of buoyancy; bright colour: high buoyancy, almost vertical ascent of fracture; dark colour: low buoyancy, fracture propagation follows direction of maximum compressive stress; small sketch: lithostatic gradient σ_m

movement is in the direction of maximum compressive stress.
Almost no focussing effect results from the deviatoric stress field. In the deeper parts of the considered mantle section, the deviatoric stress field partly even causes the fractures to move away from the ridge axis. The focussing effect in the upper part is insufficient. A high buoyancy force prevents the fractures from being directed outwards but impedes the focussing effect at shallower depths.

The effects of dynamic pressure gradient, deviatoric stress field and buoyancy cannot be separated. The combined impact of these factors is analysed in the following model. Equations used to calculate dynamic pressure and deviatoric stress field are of a similar form, but differ in sign and in the choice of trigonometric function

$$\mathcal{P} = -\frac{4\eta v}{r\pi}\cos\theta \tag{4.25}$$

$$\sigma_{r\theta} = \frac{4\eta v}{r\pi}\sin\theta \quad . \tag{4.26}$$

Both equations yield a singularity as $r \rightarrow 0$; pressure is at a minimum when $\theta \rightarrow 0°$ (directly beneath the spreading axis) and shear stress is greatest when $\theta \rightarrow 90°$. This is analogous to the observation made by Sleep (1988), who identifies an increasing importance in the mechanism of melt extraction by dyke propagation away from the ridge axis due to an increase in deviatoric stress. However, it is difficult to discuss those influences on fracture propagation by means of these equations, because both magnitude and orientation of pressure and stress determine the direction of fracture movement. Additionally, the effects of the finite fluid volume in the fracture reacting on external forces as well as buoyancy forces are essential. In contrast to the previous more simple models, the fractures are able to diverge from the direction of maximum compressive stress. The impact on the propagation paths is explained in Fig. 4.10. The upper part of the figure shows the propagation paths of fluid-filled fractures under the sole influence of dynamic pressure. The lower part of the figure represents the propagation paths under the combined influence of dynamic pressure and deviatoric stress. On the left, a small density difference is applied ($\Delta\rho$=100 kg/m^3), whereas on the right a high density contrast and apparent buoyancy force is taken into account ($\Delta\rho$=600 kg/m^3).
The focussing effect of the dynamic pressure gradient due to its minimum at the surface of the mid-ocean ridge axis is clearly visible. However, a high dynamic pressure gradient cannot occur without a high deviatoric stress (see Eqs. 4.25, 4.26). But in the more realistic model, which accounts for dynamic pressure gradient and deviatoric stress field, no focussing is attained. Depending on the density difference, several propagation paths exist between the examples on the left and on the right, similar to the various paths visible in Fig. 4.9, but not between upper and lower paths due to the fact that deviatoric stress attenuates the focussing effect of dynamic pressure. An enhancement of dynamic pressure consequently increases the shear stress, so the general behaviour of the fractures according to this model cannot be changed using the simple rheological model of the corner flow.

4.3.2 Porous flow

The basic concept of flow in porous media will shortly be summarised following Turcotte and Schubert (1982).

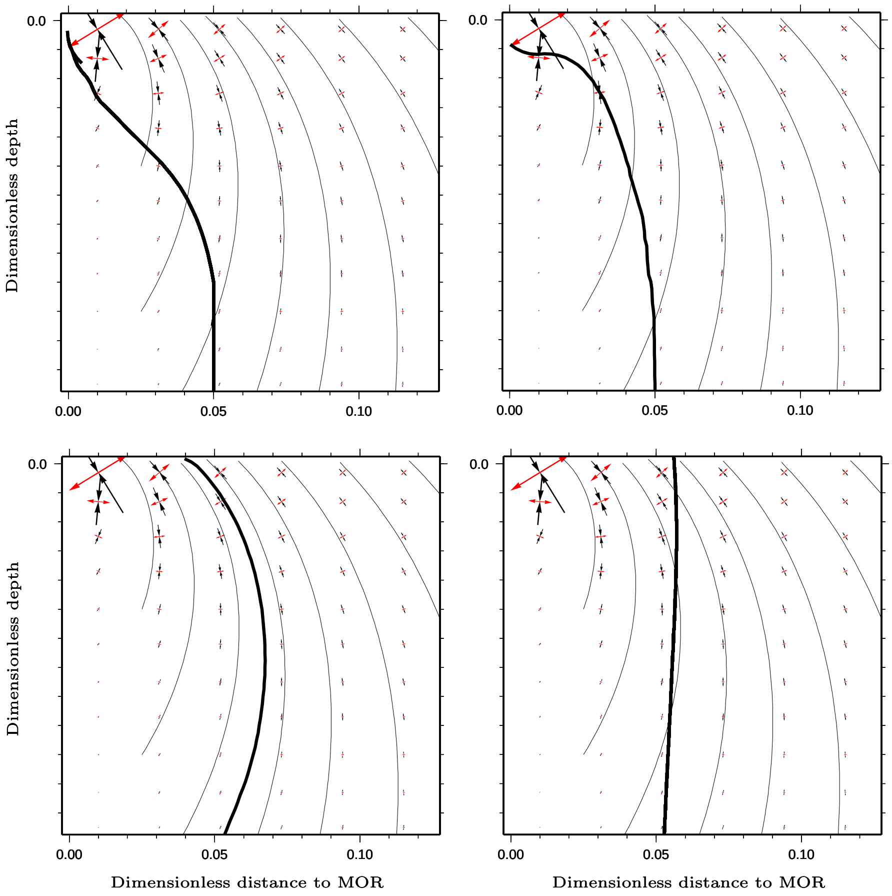

Dynamic pressure gradient only

Dynamic pressure gradient and deviatoric stress field

Small density difference

High density difference

Figure 4.10: Impact of dynamic pressure gradient and deviatoric stress field on the propagation paths of fluid-filled fractures; top: only dynamic pressure gradient is applied; bottom: model including dynamic pressure gradient as well as deviatoric stress field; left: small density difference; right: high density difference

The porosity ϕ of a rock is defined as its void volume per unit volume. The porosity of a rock results from a large number of small fractures or from the texture of a rock as a consequence of its composition (e.g. sandstone has a natural porosity because of the irregular shape of the grains building up the whole rock). The voids may be interconnected which allows for the flow of gas or fluids through the pore space. The porous flow of fluids through the pore space of a rock matrix is caused by gradients of temperature, chemical composition or pressure. More crucial than the porosity for the ability of fluid migration is the permeability which depends on size, number and tortuosity of the interconnections. The porous flow is characterised empirically by Darcy's law which states that the volumetric flow rate per unit area v_D through an isotropic porous medium is proportional to the scalar permeability k and the applied pressure gradient in x direction $\frac{dp}{dx}$ as well as inversely proportional to the dynamic viscosity η

$$v_D = -\frac{k}{\eta}\frac{dp}{dx} \quad . \tag{4.27}$$

The volumetric flow rate corresponds to the average fluid velocity per unit area (known as the Darcy velocity).

Porous flow models can be used to simulate the flow of magma through the mantle rock to model the melt extraction at mid-ocean ridges. The description follows the implementations of Spiegelman and McKenzie (1987). A similar model can be found in Phipps Morgan (1987).

Since partial melting and separation of the melt from the solid is accepted as the primary process of melt production at oceanic spreading centres, Spiegelman and McKenzie (1987) model a 2-phase corner flow of a melt saturated, deformable porous medium, where the magma moves through interconnected pore space of the mantle rock (matrix). Because of the pressure gradient resulting from shear deformation in the matrix, melt stream lines diverge from matrix stream lines and melt flow is focussed towards the ridge axis. The general equations are

$$\Gamma = \frac{\partial}{\partial t}(\rho_f \phi) + \bigtriangledown \cdot (\rho_f \phi \vec{v_f}) \tag{4.28}$$

$$-\Gamma = \frac{\partial}{\partial t}[\rho_s(1-\phi)] + \bigtriangledown \cdot [\rho_s(1-\phi)\vec{v_s}] \tag{4.29}$$

$$\vec{v_f} - \vec{v_s} = -\frac{k}{\phi\ \eta_f} \bigtriangledown \mathcal{P} \tag{4.30}$$

$$\bigtriangledown \mathcal{P} = \eta_s \bigtriangledown^2 \vec{v_s} + (\zeta + \eta_s/3) \bigtriangledown (\bigtriangledown \cdot \vec{v_s}) + (1-\phi)(\rho_s - \rho_f) g \vec{e_z} \quad . \tag{4.31}$$

Eqs. (4.28) and (4.29) are the equations of mass conservation of melt and matrix respectively. Variables denoted by "f" (fluid) refer to the melt flow whereas variables denoted by "s" (solid) are associated with the matrix flow. $\vec{v_f}$ and $\vec{v_s}$ are melt and matrix velocity and Γ is the melting function which gives the rate of mass transfer from matrix to melt.

Eq. (4.30) is a Darcy's law type equation governing the separation velocity of melt and matrix depending on the porosity, the permeability, the melt shear viscosity η_f and the "piezometric pressure" or pressure in excess of hydrostatic pressure ($\mathcal{P} = P - \rho_f g z$). Here, the permeability k is a non-linear function of grain size a_g, porosity ϕ and a dimensionless coefficient c ($k \sim a_g^2 \phi^n / c$). The authors assume a low porosity for the mantle rock to be 1.0 % and 1.5 % for slow- and fast-spreading ridges respectively and a high porosity to be 2.4 % and 3.6 % . The density typically is roughly 2800 kg/m^3 for the melt and 3300 kg/m^3 for the mantle rock.

The equation of the piezometric pressure (4.31) consists of three terms. The first term is the pressure gradient due to volume conserving shear deformation of the matrix, the second term describes the gradient due to volume changes of the matrix due to extension and compaction and the third term results from the density difference between melt and matrix. The participating variables are the matrix shear viscosity η_s, the matrix bulk viscosity ζ and the gravitative acceleration g in z direction with depth increasing downwards. The authors use values from 10^{18}–10^{21} Pa s for the matrix shear and bulk viscosity and 1 Pa s for the melt shear viscosity.

However, if density and porosity are assumed to be constant and melting is neglected ($\Gamma = 0$),

$$\bigtriangledown \cdot \vec{v_s} = 0 \tag{4.32}$$

$$\bigtriangledown \cdot \vec{v_f} = 0 \quad , \tag{4.33}$$

which means $\vec{v_s}$ and $\vec{v_f}$ can be written in potential form ($\vec{e_y}$ indicating the unit vector perpendicular to the x-z plane)

$$\begin{aligned}\vec{v_s} &= \nabla \times (\psi_s \vec{e_y}) && (4.34)\\ \vec{v_f} &= \nabla \times (\psi_f \vec{e_y}) \quad . && (4.35)\end{aligned}$$

Eq. (4.34) forms the biharmonic equation for the matrix stream function ψ_s (cp. section 4.2.1, pp. 54)

$$\nabla^4 \psi_s = 0 \tag{4.36}$$

that can be solved analytically.
The assumed model for the matrix flow is the corner flow. The equation of the dynamic pressure is quite similar to the one derived in section 4.2.2 (p. 57) but includes an additional term allowing for buoyancy effects which are considered elsewhere in the model of the propagating fractures. The second term of equation (4.31) is ignored because of constant porosity. The melt stream function is derived subsequently from equation (4.30). However, because of the inclusion of the buoyancy effect in the equation for the dynamic pressure, the equations are scaled by the length scale L_d to be dimensionless

$$L_d = \left[\frac{\eta v}{(1-\phi_0)(\rho_s - \rho_f) g} \right]^{1/2} \quad , \tag{4.37}$$

where v is the half spreading velocity of the oceanic plates.
The dimensionless equations for the dynamic pressure and the melt stream function are

$$\begin{aligned}\mathcal{P} &= \left(\frac{-2B}{r} + r \right) \cos\theta && (4.38)\\ \psi_f &= -\frac{w_0}{v} \left(\frac{2B}{r} + r \right) \sin\theta + \psi_s \quad . && (4.39)\end{aligned}$$

B is a coefficient depending on the boundary conditions ($B = \frac{2}{\pi - 2\alpha' - \sin 2\alpha'}$ with α' being the complementary angle to the previously introduced wedge angle α), w_0 means the separation velocity between the melt and the matrix in absence of melt deformation

$$w_0 = \frac{k_0 (1-\phi_0)(\rho_s - \rho_f) g}{\phi_0 \eta_f} \tag{4.40}$$

and measures the relative contribution of buoyancy-driven flow to advection by the matrix, where k_0 is the permeability at the characteristic porosity ϕ_0. The first terms of the equation for the dynamic pressure are equivalent to the equation of the dynamic pressure in section 4.2.2. The cosine ($r \cos\theta$) and the sine term ($r \sin\theta$) increasing with distance r (4.38) and (4.39) are caused by the buoyancy effect due to the density difference between the melt and the surrounding matrix.

Combinations of parameter values (spreading rate, matrix viscosity and porosity) can be found so that the melt flow lines differ from the matrix flow lines and converge towards the mid-ocean ridge because the melt will flow towards the minimum of pressure which lies directly at the ridge (see also section 4.2.2, pp. 57). A region of melt extraction is formed whose extension varies with a characteristic length scale $\approx L_d (2B)^{1/2}$. Spiegelman and

McKenzie (1987) deduce that the absolute value of the bounding stream lines depends only on the velocity ratio w_0/v and the wedge angle α. For low porosities, the effect of the singularity of the melt stream function at r=0 is diminished, hence the advection of the matrix is the dominant process and the melt stream lines approach the matrix stream lines. When the porosity increases, conditions are reached where the influence of matrix advection equals the influence of the pressure gradient towards the ridge. Mathematically, this corresponds to a saddle point in the stream function equation. At higher porosities, the melt is focussed towards the ridge. A similar explanation is valid for an approach to the ridge; the bounding stream lines pass through the saddle point. The stream lines of melt and matrix are shown in Fig. 4.11 with solid and dotted lines respectively. The assumed melt extraction region is highlighted. The different extension of the melting region is explained by the spreading velocity and the wedge angle. One basic assumption in the model of Spiegelman and McKenzie (1987) is that the permeability is isotropic. From a physical point of view this is not trivial since the corner flow of the mantle rock generates a large deviatoric stress. It is likely that deviatoric stress has an impact on the geometry of pore space and may thus lead to an anisotropic permeability.

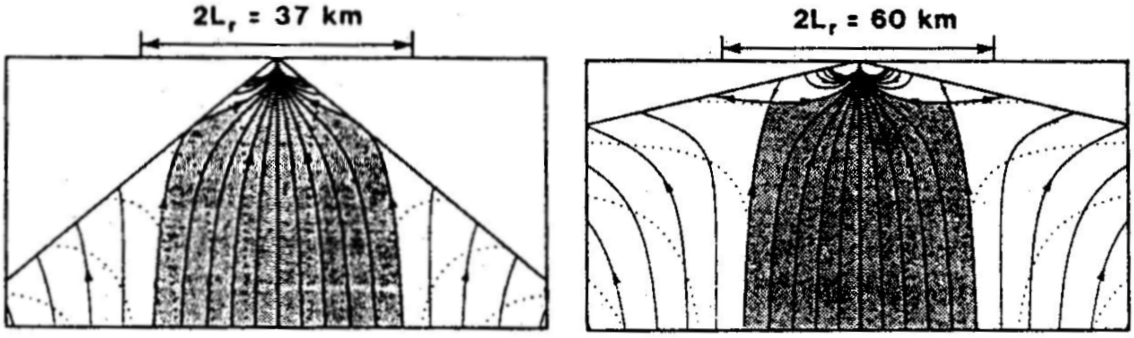

Figure 4.11: Focussing of porous melt flow towards the mid-ocean ridge; grey: melt extraction region, dotted: matrix stream line, solid: melt stream line; plate spreading velocity is lower on left picture, bounding stream lines i.e. saddle point visible on the right; figure taken from Spiegelman and McKenzie (1987)

A similar porous flow model is employed by Phipps Morgan (1987). He finds the large values of viscosity, which are required to obtain the focussing of melt flow lines onto the ridge ($\eta_s = 10^{21}$ Pa s), unreasonable. Instead, he proposes an anisotropic permeability and points out that the plate spreading induced mantle flow generates strain beneath the ridge which is visible in mantle peridotites as a strong petrofabric. He states that this anisotropy influences melt migration since melt channels are likely to form on grain boundaries between two or more different mineral species. The scalar permeability k applied in the above-mentioned model is substituted by a permeability tensor $\mathbf{K}$ and the principal permeabilities k_{aa} and k_{bb} (attained by transformation of permeability tensor in a system of principal axes) are assumed to be

$$k_{aa} = (a/b)k \qquad \text{and} \qquad k_{bb} = (b/a)k \tag{4.41}$$

for pure shear deformation and

$$k_{aa} = (1/b^2)k \qquad \text{and} \qquad k_{bb} = (1/a^2)k \tag{4.42}$$

for simple shear deformation, where k is the initial isotropic permeability and a and b are the semi-major and semi-minor axes of the strain ellipsoid respectively. He finds that the strain-dependent anisotropic permeability may shape melt flow beneath a ridge axis and cause a strong focussing effect of melt migration towards the ridge. A value for the viscosity needed to focus the melt on the ridge is not provided in his paper. The relationship of strain, rock texture and permeability is unknown.

A more complete study of the effect of deviatoric stress on porosity will be discussed below (Müller, 2003). He observes that the deviatoric stress field influences the porous flow in almost the same manner as it influences propagating fractures. In this thesis and the work of Müller (2003), the strain is created by the momentary stress field, whereas in the model of Phipps Morgan (1987), the anisotropy of permeability results from an integrated strain.

Comparison of the propagation of fluid-filled fractures to the porous melt flow

In Fig. 4.12, the propagation paths of fluid-filled fractures subjected to the dynamic pressure are compared to the melt flow lines resulting from porous melt flow. On the left, propagation paths of fluid-filled fractures are plotted (dashed lines). In order to demonstrate the connection between cause and effect, the contour lines of dynamic pressure are also displayed (solid lines). On the whole, the direction of fracture propagation is perpendicular to those contour lines. The initial vertical ascent is due to the primary orientation of the fractures that leads to a preferred propagation direction. The length of this initial vertical ascent depends on the fracture length. The right figure is taken from

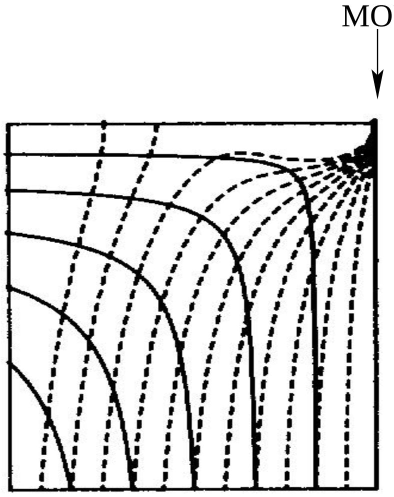

Figure 4.12: Comparison of propagation paths of fluid-filled fractures and porous flow lines (deviatoric stress field neglected in both cases); left: dashed lines: propagation paths of fluid-filled fractures for different start positions, solid lines: contour lines for dynamic pressure gradient; right: dashed lines: melt flow lines caused by porous flow, solid lines: matrix stream lines; left figure with indication of dimensionless coordinates, right figure taken from Phipps Morgan (1987), no ranges provided

Phipps Morgan (1987) using a similar model to Spiegelman and McKenzie (1987). The dashed lines represent melt flow lines whereas the solid lines show matrix flow lines of the corner flow. The similarity between propagation paths and melt flow lines is clearly visible, creating the impression that the reaction of fluid-filled fractures and porous melt flow to an existing pressure field might be comparable despite the different mechanisms of fluid transport. The question arises if the deviatoric stress field should be included as well in the porous flow models and if it would impede the focussing of melt by porous flow.

Stevenson (1989) points out that in weak regions of viscously deforming media, the pressure is slightly reduced. Thus, melt flow will be directed towards weaker regions which in turn decreases the strength of the rock further. Unstable melt-rich shear zones within a melt-poor matrix may form ("Stevenson instability"). These tabular zones of high melt fraction are aligned perpendicular to the minimum compressive stress. Thus, the increased flow of magma into regions where it has already accumulated may be a prelude to dyke initiation. Müller (2003) uses a model of porous melt flow for solving the equations for mass, energy and momentum for melt and matrix respectively. Instead of applying a dynamic pressure gradient, he uses stress fields of simple and pure shear. On the left of Fig. 4.13, the employed model of simple shear is displayed (corresponding to the passive motion of a viscous fluid beneath a moving plate). The boundary conditions contain no slip; the shear stress results from an influx of material from the left, increasing linearly in strength from the bottom to the top of the box. This influx is achieved by the choice of the streamfunction, shown by its contour lines which are more close to the top of the model, thus indicating a higher velocity. The resulting principal axes are drawn schematically at the right. Mechanic channelling may occur which is oriented parallel to the direction of the maximum compressive stress. The results are shown in Fig. 4.14. The pictures illustrate porosity fields in time. The initial porosity field is given first; the porosity distribution is random. After a certain time, zones of low and high porosity develop (equivalent to zones of high melt content) and become more significant. Their alignment is approximately in the direction of maximum compressive stress, being diverted negligibly because of the flow of material throughout the observed region. Hence, porous melt flow reacts on deviatoric stress fields apparently in the same manner as fluid-filled fractures. Thus, I conclude that if the models of porous melt flow included the deviatoric stress field in addition to the dynamic pressure gradient, the focussing of the melt towards the mid-ocean ridge might be as insufficient as is the focussing of fluid-filled fractures.

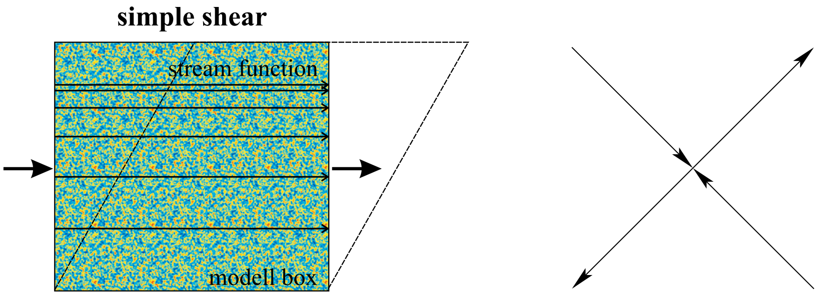

Figure 4.13: Simple shear model; left: employed box for simple shear model, boundary conditions are no slip, influx of material from the left with increasing strength from the bottom to the top of the box; right: principal axes of compression and extension for simple shear model; figure by courtesy of Müller (2003)

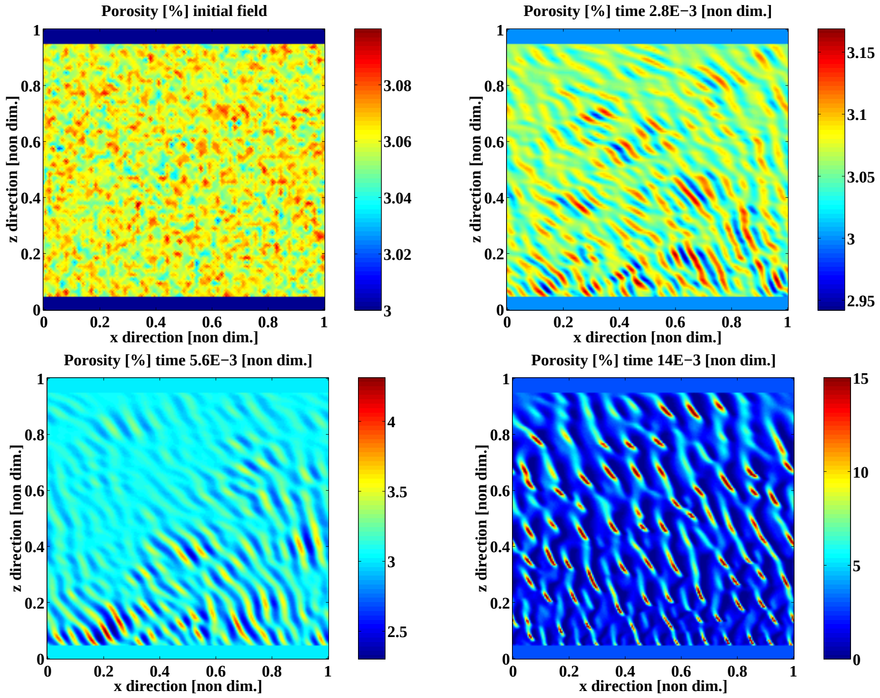

Figure 4.14: Porosity fields in time resulting from the shear stress model; upper left: initial model of randomly distributed porosity, upper right and lower left: zones of low and high porosity develop (i.e. zones of low and high melt content), orientated approximately parallel to the direction of the maximum compressive stress; lower right: final state of model (maximum of porosity fixed at 15% during calculation); figure by courtesy of Müller (2003)

Further discussion of the models is given in section 4.4.

4.3.3 Focussed flow in dunite channels

Since petrological arguments are inconsistent with a porous flow of magma through the mantle rock, Kelemen *et al.* (1995) suggest a model dealing with an initial porous flow of magma towards the ridge followed by its separation from the mantle matrix by dunite channels. Their model is based on field studies of the Oman ophiolite. Their studies reveal the existence of dunite bodies embedded in the mantle section of the ophiolites (e.g. Kelemen *et al.*, 1995, 1997; Nicolas, 1986). These dunites are tabular, up to 200 m thick and maximum 10 km in length (Kelemen *et al.*, 1997). The dunite bodies exhibit sharp irregular contacts and are discordant to banding and crystallographic lineations in the surrounding harzburgite. Therefore, they are treated as indication for conduit-like structures in which the melt is directed towards the ridge in contrast to Nicolas and Jackson (1982), who interpret the dunite bodies as remnants of mafic dykes which extracted magma from the mantle by hydrofracturing. These conduits provide another opportunity to accomplish the fast transport of melt from the segregation depth to the surface without further chemical equilibration between melt and surrounding rock. Fig. 4.15 displays a sketch of dunite conduits in mantle rock.

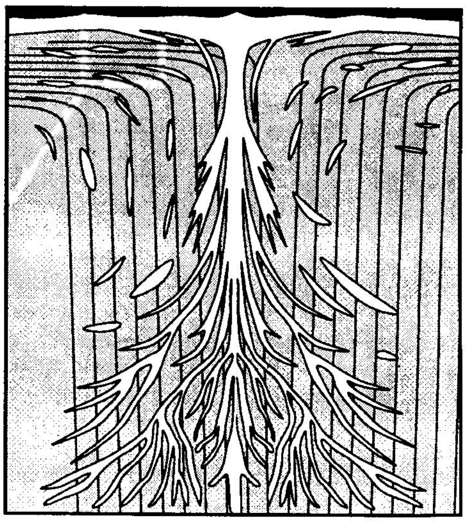

Figure 4.15: Sketch of dunite conduits in mantle rock; white: dunite channels, grey: mantle peridotite, black: lower crustal gabbros; mantle stream lines indicated by solid lines; figure taken from Kelemen *et al.* (1995)

A comparison of rare earth element data (REE) and spinel composition from the Wadi Tahin shows that the dunite conduits in the Oman ophiolite formed in equilibrium with liquids of similar composition to MORB but different from the surrounding rock (Kelemen *et al.*, 1995). This suggests that the dunites rose from the parental liquid without chemical reactions with the mantle rock (harzburgite). The Mg # (i.e. $Mg/(Mg+Fe^{2+})$) of harzburgite and olivine as a component of dunite indicate that the dunites have not evolved by partial melting of the ambient harzburgites or by crystal fractionation of melt derived out of them. Instead, the dunites were produced by dissolution of pyroxene with concomitant precipitation of olivine by reaction between the ascending melt and harzburgites as a result of a replacement reaction during magma migration of olivine-saturated melt by porous flow.

Kelemen *et al.* (1997) describe the formation of the dunite conduits as dissolution channels by a process named "reactive infiltration instability". Pyroxene dissolution combined with olivine precipitation increases the liquid mass; under adiabatic conditions, such reactions enhance the magma mass and porosity of the rock. Hence, dissolution of pyroxene in olivine-saturated magma is analogous to porous flow of fluid through a partially soluble rock and thus unstable. Initial perturbations in permeability are likely to cause increased fluid flow which causes more rapid dissolution. Therefore, diffusive flow breaks down into focussed porous flow through high porosity dissolution channels extending in the direction of fluid flow.

This explains the development of dunite conduits during fluid flow in a porous medium, but does not account for the initial focussing of flow towards the mid-ocean ridge.

4.4 Discussion

Porous melt flow, favoured in recent years as a melt extraction model beneath mid-ocean ridges, does not account for the fast ascent velocities required to prevent the MORB magma from re-equilibration with the surrounding rock at the Moho or upper mantle depth. Recently, channelling and diking has again been under discussion as an alternative or complementary mechanism for fast and efficient melt transport. The existence of dykes, channels or fractures in the upper mantle is supported by geological observations in ophiolite complexes (e.g. Nicolas and Jackson, 1982; Nicolas, 1986). The question addressed here is whether a simple corner flow model and a rigorous study of dyke ascending paths is able to explain the observed convergence of melt from a broad melting region towards the narrow extrusion zone beneath the ridge axis.
The transport of magma beneath mid-ocean ridges was modelled by the ascent of fluid-filled fractures and was compared to the porous flow of magma through the mantle rock. The various aspects are summarised in this section with a further discussion of the arguments.

According to Dahm (2000a), the propagation of fluid-filled fractures and magma dykes is an important model for the mechanism of fluid transport through the lithosphere and possibly asthenosphere. Since several authors point out that the required conditions for hydrofracturing are fulfilled in the mantle (Nicolas and Jackson, 1982; Nicolas, 1986; Sleep, 1988; Rubin, 1998), a melt extraction process from the mantle by fractures is possible. Geological observations show the existence of fluid-filled fractures in ophiolites of spreading centre origin.
The propagation path of a fluid-filled fracture is mainly influenced by the interaction of dynamic pressure, deviatoric stress field and buoyancy force. The dynamic pressure gradient as well as the deviatoric stress field are caused by the fluid dynamic model of mantle rock flow. Since geophysical and geochemical findings suggest a passive mantle motion generated by the plate spreading at mid-ocean ridges, the corner flow model is adopted. The global pressure minimum at the spreading axis causes the fractures to propagate towards it. The deviatoric stress field leads to a wholesale migration of fractures along the paths of principal compressive stress, which direct the propagation paths outwards at greater depths and up to the surface. The apparent buoyancy force originates from the density difference between the magma and the surrounding rock and also the lithostatic gradient. This effect alone would result in a vertical ascent. The combination of these effects does not tend to focus the fluid-filled fractures onto the ridge, since the impact of the dynamic pressure is smaller than the influence of the deviatoric stress field and the buoyancy force at the crucial positions.

I have presented the models of magma transport by fracture propagation as proposed by Nicolas (1986), Sleep (1988), Rubin (1998) and compared them with models of melt extraction from the mantle by porous flow (e.g. Spiegelman and McKenzie, 1987; Phipps Morgan, 1987) as well as melt flow in dunite channels (Kelemen *et al.*, 1995, 1997).
In the porous flow models, melt stream lines diverge from matrix stream lines when a dynamic pressure is applied. The melt flow is focussed towards the ridge. However, this focussing effect only becomes effective for viscosities two orders of magnitude higher than

those generally accepted for the mantle beneath mid-ocean ridges (10^{21} Pa s instead of 10^{19} Pa s). Phipps Morgan (1987) tries to overcome this deficiency by implementing an anisotropy of permeability due to the impact of total strain on the mantle rock. This causes a strong focussing effect of melt migration towards the ridge. The relationship of strain, rock texture and permeability is unknown and Phipps Morgan (1987) gives no value for the viscosity needed in this model. Dahm (2000a) notes that a porous flow model may oversimplify the situation at high confining pressures.

The behaviour of propagating fractures under the influence of a dynamic pressure gradient resembles that of a porous melt flow. This means the melt flow lines of porous flow are similar to the propagation paths of migrating fractures. The deviatoric stress field hindering the focussing of fractures in the model used here is not included in any of the porous flow models. Müller (2003) suggests that zones of high porosity generated by melt channel instabilities are aligned parallel to the direction of the maximum compressive stress. If this is the case, I conclude that models of porous melt flow including a deviatoric stress field in addition to a dynamic pressure gradient would not achieve a focussing of melt towards the spreading axis in analogy to the melt transport in fluid-filled fractures. Hence, I consider both models as equivalent regarding their capability with respect to explaining the focussing effect.

Kelemen *et al.* (1995, 1997) provide results, which suggest to a significant degree a chemical disequilibrium between mid-ocean ridge basalts and the residual peridotites that is not consistent with the porous flow model. They interpret dunite bodies observable at the Oman ophiolite to be conduits for melt flow which permit a fast flow of melt towards the surface. Because a cumulative origin (olivine precipitation in melt-filled fracture) is ruled out due to data on the Mg #, Kelemen *et al.* (1995, 1997) assume these channels to have developed during focussed porous flow through the surrounding rock. They give no explanation of how the orientation of the channels towards the mid-ocean ridge is accomplished. Looking at their model of the former position of these channels (see Fig. 4.15 on p. 73), one can see clearly that they do not comply with the melt stream lines of the porous flow (see Fig. 4.11 on p. 69).

Nicolas and Jackson (1982), Nicolas (1986) and Sleep (1988) suggest a formation of the dunite bodies in a porous reaction zone around dykes which is not excluded by Kelemen *et al.* (1995, 1997). Melt rising in fractures is likewise not in equilibrium with the surrounding medium. A former fracture generating a dunite body might have closed subsequently and is no longer detectable. The tabular form of some dunites also supports the interpretation of their relation to fractures. Kelemen *et al.* (1995) quotes a personal communication with A. Rubin who observed curving tips in a tabular dunite with medial pyroxenite in the Trinity peridotite which is taken to have formed in such a porous reaction zone around and ahead of propagating fractures.

The ascent of melt in fractures occurs much faster than the porous flow of melt. Porous melt flow may satisfy the constraint of 1 m/a imposed by the disequilibrium of ^{230}Th, but not the potential constraint of 50 m/a resulting from the excess of ^{226}Ra in fresh MORB. An ascent velocity of 50 m/a is also induced from the intensified melt ascent due to deglaciation and subsequent decompression of the mantle beneath Iceland. Magma dykes may even reach velocities in the range of 1 m/s as indicated by Dahm (2000b) and Brandsdóttir and Einarsson (1979). The solidification time of a dyke depends on its thickness and temperature difference between melt and mantle rock (Turcotte and Schubert, 1982). An ascent velocity of 1 m/s is adequate for dykes to cover distances of 50 km in about 13 h. This is possible for a dyke of 0.1 m half width and a temperature excess of 300° C to accomplish before freezing. Increasing thickness and decreasing temperature difference leads rapidly to increased freezing times.

Whereas Kelemen *et al.* (1995) observe only dykes at the base of the crust in the Oman ophiolite and conclude that porous flow of melt must be the dominant extraction process in the mantle, Nicolas (1986) finds an abundance of indigenous and intrusive dykes in the melt extraction zone with transitions of indigenous pyroxenite dykes with dunite walls to dunite veins of miscellaneous dimensions and interprets these as the residual of mafic dykes.

An incipient coalescence of melt by porous flow seems probable. The accumulation of melt in dunite channels denoted as "reaction infiltration instability" is assumed by Kelemen *et al.* (1997). The accumulation of melt in veins due to locally reduced pressure is proposed by Sleep (1988) and observed as well by Stevenson (1989) as "Stevenson instability". Rubin (1998) deals with growth and propagation of dykes caused by an interaction of channel flow and porous flow.

According to Nicolas and Jackson (1982), Nicolas (1986), Sleep (1988) and Rubin (1998), a melt extraction process where melt gathers by porous flow into veins which emerge as dykes is possible. In contrast to Nicolas (1986), who assumes a fracture extending from the surface into the mantle rock, fractures modelled by Weertman (1971) and Sleep (1988) propagate in a wholesale manner as proposed in this thesis and by models of Dahm (2000a).

The way of melt migration towards the spreading axis is unclear: be it melt transport in fluid-filled fractures, porous flow through the mantle rock or in dunite channels. With the existing models, no focussing of melt towards the ridge axis can be obtained, provided that the deviatoric stress field is included in the model of the porous melt flow. In the next section, extended approaches which might improve the situation are proposed. However, it would be beyond the scope of this thesis to integrate those effects in the employed program code.

Extended approaches

The assumed fluid-dynamical model is very simple and can be made more realistic by including additional effects.

The wedge angle, resulting from the lithospheric boundary taken as an isotherm with a constant dipping angle, is not considered in my model. There are several possibilities. First, the lithosphere can act as a "conduit" as adopted by Spiegelman and McKenzie (1987) (see Fig. 4.11 on p. 69, mantle stream lines represented by dotted lines). In this case, the dynamic pressure gradient and the deviatoric stress field generated by the mantle flow do not change compared with the model with a wedge angle of $\alpha = 90\ ^\circ$ applied in this work. Second, the flow could be modelled tangential to the lithospheric boundary which changes the stress field only marginally, (e.g. using the 1100°C isotherm which leads to a dipping angle about 6° for the first 300 km Rabinowicz *et al.*, 1984). Third, the "real" geometry of the lithospheric boundary is considered. The bulk of the oceanic crust is expected to build up its thickness of ≈ 6 km within 2 km of the ridge, which results in a wedge angle about 72 ° at the ridge, but soon gives way to a horizontal boundary. This small region can be neglected, considering that the observed range is several tenths to hundreds of kilometres on both sides of the ridge. Additionally, the flow field for such a "complicated" boundary cannot be described analytically. Likewise, a dependence of the parameter values on the depth, in particular the viscosity, may be reasonable, but results in a stream function which can only be computed numerically.

A magma chamber, which does not exert normal tension on its surroundings, but is able to compensate for the applied shear stress due to the enclosed fluid, changes the deviatoric stress field (see Fig. 4.16). The size and position of the chamber are chosen to affect the directions of principal stress components in the most effective way. The chamber covers an area of 1 km on both sides of the spreading axis and is located at a depth of 2–4 km. The position of the mid-ocean ridge axis is shown as a the dashed line. On the left (a), the deviatoric stress field and dyke ascent paths of the afore-mentioned corner flow model are represented ($v = 1$ cm/a, $\eta = 10^{20}$ Pa/s). The figure in the middle (b) illustrates the stress field under the influence of a magma chamber. The effect is not strong enough to cause focussing, but the difference in the ascent paths is clearly visible. If the magma chamber contains an additional overpressure, a focussing of dykes becomes possible (see c) on the right; an isotropic overpressure of 75 MPa has been applied). It is unclear how such an overpressure in a magma chamber may be generated, but it could be possible to construct a compressive stress barrier at the crust-mantle boundary by parallel intrusions of dykes. An accumulation of their stress fields would presumably result in a similar effect.

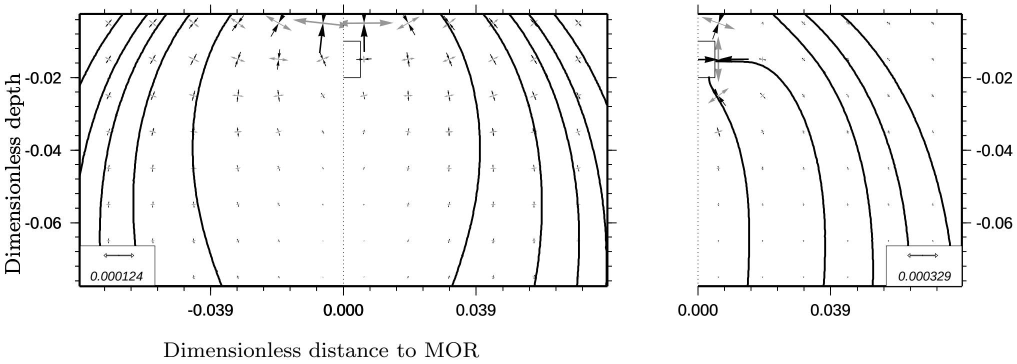

a b c

Figure 4.16: a) stress field and ascent paths of the dykes under the sole influence of the corner flow; b) effect of the stress field of a magma chamber subjected to the corner flow; c) ascent paths are focussing if magma chamber contains an overpressure; dimensionless sketch, σ normalised by $(\eta v/z_0)^{-1}$

Another possibility is the transition from a passive to an active flow model. Rabinowicz *et al.* (1984) differentiate between two kinds of flows: the mean asthenospheric flow, and a low-viscosity local flow beneath the ridge corresponding to an diapiric uprise. They state that due to partial melting and the presence of a low-velocity zone at 35 km depth (the assumed melting zone), a narrow, rapidly ascending diapir may appear and is superimposed on the general mantle flow driven by the plate spreading. A so-called "rolling mill" develops, which is a small convective cell which channels the upward flow in a narrow conduit while the remaining flow is deflected away horizontally. This is highly likely to affect the stress field near the ridge. Close to the axis and at the top boundary, the horizontal velocity of the ascended material is higher than the plate spreading velocity, thus leading to a shear stress, which is inversed to the one in my model. Due to slowing, a shear inversion takes place about 25 km from the ridge axis. A similar inversion at shallow depth is reported by Ceuleneer *et al.* (1988) from observations at the Oman ophiolite. However, geophysical and geochemical evidence favours a passive flow of the mantle due to the plate spreading which is decoupled from deep mantle flow.

An inclusion of ridge topography in the model may enhance the focussing of fractures towards the spreading axis as is indicated by numerical studies of Dahm (2000a).

Ghods and Arkani-Hamed (2000) changed the model of porous melt flow to include both matrix compaction and decompaction due to melt removal and accumulation as well as realistic conditions of melting, freezing and melt extraction at the ridge axis. Due to a temperature-dependent viscosity, the lithospheric boundary acts as impermeable barrier and moves rigidly sideways from the ridge at the spreading velocity. Melt migrates upwards to the top of the asthenospheric layer where it forms a decompacting layer with a high melt content. The melt flux becomes strongly decoupled from the matrix flow and the melt moves along the sloping boundary because of buoyancy effects towards the top region of the ridge axis, where it is extracted. Since the stress field dependends linearly on viscosity in Newtonian flow models, it is possible for the high-viscosity lithosphere to act as a stress barrier to ascending fractures which could propagate to the ridge axis along the bottom of the lithosphere in a similar manner to the melt movement described above. Phipps Morgan (1987) argues that a lithospheric impenetrability would require larger amounts of melting than presently assumed (> 40–50% instead of ~ 10–20%). Furthermore, the zone of high melt content at the top of the asthenospheric layer has not yet been observed.

Although most models assume a 2-D geometry due to the difficulties arising from more complicated models, a mid-ocean ridge could possess a 3-D structure. Ceuleneer *et al.* (1988) refer to intense plastic flow in the direction of the ridge axis at the Oman ophilite, which means that a whole ridge segment is fed by one diapir. This ridge segmentation is on a smaller scale than the spacing between major transform offsets. 3-D models of the mantle flow beneath mid-ocean ridges are given for example by Sparks *et al.* (1993). In their model, local buoyancy sources are responsible for the three-dimensionality of spreading centers. Beneath transform faults, the upwelling is reduced and thus brings about temperature and melting gradients. Additionally, thermal expansion and melt extraction cause density differences. The pattern of mantle flow is hence designed by the relative strength of buoyancy forces and passive flow due to plate spreading. Sparks *et al.* (1993) detect concentrated upwelling beneath the centres of ridge segments. At a low viscosity and spreading rate, a time-dependent flow develops beneath the spreading axis which induces the now plume-like upwellings to migrate along and across the axis with the formation of axis-parallel convection cells. In the model of Rabinowicz *et al.* (1993), only thermal buoyancy is included as well as a layered viscosity, which leads to strong localised downwelling beneath the transform faults. Such downwelling locally inverses the direction of the deviatoric stress field and may add to a focussing effect. The actual implementation of 3-D models is beyond the scope of this work.

4.4.1 Conclusions

In this chapter, I studied melt ascent in a mantle corner flow beneath a mid-ocean ridge by means of wholesale movement of fractures. The numerical modelling results are compared with porous flow models. The melt ascent by fracturing is able to explain the fast transport velocities required by geochemical data. It is not able to account for the strong focussing effect of melt from a large production zone to a narrow extrusion area beneath the ridge axis. However, my results indicate that the porous flow model has the same deficiency if deviatoric stress of the corner flow is taken into account.

Therefore, a mechanism must exist to alter the stress field in the mantle beneath the ridge axis. A temperature dependent viscosity or more complex convection rolls are candidate mechanisms. I showed that a magma reservoir under overpressure could also generate a focussing effect for magma-filled fractures.

Chapter 5

Interaction of dykes and modelling of oceanic crust formation

Most models dealing with oceanic crust formation involve the origin of the eruptive layer (Macdonald, 1982; Gràcia and Escartín, 1999; Smith and Cann, 1999) or the gabbro layer (Henstock *et al.*, 1993; Morgan and Chen, 1993; Boudier *et al.*, 1996; Lissenberg *et al.*, 2004) and the location and influence of magma chambers (Macdonald, 1982; Sempere and Macdonald, 1987; Gudmundsson, 1990b; Gràcia and Escartín, 1999), but rarely effective dyke emplacement (Gudmundsson, 1990a, 1990b) and generation of the sheeted dyke complex (Weertman, 1971, 1973) and to my knowledge never the astonishing parallelity of dykes within the complex.

Weertman (1971, 1973), Sempere and Macdonald (1987), Gudmundsson (1990a, 1990b) and Lissenberg *et al.* (2004) give suggestions as to the magmatic processes creating dykes in oceanic crust. For the origin of the sheeted dyke complex, the consideration of dyke interaction is important, but rarely analysed (Wei and De Bremaecker, 1995; Ito and Martel, 2002). Wei and De Bremaecker (1995) research the interaction of two empty fractures, whereas Ito and Martel (2002) examine the simultaneous ascent of liquid-filled dykes which show coalescence or repulsion depending on their initial vertical and horizontal spacing.

Oceanic crust is formed at mid-ocean ridges. It consists of a thin layer of sediments and pillow lavas, where magma extruded on the seafloor (see also Fig. 4.1, p. 49, chapter 4). The sheeted dyke complex is built up by vertical, parallel dykes. Underneath is a gabbro layer which may contain sheeted sills and the upper mantle composed of mainly peridotites and dunites.

Magma dykes are the most important structural element of the crust and dykes are a key factor in the mechanism of spreading at divergent plate boundaries. In this work, the attention is particularly concentrated on the origin of the sheeted dyke complex. It can be observed in ophiolites, which include a section where 100 % of rock consists of subvertical dykes. In the Oman ophiolite, the sheeted dyke complex is 600–2000 m thick with the thickness of dykes varying from 0.1 to 4.4 m, but with most dykes ranging between 0.5 and 1 m (Lippard *et al.*, 1986).

Since Iceland matches the volcano-tectonic structures of oceanic ridges very well, it is also instructive to observe dyke behaviour there. The width of dyke swarms correlates with the width of the dyke injection zone at mid-ocean ridges, and the basaltic composition of most dykes is similar. In Iceland, local sheet swarms as well as regional dyke swarms can be observed (Gudmundsson, 1990a). The dykes in the swarms are subparallel and subvertical. The majority of dykes occupies pure extension fractures. Local sheet swarms are circular or slightly elliptical, have several kilometres in radius and are confined to central volcanoes. Regional dyke swarms are 5–10 km wide and tens of km long. The thickness of individual dykes may range from a few centimetres up to 20 m for the largest dykes, but relatively thin dykes are the most common. Thicknesses in East Iceland range from 0.05 to 25 m with an average of 4.1 m, in North-West Iceland from 0.01 to 22 m with an average of 4.3 m and in South-West Iceland from 0.02 to 25 m with an average of 1.4 m. The sheets follow the trajectories of the local stress field associated with the shallow chamber, whereas regional dykes follow the trajectories of the regional stress field associated with the divergent plate movement. Many dykes are non-feeders and not connected to lava flows (Gudmundsson, 1990a). Most dykes at great distance from the central volcanoes are emplaced in essentially vertical flows of magma from reservoirs at the bottom of the crust. Shallow chambers in Iceland do not appear to have partly molten, porous roots (Gudmundsson, 2000).

For a sketch of a regional dyke swarm, see Fig. 5.1.

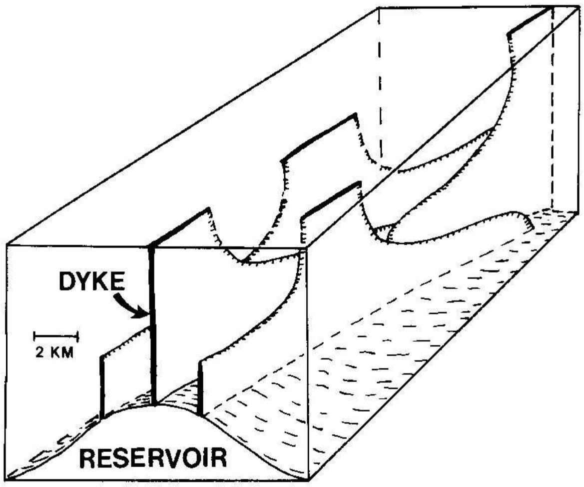

Figure 5.1: Sketch of a regional dyke swarm: Dykes are subvertical and subparallel and extend along the axis of the mid-ocean ridge. Dykes tend to be longer and thinner with increasing depth in the crust; figure taken from Gudmundsson (1990a).

Generally, the sheeted dyke complex at mid-ocean ridges is formed by solidification of episodic intrusions from either deep-seated or shallow magma reservoirs.

The magma flow into and within the reservoir may occur by porous flow, whereas the magma transport from the deep reservoir to the shallow magma chamber and to the surface most likely happens by fluid-filled fracture propagation.

The nature of influencing factors is unclear. Until now, most models are qualitative and tend to neglect stress fields arising from dyke openings and thus lose sight of the self-induced stress field of dykes which can locally surmount the effect of regional stress fields. Since those self-induced stress fields of dykes tend to focus them instead of allowing parallelity (see Fig. 5.2), they are important to consider and include in models for the formation of the sheeted dyke complex. In this model, heterogeneities of the stress field are quantified and are taken into account.

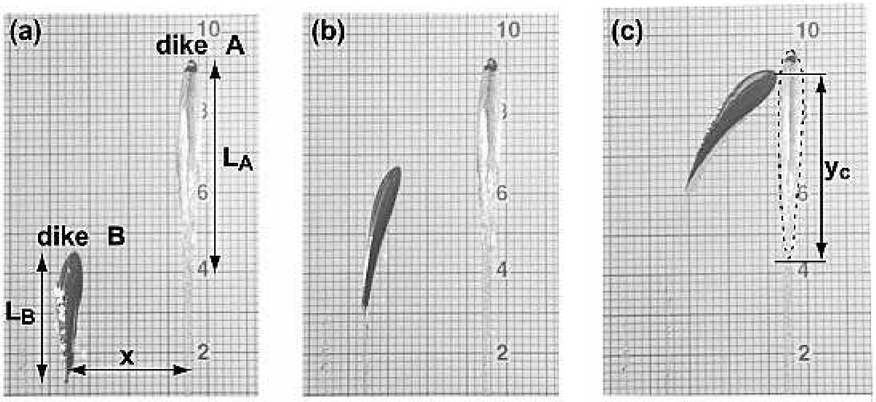

Figure 5.2: Time series of photographs illustrating the interactions of dykes; quasi-static buoyancy-driven fracture movement was observed in solidified gelatine on air-filled dyke B and hexane-filled dyke A. Only dyke heads are visible, dyke tails are too thin. Although both dykes are initiated parallel to each other, dyke B curves toward dyke A during ascent (taken from Ito and Martel, 2002).

Weertman (1971) designed a simple model of oceanic crust formation by dyke interaction (see Fig. 5.3). One assumption is that repeated intrusions beneath the spreading axis and their solidification in the cold upper crust lead to a vertical column of dykes trapped below each other and, after successive intrusions, to the formation of an intrusion zone that acts similar to an "ever expanding mega-dyke" to accommodate the plate spreading.

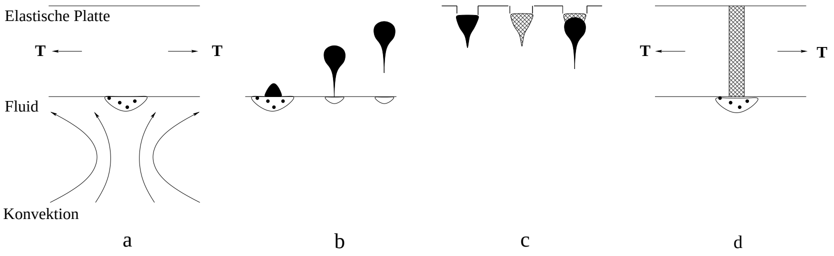

Figure 5.3: (a) Magma reservoir beneath an elastic plate created by convective mantle motion; (b) magma-filled fracture develops, grows and ascends; (c) dyke reaches surface of plate and magma freezes, successive dyke is trapped beneath frozen dyke; (d) formation of an intrusion zone acting as an "ever expanding mega-dyke" by repetition of cycle; sketch after Weertman (1971)

The structure of an oceanic ridge is very complex and seems to be 3- rather than 2-dimensional. Nevertheless, because of the large extension of dykes parallel to the ridge axis compared with the small cross-sectional area, I assume that their behaviour during ascent varies not as much in direction of the spreading axis, but at right angles because of the influence of neighbouring dykes. Since the questions addressed in this thesis are very basic, it is adequate to keep the model as simple as possible. Therefore, all models

considered are 2-D.
Another item, which is not considered here, is the segmentation of oceanic ridges. For fast-spreading centres, ridge segments are generally straighter and longer (> 100 km) than for slow-spreading centres built up from shorter sections (< 10 km), which may be displaced laterally by several hundred kilometres. The crust is systematically thicker at the centre of segments and thins toward their ends (Gràcia and Escartín, 1999). Models presented here can be regarded as typical for the undisturbed sections of a mid-ocean ridge.
An assumption of my model for dyke interaction is that the recurrence frequency of dyke ascent is low enough for the dykes already risen to freeze before subsequent dykes follow, but at the same time high enough such that the stress field of the previously ascended dykes is maintained. The next section deals with the thermodynamics of dyke solidification as well as viscoelastic relaxation and decay of stress fields.

5.1 Estimation of thermodynamic and viscoelastic time ranges

With the help of the boundary element code, it is possible to study the interaction of dykes ascending simultaneously, since boundary element coefficients as well as stress fields and displacements are calculated for each segment regardless of their possible connection. For our purposes, it is more interesting to observe the case of a dyke that freezes at a certain depth and preserves its stress field, which then influences successive dykes. Therefore, it is important to estimate the time range of the solidification process as well as decay of the generated stress field by creep processes in viscoelastic material.
The basic principles describing heat transfer and solidification are gathered from Turcotte and Schubert (1982). Heat transfer is possible by mechanisms of conduction, convection and radiation. Intrusions of igneous bodies are cooled both by conduction and convection of circulating groundwater. Here, only the effect of cooling by conduction is considered. An additional cooling by convection of circulation of sea water is probable. But since it clearly tends to shorten the time needed to solidify the fluid enclosed in the dyke and lengthen the time of viscoelastic decay of the stress field, it strengthens the assumption of a dyke that solidifies before the ascent of the next dyke and that maintains its stress field. A derivation is given in detail in appendix A.3. Only the most important equations are repeated in this section.

1-D time-dependent heat conduction in the direction of the x axis without internal heat production is described by

$$\frac{\partial T}{\partial t} = \kappa \frac{d^2 T}{dx^2} \; . \tag{5.1}$$

κ is the thermal diffusivity related to the thermal conductivity k_t by density ρ and specific heat c of the material such that $\kappa = k_t/\rho c$. t is time and T is the temperature.
The problem of magma solidifying by cooling has to take into account the phase change of fluid magma to a solid intrusion. The location of a phase change boundary has to be evaluated continuously since it shifts during the solidification process. Latent heat is released which must be conducted away from the phase change boundary ("Stefan problem", Stefan, 1891). This technique is applied to calculate the solidification of a dyke or

sill. Most of the oceanic crust is built up of intrusions rather than lava extruding on the seafloor. Dykes and sills are common types of intrusive bodies; sills are horizontal layers of solidified magma, whereas dykes are vertical.

Consider the instantaneous heating of the half-space $x > 0$ (see Fig. 5.4). At time $t = 0$, its temperature is T_0. It is heated instantaneously at $t > 0$ by a change of surface temperature to T_S. As a result of heat conduction, the half-space is warmed.

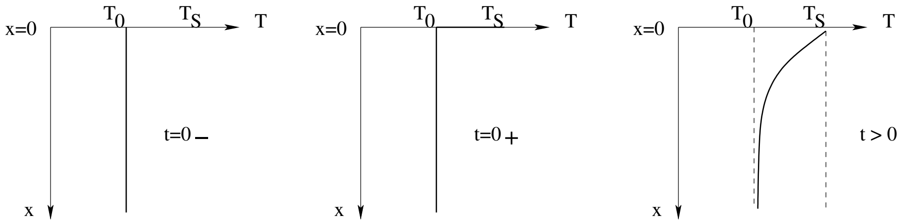

Figure 5.4: Left: half-space $x > 0$ with temperature T_0 at time $t = 0$; middle: subsequent, instantaneous heating at $t > 0$ by change of surface temperature to T_S; right: as a result of heat conduction, the half-space is warmed (after Turcotte and Schubert, 1982)

The instantaneous cooling of a dyke can be treated similarly (see Fig. 5.5). At time $t = 0$, the dyke, which occupies the region $-w < x < 0$, is at its melt temperature T_m, whereas its surroundings ($x > 0$) possess the temperature T_0. At time $t = t_1$, the dyke has begun to cool down, whereas the country rock heats up. The solidification boundary moves inside the dyke and has the time-dependent position $x = x_m(t)$. A detailed calculation can be found in appendix A.3.

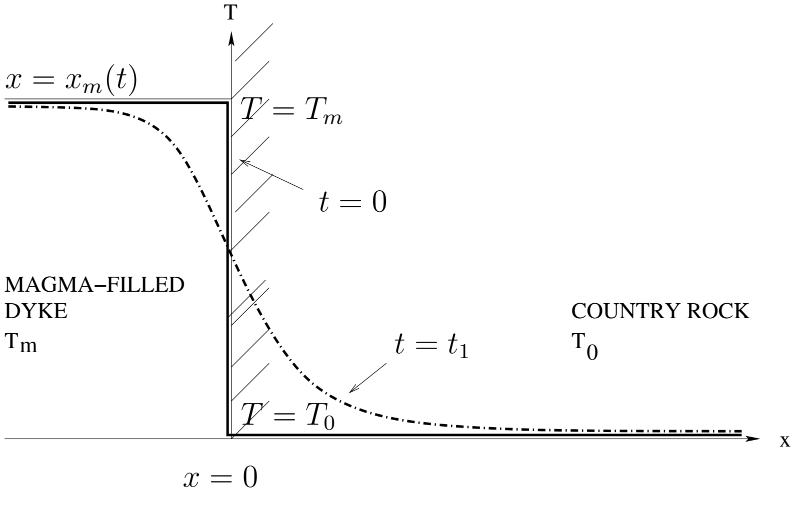

Figure 5.5: At time $t = 0$, the dyke is at its melt temperature T_m, whereas its surroundings possess the temperature T_0; at time $t = t_1$, the dyke has begun to cool down, whereas the country rock is heated up; magma-rock interface situated at $x = 0$, solidification boundary at $x = x_m(t)$

A dimensionless temperature Θ is introduced

$$\Theta = \frac{T - T_0}{T_m - T_0} \quad . \tag{5.2}$$

To emphasise that solutions at different times are similar to each other in the sense that the spatial dependence at one time can be obtained from the spatial dependence at a different time, a similarity variable λ is defined by

$$\lambda = \frac{x}{2\sqrt{\kappa t}} \ . \tag{5.3}$$

$\sqrt{\kappa t}$ is called "characteristic thermal diffusion length"; it indicates the distance over which the effect of a sudden, localised change in temperature can be felt after a time t has elapsed from the onset of the change. The position of the phase change boundary has negative coordinates and can be scaled to become a constant

$$\frac{x_m}{2\sqrt{\kappa t}} = -\lambda_2 \ . \tag{5.4}$$

The similarity approach leads to the reduction of a partial differential equation to an ordinary differential equation as well as the transition of separate boundary conditions in t, x to consistent conditions involving only λ.

Temperature profiles can be evaluated through the use of errorfunction erf and complementary errorfunction erfc by (see appendix for definitions)

$$\begin{aligned} \Theta &= \frac{\mathrm{erfc}(\lambda)}{1+\mathrm{erf}(\lambda_2)} = \frac{T - T_0}{T_m - T_0} \\ \Rightarrow T &= \frac{T_m - T_0}{1+\mathrm{erf}(\lambda_2)} \cdot [1 - \mathrm{erf}\,(\lambda)] + T_0 \ . \end{aligned} \tag{5.5}$$

The temperature of the boundary between dyke and country rock is constant during solidification

$$\Theta_b = \frac{1}{1+\mathrm{erf}(\lambda_2)} = \frac{T_b - T_0}{T_m - T_0} \ . \tag{5.6}$$

The following values are used to calculate temperature profiles for the cooling of a dyke intruding into the oceanic lithosphere (Turcotte and Schubert, 1982): L = 396 kJ kg^{-1}, c = 1.5 kJ kg^{-1} K^{-1}, T_0 = 800 °C, ρ = 2700 kg m^{-3}, k = 1.5 W m^{-1} K^{-1}; L is the latent heat of fusion. The result is displayed in Fig. 5.6. Solidus temperature T_m of basalt is assumed to be 1300 °C on the left, 1200 °C in the middle and 1100 °C on the right. The original position of the dyke-rock interface is situated at $x = 0$ such that the dyke is positioned at negative x coordinates and the country rock at positive x coordinates.

The solidification time t_s for a dyke of width w is specified by Eq. (5.4) to be

$$\begin{aligned} x_m &= -2\lambda_2\sqrt{\kappa t} \ , \qquad \text{with} \quad x_m = w/2 \\ t_s &= \frac{(\frac{w}{2})^2}{4\kappa\lambda_2^2} \end{aligned} \tag{5.7}$$

and illustrated in Fig. 5.7. The bigger the temperature difference, the faster the excess heat can be conducted away from the dyke and the shorter is the solidification time. For a temperature difference of $T_m - T_0$ = 500 °C, a dyke with a halfwidth of 0.5 m needs 7 days to solidify, whereas a temperature difference of only 100 K results in a solidification time of 65 days. A rapid cooling of dykes is indicated by the grain of the dyke rock (Gudmundsson, 1990a).

Magma dykes may reach propagation velocities in the range of 0.1–1 m/s as indicated by

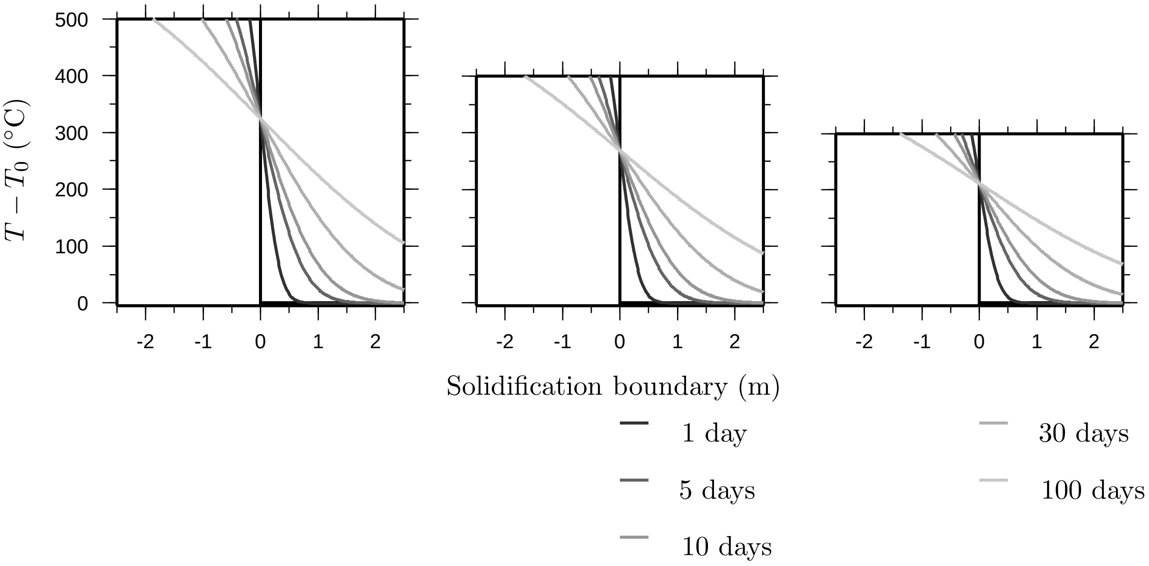

Figure 5.6: Temperature profiles for solidifying dyke after 1, 5, 10, 30 and 100 days; original dyke-rock interface is situated at $x = 0$: dyke is positioned at negative x coordinates and country rock at positive x coordinates; maximum temperature difference between melt and solidified material is 500 °C (left), 400 °C (middle) or 300 °C (right)

numerical studies of Dahm (2000b). Thus even a distance of 50 km in the case of a dyke ascending from mantle depth can be covered in about 14 h up to 5.8 days. Hence, the risk of dykes freezing en route is low.

Since even for the extreme example of a dyke cooling from 1300 °C to 800 °C, thermal expansion is only in the range of 0.04 m per 100 °C (Nishihara *et al.*, 2005), thermal contraction of basalt is neglected. Thus, the stress field resulting from dyke opening is assumed to be similar for the fluid-filled and solidified dyke.

Estimated dyke injection frequencies are one dyke every 2 years for fast-spreading and one dyke every 118 years for slow-spreading ridges (Gudmundsson, 1990a). In most models computed in this thesis, the interaction of roughly 20 dykes is analysed. Hence, to guarantee the constancy of their stress fields through the model cycle, stress fields have to persist at least for 40 or 2360 years respectively.

At the same time, the viscoelastic decay of a shear stress field in a very viscous fluid can be estimated by Landau and Lifschitz (1989)

$$\tau = \frac{\eta}{\mu} \quad , \tag{5.8}$$

where τ is the viscoelastic relaxation time for Maxwell material, η is the viscosity and μ is the shear modulus. The relaxation time indicates the decrease of the stress field to $1/e$ of the original value. With an estimated shear modulus of 30 GPa for oceanic basalt as it is assumed in the following, a viscosity of at least 10^{20} and 10^{22} Pa s is required, resulting in relaxation times of 110 and 11000 a. D'Acremont *et al.* (2003) give values of 10^{20}–10^{22} Pa s

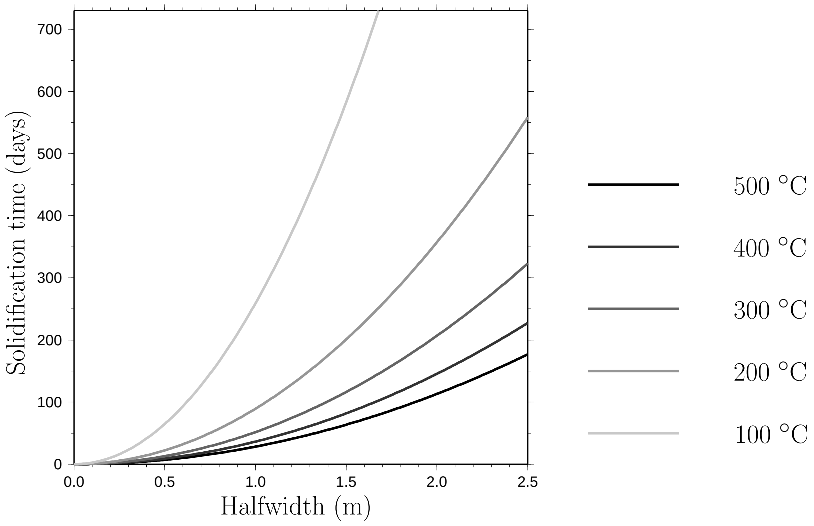

Figure 5.7: Solidification times in days for a dyke of halfwidth $w/2$ and temperature differences between melt and solidified material of 100–500 °C

for the deep mantle, 10^{19} Pa s for the low viscosity zone at the base of the lithosphere and 10^{25}–10^{27} Pa s for the brittle-ductile transition in oceanic crust. Since the dykes are thought to be arrested at the level of neutral buoyancy situated above the brittle-ductile transition, I think the conservation of stress fields can safely be guaranteed for the required time span, even in the case of a lowered crustal viscosity because of temperature effects near to the spreading axis.

Hence, the time span of solidification (days to months) is much shorter than the dyke recurrence time (years to one century), and this in turn falls below the time of viscoelastic relaxation (centuries to millennia). A freezing of the dyke on its way to the surface is excluded as well, since dykes can reach ascent velocities in the range of m/s.

5.2 Dyke-dyke interaction

Because of the fracture opening, dyke emplacement leads to a local variation in the regional stress field. To examine dyke interaction, these local effects of the stress field have to be preserved. An advantage of the boundary element method is that not the whole modelling region is discretised, but only the fracture surfaces. Stress and displacement fields can be computed with high accuracy at any point outside the fracture. I made the most out of it by developing a method not storing the stress field directly. Only the geometry of segments (midpoint coordinates, angle to global coordinate system, segment length) as well as the normal and shear displacement discontinuities are saved to a file. At the time of the next dyke ascent, the main program reads these parameters in and computes the stress field generated by displacements at boundary elements of previously ascended dykes at the required point, e.g. the crack tip of currently ascending dyke (see appendix B.4, pp. 160). This stress field is added to the background stress field which consists of the lithostatic gradient and may contain a regional stress field additionally (see appendix B.2, pp. 158). Again, the boundary element method with modifications for the simulation of quasistatic propagation is used for calculations, as described in chapter 3 (section 3.3.2, pp. 41).

To be able to understand the mechanism of dyke interaction and the consequences for the formation of the sheeted dyke complex, observations are at first confined to the interaction of two dykes. The principle is presented in Fig. 5.8. Dykes ascend one after the other from their initial position in depth and stop at a level of neutral buoyancy. The initial position is marked by a blue, the end position by a red and the ascent path by a black line. Depth of initial position and level of neutral buoyancy are arbitrary and do not indicate geological conditions. The initial depth is chosen such that dyke interaction becomes clearly visible. Distances are displayed in kilometres and not dimensionless as in the previous chapter, since no models from other authors are available for comparison.
The stress field is indicated by the principal axes of compression and extension; black arrows mark the principal axis of compression, red arrows show the principal axis of extension. The second dyke orients itself at the stress field of the first dyke during its rise. Propagation is mainly in the direction of maximum compression, but may deviate because of effects of enclosed fluid mass, apparent buoyancy and dyke length.

Figure 5.8: Exemplary scheme of dyke-dyke interaction; initial position: blue line, ascent path: black line, end position: red line; stress field of first dyke indicated by arrows (black arrows: principal axis of maximum compression σ_1; red arrows: principal axis of maximum extension σ_3)

The first model was chosen to be very simple and serves to highlight stress fields generated by dyke and sill openings. Only results are briefly quoted here, a more detailed explanation can be found in appendix A.3. A large dyke or sill is placed at a certain depth. Small dykes ascend and interact with the stress field of the large "test dyke", but not among themselves. The result can be seen in Fig. A.8, p. 150. Successive dykes accumulate horizontally alongside the test dyke and vertically beneath the test sill. In both instances, successive dykes try to follow the direction of maximum compression, which lead to the fracture surface where the opening is largest. The circle of influence depends on the internal pressure of the test dyke.

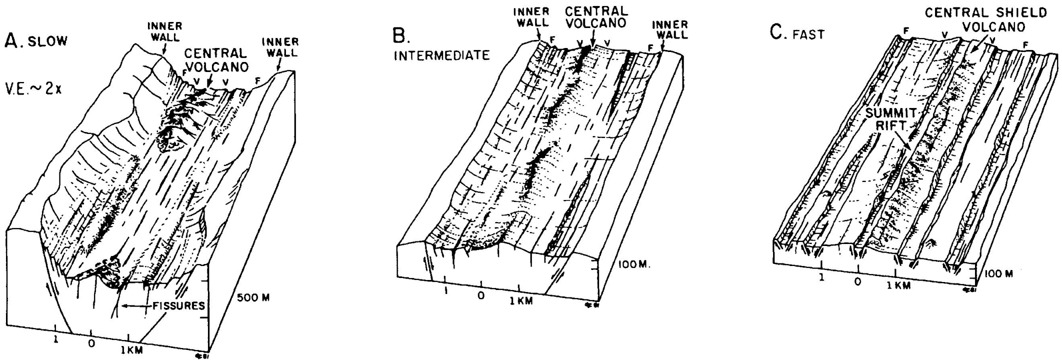

Figure 5.9: Comparison of ridge topographies for different spreading rates; left: slow-spreading, middle: intermediate-spreading, right: fast-spreading ridge; figure taken from Macdonald (1982)

This model is made more realistic by including the following:

- All dykes have the same length.
- All dykes ascend from beneath including the "test dyke".
- Dykes stop at a level of neutral buoyancy (=LNB; e.g. Mège and Korme, 2003; Dahm, 2000a).

The magnitude of the stress field is lower than in the previous model, since the internal pressure of the dyke is assigned a reasonable value (see Fig. A.9, p. 151). The circle of influence decreases as well because of the comparability of dyke lengths and stress fields. Dykes align vertically and not horizontally to the test dyke, since the ratio between stress field magnitude and their length prevents them of a quick adjustment to the direction of maximum compression.

Ascent paths chosen by subsequent dykes depend on their length (see Fig. A.10, p. 151). Large fractures have a strong preferred orientation in the vertical direction. The deviation from this orientation occurs only at depth of the test dyke and is largest for the close-up range. Small fractures are able to adapt quickly to preexisting stress fields. The deviation from a vertical path occurs near their initial positions and is largest for the middle range because of the orientation of the stress field.

5.3 Structure of oceanic crust at different spreading rates

A paradox exists between different characteristics of spreading centres of variable spreading rates and the high degree of geophysical, petrological and geochemical uniformity in mature oceanic crust (Henstock *et al.*, 1993). The main difference between slow- and fast-spreading ridges lies in the lack of the central rift valley and a smoother topography at fast-spreading ridges (Wilson, 1989). This is illustrated in Fig. 5.9, where the topography of a slow-spreading ridge is depicted on the left (A), an intermediate-spreading ridge in the middle (B) and a fast-spreading ridge on the right (C; figure taken from Macdonald, 1982). Slow-spreading ridges possess an axial magma chamber only at the crust-mantle boundary, whereas fast-spreading ridges feature permanent crustal magma chambers in addition (e.g. Macdonald, 1982; Sempere and Macdonald, 1987; Morgan and Chen, 1993;

Gràcia and Escartín, 1999; Lissenberg *et al.*, 2004). Slow-spreading ridges show a higher variability in crustal composition; at the ends of ridge segments peridotites and gabbros are dredged, which are either exposed on the seafloor due to tectonic extension or contained in a more heterogeneous crust, which is not fully magmatic (Gràcia and Escartín, 1999).

One theory is that fast-spreading ridges feature a continuous and robust supply of magma such that the magmatic accretion can keep up with the spreading, only little deformation can be expected and the stratigraphy is thick, continuous and coherent. Slow-spreading ridges on the other hand undergo discontinuous melt supply. The extension at the spreading centre is accompanied by crustal thinning, which leads to normal faults, large-scale detachment faults, block rotation, tilting of units and formation of core-complexes that expose lower crust and mantle on the seafloor. Thus, the crustal section is tectonically and stratigraphically complex and the crustal thickness is extremely variable (Lissenberg *et al.*, 2004). Despite the unequal magma supply, the end product – the layered oceanic crust – looks in principle the same, always including the sheeted dyke complex on whose formation attention is concentrated in this work. This similarity implies that the igneous processes involved in crustal formation are the same across a range of spreading rates (Henstock *et al.*, 1993). Macdonald (1982) supports this hypothesis and states that beyond first-order differences of the morphology with deep rift valleys at slow-spreading ridges and shallow rift valleys or axial highs at fast-spreading ridges, the pattern of fine scale crustal structure and tectonics is largely independent of spreading rate. The spreading rate seems to influence primarily the continuity in time and in space of volcanic, magmatic and tectonic processes as well as the amplitude of faulting, but the fundamental processes and structural evolution seem to change little.

Weertman (1973) specifies three kinds of tensile stresses that can develop at mid-ocean ridges. Extensional stress is produced by divergent convective flow in the asthenosphere which couples to the oceanic plate. Additionally, extensional stresses are generated by "floating" of the lighter density material of the ridge in a sea of heavier density material. Since a fracture produces extensional stress below its tip, tensile stress originates also beneath the magma freezing zone considered to present an "ever expanding crack".

Earthquake focal mechanisms show that the horizontal stress field in the oceanic lithosphere generally has three components: ridge-perpendicular tensile stresses directly at the spreading axis and near to it, ridge-parallel tensile stresses in young oceanic lithosphere, and compressive stresses in old oceanic lithosphere (Neves *et al.*, 2004).

Ridge-perpendicular extension is indicated by normal faulting near the spreading axis and extensive active normal faulting in a zone up to 10–20 km from the spreading axis, striking parallel to it. Fialko (2001) discusses the generation of normal faults, which are inward-dipping at slow-spreading mid-ocean ridges and may accommodate up to 10–20 % of extension generated by plate spreading; intermediate to fast-spreading ridges may show outward-dipping normal faults in addition. Neves *et al.* (2004) and references therein explain those tensile stresses ("ridge resistance") by a stress deficiency at the spreading axis relative to the lithostatic state of stress of the nearby lithosphere. Additionally, the elevation of the ridge above its surrounding due to the greater buoyancy of the thinner, hotter lithosphere drives the lithosphere away from the ridge crest. Gravitational sliding (or "ridge push") is one of the important forces driving plate spreading (Turcotte and

Schubert, 1982).
Ridge-parallel tensile stresses in 1–35 Ma old lithosphere originate from thermoelastic stresses resulting from cooling and contraction of the lithosphere. Lithosphere older than 35 Ma is subjected to compression caused by "ridge push" forces (Neves *et al.*, 2004). Assuming a spreading rate of 5 cm/a, lithosphere with an age of 1 Ma is dislocated by 50 km from the spreading axis, whereas an age of 35 Ma corresponds to a distance of 1750 km. Thus, only ridge-perpendicular tensile stresses are of importance in the model area.
The tensile strength at divergent plate boundaries is in the order of a few megapascals (Gudmundsson, 1988). In situ tensile strength measurements for the upper part of Icelandic crust yield around 1–6 MPa with an average of 3.5 MPa. Coblentz and Sandiford (1994) predict stresses of 9 MPa at mid-ocean ridges on the African Plate by modelling of lateral variations in the gravitational potential energy of the lithosphere arising from lithospheric density variations. Unfortunately, no measurements of stress magnitudes at mid-ocean ridges are available because of costliness of the experiments and the impossibility to derive them with standard methods. Worldwide, only very few scientific boreholes exist including such measurements (Oliver Heidbach, University of Karlsruhe, personal communication). So far, only one scientific borehole drilled in oceanic crust reached the depth of the sheeted dyke complex (Wilson *et al.*, 2003, ODP-Leg 206).

In the following table (Table 5.1), the most striking properties of mid-ocean ridges at different spreading rates are highlighted and divided into four schemes: fast-spreading, intermediate-spreading and slow-spreading. Total spreading rates for fast-, intermediate- and slow-spreading are classified after Gudmundsson (1990a). In the following, a more detailed description of fast-, intermediate- and slow-spreading ridges is given.

Ridge type	*Total spreading rate*	*Magma reservoir*	*Dyke injection zone*
Fast-spreading	9–18 cm/a	Crustal magma chamber ("infinite onion" model)	narrow
Intermediate-spreading	5–9 cm/a	Dykes feeding from underlying sills	broad, but discontinuous
Slow-spreading	1–5 cm/a	Reservoir at crust-mantle boundary Temporary high-level chamber ("infinite leek" model)	broad and continuous

Table 5.1: Simplified overview of ridge types

Fast-spreading ridges

Slow- and fast-spreading ridges differ mostly by their topography, that of fast-spreading ridges being smoother and lacking a central rift valley (Wilson, 1989, this and following comments). The ridge morphology with constructive volcanism at the spreading axis and destructive tectonics along the margins is similar at both types of ridges as is the character of extrusions. In addition to the volcanic hills, fast-spreading ridges feature plains of low relief consisting of lava lakes caused by high extrusion rates. Margins of the extrusion zone (e.g. 2.5–3.0 km width, East Pacific Rise, EPR) consist of horst-like highs created by fissures and normal faults, which show less displacement than the faults bounding the inner rift zone at slow-spreading ridges. The spatial sequence from primitive basalts at the spreading axis to more evolved at the margins is the same for both fast- and slow-spreading ridges, but the fractionation of most common rock types sampled indicates a fundamental difference in magma chamber processes.

Due to thermal modelling, crustal magma chambers beneath spreading axes require half-spreading rates greater than 0.5–0.9 cm/a to guarantee their potential existence. Increasing spreading rates lead to expanding magma chambers, a half-spreading rate of 6 cm/a resulting theoretically in a magma chamber with an extension of 10 km to both sides of the spreading axis. Only small discontinuous magma chambers can be present at slower spreading ridges, whereas fast-spreading ones have large continuous magma reservoirs. Small magma chambers may experience extensive differentiation to erupt a wide compositional range from primitive basalt to more evolved ferrobasalts. Large magma reservoirs undergo fractional crystallisation and magma mixing, resulting in eruption of compositional uniform, somewhat differentiated magma dependent on the efficiency of the mixing process.

Shallow magma chambers are likely to come into existence above great accumulations in the source reservoir (Gudmundsson, 2000). Several conditions have to be satisfied. A trap is needed, where upward propagating dykes change into sills, for example lithological or structural boundaries or stress barriers. Frequent input from the underlying reservoir is required. The shallow chamber acts as a sink and source simultaneously.

At mid-ocean ridges, roofs of shallow, crustal chambers are commonly at depths of 1.2–3.5 km below the surface of the oceanic crust (Gudmundsson, 1990a). The width of the chambers perpendicular to the axis of the ridge is commonly from 2–3 km up to 8 km and may extend several kilometres along the axis of the ridge. The source reservoirs for the crustal magma chambers may occupy almost the whole length of the associated ridge segments which is about 50–200 km.

Two different kinds of models for axial magma chambers beneath mid-ocean ridges have been defined: the "infinite leek" model is appropriate for slow-spreading, the "infinite onion" model fits fast-spreading ridges. The magma chamber model for fast-spreading ridges was proposed by Cann (1970, 1974), but is described here along the lines of Wilson (1989, see Fig. 5.10). During spreading, lava is erupted through dykes fed from the roof of the chamber and magma crystallises at the walls to form isotropic gabbros. Layered basic and ultrabasic rocks are produced at the floor by crystal fractionation processes. In this case, open-system fractionation combined with efficient magma mixing will take place compared with the closed-system fractional crystallisation that can be found in small high-level, non permanent chambers at slow-spreading ridges.

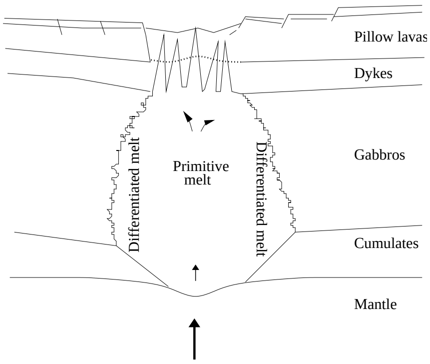

Figure 5.10: "Infinite onion" model for axial magma chamber beneath fast-spreading ridges, sketch after Wilson (1989)

Intermediate-spreading ridges

By studying the Annieopsquotch ophiolite (Newfoundland), which is thought to have been formed at an intermediate- to fast-spreading ridge, Lissenberg *et al.* (2004) deduce that sill intrusions are by far the most important lower crustal accretion process. Although they focus on the origin of lower oceanic crust, the results have consequences for the formation of the sheeted dyke complex.

Two different kinds of models exist for the development of the gabbro layer situated beneath the sheeted dyke complex: the "gabbro glacier model" as well as the "sheeted sill model". The first model implies the formation of the lower oceanic crust by partial crystallisation within the axial magma chamber (AMC), followed by subsidence and outward flow. The sheeted sill model, which Lissenberg *et al.* (2004) suppose to be true for the Annieopsquotch ophiolite, consists of crust generation by direct intrusions from the mantle. The implication is that the sheeted dyke complex is fed by dykes originating from sills in the lower crust rather than by dykes from a magma chamber (see Fig. 5.11). This assumption is supported by the observation of a higher degree of evolution of magmas with increasing stratigraphic height. The presence of crosscutting dykes and discordant feeder channels within some of the gabbroic sills shows the importance of hydrofracturing as transportation process for residual melts from the sills to the upper crust.

Slow-spreading ridges

In general, slow-spreading ridges have a much more rugged topography than fast-spreading and have a median valley (Wilson, 1989, this and following comments). A known example for a slow-spreading ridge is the Mid-Atlantic Ridge (MAR) with the extensively investigated FAMOUS area between 36 and 37°N. The MAR possesses a wide axial valley (25–30 km), bounded by rift mountains, which includes a narrow inner valley (3–9 km) where the current volcanic activity is concentrated. Since the volcanic activity is neither spatially nor temporarily constant, distinct volcanic hills (less than 300 m high) are formed, which are transported to one side of the rift valley where they become fragmented by the fault-controlled rift flanks. Additionally, those flanks are coated by thin lava flows emanating from the valley walls and flowing inwards towards the rift axis. Basalts erupted

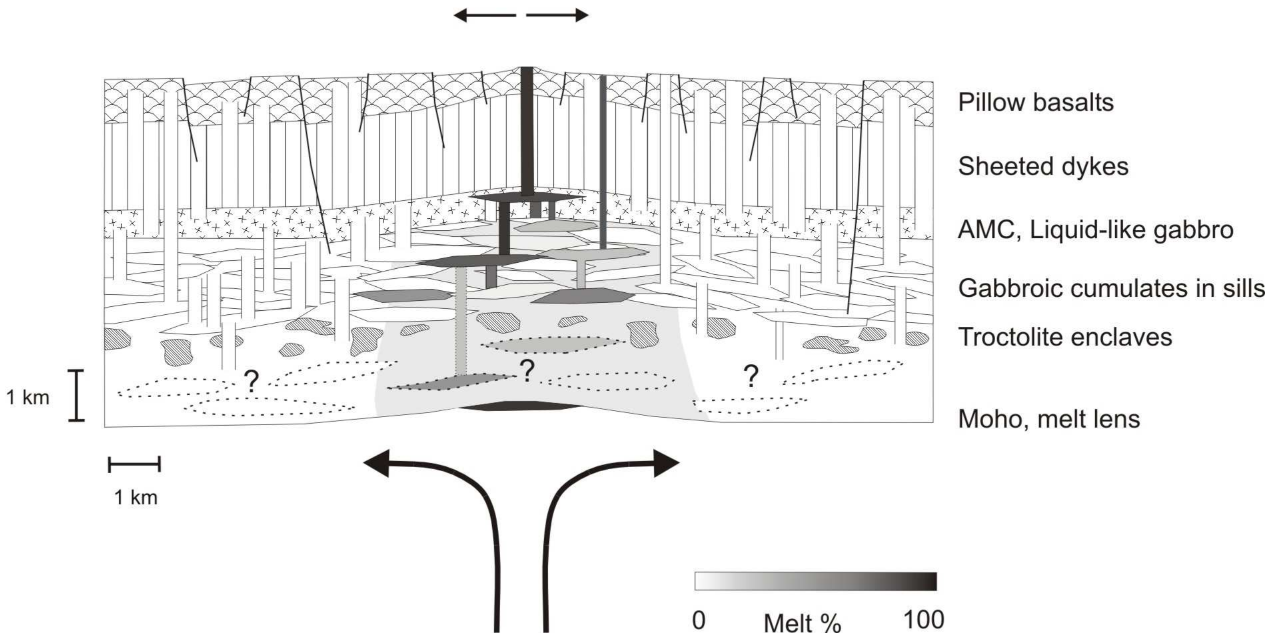

Figure 5.11: Schematic model for oceanic crust accretion taken from Lissenberg *et al.* (2004): Lower crustal sills are fed by melt gathered at Moho level. Subsequently, the magma moves up either to form higher-level sills, to feed an AMC below the sheeted dyke complex, to feed the upper crustal dykes or to erupt. Note that sills are not to scale.

at the central volcanic hills are the most primitive, whereas eruptions at the margins of the rift provide more evolved basalts. The presence of large crustal magma chambers at slow-spreading ridges is excluded by geophysical data. Low-pressure crystal fractionation processes generating compositional variations are thought to take place in small, isolated magma chambers situated directly beneath the volcanic hills. I assume that these very high-level magma chambers which tend to lead to eruption are not essential for the formation of the sheeted dyke complex. They are therefore not covered in my modelling.

At slow-spreading ridges, deep reservoirs at the crust-mantle boundary are probably the only available sources for dykes and thus, dykes are injected directly (Gudmundsson, 1990a). The crust-mantle boundary may act as a magma-trapping interface, when stress intensity factors at the tip of dykes ascending in the mantle are too small to overcome the fracture toughness of the lower crust (rigidity barrier effect; Rivalta *et al.*, 2005). Nisbet and Fowler (1978) propose the "infinite leek" model for magma ascent at slow-spreading ridges in contrast to the "infinite onion" model explained above (Fig. 5.12). It results in temporary magma chambers in contrast to the permanent magma chambers found at fast-spreading ridges. Magma rises by crack propagation through the brittle crust; storage occurs only in small chambers at very high levels.

Additionally, an ultraslow-spreading class of oceanic ridges exists, which seems to be as different from slow-spreading ridges as slow-spreading ridges are from fast-spreading ones. They consist of linked magmatic and amagmatic accretionary segments, lack the gabbro section (layer 3) and expose abundant mantle peridotites (Dick *et al.*, 2003). Since they do not benefit the study of the origin of sheeted dyke complexes, they are disregarded in

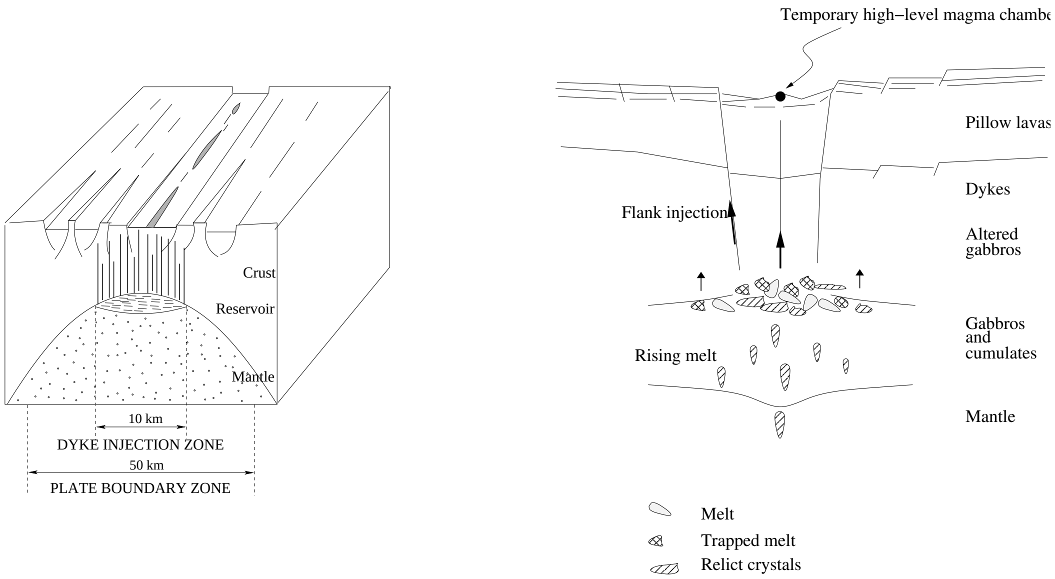

Figure 5.12: Left: Magma reservoir at crust-mantle boundary resulting in broad dyke injection zone, sketch after Gudmundsson (1990a); right: close-up view on the crust; "infinite leek" model for axial magma chamber beneath slow-spreading ridges, sketch after Nisbet and Fowler (1978)

this study.

5.3.1 Open questions

The objective of the modelling of dyke ascent and interaction is to understand better the formation of oceanic crust at mid-ocean ridges. The following questions occupy a central position:

- **Formation of the sheeted dyke complex**
  The difficulty of the generation of sheeted dyke complex arises from the high parallelity of dykes within the complex despite their self-induced stress fields. Will an initial parallel ascent suffice to explain this phenomenon? The stress field generated by a test dyke leads to focussing of the successive dykes. In the following models, the interaction of more than two dykes is analysed. A superposition of stress fields induced by several dykes enhances the focussing effect. Is it possible at all to simulate the alignment of parallel dykes as observed in the sheeted dyke complex?
- **Dependence of crust formation processes on spreading rate**
  Is the apparent higher variability in the composition of oceanic crust generated at slow-spreading ridges induced by larger heterogeneity of the crust or are peridotites and gabbros exposed on the seafloor because of tectonic extension?
  The existence of a sheeted dyke complex is proven at both slow- and fast-spreading ridges. Are different magmatic processes required to explain their formation at varying spreading rates?
- **Development of crustal magma chambers**
  Why do crustal magma chambers exist at fast-spreading ridges, while slow-spreading ridges possess only deep magma reservoirs at the crust-mantle boundary? Do they

originate solely due to the higher amount of available magma?
Magma chambers at high crustal level are also required to explain the formation of off-axis seamounts. The development of a magma chamber calls for the gathering of large amounts of magma. The storage and solidification of a dyke enclosing hot magma in the crust will heat the surroundings. When and where will partial melting take place e.g. in the gaps between neighbouring dykes? Can it lead to the formation of magma chambers in the crust?

- **Ever expanding mega-dyke model**
  Weertman (1971) presents a very simple model for oceanic crust formation by ascending dykes and names it the "ever expanding mega-dyke" model. A vertical column of crust is formed by trapping successively ascending dykes below each other (see also Fig. 5.3). Is this scenario tenable?
- **Sill formation in the gabbro layer**
  In the gabbro layer beneath the sheeted dyke complex, the formation of sills is observed. Why are magma-filled fractures turned horizontal instead of ascending? Is it possible to build up a compressive stress field by the accumulation of vertical intrusions such that a further ascent of dykes is inhibited?

In the next section, the numerical models of dyke interaction are presented. They are interpreted in terms of the questions posed here in section 5.4.1 (pp. 104) and discussed in section 5.5 (pp. 116).

5.4 Numerical models of dyke interaction

Fractures start from an initial position. Their generation by either porous flow of melt or breakout from a magma reservoir is not considered here. In contrast to the models shown before, the stress field of all dykes already ascended is superposed. Since the governing equations are linear, superposition is performed by simple summation of the stress fields. Hence, stress fields are not displayed in figures apart from special cases, since they vary during iterative ascents of dykes. Fractures are stopped at a level of neutral buoyancy. Depth of initial position and LNB are chosen arbitrarily and do not indicate geological conditions.
Numerical models can be classified by

- initial positions of dykes
- external stress field
- dyke length.

In the following, results of the modelling are sorted by the distribution of initial dyke positions. Models ex- and including an extensional stress field are juxtaposed to compare the influence of the local, dyke-induced stress field with the regional, ridge-induced. A test of the impact of dyke lengths is presented at the end of the section.

Same initial position

In the simplest possible model, the initial position is the same for all dykes. Fig. 5.13

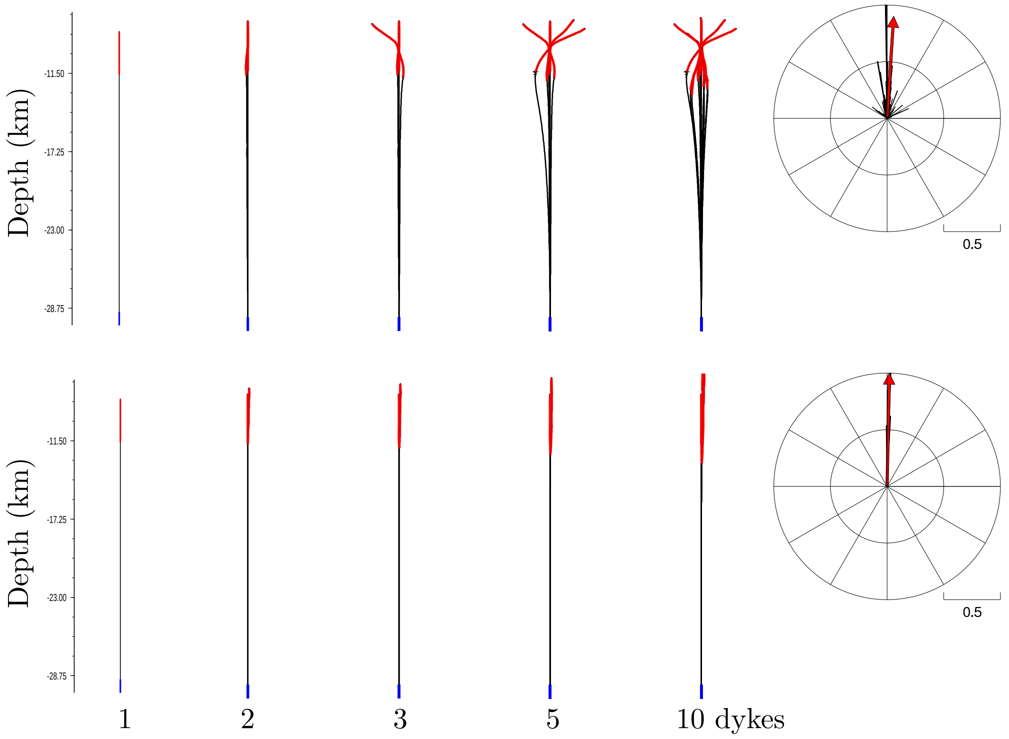

Figure 5.13: Ascent of dykes from the same initial position; left: ascent paths of one, two, three, five and ten dykes, right: sector histograms; top: sole influence of superposed stress fields; bottom: effect of a regional, extensional stress field included

(top) shows the sole influence of the superposed stress fields on the ascent of one, two, three, five and ten dykes. Despite the simple geometry of the model, the dyke pattern is quite complex. Fig. 5.13 (bottom) includes the effect of a regional, extensional stress field as it can be observed at mid-ocean ridges. All dykes follow the same ascent path; only the "solidification depth" differs slightly. To the right, the orientation of dykes is indicated by a sector diagram. All dyke segments have the same length. Their angle to the vertical is plotted by black lines. Segments with the same angle are summed up and the maximum is fixed to 1. The red arrow indicates the main orientation of segments both in direction and magnitude. In both cases, the main orientation of dyke segments is approximately vertical, but the deviations are larger in Fig. 5.13 (top), where no extensional stress field is included.

Distributed initial dyke positions

Since the greatest magma accumulation is not necessarily in the central part of a reservoir (Gudmundsson, 2000), the distribution of dyke ascent starting points from a broad dyke injection zone is difficult to predict. A variety of distributions of initial dyke positions was tested ranging from random to positions shifted by a constant distance. The randomness of the start positions is created using the random number generators from Press *et al.* (1989). First of all, a model with randomly distributed initial positions is presented. Afterwards, two modifications are shown where the **order of dyke ascent** is still random, but the **distribution of initial positions** is varied according to certain criteria: first, start positions are subjected to a Gaussian distribution and second, they are arranged at regular intervals. Finally, the order of ascent is controlled as well. Dyke injection zones are assumed to have a width of 10 km and a quantity of 18 dykes ascending consecutively was chosen.

The first model of randomly distributed initial positions is used to show in detail the influence of the dyke-induced stress field on the propagation of subsequent dykes. In Fig. 5.14, propagation paths of dykes reacting only to the stress field of preceding dykes are shown. On the left, the distance axis is exaggerated to point out the propagation paths of dykes; on the right, the real aspect ratio is shown. Dykes ascend one after the other. In the uppermost figure, only the first dyke is visible; in the following figures 2, 4 and 18 dykes are present.

The 2nd dyke starts its ascent near to the 1st. Also the 4th fracture, situated 4 km away from the 1st, is focussed toward the 1st dyke. The subsequent cracks seem to be more influenced by the 4th dyke located more horizontally than by the combined stress field of the first 3 dykes and more dykes are focussed towards it. Several model runs with different random distributions of fractures have been performed, always leading to a similar result (see Fig. A.11, appendix A.3, p. 153).

Ascent paths of dykes responding to a regional, extensional stress field are depicted in Fig. 5.15. The inclusion of an additional ridge-perpendicular extensional stress field decreases the influence of the dyke-induced stress field and leads to more parallel dyke alignment. An overpressure of roughly 7 MPa (estimated during ascent) is encountered by an extensional stress field of 5 MPa. The influence of preceding dykes in the neighbourhood of a newly ascending dyke is still recognisable; nevertheless, dyke end positions are more vertical and sub-parallel. The effect of the dyke-induced stress field is weakened.

The difference in dyke orientations with and without the influence of an extensional stress field is highlighted by sector diagrams in Fig. 5.16. On the left, orientations of dyke segments for the model without the regional stress field are shown; they are much more diversified than in the case of an additional, extensional stress field (on the right). The main orientation is approximately 15° to the left which results from the position of the "focussing area" relative to the initial position distribution. Under the influence of an extensional stress field, the main orientation is vertical.

The influence of the initial position distribution is further highlighted in Fig. 5.17. The same number of dykes is used for all models. From top to bottom, initial positions are distributed randomly, subject to a Gaussian distribution and at regular intervals. In all models, the order of ascent is random. Finally in the bottom part, the order of ascent is regular and progresses from left to right (leftmost dyke first). The dyke ascended first is always distinguishable by its straight propagation path. Despite the different start position distributions, the results for a random order of ascent look surprisingly similar. On the left of Fig. 5.17, only the dyke-induced stress fields are considered. The location of the "focussing area" shifts depending on the order of crack ascent. It is formed where two dykes happen to be situated close-by. Dyke ascent is mostly vertical at greater depth. Only when a fracture approaches the previously ascended dykes does the curvature of the ascent path change. The end length of the first dyke is 3 km. The fractures seem to grow in length when propagating more horizontally near the LNB (be careful to only use

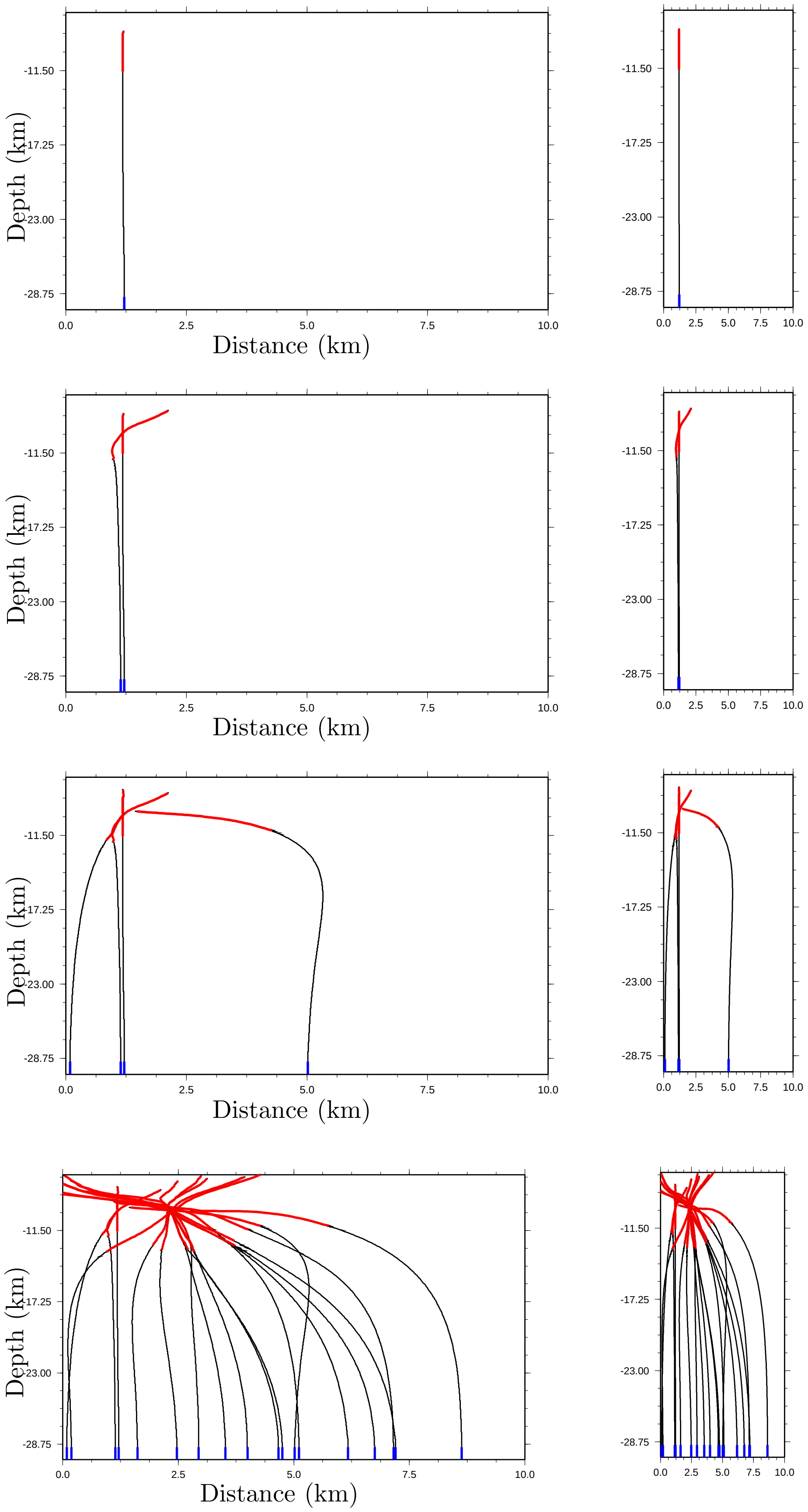

Figure 5.14: Subsequent ascent of dykes with randomly distributed initial positions without application of regional stress field; from top to bottom: ascent path of 1, 2, 4 and 18 dykes; left: distance axis is exaggerated; right: real aspect ratio is shown

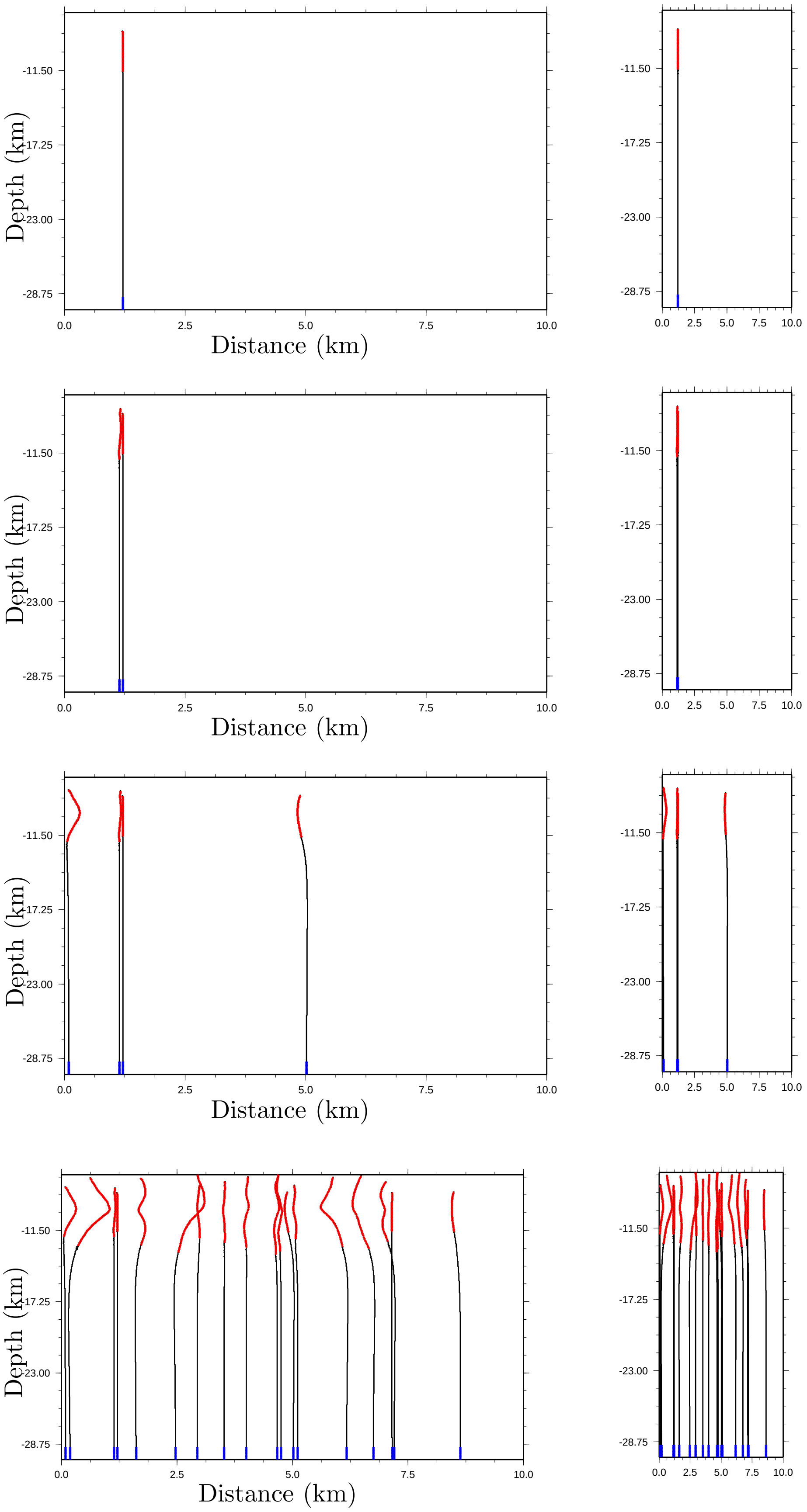

Figure 5.15: Subsequent ascent of dykes with randomly distributed initial positions, extensional stress field included; from top to bottom: ascent path of 1, 2, 4 and 18 dykes; left: distance axis is exaggerated; right: real aspect ratio is shown

Figure 5.16: Sector diagram for comparison of directions of dyke segments in model of subsequent ascent of dykes with randomly distributed initial positions; left: without application of regional stress field, right: extensional stress field included

real-aspect ratio figure for comparison).

Adding an extensional stress field of 5 MPa leads to a more vertical arrest of dykes. The predominance of the dyke-induced stress field over the regional stress field is not large enough to keep on focussing the cracks.

The largest deviation from this behaviour occurs when the ascent is no longer random (lowest model). The focussing of dykes is very strong and is visible as well on the right of Fig. 5.17, despite the application of an extensional stress field. Dykes are still separated and do not cross each other. Deviations from vertical end positions can be seen in Fig. 5.18. Without a regional stress field, dyke segment directions are almost evenly distributed. In the case of a determined order of ascent, the segments exhibit a striking horizontal orientation. If an extensional stress field is included, both the random distribution of initial positions and the regular distribution feature an almost perfectly vertical orientation of segments. The Gaussian distribution as well as the distribution subjected to a determined order of ascent show a broader range of segment orientations, the last exhibiting a spectrum with two peaks.

The study of length-dependent behaviour is conducted with a regular distribution of initial dyke positions and a random order of ascent, since this guarantees a high density of dykes and thus distinct patterns. If the inner pressure of a dyke only depends on the density of the magma inside it and the bulk modulus stays the same, short dykes possess a minor stress field in comparison with long dykes. The influence of the magnitude of the stress field, even for dykes of equal length, is surprisingly high. In Fig. 5.19, the effect of dyke length on their ascent path is shown. Dykes start from the same initial positions and feature equal length during one model cycle, but lengths change between cycles. Dyke end lengths are used for comparison. From top to bottom, dyke end lengths are 0.5 km (extremely small), 1 km (small), 1.5 km (medium) and 3 km (long). Ascent paths of 49 dykes are shown on the left. On the right, a "segment density" is illustrated corresponding to the quantity of dyke segments per unit area. All segments possess the same length per definition, thus the segment density is a measure not only for the number of segments, but for the enclosed amount of magma and its distribution. The influence of extremely small

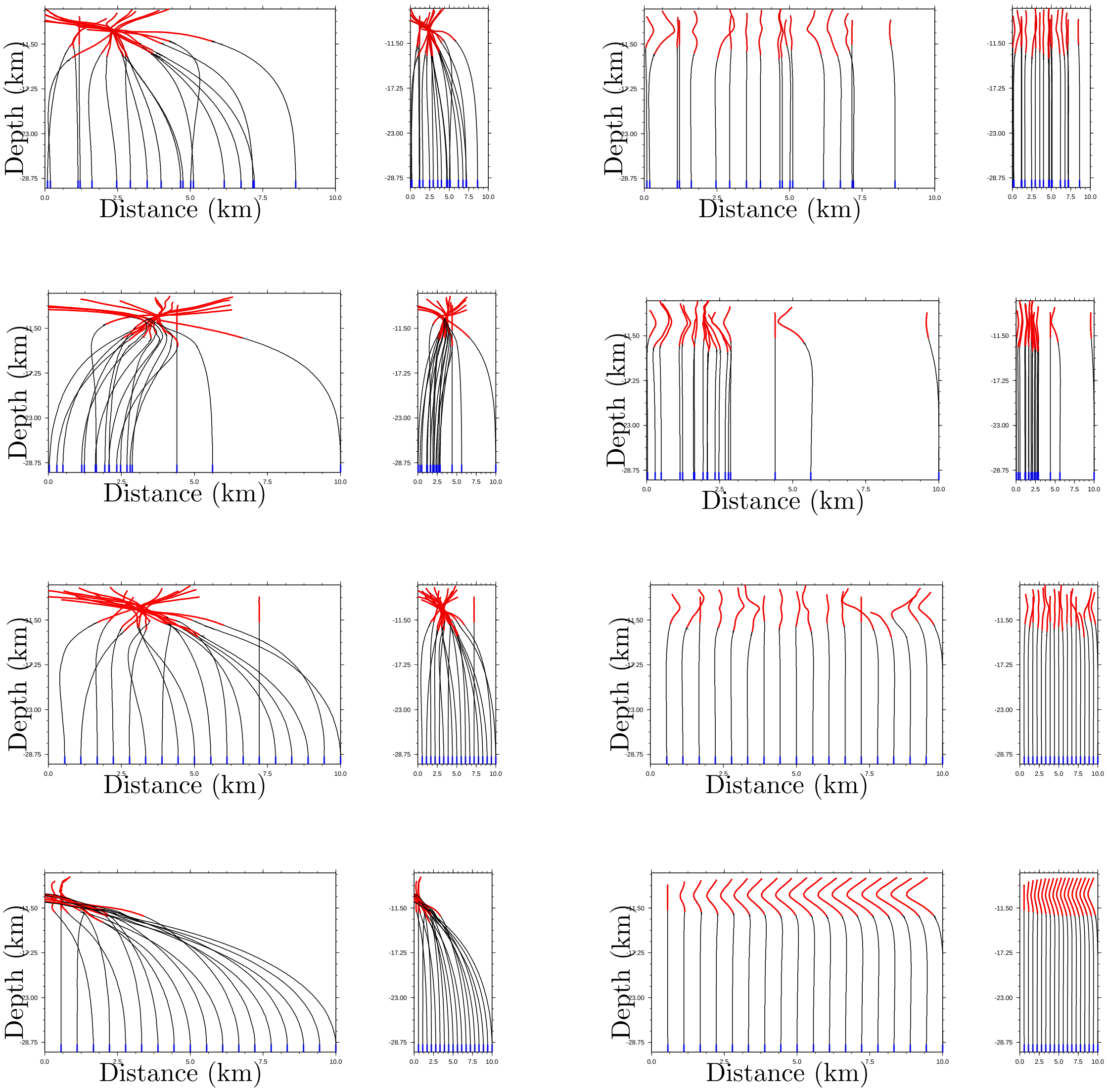

Figure 5.17: Comparison of influence of initial positions; from top to bottom: 1) initial positions randomly distributed, 2) subjected to Gaussian distribution, 3) arranged at regular intervals, 4) ascent order from left to right; left: without a regional stress field, right: extensional stress field of 5 MPa included; figures shown both with exaggerated horizontal axis and real aspect ratio

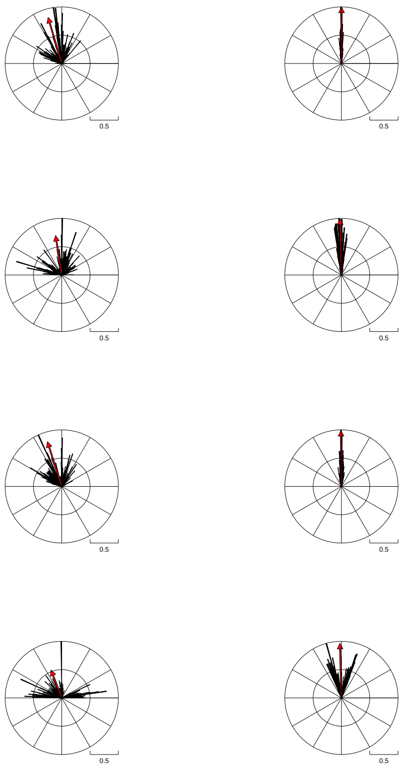

Figure 5.18: Sector diagram comparison of influence of initial positions; from top to bottom (same order as before): 1) initial positions randomly distributed, 2) subjected to Gaussian distribution, 3) arranged at regular intervals, 4) ascent order from left to right; left: without a regional stress field, right: extensional stress field of 5 MPa included

dykes on each other is low; dykes ascend and freeze vertically. In general, the longer the dykes get, the more they interfere with each other and the stronger is the focussing. This is best seen in Fig. 5.19 (bottom), where the segment density is concentrated in a roughly circular area. Surprisingly, in contrast to small and long dykes, fractures with a medium length orient themselves more horizontally and form a sill-like layer. This behaviour is highlighted further by the sector diagrams in Fig. 5.20. The diagrams for small and long dykes are very similar to each other, whereas the segment orientation of extremely small dykes is approximately vertical and, for dykes of medium length, rather horizontal.

5.4.1 Geological Interpretation

Examples of focussed as well as parallel diking can be easily found in nature. Fig. 5.21 (left) depicts subvertical, parallel dykes at the Madeira rift zone. An example of crossing dykes at the Caldera de Taburiente, La Palma is shown on the right (both photographs by courtesy of Andreas Klügel, University of Bremen).

The aim of the modelling is to gain further insight into the formation of the sheeted dyke

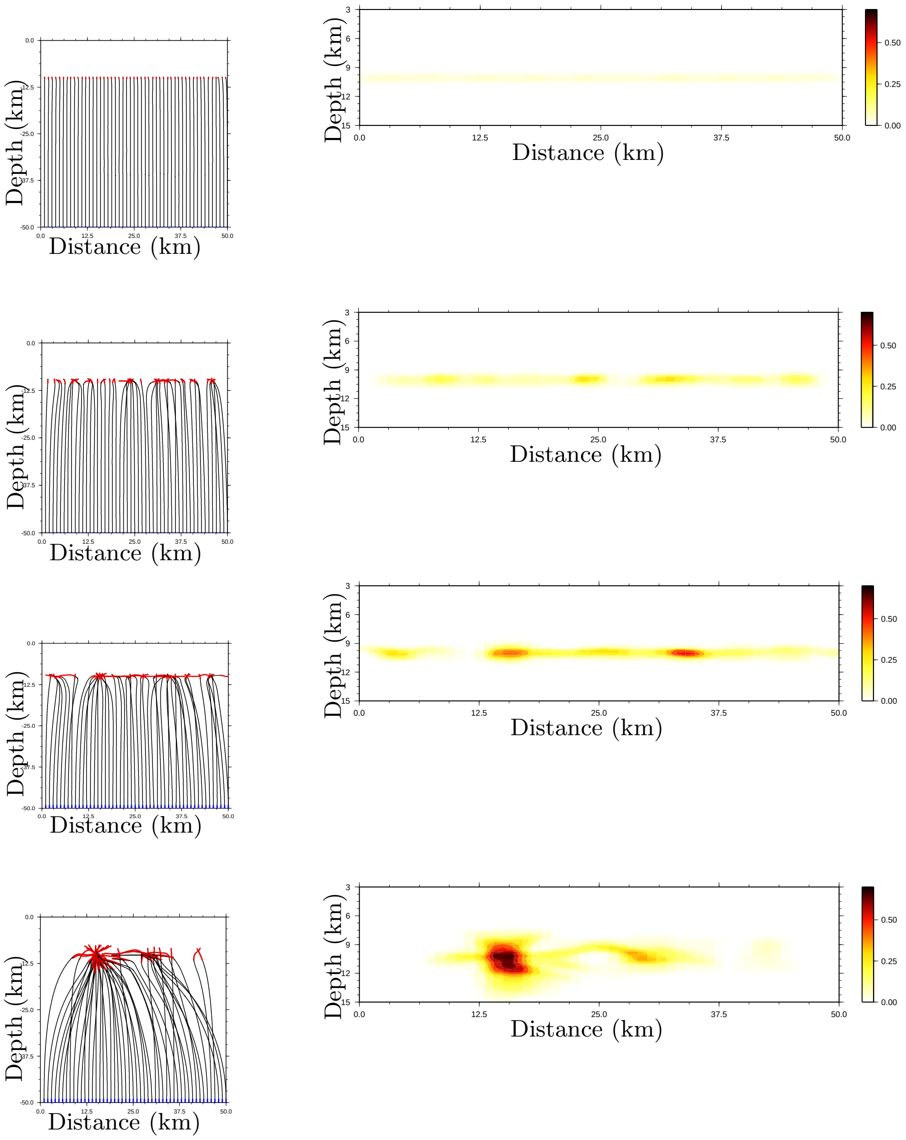

Figure 5.19: Study of length-dependent behaviour of dykes with initial positions distributed at regular intervals, random order of ascent; dyke end lengths (undisturbed) from top to bottom: 0.5 km (extremely small), 1 km (small), 1.5 km (medium) and 3 km (long); left: ascent paths of 49 dykes, right: density of segments per unit area

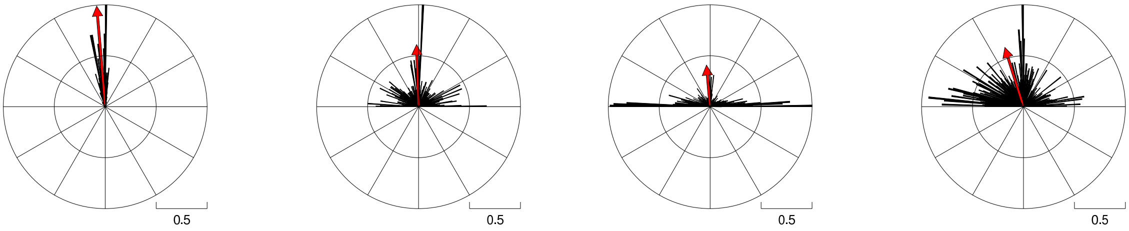

Figure 5.20: Sector diagrams for study of length-dependent behaviour of dykes with initial positions distributed at regular intervals, random order of ascent; dyke end lengths (undisturbed) from left to right: 0.5 km (extremely small), 1 km (small), 1.5 km (medium) and 3 km (long)

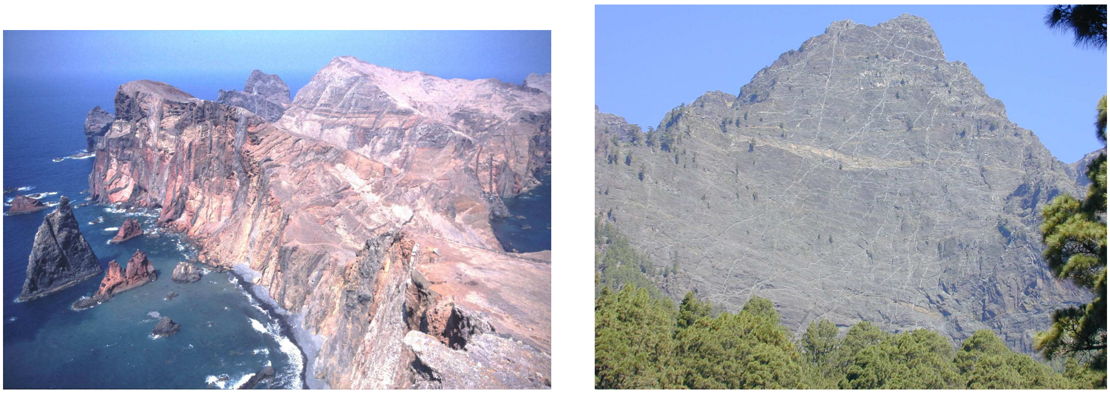

Figure 5.21: Left: subvertical, parallel dykes at the Madeira Rift Zone; right: crossing dykes at the Caldera de Taburiente, La Palma; both photographs by courtesy of Andreas Klügel, University of Bremen

complex and the upper layer of oceanic crust. For a reasonable interpretation of results, numerical models are transferred to geological settings (see Fig. 5.22). On the left, the

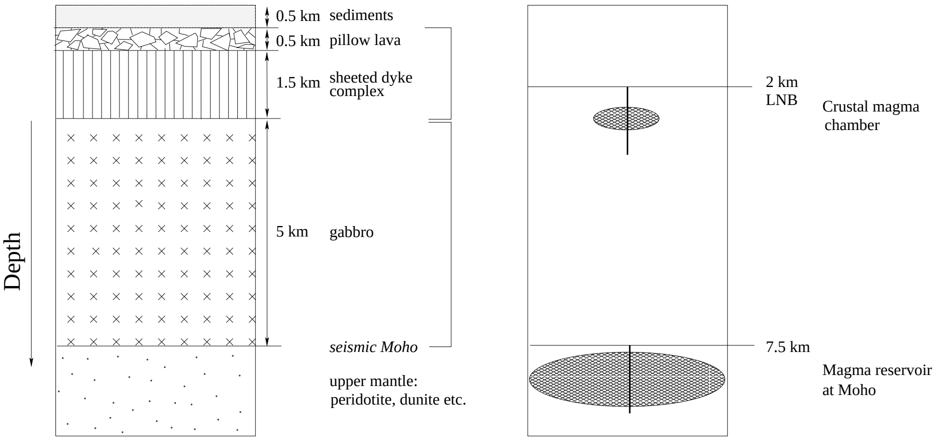

Figure 5.22: Transfer of geological settings into numerical model; left: section of oceanic crust, right: model of crustal magma chamber and magma reservoir at crust-mantle boundary

sketch of an oceanic crust section is shown again, on the right, the corresponding parameters for the numerical model are depicted. There are two classes of models: Dykes either start from a "magma reservoir" at the crust-mantle boundary or from a "crustal magma chamber" between the gabbro and the sheeted dyke layer. In both instances, they are arrested at the LNB at 2 km depth, which they overshoot so that their end position lies near the true depth of the sheeted dyke complex. Note that the initial dyke length is irrelevant, since dykes adapt to the fracture surface area given in the input file. The area is chosen so that the dyke end length is roughly 1.5 km, which matches the required thickness for the sheeted dyke complex.

The plate boundary zone or the zone of active faulting is 8 to 20 km at intermediate and fast-spreading ridges and 60 km at slow-spreading ridges. The magnetic plate boundary is 20 to 40 km. The zone of dyke injection is 1 to 8 km for intermediate to fast-spreading and 2 to 10 km for slow-spreading ridges. In general, crustal magma chambers are much smaller than reservoirs at the crust-mantle boundary (Gudmundsson, 1990a).

Another modification is to include the effect of the free surface at the ocean bottom into the computation of stress and displacement fields. This is performed by using the method of images, where the actual discontinuities situated in the crust at $z > 0$ are mirrored to $z < 0$ and the results are superposed. Thus, shear and normal traction on $z = 0$ vanish. Equations are not given here, but can be found in Crouch and Starfield (1983). A comparison of models with and without the free surface can be found in appendix A.3 (see Fig. A.12–A.14, pp. 154). The influence on the dyke propagation paths is noticeable, but does not change the results substantially. The free ocean bottom interface hinders slightly the focussing of fractures. Nevertheless, the formation of a dyke cluster is still clearly visible. If an extensional stress field is included in the model, the parallel alignment of dykes seems to be quite unaffected of the presence of a free surface.

Crustal magma chamber

The idea of a narrow dyke injection zone due to a shallow magma reservoir is represented by ascent of dykes in the same channel implemented by ascent from the same initial position. In Fig. 5.23, the results for different depths of initial positions are compared. Calculations are made with 10 dykes each and do not include the influence of a regional stress field. The figure on the left is the same as in Fig. 5.13, the fractures start their ascent at an arbitrary depth of 30 km and are arrested at a LNB at 10 km depth. In the middle, dykes emerge from a reservoir at the Moho, whereas on the right, the ascent from a crustal magma chamber is simulated. The first two figures look similar. But in the case of a short ascent path, dyke propagation is vertical. The shortness of the ascent

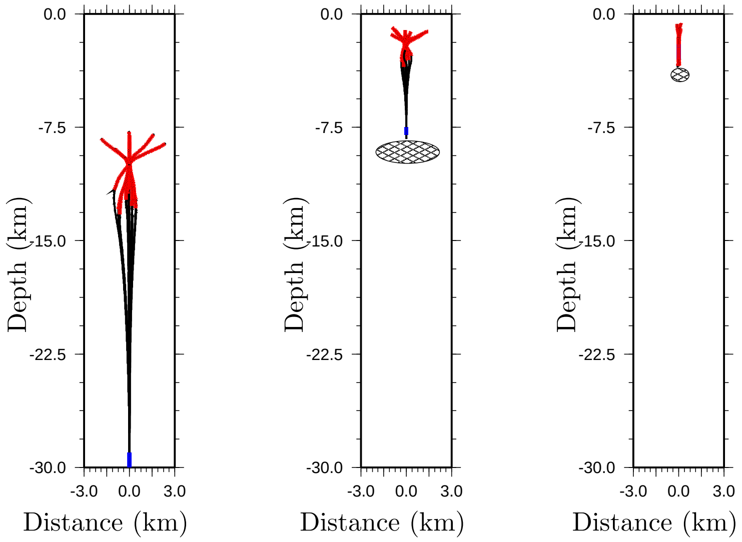

Figure 5.23: Model of narrow dyke injection zone: comparison of results for different depths of initial positions; left: arbitrary depth of 30 km, middle: reservoir at crust-mantle boundary, right: crustal magma chamber

path inhibits dyke interaction and causes the fractures to form an almost straight line, even without the help of an extensional stress field. This effect can also arise from the fact, that due to the short propagation distance, the dyke cannot fully adapt to the given initial conditions and thus, no equilibrium condition can be reached numerically. On the other hand, a dyke in nature having just formed at the roof of the magma chamber might have similar difficulties adjusting to this situation and might act in the same manner.
Crossing of dykes starting from a depth of 7.5 km can be prevented by applying an extensional stress field (see Fig. 5.24). If the injection is repeated, the dyke end positions are consecutively situated deeper (similar to the sketch of Weertman, 1971, see Fig. 5.3 on p. 83). Successive dykes are trapped beneath already frozen dykes which makes the intrusion zone act as an "ever expanding mega-dyke".

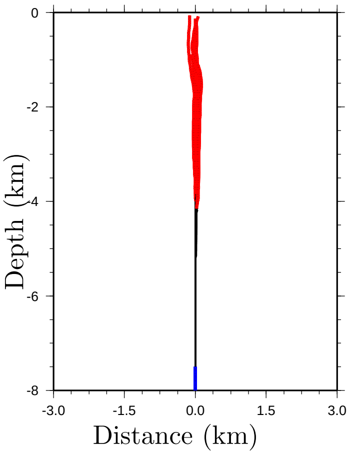

Figure 5.24: Ascent from magma reservoir at crust-mantle boundary including extensional stress field, dyke end positions situated consecutively deeper, 30 cycles shown

If a lower dyke injection rate is assumed, the effect of plate drift has to be taken into account. Fig. 5.25 depicts a schematic model for the influence of plate spreading, where fractures ascend directly beneath the axis and solidify, the crust shifts outwards and the cycle repeats. If the dyke-induced stress field is neglected, this results in parallel alignment of fractures and hence the formation of the sheeted dyke complex. As can be seen in the bottom part of Fig. 5.17 (p. 103), the model of continually shifting initial positions corresponds to a model with plate spreading. The first dyke ascends on the left, the last one on the right, producing a plate drift from right to left. This results in a very strong dyke focussing, since the immediate vicinity of fractures leads to strong interaction. Only if an extensional stress field is applied, can parallel dyke alignment be observed.
But again, the ascent from a crustal magma chamber makes the application of a regional, extensional stress field unnecessary and leads to the formation of a sheeted dyke complex (see Fig. 5.26). Both figures on the left are kept in the same scale as the figures above for better comparison, figures on the right are zoomed. a) displays the ascent from the same initial position shown before, b) features a plate drift of 5 cm/a with a dyke recurrence time of 20 a resulting in a shift of initial positions of about 100 m each. The first dyke ascends on the left, thus the plate drifts from right to left. c) is a zoom of b); a small deflection of upper fracture parts is visible. This effect is not caused by dyke interaction, since it is

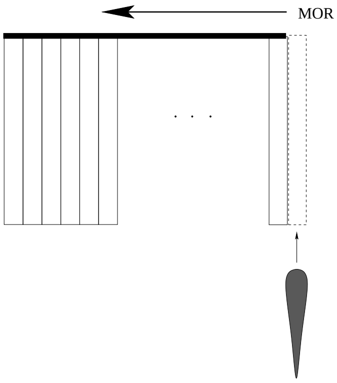

Figure 5.25: Simple model for the formation of the sheeted dyke complex by shifting dykes outwards through plate spreading: fractures ascend directly beneath the axis and solidify, the crust shifts outwards and the cycle repeats

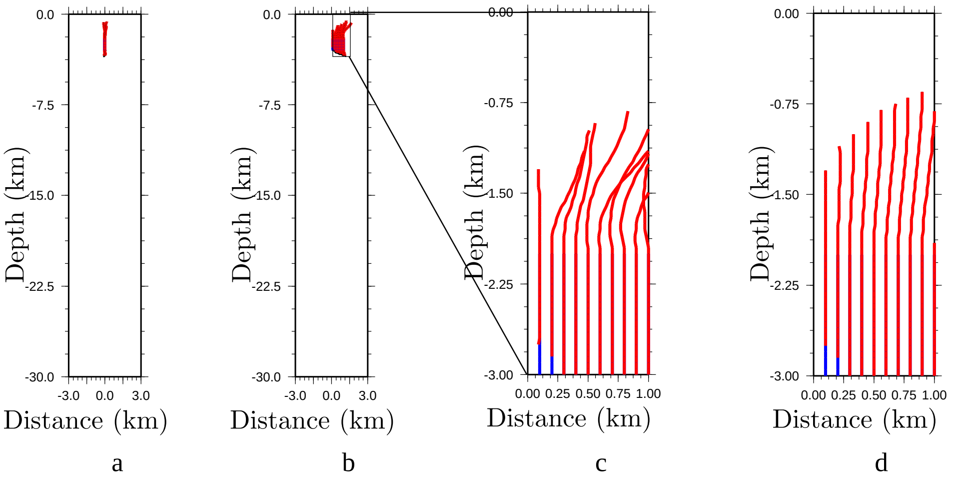

Figure 5.26: Dyke ascent from a crustal magma chamber including plate drift; a) ascent from the same initial position, b) featuring a plate drift resulting in a shift of 100 m for each initial position, c) zoom of b), d) extensional stress field applied

directed towards the spreading axis and not towards the previous fracture. It rather is a question of the magnitude of the stress field. The strain-energy release-rate offers no clear maximum to determine the direction of the next fracture segment to be appended. The effect can be minimised by introducing an extensional stress field of 5 MPa (d), but it is doubtful if a similar situation arises in nature at all. Most likely, it is prevented by the fracture toughness of the surrounding rock and thus, again the short propagation path offers no possibility of dyke interaction.

Reservoir at crust-mantle boundary

The models of randomly ordered dyke ascent fit the idea of a broad dyke injection zone, which corresponds to a magma reservoir at deeper crustal levels or at the Moho. Lissenberg *et al.* (2004) propose a feeding of dykes by sills from the gabbro layer, resulting in a discontinuous source, matching the model of the totally random distribution of dyke initial positions. A reservoir at the crust-mantle boundary results in a continuous source, fitting the models of constant distance intervals between start positions or a Gaussian distribution. In the first case, it is assumed that there is no reason for fractures to be generated only in the middle of a magma chamber. In the latter case, the middle of the magma chamber is situated at the position of the peak of the Gauss curve, implying that fractures can come to existence at every point in the chamber roof, but are more likely to in its middle, where the magma supply may be largest. In the following, the results for the random distribution of initial positions are shown (see Fig. 5.27). The upper edges of the dyke starting positions are located at a depth of 7.5 km, although this might be somewhat too deep for the dyke ascent out of the gabbro layer. The results do not differ substantially from the ones shown before (see Fig. 5.17, p. 103) and the comparison of all models is not shown again. Without a regional stress field, dykes tend to focus and form a dyke cluster, thus accumulating magma. The coalescence of magma from different dykes is not computed by the code; the question is if the thermal anomaly is strong enough to melt rocks in the gaps and the surroundings to build a magma reservoir. A melting of autoliths (surrounding rock of the same magmatic composition) could explain the simultaneous development of silica-saturated magma and mafic magma at a single volcano or in the case of Iceland. On the right, an extensional stress field of 5 MPa is included. Fractures align parallel and thus are able to build up a sheeted dyke complex.

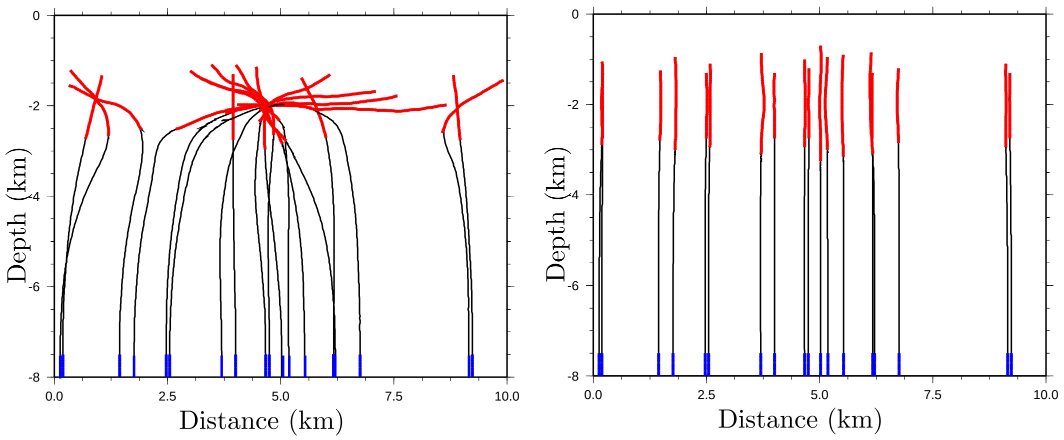

Figure 5.27: Subsequent ascent of 18 dykes with randomly distributed initial positions from a magma reservoir at Moho level; left: without application of regional stress field, right: extensional stress field included

The stress field of dykes resulting from randomly distributed initial positions without an regional stress field is considered in more detail in Figs. 5.28 and 5.29. The model with dyke ascent from an arbitrary depth is used, since it exhibits a particularly obvious pattern of dyke interaction. From the top to the bottom, following sequence is illustrated: The first image includes the dyke ascended first and its stress field resulting from dyke opening. The 2nd dyke rises and orients itself at the stress field of the 1st dyke. The stress fields are superposed. The rise of the 3rd dyke under the influence of this stress

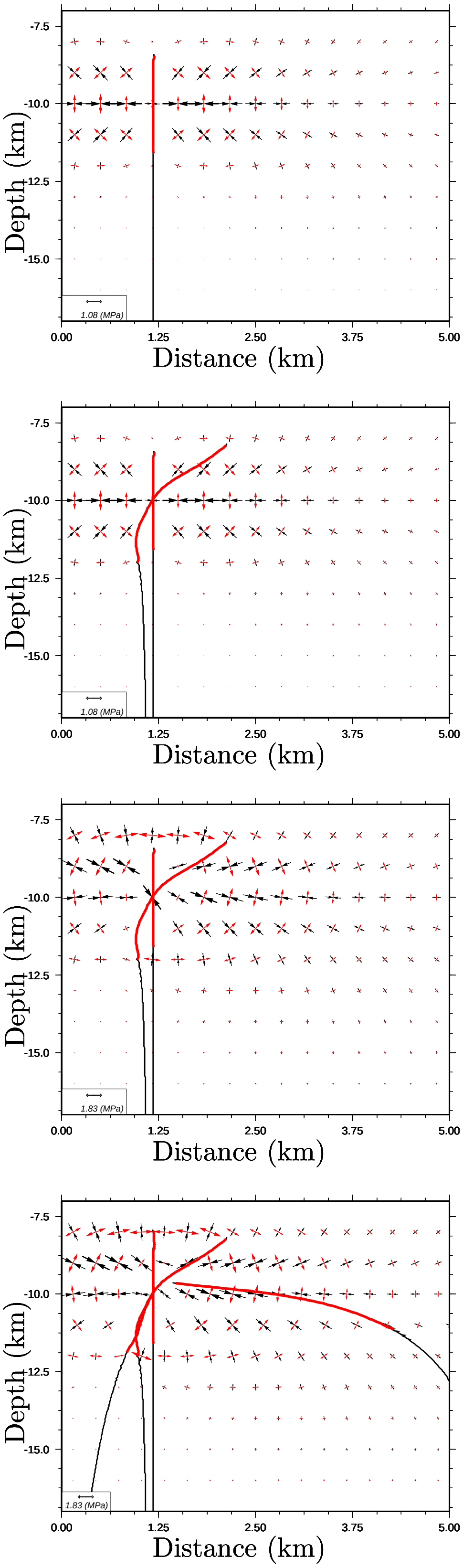

Figure 5.28: Stress field resulting from randomly distributed initial positions without external stress field; from top to bottom: 1) stress field and ascent path of 1st dyke, 2) ascent path of 2nd dyke under influence of 1st dyke, 3) superposed stress fields of 1st and 2nd dyke, 4) ascent path of 4th dyke under the influence of superposed stress field of 1st to 3rd dyke; to be continued on following page

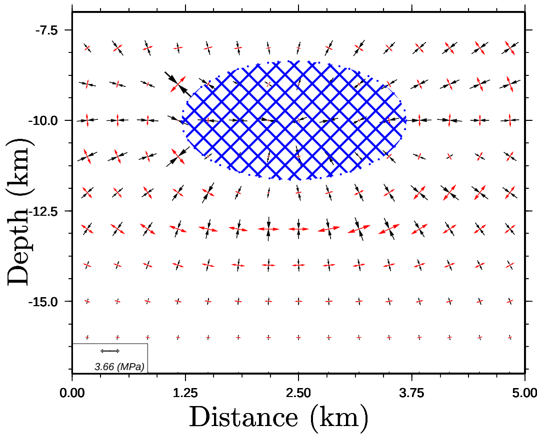

Figure 5.29: Stress field resulting from randomly distributed initial positions without external stress field; superposed stress field of all 18 dykes shown in Fig. 5.14, which is similar to the stress field of a magma reservoir indicated by crosshatched, blue lines

field as well as the appropriate accumulated stress field of 1st, 2nd and 3rd dyke is not shown, since this stress field is visible in the next graphic representing the ascent path of the 4th dyke. Its orientation in the direction of maximum compression is obvious. The overall stress field of all 18 dykes shown in Fig. 5.14 (p. 100) is represented in Fig. 5.29. Surprisingly, its appearance is not as chaotic as one could suspect, instead it shows a kind of self-organisation. Another interesting feature is the general shape of this stress field which is similar to the stress field of an elliptical magma chamber with the trajectories of maximum compression emanating radially. In reality, few magma chambers meet the ideal geometry of ellipsoids, but the time-averaged shape of long-lived chambers may approach this form (Gudmundsson, 1988).

To analyse the temperature field arising from the dyke cluster, an energy balance between the energy released from the hot dyke and the energy required to melt its surroundings is computed by subdividing the modelling region in blocks (see Fig. 5.30). The background temperature field at the mid-ocean ridge is calculated after Turcotte and Schubert (1982) to be

$$T = (T_m - T_s)\ \mathrm{erf}\left(\frac{z}{2\sqrt{\kappa x/v}}\right) + T_s \quad , \tag{5.9}$$

where T is the temperature, z the depth and x the distance from the ridge. Since the location of the spreading axis has no influence on the dyke ascent paths, its location is chosen arbitrarily to be situated at $x = 0$ km. Parameters are: surface temperature at the ocean bottom $T_s = 0°\mathrm{C}$, dry solidus of basalt 1080°C, dyke temperature equal to mantle temperature $T_m = 1100°\mathrm{C}$, spreading rate $v = 5$ cm/a, specific heat $c = 1.48$ kJ kg^{-1} K^{-1} and thermal conductivity $k_t = 2.6$ W m^{-1} K^{-1} (partly according to Annen and Sparks, 2002). The initial dyke area of 20 m^2 (corresponding to a volume in 2-D) is shared equally between all dyke segments. Fig. 5.30 (top), the number of dyke segments for the model without a regional stress field (a) and including an extensional stress field (b) are shown (for fracture positions, cp. with Fig. 5.27). Segments are counted in boxes, the x and

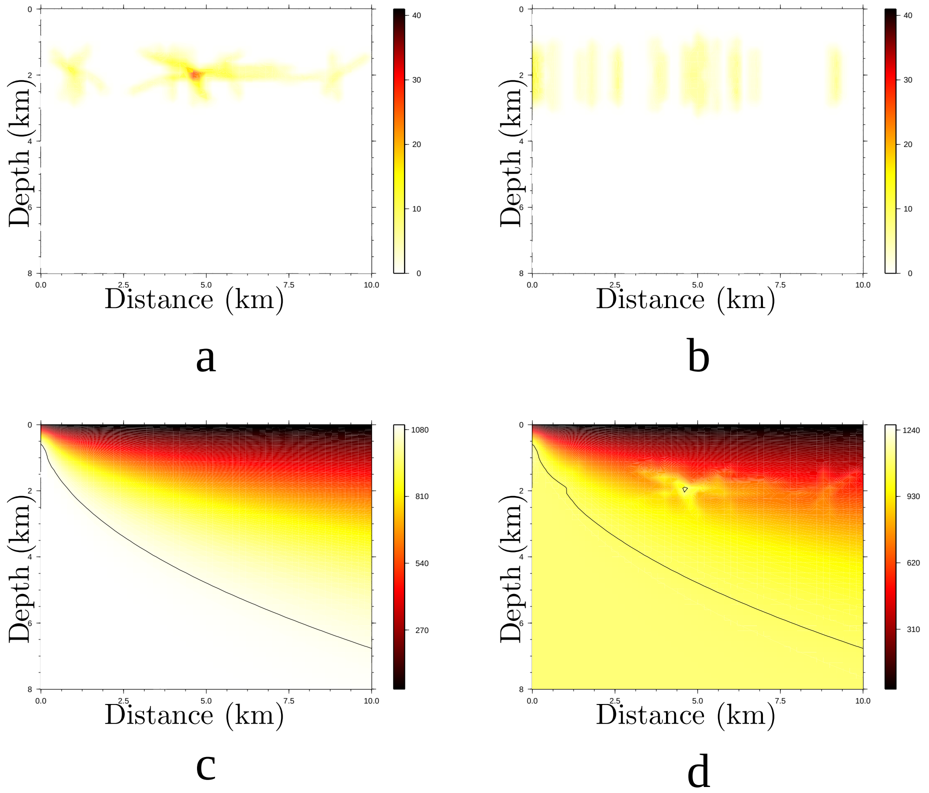

a b

c d

Figure 5.30: Estimation of dyke cluster-induced melting; a) number of dyke segments per box for model without a regional stress field, b) including extensional stress field (for fracture positions, compare with Fig. 5.27), c) estimation of temperature field in °C including ridge geometry: no melting near dyke cluster, d) temperature field in °C with energy released by fluid enclosed in dykes multiplied by arbitrary factor: formation of small magma chamber

z axes are each subdivided into 100 boxes. In the case of dyke focussing, the centre is clearly distinct, whereas in the case of parallel alignment, the segment density is lower. The estimated temperature field (c) displays no signs of melting. The 1080°C-isotherm is contoured, its slope is similar to the normal temperature distribution at a ridge. Only if the amount of energy, which is released from the magma enclosed in the fracture, is multiplied by an arbitrary factor of 4000 (corresponding e.g. to the $\approx$ 100-fold of melt volume per segment required to be available), the formation of a small magma chamber is observed. Obviously, the energy provided by the dykes does not heat the surroundings sufficiently. The mass ratio between magma transported in dyke segments and rock is too unfavourable. The energy released from the dykes can be increased further.

- The dyke cluster can include far more dykes, because the number of dyke propagation paths computed here is arbitrary. I tested that an increase in the number of dykes decreases the arbitrary multiplicative factor required to enhance the amount of energy available for heating the surroundings. The minimum number of dykes in a cluster able to melt the surrounding rock can be estimated e.g. by a trial-and-error-method, but proved to be too time-consuming within the scope of this thesis.

- The melt is not equally distributed in the dyke, since the opening is largest at its middle. On the left of Fig. 5.27 is visible, that this corresponds to the zone where most dykes cross each other. Thus, the amount of melt located at the "focussing area" is increased.
- In nature, dyke openings are larger than predicted here. Lippard *et al.* (1986) observe dyke thicknesses of 0.1–4.4 m for the sheeted dyke complex in the Oman ophiolite with an average of 0.5–1 m. Openings of dykes modelled in this work are in the range of centimetres up to a decimetre. Hence, a dyke is able to transport more magma with respect to its length, also increasing the amount of magma available.
- Once a dyke has ascended, it leaves a channel of increased temperature and decreased viscosity. Subsequent fractures are likely to follow its path instead of breaking unaffected rock (Matthias Hort, University of Hamburg, personal communication). Magma is accumulated more effectively at the level of neutral buoyancy.
- Parameters as the specific heat, thermal conductivity and dyke temperature are crude estimates, partly based on values gained in laboratory experiments. There is no guarantee of them applying to the setting of a mid-ocean ridge.

On the other hand, not all energy released from the dyke is available to melt the surrounding rock. The estimated energy balance completely neglects heat conduction out of the considered box. Moreover, dykes are placed in the crust simultaneously, which neglects the fact that the previous fracture cools down before the ascent of the subsequent dyke.

Another application of the model with randomly distributed initial dyke positions is to reproduce the distribution of volcanic centres. Iceland, which represents a special case of a mid-ocean ridge, possesses volcanic centres which are aligned at approximately regular intervals both along the spreading axis and at right angles to it. An example of the latter is marked by a red line in Fig. 5.31 (top). In the middle, the topography profile along the red line is shown; the spacing of volcanic edifices is almost regular and the most striking features are marked by arrows. The applied model consists of randomly distributed initial positions across a distance of 200 km, where no extensional stress field is applied (see Fig. 5.31, bottom). Dykes focus on clusters with almost regular spacing in the same order of magnitude. The spacing of the dyke clusters depends on the properties of the dyke-induced stress field. As shown in Fig. 5.19 (p. 105), the dyke pattern depends strongly on the fracture length. If the length was chosen to be different, a network of sills could be generated, comparable to the conducting layer observable with magnetotelluric measurements in a depth of 10–15 km beneath Iceland.

Another interesting topic is the simultaneous formation of the sheeted dyke complex, which requires a parallel alignment of dykes, and seamounts, which are presumably fed by small, isolated magma chambers and thus need a kind of focussed magma supply. Since the width of the zone undergoing tensile strain is normally less than the width of the volcanic rift zone (Gudmundsson, 1988), a possibility to achieve this simultaneity is the rapid decrease of the ridge-perpendicular stress field responsible for dyke separation. The effect is depicted in Fig. 5.32. Again, the model of randomly distributed initial positions is used. At the spreading axis, the magnitude of the extensional stress field is 5 MPa and decreases laterally by either 0.5 MPa/km (a), 1 MPa/km (b) or 2 MPa/km (c). In all

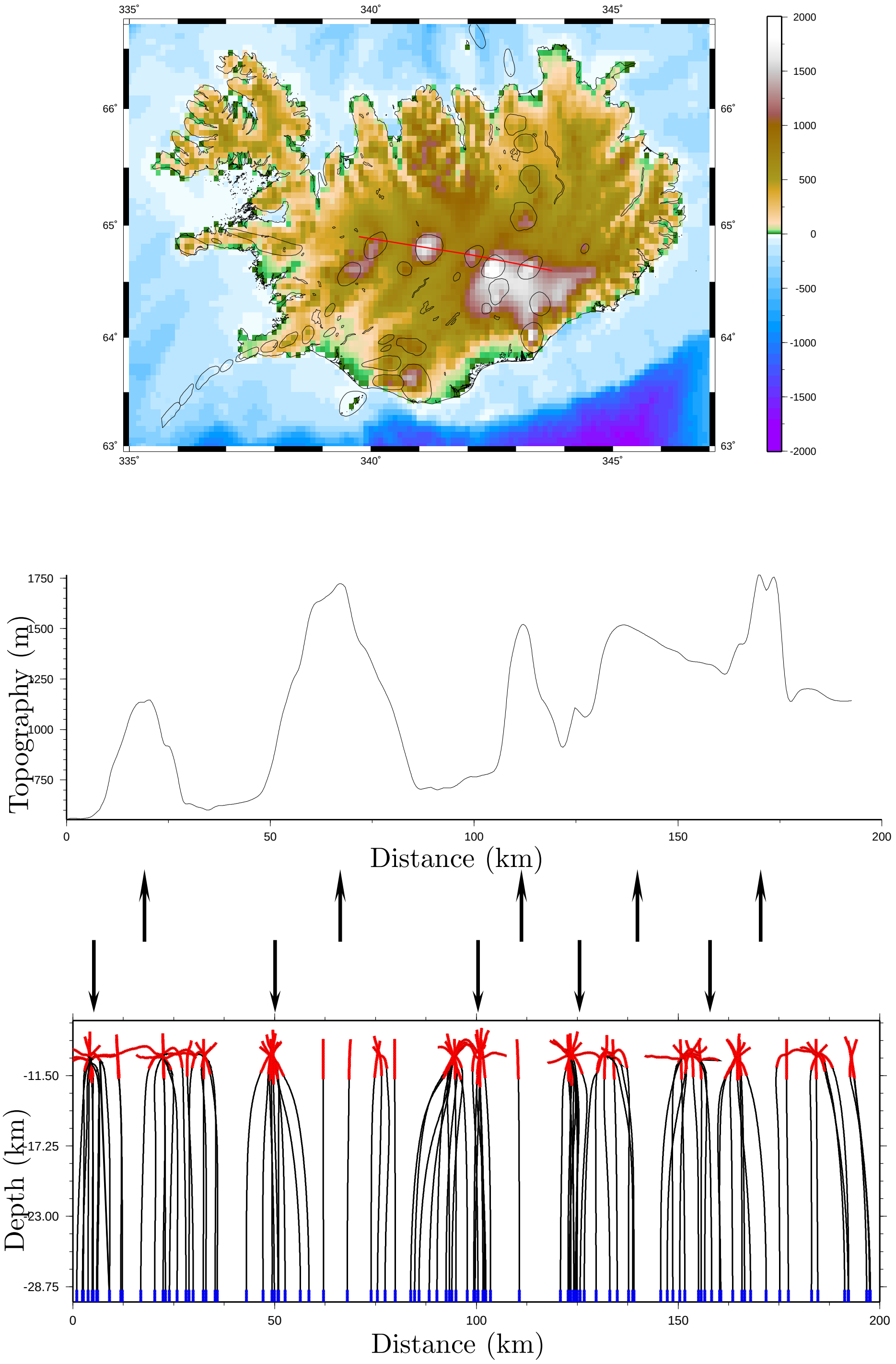

Figure 5.31: Modelling of regular spacing of volcanic edifices in central Iceland; top: topography of Iceland including volcanic centres, exemplarily connected by red line, middle: topography profile along the red line; bottom: model of randomly distributed initial positions for dykes and their ascent paths

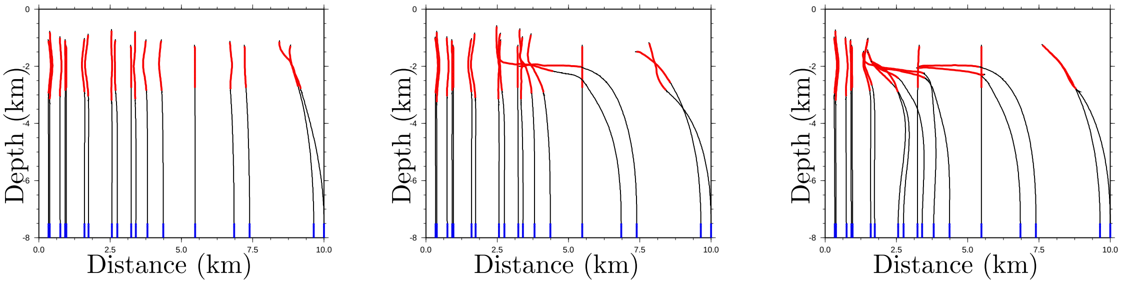

a b c

Figure 5.32: Contemporaneous formation of sheeted dyke complex and seamounts; magnitude of stress field at spreading axis (x=0 km) is 5 MPa and decays laterally by a) 0.5 MPa/km, b) 1 MPa/km and c) 2 MPa/km

cases, a sheeted dyke complex is recognisable and a dyke cluster begins to form at a certain distance from the spreading axis. In b) and c), the "focussing area" is situated where the extensional stress field dropped to 1.25 MPa, which corresponds to a distance of 7.5 km in a). Unfortunately, there is a gap just at this point in the initial position distribution. Although in this model the depth of start positions is the same for all fractures, they are allowed theoretically to emerge from different reservoirs at various depths such that magma of different chemical composition than the sheeted dyke complex basalt may feed the seamounts. During the MELT experiment conducted at the East Pacific Rise, Scheirer *et al.* (1998) discover that a greater number of seamounts is present on the faster spreading Pacific plate than on the slower spreading Nazca plate. The above models can be used to analyse the correlation between spreading rate and extensional stress field at a ridge by comparing positions of dyke clusters with geographical locations of seamounts. However, this exceeds the frame of this thesis.

5.5 Discussion

Information on geological settings and magmatic processes at mid-ocean ridges can be gained by various methods. At slow-spreading ridges, peridotites and gabbros from the lower crust and upper mantle can be dredged (Gràcia and Escartín, 1999), though it is not clear if they originate from a more heterogeneous crust or are exposed due to tectonic extension. The most special situation in Iceland, where a spreading axis rises above sea level, shows that dykes are a key factor in the mechanism of spreading (Gudmundsson, 1990a). Ophiolites include a layer where 100 % of rock consists of subvertical dykes. In the Oman ophiolite, the sheeted dyke complex is 600–2000 m thick (Lippard *et al.*, 1986). Nevertheless, those features provide informations about the appearance, but not the circumstances during its formation. Geophysical experiments conducted at mid-ocean ridges, e.g. seismology, seismic, magnetotelluric as in the MELT experiment (Forsyth *et al.*, 1998a), are able to distinguish coarsely between distinct geological units, but cannot resolve in detail the finely structured dyke complex. Besides, they mostly deliver snapshots and again, no conclusions can be drawn on temporal developments. The Wilson *et al.* (2003) of ODP-Leg 206 states that despite more than 30 years of ocean drilling only relatively few drill holes in oceanic crust have been obtained and no conclusions can be drawn on the dependence of crustal structure and composition on basement depth, crustal age and spreading rate. The drilling of a complete section of oceanic crust has not yet been achieved, although the recovery of in situ oceanic crust is essential to understand igneous processes. In Fig. 5.33, the in situ basement drillholes during DSDP (Deep Sea Drilling Project) and ODP (Ocean Drilling Program) from 1968–2003 is shown. Black lines tag DSDP drillholes, blue lines are ODP drillholes and red lines are holes 1256 C and D. Only one drillhole ever reached down into the sheeted dyke complex (Hole 504B, Leg 148, Alt *et al.*, 1993). To my knowledge, so far only one sheeted dyke complex was observed in situ by a submersible (Auzende *et al.*, 1989). But since it was exposed at a transform fault, geological units were partly disturbed. Almost no information is available on the magnitude of the regional stress field at mid-ocean ridges, only stress regimes can be characterised. Unfortunately, regional stress fields turned out to be very important for dyke alignment during simulations.

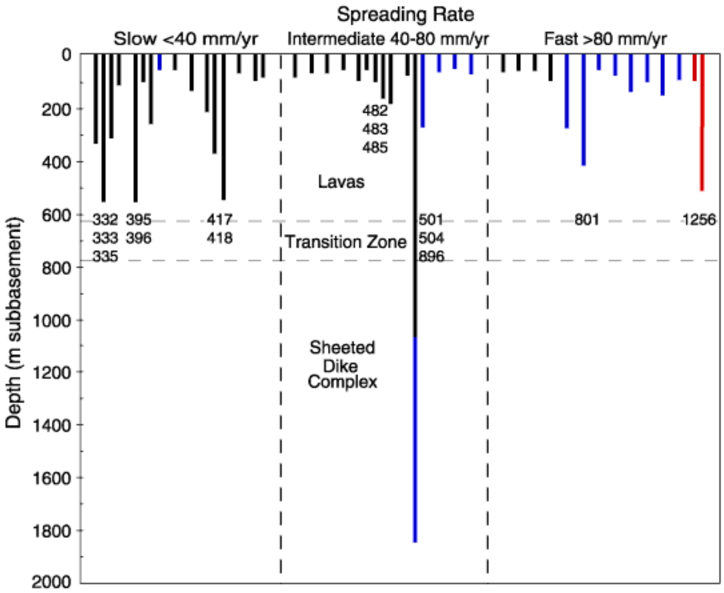

Figure 5.33: In situ basement drillholes during DSDP and ODP from 1968–2003

Because of the sparseness of available data on geological settings and magmatic processes at mid-ocean ridges, numerical modelling is a vital tool to gain further insights. At the same time, verification and interpretation of the numerical models is difficult.

Dyke emplacement at mid-ocean ridges is analysed to gain insight into the formation of the sheeted dyke complex and the development of magma chambers. The self-induced stress fields of dykes and thus dyke interaction is taken into account quantitatively, since it may locally be more significant than regional stress. A variety of results is obtained by the unique combination of a dyke propagation algorithm with a dyke interaction routine, integrated at the geological setting of a mid-ocean ridge. At first, initial positions of dykes before their ascent, the presence of an external stress field and the dyke length appeared to be crucial factors governing dyke interaction. Surprisingly, the resulting pattern of dykes at their end positions turns out to be independent of their initial position, as long as the order of ascent is random. Instead, the length of the ascent path emerges as being the decisive factor, since short ascent paths prevent dyke interaction.

In general, dykes focus towards each other when no regional stress field is present. The implementation even of a weak extensional stress field hinders dyke focussing effectively (5 MPa compared with an overpressure of 7 MPa in the dyke). The implementation of free surface effects on the ocean bottom interface slightly obstructs the dyke clustering, but the influence is not strong enough to prohibit focussing. The effects are weaker than those of the extensional stress field. If no extensional stress field is applied, the pattern of dyke accumulation depends on their length. Even considering the interaction of only two dykes, the ascent paths are controlled by dyke length insofar as small dykes are able to quickly adapt to a given stress field, whereas long dykes prefer a vertical orientation. For the interaction of a multitude of dykes, three distinct patterns can be recognised. Extremely small dykes ascend vertically, since the superposed stress field is not large enough. Small and large dykes tend to form distinct dyke clusters whose circle of influence is governed by the dyke length. Dykes of a medium length favour a horizontal, sill-like pooling. Ito and Martel (2002) discover by means of numerical modelling of simultaneously ascending dykes, that dykes show different modes of interaction: strong coalescence, weak coalescence or repulsion, depending on the initial vertical offset of dykes and the ratio between horizontal spacing and dyke length. In my model, dyke ascent is not contemporaneous, but consecutive. Repulsion is no longer possible, but strong and weak interaction can be observed.

Formation of sheeted dyke complex at various spreading rates

The stress field caused by dyke emplacement cannot be neglected in any models for the formation of upper oceanic crust, since it inhibits the specific orientation of dykes observed in the sheeted dyke complex. An initial parallel ascent is not sufficient for the parallel alignment of vertical dykes.

In general, slow-spreading ridges only have a magma reservoir at the crust-mantle boundary, thus featuring continuous magma supply in a broad dyke injection zone. Numerical models fitting this pattern are the models of Gaussian as well as a constant distance distribution subjected to a random order of ascent. For an intermediate-spreading ridge, Lissenberg *et al.* (2004) proposed the feeding of the sheeted dyke complex from sills situated in the gabbro layer. This results in a broad dyke injection zone which is discontinuous corresponding to the model of initial dyke positions distributed at random. Fast-spreading ridges feature also small crustal magma chambers, thus creating a narrow dyke injection zone. The model of dyke propagation in the same ascent channel is a vigorous simplification, the model featuring a determined order of ascent and thus including the effect of plate spreading is more realistic. Nevertheless, dyke behaviour seems to be mostly independent of the initial distribution of dykes. Since the majority of dykes contains no selvage, no order of ascent can be registered (Gudmundsson, 1990a).

Another difference between a magma reservoir at the crust-mantle boundary, sill reservoirs in the lower crust and a magma chamber at higher crustal level is the length of ascent path. In the latter case, the ascent path until the dyke is stopped at the level of neutral buoyancy can only be short. There is little chance for successive dykes to interact with a local dyke-induced stress field. Dykes can even propagate horizontally along the spreading axis (e.g. see Fig. 5.34, taken from Smith and Cann, 1999). Ridge-parallel propagation is not possible with the program presented here, since it is a 3-D problem. Because of the shortened ascent path and the lesser influence of dyke interaction, the extensional stress required for parallelity of dykes is consequently lower above magma chambers at crustal level, i.e. at fast-spreading ridges.

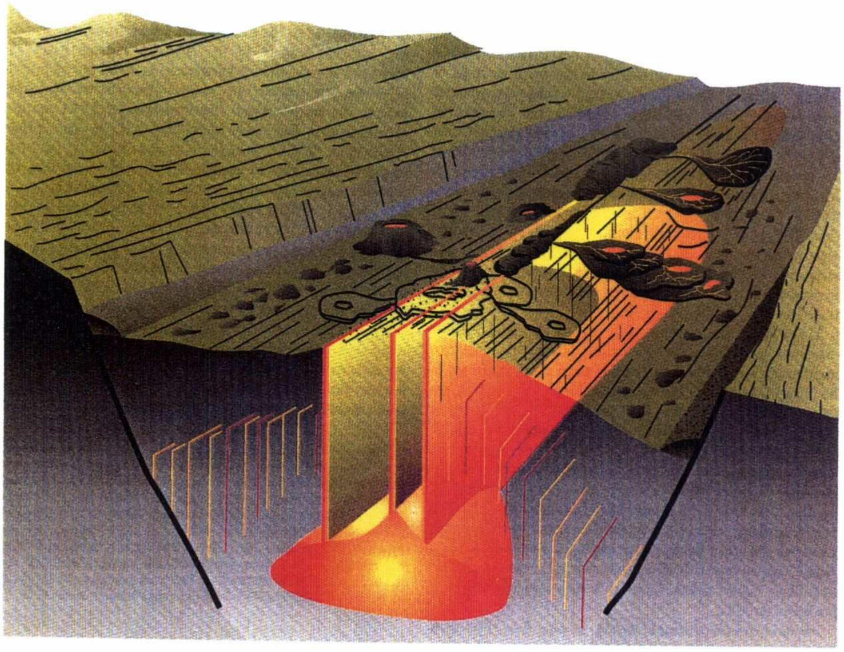

Figure 5.34: Dykes rising vertically from a shallow crustal magma chamber and propagating horizontally along the spreading axis; 3 dykes shown in detail. Where the dyke breaks the surface at the spreading axis, volcanic edifices are build. Off-axis seamounts and flank highs are secondary vents fed by lava tubes; figure taken from Smith and Cann (1999).

Interestingly, fast-spreading ridges feature rather a strike-slip regime. Hitherto, no model has been developed to explain this effect (Oliver Heidbach, University of Karlsruhe, personal communication, see also Fig. 5.35). In contrast, slow-spreading ridges exhibit an extensional normal fault regime, which is caused by discontinuous melt supply. The magmatic accretion cannot keep up with the spreading. Thus, the extension is accompanied by crustal thinning, which leads to normal faulting (e.g. Lissenberg *et al.*, 2004). At fast-spreading ridges, the magma supply is more continuous; hence it is possible to accumulate an amount of magma that is large enough to build up an additional magma chamber in the crust. Because of the higher temperature at fast-spreading ridges, fewer earthquakes occur. For the same reason, the relaxation time of the local dyke-induced stress field is shorter, further enhancing a parallel alignment of dykes.

Therefore, I draw the conclusion that the key factor in the formation of the sheeted dyke complex is the interplay between dyke interaction and regional stress field. Without an regional stress field, even simple model geometries may lead to complicated dyke patterns provided that an opportunity for interaction with the local stress field induced by the em-

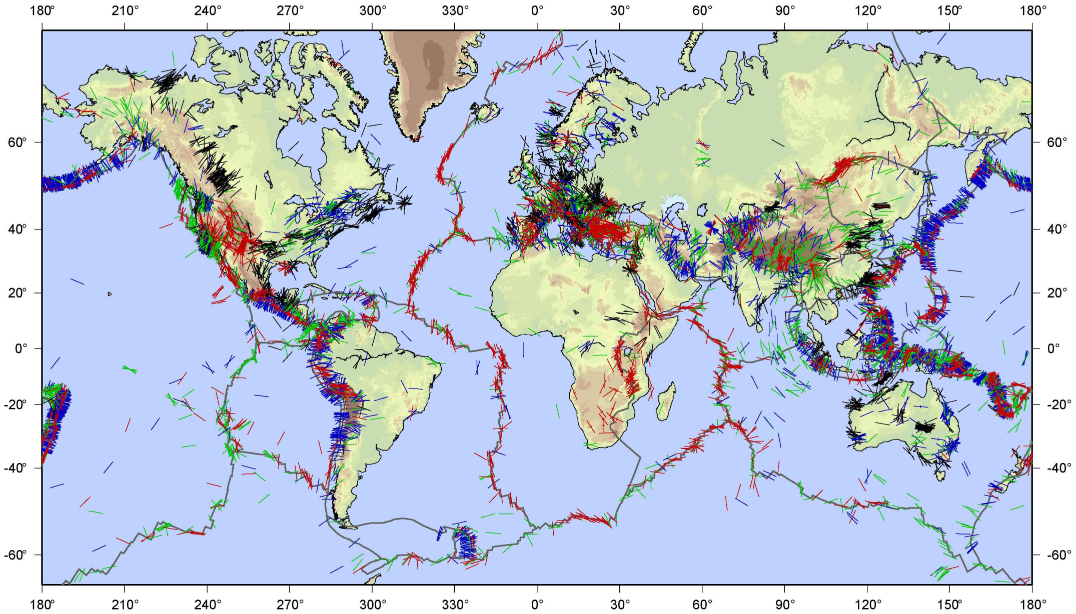

Heidelberg Academy of Sciences and Humanities & Geophysical Institute, University of Karlsruhe

Figure 5.35: World stress map, showing mostly a strike-slip regime (green) at fast-spreading and a normal fault regime (red) at slow-spreading ridges; blue lines indicate thrust faulting and black lines are an unknown stress regime; figure by courtesy of Oliver Heidbach

placement of foregoing intrusions is offered, e.g. by a sufficient length of the ascent path. The extensional stress field required to prevent dyke focussing and crossing is not very large; in my tests, a regional, extensional stress field of 5 MPa was sufficient to overcome an average overpressure of 7 MPa in the dyke. Thus, the basic magmatic processes in oceanic crust formation are the same for all spreading rates, irrespective of the position of the magma reservoir feeding the dykes. Hence, there is no paradox between the different characteristics of spreading centres of variable spreading rates and the high degree of uniformity in mature oceanic crust as stated by Henstock *et al.* (1993), since those characteristics – position of magma reservoir and ridge topography – are not decisive for the magmatic processes forming the crust. The apparent higher variability in the composition of oceanic crust at slow-spreading ridges (Gràcia and Escartín, 1999) is more likely induced by tectonic extension exposing lower crustal layers at the end of ridge segments than a genuinely larger heterogeneity of the crust.

The cyclic model of oceanic crust formation described by Weertman (1971) (see Fig. 5.3, p. 83) is clearly a strong simplification. It completely ignores the possibility of dyke interaction, assuming that subsequent dykes are trapped beneath already solidified magma-filled fractures.

However, if dyke interaction is inhibited due to a regional, extensional stress field, dykes act in a similar fashion to the one discussed by Weertman (1971). This can be observed in the models of dykes using the same ascent channel for propagation and starting at the same initial position respectively. The geological interpretation of the Weertman model is more complicated, since he assumes fracture ascent in a very narrow injection zone, although the magma reservoir is situated at the crust-mantle boundary. As can be seen above, magma chambers situated at the Moho tend to be broad and there is no reason for dykes being released only at the centre of the reservoir. Furthermore, the model does not explain the formation of the underlying gabbro layer; instead, the whole crust is built up by vertical dykes. Only if the "ever expanding mega-dyke" model is transferred to the brittle, upper crustal layer can it be adopted as a simplified description of crust formation. Weertman (1973) proposes the generation of a small magma chamber at the transition from the ductile, lower crust to the brittle upper crust, which would fit with this (see below).

Development of crustal magma chamber

Crustal magma chambers form at fast-spreading ridges in contrast to slow-spreading ridges, which feature only a magma reservoir at the crust-mantle boundary. An obvious explanation is the larger supply of magma. Additionally, no or only a weak extensional regime seems to be present. Thus, if dykes ascend from the lower reservoir at the crust-mantle boundary, the risk of focussing due to a dyke-induced stress field is high. Indications for the origin of crustal magma chambers at the "focussing area" of an adequate number of dykes have been listed in section 5.4.1. The stress field at such a domain resembles suspiciously that of an elliptical magma chamber. A temperature anomaly might develop, eventually large enough to melt the rock in the gaps between dykes and their surroundings.

Unfortunately, the formation of a magma chamber at high crustal level could not be proven by the estimation of the energy balance between heat released by the fluid enclosed in the dyke and energy required to melt the surrounding rock. The mass ratio between melt and rock is too unfavourable. I am convinced that either a more exact computation or the accumulation of a larger amount of magma through a higher transport rate in the dykes or stronger focussing could help to confirm the hypothesis. To include temporal effects, equations for heat conduction and dyke solidification would have to be solved (see also section 5.1). For complex patterns such as the dyke cluster considered here, this is not possible analytically; a numerical computation is required. Annen and Sparks (2002) observed the problem of repeated intrusions of basaltic sills on the thermal evolution and melt generation in the crust. However, the model is only 1-D and sills are placed artificially at certain positions. In combination with the model of dyke propagation, the possibility arises to calculate heat generation by dykes and to reconsider the requirements for the generation of magma chambers. However, this exceeds by far the frame of this thesis.

The clustering of dykes at very high crustal level due to an alleviated extensional stress field may also account for the formation of off-axis seamounts.

Sill formation in the gabbro layer

In the gabbro layer beneath the sheeted dyke complex, the formation of sills can sometimes be observed. Even with high dyke densities resulting in a horizontal distance of initial positions of 100 m (100 dykes on 10 km), it was not possible to build up a compressive stress barrier in order to turn subsequent dykes into sills. The reason may be that in the case of parallel diking, the orientation of dyke-induced stress fields is the same, but the additional extensional stress field has to be overcome before compressive stress can be

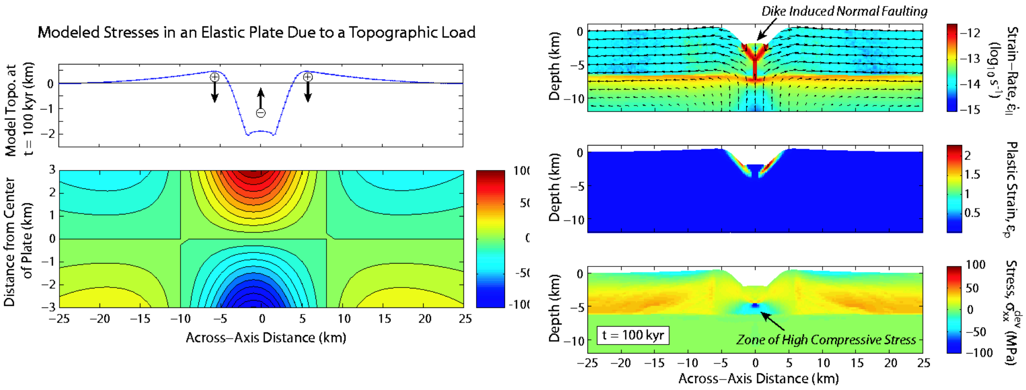

Figure 5.36: Interactions of magma injection by dykes, faulting and topography at mid-ocean ridges;left: stresses in elastic plate due to topographic load of a rift valley, right: modelling results for repeated dyke intrusions into a viscous-elastic-plastic layer in terms of strain rate (top), plastic strain (middle) and horizontal deviatoric stress (bottom), dyke-induced normal faulting and the zone of high compressive stress in the lower crust indicated; figure by courtesy of Mark Behn, WHOI

built up, whereas in the case of no regional stress field, superposed dyke-induced stress fields have different orientations due to the unsystematic end positions of dykes.

Behn *et al.* (2004) show a more complex possibility of sill formation beneath a mid-ocean ridge by dealing with interactions of magma injections by dykes, faulting and topography at mid-ocean ridges (see Fig. 5.36). They point out that repeated dyke intrusions at depth lead to the development of a rift valley, since dyke intrusions influence faulting at mid-ocean ridges through a combined effect on the crustal temperature and the local stress field. If the accretion rate is near to the spreading rate, the topography causes compression at the base of the plate, inhibiting further dyke injection and favouring sill formation. On the left of Fig. 5.36, modelled stresses in an elastic plate due to the topographic load of a rift valley are displayed. On the right, modelling results for repeated dyke intrusions into a viscous-elastic-plastic layer in terms of strain rate (top), plastic strain (middle) and horizontal deviatoric stress (bottom) are illustrated. Dyke-induced normal faulting and the zone of high compressive stress in the lower crust are indicated. The plastic failure associated with faulting decreases the horizontal stresses in the upper half of the plate compared with the elastic solution.

Ridge topography, especially its difference between slow- and fast-spreading ridges, was not included in my modelling. It is more pronounced at slow-spreading ridges, but according to Behn *et al.* (2004), its influence grows when the crustal accretion rate matches the spreading rate which is the case for fast-spreading ridges. Nevertheless, comprising the topography could help in generating sills.

Building a stress trap in the crust

The existence of the LNB mentioned e.g. by Mège and Korme (2003) is controversially discussed. Nevertheless, the arrest of dykes at a level of neutral buoyancy in oceanic crust is plausible, since the density of the rock drops between the crustal layers. But there are more possibilities to stop the ascent of fluid-filled fractures.

Shallow magma chambers are likely to come into existence above large accumulations in the source reservoir. Several conditions have to be satisfied. A trap is needed, for example lithological or structural boundaries or stress barriers. Frequent input from the underlying reservoir is required (Gudmundsson, 2000).

Weertman (1973) proposes the arrest of ascending dykes at the transition between brittle upper crust and ductile lower crust because of an anomalous stress distribution (see Fig. 5.37). The crust is divided into a cold, brittle upper part of thickness H_0 and a hot,

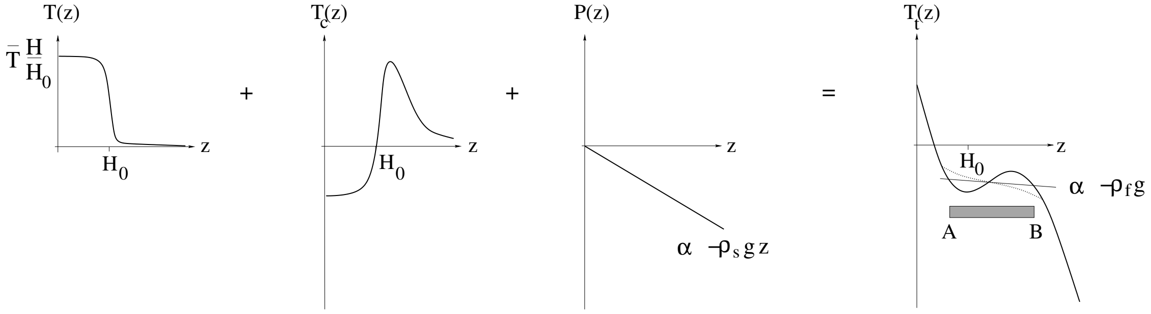

Figure 5.37: Arrest of ascending dykes because of anomalous stress distribution in the crust; summation of $T(z)$, $T_c(z)$ and $P(z)$ yields curve $T_t(z)$ (for further explanations see text), trapping of dykes in area $\overline{A\ B}$; sketch after Weertman (1973)

ductile lower part. The total crustal thickness is H. The tensile stress $T(z)$, assumed to be positive by Weertman (1973), is caused by the floating of the lighter dense crustal material on the denser mantle rock. Superposed is another kind of tensile stress $T_c(z)$, which results from the view of the spreading zone as an ever expanding mega-dyke being situated in the upper part of the crust. It causes a compressive stress field to its sides and a tensional stress field below its tip. The extensional stress in the lower part of the crust is accommodated by creep controlled by dislocation-glide which becomes possible because of the higher temperatures. $P(z)$ is the lithostatic pressure and results from the gravitational acceleration g and the density of the solid crust ρ_s. The total tensile stress is $T_t(z)$. Cracks become trapped in the anomalous zone between A and B if the stress follows the solid line, where $\frac{dT_t}{dz} > -\rho_f g$. If accumulated stress is given by the dotted line, no dykes are arrested. Since the anomalous increase is larger the greater the spreading rate is, this indicates once again that dykes are more likely to be stopped at crustal levels beneath fast-spreading ridges.

However, the required equations are not given in detail in Weertman (1973). The attempt to reproduce the results failed, since necessary proportionality constants are not known. Despite persistent trying, $T_c(z)$ remained some orders of magnitude smaller than $T(z)$ such that an addition of both curves does not lead to the desired trend of $T_t(z)$. An arrest of dykes at the transition between the ductile lower and the brittle upper crust is nevertheless imaginable because of the change in the rock's fracture toughness (Hahn, 1976) or Young's modulus (Gudmundsson, 1988), without the need of complicated regional stress fields.

I propose a kind of self-regulating mechanism for oceanic crust formation, particularly the sheeted dyke complex (see Fig. 5.38). On the left, a model for the formation of oceanic crust at a fast-spreading ridge is visible (a), whereas on the right, a sketch for a slow-spreading ridge is shown (c). In the middle, the geological layering of mature oceanic

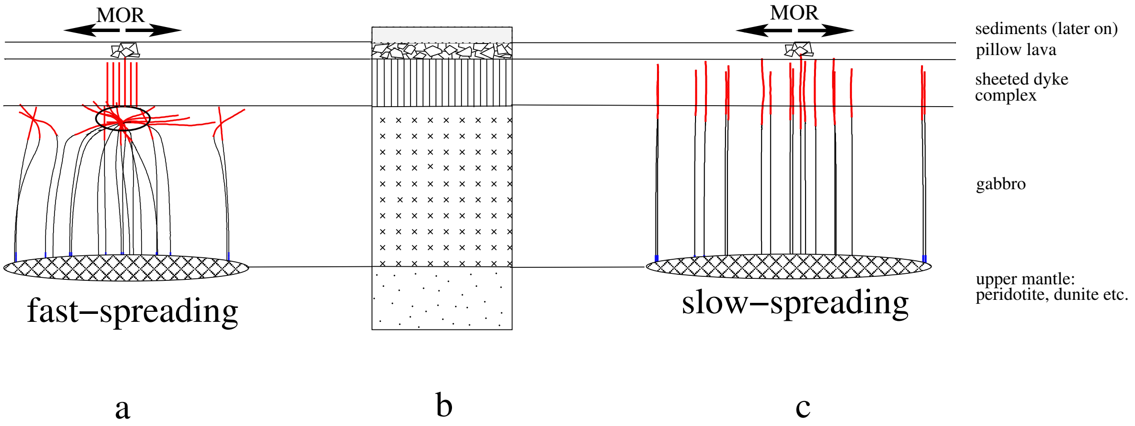

Figure 5.38: Model for oceanic crust formation; a) fast-spreading ridge, b) geological layering of oceanic crust, c) slow-spreading ridge; layers indicated by horizontal lines; mid-ocean ridge marked by arrows

crust is displayed for comparison (b). This model leads to some important implications:

- An initial parallel dyke ascent is insufficient to produce the sheeted dyke complex built up by parallel dykes.
- A crustal magma reservoir (indicated by a black ellipse in Fig. 5.38, left), resulting from the focussing of dykes can only be generated when no regional, extensional stress field is present, which is more likely at fast-spreading ridges.
- A sheeted dyke complex can be formed with or without the presence of a regional, extensional stress field.

The oceanic crust is formed as follows. A mechanism of melt focussing in the mantle leads to the generation of a magma reservoir at the crust-mantle boundary both in the case of a slow- and a fast-spreading ridge (see chapter 4). Dykes ascend in a broad dyke injection zone and are arrested at a certain depth. Because of the low extensional stress field at fast-spreading ridges, dykes tend to focus towards each other (see Fig. 5.38, left). At the location of the dyke cluster, a small crustal magma chamber develops, if the mass ratio between magma enclosed in dykes and surrounding rock is sufficiently high. Once a dyke cluster is established, its circle of influence grows with increasing size. If enough magma is gathered that the plain strain fracture toughness of the surrounding rock is overcome, dykes may start to ascent further. Since the dyke injection zone now is only narrow because of the small size of the magma chamber and the ascent path up to the level of neutral buoyancy is short, further crack focussing is inhibited and a sheeted dyke complex with parallel, vertical dykes is generated. Whether or not plate drift has to be incorporated depends on the recurrence time of dyke ascent, but does not hinder the sheeted dyke complex formation.

The pattern of dykes in the cluster seems to be independent of their initial position, i.e. the location of fracture generation in the roof of the magma reservoir. The length of ascent path and the presence of regional stress fields proves to be more important to allow or to prevent dyke interaction.

At slow-spreading ridges, dyke focussing is prevented because of the extensional stress regime (see Fig. 5.38, right). No crustal magma chamber develops, but the formation of the sheeted dyke complex at the level of neutral buoyancy is nevertheless guaranteed, since the regional stress field causes a parallel, vertical dyke alignment. Thus, the **cause of the parallel alignment** is different at slow- and fast-spreading ridges, but the **magmatic processes** stay the same.

Since dykes are not stopped abruptly at the level of neutral buoyancy and tend to overshoot depending on the magnitude of the buoyancy force driving their ascent, dykes enclosing an unusual large volume of magma are able to penetrate the surface, where pillow lavas are generated through the contact with seawater. The sedimentary layer is formed further away from the spreading axis. This model does not allow for conclusions concerning the origin of the lower crust.

In the case of the fast-spreading ridge, dykes are arrested beneath the level of neutral buoyancy. This can be achieved either by the stress trap proposed by Weertman (1973) or by a change in the rock's fracture toughness or Young's modulus at the transition between a more ductile lower crust and the brittle upper crust. The stress trap is more effective the larger the spreading rate is.

In the model of a fast-spreading ridge, a tendency to form several smaller off-axis dyke clusters is visible. They present a possibility to feed off-axis seamounts, since their presence is limited to a certain distance range from the spreading axis. Dykes, which are released near to the axis from the magma reservoir at Moho level, are focussed towards the "main" cluster. If the distance from the spreading axis becomes to large, no magma is available. From observations at the EPR, Scheirer *et al.* (1998) state that most seamounts are generated 5–50 km away from the spreading axis and none can be found directly at the spreading axis. There are more seamounts on the faster spreading Pacific plate than on the slower spreading Nazca plate. However, crustal magma chambers thought to feed off-axis seamounts are commonly assumed to be located at a very high crustal level and not at the top of the gabbro layer.

Note that the width of the melt reservoir at the crust-mantle boundary was the same for both models resulting in a dyke injection zone of 10 km, although in general, magma reservoirs are assumed to be smaller beneath slow-spreading ridges.

This model combines aspects of previous models with new insights in dyke interaction processes. The model of Weertman (1971) comparing the spreading zone to an "ever expanding mega-dyke" is very simple and completely ignores the possibility of dyke interaction. Only if it is transferred to the brittle upper crust can it be understood as a crude simplification of oceanic crust formation. Weertman (1971) assumed the whole crust to be formed by vertical dykes, solidifying beneath each other. My model shows that it is possible to trap dykes at slightly different depths. Nevertheless, a single dyke is long enough to build up a whole slice of the sheeted dyke complex. Weertman (1973) proposes the arrest of dykes at the transition from lower to upper crust because of an anomalous stress distribution. Even if it is taken into account that his results are irreproducible, the idea of dykes getting stuck in this transition zone is reasonable and can explain the formation of a crustal magma chamber at the top of the gabbro layer. Magma supply can be provided by the focussing of dykes originating from a broad magma reservoir at Moho level. The existence of the stress trap presented by Weertman (1973) is more probable for higher spreading rates as is the focussing of dykes because of the change of stress regime from extensional to strike-slip.

Sempere and Macdonald (1987) link the width of the magnetic polarity transition zone to the broadness of the zone of crustal accretion. They state a narrow zone of dyke injection at both slow- and fast-spreading ridges. But whereas the zone of crustal accretion is likewise narrow at fast-spreading ridges (1–2 km), it constitutes the entire width of the inner valley at slow-spreading ridges (2–10 km) because the location of accretion is subjected to lateral shifts. They explain this dislocation by dykes being fed from small, transient magma chambers, whose existence is not proven. In my model, slow-spreading ridges also possess a broader zone of crustal accretion than fast-spreading ridges, because the sheeted dyke complex is fed directly from the expanded magma reservoir at the crust-mantle boundary, causing a shift in dyke ascent positions. At fast-spreading ridges, dykes are focussed at a small crustal magma chamber beforehand.

Gudmundsson (1990b, 1990a) gives models for magma chamber formation and dyke arrest in the crust with regards to the generation of regional dyke swarms in Iceland. He states that the formation of a crustal magma chamber from a sill (horizontal dyke) is thermally and tectonically possible and that the probability of its generation increases with the spreading rate. He explains why and how often dykes are arrested in the crust, but neglects the possibility of dyke interaction.

The model of Lissenberg *et al.* (2004) for intermediate-spreading ridges predicts a feeding of dykes from sills in the gabbro layer, which is also feasible with my model. The presence of an axial magma chamber shows that extensional stresses at the spreading axis during its lifetime were probably low. Dykes emerging from sills at lower levels in the gabbro layer have a long ascent path and thus are able to focus on the axial magma chamber which acts in the same manner as in the case of a fast-spreading ridge. Dykes originating from sills at higher levels only possess a short ascent path up to the level of neutral buoyancy and thus can be injected directly into the sheeted dyke complex parallel to the already existing dykes. Hence, mixtures between models for slow- and fast-spreading ridge are possible.

A few questions remain open for future work. The development of a crustal magma chamber from a dyke cluster needs to be analysed in more detail. The design of a time-dependent program code is desirable. It has to be able to deal with heat conduction and dyke solidification equations to estimate the melting of rock surrounding the arrested dykes.

The simultaneous formation of a sheeted dyke complex and off-axis seamounts is interesting. It is worthwhile to compare bathymetrical data providing information on the seamount distribution for mid-ocean ridges at various spreading rates.

The problem of sheeted sills included in the gabbro layer remains unsolved. Sheeted sills can be either produced due the presence of a compressive stress barrier resulting from the formation of the sheeted dyke complex or through the influence of the ridge topography as proposed by Behn *et al.* (2004). In the latter case, their existence is more probable at fast-spreading ridges.

More types of stress fields are imaginable at mid-ocean ridges, whose influences on dyke propagation paths and interaction are noteworthy. A tensile stress resulting from the "floating" of the ridge on the "mantle sea" decreases with depth. The application of creep leads to a similar result, destroying partly the influence of the dykes which have already ascended. An extensional stress resulting from mantle corner flow increases with depth. Earthquakes indicate that ridge-perpendicular tensile stress decreases with horizontal distance to the spreading axis and a regime of ridge-parallel stresses comes into existence

Neves *et al.* (2004).

Consideration of dyke interaction may help the understanding of further magmatic and volcanic processes. I presented a model for the generation of volcanic edifices in Iceland, which form at regular distance intervals. Implementing a different dyke length in the same model can result in pooling of sills, leading to a magma layer across the whole modelling distance and thus explaining the presence of a conducting layer in a certain depth. In addition, a model for the contemporaneous generation of a sheeted dyke complex and off-axis seamounts has been derived. In general, the algorithm implemented here can be used to study the influence of dyke interaction on the formation of volcanoes, their location and their magma supply by dykes. A variety of possibilities is offered by the high potential of the method.

5.5.1 Conclusions

Interesting insights into oceanic crust formation, magmatic processes and the generation of the sheeted dyke complex have been gained by a novel analysis of dyke propagation subjected to dyke interaction at mid-ocean ridge settings. Because of the sparseness of available data, numerical modelling is a vital tool to analyse crust formation processes.

The dyke-induced stress field turns out to be potentially more important on local scales than the present regional stress field. Surprisingly, the initial position of dykes in depth is not decisive for the result, as long as the order of dyke ascent is random. Instead, the interplay between dyke interaction and the regional stress field as well as the length of the ascent path and the dyke length emerge as crucial.

There is no paradox between different characteristics of spreading centres of variable spreading rate and the high degree of uniformity in mature oceanic crust. A self-regulating mechanism is proposed, where in the case of non-existence of a regional, extensional stress field, a crustal magma chamber is generated by dyke focussing The remaining ascent path is short and thus prevents further dyke interaction, resulting in the parallel, vertical alignment of dykes in the sheeted dyke complex. If an extensional stress regime is present, the formation of a crustal magma chamber is impeded, but at the same time, a vertical dyke ascent is guaranteed despite the long ascent path, leading to the parallel, vertical alignment of dykes. Hence, the cause of this alignment is different at variable stress regimes corresponding to different spreading rates, but the magmatic processes involved are the same.

Chapter 6

Conclusions

Magma dykes are important pathways for magma ascent at mid-ocean ridges and therefore, essential in building oceanic crust (Gudmundsson, 1990b). Solidified dykes have also been studied extensively on Iceland (e.g. Gudmundsson, 1990a).
Existing analytical models for upward fracture migration are not able to take into account inhomogeneous media and heterogeneous stress fields (Dahm, 2000a). Most models have been qualitative and neglected the stress field heterogeneities induced by dyke emplacement, although these may be important on local scales, in particular regarding crust formation processes. Only few authors have simulated magma transport by dykes (Rubin, 1998; Dahm, 2000a, 2000b) and none apart from Ito and Martel (2002) interprete their results with regard to mid-ocean ridges. Gudmundsson (1990b) states that little attention has been paid to a coherent tectonic model of dyke emplacement and crustal magma chambers that includes their stress fields.

These points have been addressed in this work in order to clarify interactions of stress fields of dykes including the aspect of possible magma chamber generation and its role in crustal accretion. The interaction between deep-seated and shallow magma reservoirs and repeated dyke injection are the most important oceanic crust building processes. Essential contributions have been made to elucidate processes of oceanic crust formation, in particular the sheeted dyke complex.
In Chapter 4, mechanisms of melt extraction from the mantle were discussed including the focussing from a broad melting zone at depth to the narrow extrusion area at the spreading axis. In Chapter 5, the differences of various characteristics of slow-and fast-spreading ridges at increasing spreading rates and the relative uniformity of properties of mature oceanic crust were explained. The ascent of magma-filled dykes was analysed including effects of buoyancy, a constant fluid volume enclosed in the fracture and the influence of external stress fields including possible heterogeneities. The geological settings of mid-ocean ridges were taken into account by a corner flow representation of mantle convection as well as the inclusion of regional stress fields, positions of magma reservoirs and dyke-induced stress fields for the dyke ascent in the crust. To my knowledge, magma ascent by dykes has never before been studied in such complexity either in the mantle or in the crust beneath mid-ocean ridges.

Few observational data are available from mid-ocean ridge experiments. The penetration depth of direct measurements is too shallow. Indirect methods mainly are too crude to resolve the fine-scale structure of the sheeted dyke complex and are usually unable to observe temporal developments. Because of the sparseness of data, numerical modelling is a vital tool for gaining further insight into crust formation processes. A boundary element method was used for the numerical simulations. The static version was developed by Crouch and Starfield (1983) and expanded by Dahm (1996, 2000a, 2000b) to obtain a quasi-static code, capable of considering the effect of the enclosed fluid volume, preventing overlapping fracture surfaces and determining the direction of fracture propagation by means of a maximum strain-energy release-rate criterion.

To represent dyke interaction in the models of oceanic crust formation, I included the influence of stress fields from previously ascended dykes into the computation of dyke movement. The advantage of the boundary element method is not to discretise the whole region of modelling, but only the surfaces of fractures. Thus, stress and displacement fields can be obtained with high accuracy at any point outside the fractures. I have developed a method which does not directly store the stress fields of previously ascended dykes on a grid, but only the parameters required for their calculation at the positions of boundary elements forming the fracture surfaces such that stress fields can be computed when- and wherever needed.

In addition, I combined the approaches to simulate dyke propagation and dyke interaction with the geological setting of a mid-ocean ridge. Since passive mantle motion generated by plate spreading is suggested to be the dominant flow process beneath mid-ocean ridges (Forsyth *et al.*, 1998a), the influence of convection on magma transport was represented by a corner flow model (Batchelor, 1967). The modelling of oceanic crust formation includes regional, extensional stress fields as well as deep-seated and shallow magma reservoirs.

Several requirements must be fulfilled by models for melt extraction from the mantle beneath mid-ocean ridges: a fast transport velocity, a separation of melt and rock to preclude chemical reactions and a focussing from a broad melting region to a narrow extrusion zone at the spreading axis. Magma transport by fractures has been simulated and compared with models of porous melt flow and melt flow through dunite channels.

Models of porous melt flow accomplish the focussing of melt, but neglect the deviatoric stress field, which has a high influence on the direction of melt propagation. Furthermore, they require an unlikely high mantle viscosity and allow for re-equilibration of melt because of the low transport velocity. Dunite bodies have been found in the Oman ophiolite (e.g. Kelemen *et al.*, 1995, 1997). The formation of dunite conduits as a consequence of initial porous flow through mantle rock is regarded as possible and is similar to models for the generation of melt-rich shear zones proposed by Stevenson (1989) or the formation of dykes from melt-filled veins suggested by Sleep (1988). But no explanation for the focussing of conduits towards the spreading axis is provided and the pattern of channels does not even correspond to the melt flow lines of the postulated initial porous flow as presented by Spiegelman and McKenzie (1987) or Phipps Morgan (1987).

The propagation of fluid-filled dykes fulfils the requirements of a fast melt transport separating melt from mantle rock. Hydrofracturing at mantle depth is thought to be feasible from observations at the Oman ophiolite (Nicolas and Jackson, 1982; Nicolas, 1986). Fracture propagation is mainly influenced by the dynamic pressure and the deviatoric stress field, which arise from the corner flow, as well as the buoyancy of the enclosed fluid. The global pressure minimum at the spreading axis causes the fractures to propagate towards it, whereas the deviatoric stress field forces the dykes to move in the direction of maximum compression and thus hinders the focussing. The apparent buoyancy results in a vertical ascent. Unfortunately, a combination of these effects does not lead to focussing of the dykes. Since an enhancement of the magnitude of dynamic pressure produces a simultaneous intensification of the deviatoric stress field, no focussing of fractures can be obtained by means of the simple rheological model of the corner flow in general. However, there are indications that porous melt flow and dykes react in a similar manner to external stress fields (Müller, 2003). If this is the case, I conclude that models of porous melt flow including a deviatoric stress field in addition to a dynamic pressure gradient would not achieve a focussing of melt towards the spreading axis in analogy to the melt transport in fluid-filled fractures. Hence, I consider both models as equivalent regarding their capability with respect to explaining the focussing effect.

A change of the deviatoric stress field is required to allow for the focussing of melt towards the spreading axis. Possibilities for future work are the transition from a passive to an active flow model, the influence of the ridge topography, a temperature-dependent viscosity or the application of 3-D instead of 2-D models. The inclusion of a magma chamber near the crust-mantle boundary could also result in focussing. Its existence is documented beneath slow- and fast-spreading ridges.

Until now, few authors have paid attention to the origin of the sheeted dyke complex (Weertman, 1971, 1973), the consequences of dyke emplacement (Gudmundsson, 1990a, 1990b) or to the interaction of dykes (Wei and De Bremaecker, 1995; Ito and Martel, 2002). Never before has a combination of dyke interaction and the formation of the sheeted dyke complex been taken into consideration and to my knowledge, nobody has studied the astonishing parallelity of dykes within the complex. In this work, a first in the models of oceanic crust formation, the dyke-induced stress field and its influence on subsequently ascending dykes has been analysed. The different characteristics of spreading centres at various spreading rates have been taken into account. Since the time span of solidification is much shorter than the dyke recurrence time which is in turn shorter than the time of viscoelastic relaxation, it is sensible to assume that a dyke completes its ascent and solidifies before the ascent of the next dyke, but maintains its stress field.

Surprisingly, the resulting pattern of dykes after their ascent is mostly independent of the distribution of their initial positions, as long as the order of ascent is random. The length of the ascent path, the presence of regional stress fields and the dyke length turn out to be more important. An initial parallel ascent of dykes is not sufficient to guarantee the parallelity of dykes in the sheeted dyke complex, since the dyke-induced stress field leads to focussing. A clustering of dykes is prohibited by a regional, extensional stress field exceeding the influence of the self-induced stress fields of dykes or by a shortening of the ascent path.

The main differences between fast- and slow-spreading ridges are the following. Fast-spreading ridges have an additional crustal magma chamber, a smooth topography and the regional stress field is partly affected by a strike-slip regime. The melt supply is continuous such that the magmatic accretion of crust can keep up with the spreading of plates. Slow-spreading ridges possess only a magma reservoir at the crust-mantle boundary, a rough topography and underlie a normal-faulting regime. I assume that a discontinuous melt supply leading to tectonic extension is responsible for the exposure of lower crust and mantle rocks to the seafloor as proposed by Lissenberg *et al.* (2004) and not a more heterogeneous crustal composition as suggested by Gràcia and Escartín (1999).

My results imply a kind of self-regulating mechanism. Because of the weak or non-existent extensional stress field at fast-spreading ridges, dykes ascending from the reservoir at Moho depth focus towards each other to form a crustal magma chamber. Indications in the stress and temperature field support the existence of such a process, but details remain open for future work. A crustal magma reservoir results in a very narrow dyke intrusion zone combined with a short ascent path and thus hinders further focussing of the dykes, producing a complex of parallel dykes. The extensional stress field at slow-spreading ridges prevents dyke focussing and thus the generation of a crustal magma chamber, but simultaneously causes a vertical dyke ascent from the reservoir at the crust-mantle boundary to the level of neutral buoyancy and thus also results in a layer of vertical, parallel dykes. Hence, the sheeted dyke complex might have different origins depending on the spreading velocity, but the basic magmatic processes are the same for the whole range of spreading rates.

Dyke interaction was not included in the models of magma transport in the mantle, since dyke-induced local stress fields are much lower in magnitude than pressure and stress fields resulting from the corner flow. It proved to be very important for dyke propagation in the crust.

Nicolas and Jackson (1982), Nicolas (1986), Phipps Morgan (1987) and Sleep (1988) proposed a dyke propagation in the direction of maximum compressive stress. Dahm (2000a) showed that fractures may diverge from them because of the effect of the enclosed fluid volume and buoyancy forces. I was able to verify this conclusion and to point out a further factor which leads to the divergence of dyke propagation, which is the dyke length, influencing the ability of fractures to adapt to an external stress field.

In future work, more attention has to be paid to the consequences of dyke interaction. Ito and Martel (2002) propose that it may even help melt focussing in the mantle. Dyke interaction can be important everywhere where dykes can be found, e.g. in predictions of volcanic eruptions. The influence of dyke interaction on the generation of volcanic centres and on the simultaneous formation of the sheeted dyke complex and seamounts near mid-ocean ridges was shown.

Melt transport in the mantle calls for more complex models. I advise caution in using porous melt flow models, since petrological arguments argue against them and until now, they do not include the deviatoric stress field which prevents fluid-filled dykes from focussing towards the spreading axis.

It is desirable to consider further the formation of the sheeted dyke complex instead of only dealing with the formation of the eruptive layer or the gabbro layer.

Bibliography

Aliabadi, M. H. and Rooke, D. P. (1991). *Numerical Fracture Mechanics.* Kluwer Academic Publishers.

Alt, J. C., Kinoshita, H. and L. B. Stokking et al. (1993). *Proceedings of Ocean Drilling Program, Initial Reports*, Vol. 148, chapter 2. Texas A&M University.

Annen, C. and Sparks, R. S. J. (2002). Effects of repetitive emplacement of basaltic intrusions on thermal evolution and melt generation in the crust. *Earth and Planetary Science Letters*, **203**, 937–955.

Auzende, J.-M., Bideau, D., Bonatti, E., Cannat, M., Honnorez, J., Lagabrielle, Y., Malavieille, J., Mamaloukas-Frangoulis, V. and Mevel, C. (1989). Direct observation of a section through slow-spreading oceanic crust. *Nature*, **337**, 726–729.

Batchelor, G. K. (1967). *An Introduction to Fluid Dynamics.* Cambridge University Press.

Battaglia, J. (2001). *Quantification sismique des phénomènes magmatiques sur le Piton de la Fournaise entre 1991 et 2000.* PhD Thesis, Université Paris 7 Denis Diderot.

Behn, M. D., Buck, W. R., Sacks, I. S. and Ito, G. (2004). Influence of magma injection on faulting and topography at mid-ocean ridges. *EOS, Transactions of the American Geophysical Union*, **85**(47). Fall Meeting Supplements, Abstract V23B-0629.

Berckhemer, H. (1990). *Grundlagen der Geophysik.* Wissenschaftliche Buchgesellschaft.

Bonafede, M. and Rivalta, E. (1999a). On tensile cracks close to and across the interface between two welded elastic half-spaces. *Geophysical Journal International*, **138**, 410–434.

Bonafede, M. and Rivalta, E. (1999b). The tensile dislocation problem in a layered elastic medium. *Geophysical Journal International*, **136**, 341–356.

Boudier, F., Nicolas, A. and Ildefonse, B. (1996). Magma chambers in the Oman ophiolite: fed from the top and the bottom. *Earth and Planetary Science Letters*, **144**, 239–250.

Brandsdóttir, B. and Einarsson, P. (1979). Seismic activity associated with the September 1977 deflation of the Krafla central volcano in north-eastern Iceland. *Journal of Volcanology and Geothermal Research*, **6**, 197–212.

Bronstein, I. N., Semendjajew, K. A., Musiol, G. and Mühlig, H. (1995). *Taschenbuch der Mathematik*. Verlag Harri Deutsch.

Bueckner, H. F. (1958). The propagation of cracks and the energy of elastic deformation. *Transactions of the American Society of Mechanical Engineers*, **80**(E), 1225–1230.

Cann, J. R. (1970). New model for the structure of the ocean crust. *Nature*, **226**, 928–930.

Cann, J. R. (1974). A model for oceanic crustal structure developed. *Geophysical Journal of the Royal Astronomical Society*, **39**, 169–187.

Ceuleneer, G., Nicolas, A. and Boudier, F. (1988). Mantle flow patterns at an oceanic spreading center: the Oman peridotites record. *Tectonophysics*, **151**, 1–26.

Coblentz, D. D. and Sandiford, M. (1994). Tectonic stresses in the African Plate: constraints on the ambient lithospheric stress state. *Geology*, **22**, 831–834.

Crouch, S. L. (1976a). Analysis of stresses and displacements around underground excavations: an application of the displacement discontinuity method. Technical report, University of Minnesota.

Crouch, S. L. (1976b). Solution of plane elasticity problems by the displacement discontinuity method. *International Journal for Numerical Methods in Engineering*, **10**, 301–343.

Crouch, S. L. and Starfield, A. M. (1983). *Boundary Element Methods in Solid Mechanics*. George Allen and Unwin Ltd, London.

Curewitz, D. and Karson, J. (1998). Geological consequences of dyke intrusions at mid-ocean spreading centers. In R. Buck, Editor, *Faulting and Magmatism at Mid-Ocean Ridges*, Vol. 106 of *Geophysical Monograph Series*, pages 117–136. American Geophysical Union.

D'Acremont, E., Leroy, S. and Burov, E. B. (2003). Numerical modelling of a mantle plume: the plume head-lithosphere interaction in the formation of an oceanic large igneous province. *Earth and Planetary Science Letters*, **206**, 379–396.

Dahm, T. (1996). Elastostatic simulation of dislocation sources in heterogeneous stress fields and multilayered media having irregular interfaces. *Physics and Chemistry of the Earth*, **21**(4), 241–245.

Dahm, T. (2000a). Numerical simulations of the propagation path and the arrest of fluid-filled fractures in the earth. *Geophysical Journal International*, **141**, 623–638.

Dahm, T. (2000b). On the shape and velocity of fluid-filled fractures in the earth. *Geophysical Journal International*, **142**, 181–192.

Dick, H. J. B., Lin, J. and Schouten, H. (2003). An ultraslow-spreading class of ocean ridge. *Nature*, **426**, 405–412.

Dutch, S. (2002). Crustal movements. Available from World Wide Web: http://www.uwgb.edu/dutchs/structge/shear.html. Lecture notes, Natural and Applied Sciences, University of Wisconsin, Green Bay.

Fialko, Y. (2001). On origin of near-axis volcanism and faulting at fast spreading mid-ocean ridges. *Earth and Planetary Science Letters*, **190**, 31–39.

Forsyth, D. W., Scheirer, D. S., Webb, S. C., Dorman, L. M., Orcutt, J. A., Harding, A. J., Blackman, D. K., Phipps Morgan, J., Detrick, R. S., Shen, Y., Wolfe, C. J., Canales, J. P., Toomey, D. R., Sheehan, A. F., Solomon, S. C. and Wilcock, W. S. D. (1998a). Imaging the deep seismic structure beneath a mid-ocean ridge: the MELT experiment. *Science*, **280**, 1215–1218.

Forsyth, D. W., Webb, S. C., Dorman, L. M. and Shen, Y. (1998b). Phase velocities of Rayleigh waves in the MELT experiment on the East Pacific Rise. *Science*, **280**, 1235–1237.

Ghods, A. and Arkani-Hamed, J. (2000). Melt migration beneath mid-ocean ridges. *Geophysical Journal International*, **140**, 687–697.

Gràcia, E. and Escartín, J. (1999). Crustal accretion at mid-ocean ridges and backarc spreading centers: insights from the Mid-Atlantic Ridge, the Bransfield Basin and the North Fiji Basin. *Contributions to Science*, **1**(2), 175–192.

Griffith, A. A. (1921). The phenomena of rupture and flow in solids. *Philosophical Transactions of the Royal Society London*, **A 221**, 163–198.

Gudmundsson, A. (1988). Effect of tensile stress concentration around magma chambers on intrusion and extrusion frequencies. *Journal of Volcanology and Geothermal Research*, **35**, 179–194.

Gudmundsson, A. (1990a). Dyke emplacement at divergent plate boundaries. In A. J. Parker, P. C. Rickwood, and D. H. Tucker, Editor, *Mafic Dykes and Emplacement Mechanisms*, pages 47–62. Balkema, Rotterdam. Proceedings of the second international dyke conference Adelaide, South Australia, 12-16 September 1990.

Gudmundsson, A. (1990b). Emplacement of dikes, sills and crustal magma chambers at divergent plate boundaries. *Tectonophysics*, **176**, 257–275.

Gudmundsson, A. (2000). Dynamics of volcanic systems in Iceland: example of tectonism and volcanism at juxtaposed hot spot and mid-ocean ridge systems. *Annual Review of*

Earth and Planetary Science, **28**, 107–140.

Hahn, H. (1976). *Bruchmechanik - Einführung in die theoretischen Grundlagen.* B.G. Teubner, Stuttgart.

Heimpel, M. and Olson, P. (1994). Buoyancy-driven fracture and magma transport through the lithosphere: Models and experiments. In M. P. Ryan, Editor, *Magmatic Systems*, chapter 10, pages 223–240. Academic Press.

Henstock, T. J., Woods, A. W. and White, R. S. (1993). The accretion of oceanic crust by episodic sill intrusions. *Journal of Geophysical Research*, **98**(B3), 4143–4161.

Irwin, G. R. (1948). Fracture dynamics. *American Society for Metals Symposium on "Fracturing of Metals", Cleveland*, pages 147–166.

Ito, G. and Martel, S. J. (2002). Focusing of magma in the upper mantle through dike interaction. *Journal of Geophysical Research*, **107**(B10). doi:10.1029/2001JB000251, ECV 6-1 – ECV 6-17.

Kanninen, M. F. and Popelar, C. H. (1985). *Advanced Fracture Mechanics.* Oxford University Press. Oxford Engineering Science Series.

Kelemen, P. B., Shimizu, N. and Salters, V. J. M. (1995). Extraction of mid-ocean-ridge basalt from the upwelling mantle by focused flow of melt in dunite channels. *Nature*, **395**, 747–753.

Kelemen, P. B., Hirth, G., Shimizu, N., Spiegelman, M. and Dick, H. J. B. (1997). A review of melt migration processes in the adiabatically upwelling mantle beneath oceanic spreading ridges. *Philosophical Transactions: Mathematical, Physical and Engineering Sciences*, **355**, 283–318.

Kolosov, G. V. (1909). *Über die Anwendung der komplexen Funktionentheorie auf das ebene Problem der mathematischen Elastizitätstheorie.* PhD Thesis, University of Yuriew (Dorpat). Original document in Russian.

Landau, L. D. and Lifschitz, E. M. (1989). *Elastizitätstheorie*, Vol. 6 of *Lehrbuch der Theoretischen Physik.* Akademie-Verlag.

LAPACK (1994). The lapack project. LAPACK - Linear Algebra PACKage. Available from World Wide Web: http://www.netlib.org/lapack.

Lawson, C. and Hanson, R. (1974). *Solving Least Square Problems.* Prentice Hall.

Lippard, S. J., Shelton, A. W. and Gass, I., Editor (1986). *The Ophiolite of Northern Oman.* Published for The Geological Society of London by Blackwell Scientific Publications. Memoirs no. 11.

Lissenberg, C. J., Bédard, J. H. and van Staal, C. R. (2004). The structure and geochemistry of the gabbro zone of the Annieopsquotch ophiolite, Newfoundland: implications for lower crustal accretion at spreading ridges. *Earth and Planetary Science Letters*, **229**, 105–123.

Macdonald, K. C. (1982). Mid-ocean ridges: fine scale tectonics, volcanic and hydrothermal processes within the plate boundary zone. *Annual Review of Earth and Planetary Science*, **10**, 155–190.

McKenzie, D. P. (1969). Speculations on the consequences and causes of plate motions. *Geophysical Journal of the Royal Astronomical Society*, **18**, 1–32.

McKenzie, D. P. (1979). Finite deformation during fluid flow. *Geophysical Journal of the Royal Astronomical Society*, **58**, 689–715.

Mège, D. and Korme, T. (2003). Fissure eruption of flood basalts from statistical analysis of dyke fracture length. *Journal of Volcanology and Geothermal Research*, **131**, 77–92.

Morgan, J. P. and Chen, Y. J. (1993). The genesis of oceanic crust: magma injection, hydrothermal circulation, and crustal flow. *Journal of Geophysical Research*, **98**(B4), 6283–6297.

Müller, K. (2003). Der Einfluss eines Spannungsfeldes auf die Kanalisierungsinstabilität in partiell geschmolzenen Mantelbereichen. 63. Jahrestagung der DGG, Conference proceedings, abstract. Friedrich-Schiller-Universität Jena.

Muskhelishvili, N. I. (1953). *Some Basic Problems of the Mathematical Theory of Elasticity.* Groningen.

Neves, M. C., Bott, M. H. P. and Searle, R. C. (2004). Patterns of stress at midocean ridges and their offsets due to seafloor subsidence. *Tectonophysics*, **386**, 223–242.

Nicolas, A. (1986). A melt extraction model based on structural studies in mantle peridotites. *Journal of Petrology*, **27**, 999–1022.

Nicolas, A. and Jackson, M. (1982). High temperature dikes in peridotites: Origin by hydraulic fracturing. *Journal of Petrology*, **23**, 568–582.

Nisbet, E. G. and Fowler, C. M. R. (1978). The Mid-Atlantic Ridge at 37° and 45°n: some geophysical and petrological constraints. *Geophysical Journal of the Royal Astronomical Society*, **54**, 631–660.

Nishihara, Y., Aoki, I., Takahashi, E., Mabukage, K. N. and Funakoshi, K. (2005). Thermal equation of state of majorite with morb composition. *Physics of the Earth and Planetary Interiors*, **148**, 73–84.

Orowan, E. (1952). Fundamentals of brittle behaviour in metals. In W. M. Murray, Editor, *Fatigue and Fracture of Metals; a Symposium Held at the Massachusetts Institute of Technology, June 19-22, 1950*, pages 139–167. Technology Press of MIT and Wiley, New York.

Phipps Morgan, J. (1987). Melt migration beneath mid-ocean spreading centers. *Geophysical Research Letters*, **14**(12), 1238–1241.

Plank, T., Spiegelman, M., Langmuir, C. H. and Forsyth, D. W. (1995). The meaning of "mean f" : clarifying the mean extent of melting at ocean ridges. *Journal of Geophysical Research*, **100**(B8), 15,045–15,052.

Press, W. H., Flannery, B. P., Teukolsky, S. A. and Vetterling, W. T. (1989). *Numerical Recipes (FORTRAN Version).* Cambridge University Press.

Rabinowicz, M., Nicolas, A. and Vigneresse, J. L. (1984). A rolling mill effect in the asthenosphere beneath oceanic spreading centers. *Earth and Planetary Science Letters*, **67**, 97–108.

Rabinowicz, M., Rouzo, S., Sempere, J. C. and Rosemberg, C. (1993). Three-dimensional mantle flow beneath mid-ocean ridges. *Journal of Geophysical Research*, **98**(B5), 7851–7869.

Rivalta, E., Böttinger, M. and Dahm, T. (2005). Gelatine experiments on dike ascent in layered media. *Journal of Volcanology and Geothermal Research.* in press.

Rubin, A. M. (1998). Dike ascent in partially molten rock. *Journal of Geophysical Research*, **103**(B9), 20,901–20,919.

Scheirer, D. S., Forsyth, D. W., Cormier, M.-H. and Macdonald, K. C. (1998). Shipboard geophysical indications of asymmetry and melt production beneath the East Pacific Rise near the MELT experiment. *Science*, **280**, 1221–1224.

Sempere, J.-C. and Macdonald, K. C. (1987). Marine tectonics: processes at mid-ocean ridges. *Reviews of Geophysics*, **25**(6), 1313–1347.

Sleep, N. H. (1988). Tapping of melt by veins and dikes. *Journal of Geophysical Research*, **93**(B9), 10,255–10,272.

Smith, D. K. and Cann, J. R. (1999). Constructing the upper crust of the Mid-Atlantic Ridge: a reinterpretation based on the Puna Ridge, Kilauea volcano. *Journal of Geophysical Research*, **104**, 25,379–25,399.

Sneddon, I. N. (1946). The distribution of stress in the neighbourhood of a crack in an elastic solid. *Proceedings of the Royal Society of London*, **187**(A), 229–260.

Sparks, D. W., Parmentier, E. M. and Phipps Morgan, J. (1993). Three-dimensional mantle convection beneath a segmented spreading center: implications for along-axis variations in crustal thickness and gravity. *Journal of Geophysical Research*, **98**(B12), 21,977–21,995.

Spiegelman, M. (1996). Geochemical consequences of melt transport in 2-d: The sensitivity of trace elements to mantle dynamics. *Earth and Planetary Science Letters*, **139**, 115–132.

Spiegelman, M. and McKenzie, D. P. (1987). Simple 2-d models for melt extraction at mid-ocean ridges and island arcs. *Earth and Planetary Science Letters*, **83**, 137–152.

Spiegelman, M. and Reynolds, J. R. (1999). Combined dynamic and geochemical evidence for convergent melt flow beneath the East Pacific Rise. *Nature*, **402**, 282–285.

Stacey, F. D. (1969). *Physics of the Earth*. John Wiley & Sons.

Stefan, J. (1891). Über die Theorie der Eisbildung, insbesondere über die Eisbildung im Polarmeere. *Annalen der Physik und Chemie*, **42**, 269–286.

Stevenson, D. J. (1989). Spontaneous small-scale melt segregation in partial melts undergoing deformation. *Geophysical Research Letters*, **16**(9), 1067–1070.

Takada, A. (1990). Experimental study on propagation of liquid-filled crack in gelatine: shape and velocity in hydrostatic stress conditions. *Journal of Geophysical Research*, **95**, 8471–8481.

Turcotte, D. L. and Schubert, G. (1982). *Geodynamics: Applications of Continuum Physics to Geological Problems*. John Wiley & Sons.

Webb, S. C. and Forsyth, D. W. (1998). Structure of the upper mantle under the EPR from waveform inversion of regional events. *Science*, **280**, 1227–1229.

Weertman, J. (1971). Theory of water-filled crevasses in glaciers applied to vertical magma transport beneath oceanic ridges. *Journal of Geophysical Research*, **76**(5), 1171–1183.

Weertman, J. (1973). Oceanic ridges, magma filled cracks, and mantle plumes. *Geofísica Internacional*, **13**, 317–336.

Wei, K. and De Bremaecker, J.-C. (1995). Fracture growth - II. Case studies. *Geophysical Journal International*, **122**, 746–754.

Westergaard, H. M. (1939). Bearing pressure and cracks. *Journal of Applied Mechanics*, **6**(A), 49–53.

Wilson, D. S., Teagle, D. A. H. and G. D. Acton et al. (2003). Proceedings of Ocean Drilling Program, Initial Reports, 206 [online]. Available from World Wide Web: http://www-odp.tamu.edu/publications/206_IR/chap_01/chap_01.htm.

Wilson, M. (1989). *Igneous Petrogenesis.* Chapman and Hall, London, United Kingdom.

Zabaras, N. (2001). Mechanical properties and processing of engineering materials. Available from World Wide Web: http://www.mae.cornell.edu/zabaras/Courses/MAE212/MAE212.html#lectures. Lecture notes, Cornell University, Spring 2001.

Appendix A

Extended explanations

Definitions of variables are similar to those given in the corresponding chapters and are explained in the notation table.

A.1 Extensions to elasticity

Stress

Stress can be written in matrix form:

$$\sigma = \begin{bmatrix} \sigma_{xx} & \sigma_{xy} & \sigma_{xz} \\ \sigma_{yx} & \sigma_{yy} & \sigma_{yz} \\ \sigma_{zx} & \sigma_{zy} & \sigma_{zz} \end{bmatrix} . \tag{A.1}$$

The direction of stresses is depicted in Fig. A.1. The first subscript of σ denotes the direction of the normal to the surface where the stress is applied, and the second subscript describes the direction in which the stress acts. Thus, σ_{xx}, σ_{yy} and σ_{zz} describe normal stresses, whereas σ_{xy}, σ_{xz}, etc. denote shear stresses.

Fig. A.2 shows 4 examples of stress conditions to clarify the meaning of the principal stresses. The associated diagonal matrices in terms of principal stress component are

$$\sigma_a = \begin{bmatrix} -\sigma_1 & 0 & 0 \\ 0 & 0 & 0 \\ 0 & 0 & 0 \end{bmatrix} \tag{A.2}$$

$$\sigma_b = \begin{bmatrix} -\sigma_1 & 0 & 0 \\ 0 & -\sigma_2 & 0 \\ 0 & 0 & 0 \end{bmatrix} \tag{A.3}$$

$$\sigma_c = \begin{bmatrix} P & 0 & 0 \\ 0 & P & 0 \\ 0 & 0 & P \end{bmatrix} \tag{A.4}$$

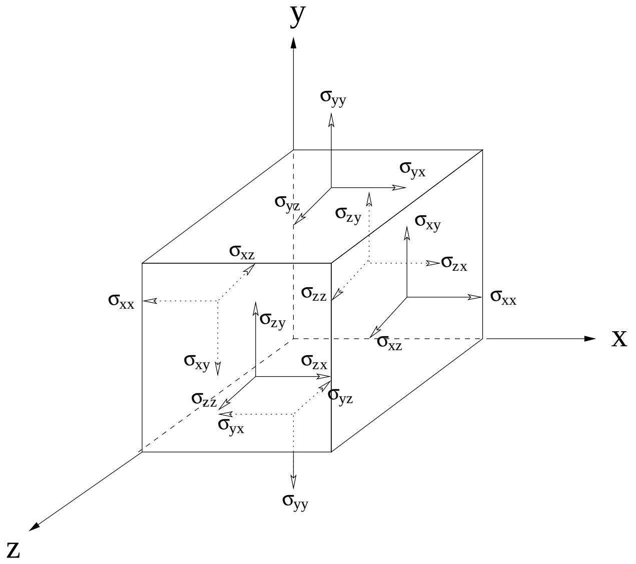

Figure A.1: Stress components of the traction vectors and their directions relative to xy, yz and xz plane; please note that since compression is considered positive in this thesis, values of components shown above have a negative sign

$$\sigma_d \;=\; \begin{bmatrix} -\sigma_1 & 0 & 0 \\ 0 & -\sigma_2 & 0 \\ 0 & 0 & -\sigma_3 \end{bmatrix} \;, \tag{A.5}$$

where σ_a denotes uniaxial tension, σ_b biaxial tension, σ_c hydrostatic pressure and σ_d a state of triaxial tension.

Strain

Fig. A.3 illustrates the meaning of various elastic moduli. The application of compression axial stress σ which leads to shortening and broadening is depicted in a). At the same time a material of original length l is shortened by Δl if an applied uniaxial stress is positive, the cross section d is enlarged by Δd. The ratio

$$\nu = \frac{\Delta d}{d} / \frac{\Delta l}{l} \tag{A.6}$$

is called Poisson's ratio. Hydrostatic pressure P leads to a volumetric change ΔV in the specimen without deformation, which can be described by

$$\frac{\Delta V}{V} = -\frac{1}{K}P \;, \tag{A.7}$$

where K is the bulk modulus, the reciprocal to the compressibility (Turcotte and Schubert, 1982); A tangential shear stress σ_s leads to deformation without volumetric change (c) with the angle of shear γ being dependent on the shear modulus μ

$$\gamma = \frac{1}{\mu}\sigma_s \;. \tag{A.8}$$

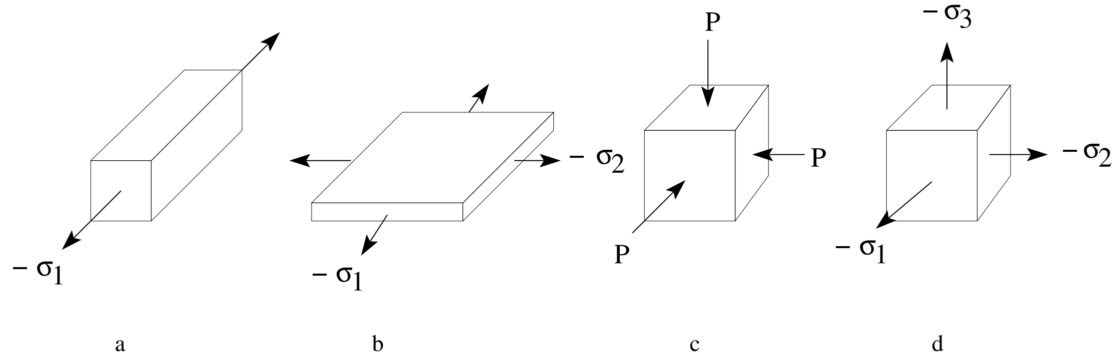

Figure A.2: Examples of stress conditions: a) uniaxial tension, b) biaxial tension, c) hydrostatic pressure, d) triaxial tension; associated diagonal matrices in terms of principal stress components see text; sketch after Zabaras (2001)

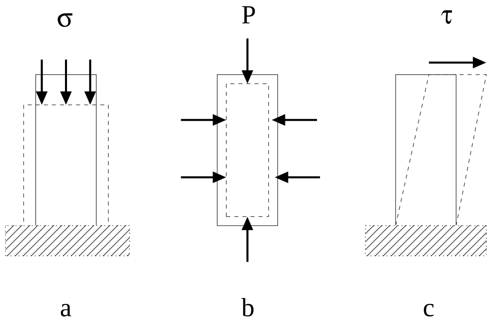

Figure A.3: Elastic deformation of a specimen to illustrate elastic moduli; a) axial compression, b) hydrostatic pressure, c) shear strain; sketch after Berckhemer (1990)

A.2 Extensions on numerical method

Derivatives of Eq. 3.8 are obtained to be

$$f_{,x} = \frac{+1}{4\pi(1-\nu)}\Big[\ \ln\sqrt{[(x-a)^2+z^2]}\ -\ \ln\sqrt{[(x+a)^2+z^2]}\ \Big] \tag{A.9}$$

$$f_{,z} = \frac{-1}{4\pi(1-\nu)}\Big[\ \arctan\frac{z}{x-a}\ -\ \arctan\frac{z}{x+a}\ \Big] \tag{A.10}$$

$$f_{,xz} = \frac{+1}{4\pi(1-\nu)}\Big[\ \frac{z}{(x-a)^2+z^2}\ -\ \frac{z}{(x+a)^2+z^2]}\ \Big] \tag{A.11}$$

$$f_{,xx} = \frac{+1}{4\pi(1-\nu)}\Big[\ \frac{x-a}{(x-a)^2+z^2}\ -\ \frac{x+a}{(x+a)^2+z^2}\ \Big] \tag{A.12}$$

$$f_{,zz} = -f_{,xx} \tag{A.13}$$

$$f_{,xzz} = \frac{+1}{4\pi(1-\nu)}\Big[\ \frac{(x-a)^2-z^2}{\{(x-a)^2+z^2\}^2} - \frac{(x+a)^2-z^2}{\{(x+a)^2+z^2\}^2}\ \Big] \tag{A.14}$$

$$f_{,zzz} = \frac{+2z}{4\pi(1-\nu)}\Big[\frac{x-a}{\{(x-a)^2+z^2\}^2} - \frac{x+a}{\{(x+a)^2+z^2\}^2}\Big] \tag{A.15}$$
$$f_{,xxx} = f_{,xzz} \tag{A.16}$$
$$f_{,xxz} = f_{,zzz} \ . \tag{A.17}$$

For the case of displacements being situated on the line $z = 0$, three cases can be told apart:

(1) $|x| > a, z = 0_\pm$

$$u_x(x,0) = -\frac{1-2\nu}{4\pi(1-\nu)}\ D_z\ \ln|\frac{x-a}{x+a}| \tag{A.18}$$
$$u_z(x,0) = +\frac{1-2\nu}{4\pi(1-\nu)}\ D_x\ \ln|\frac{x-a}{x+a}| \tag{A.19}$$

(2) $|x| < a, z = 0_+$

$$u_x(x,0_+) = -\frac{1}{2}D_x\ -\ \frac{1-2\nu}{4\pi(1-\nu)}\ D_z\ \ln|\frac{x-a}{x+a}| \tag{A.20}$$
$$u_z(x,0_+) = +\frac{1-2\nu}{4\pi(1-\nu)}D_x \ln|\frac{x-a}{x+a}|\ -\ \frac{1}{2}\ D_z \tag{A.21}$$

(3) $|x| < a, z = 0_-$

$$u_x(x,0_-) = +\frac{1}{2}D_x\ -\ \frac{1-2\nu}{4\pi(1-\nu)}\ D_z\ \ln|\frac{x-a}{x+a}| \tag{A.22}$$
$$u_z(x,0_-) = +\frac{1-2\nu}{4\pi(1-\nu)}\ D_x\ \ln|\frac{x-a}{x+a}|\ +\ \frac{1}{2}D_z\ ; \tag{A.23}$$

this means that displacements u_x, u_z are continuous for $|x| > a$ on $z = 0$, but have constant discontinuities D_x, D_z for $|x| < a$ as assumed in Eqs. 3.1. In a similar manner, stresses on the line $z = 0$ can be derived:

$$\begin{aligned}\sigma_{xx}(x,0) &= \frac{-\mu}{2\pi(1-\nu)}\ D_z\ \left(\frac{1}{x-a} - \frac{1}{x+a}\right)\\ &= \frac{-a\mu}{\pi(1-\nu)}\ D_z\ \frac{1}{x^2-a^2}\end{aligned} \tag{A.24}$$
$$\sigma_{zz}(x,0) = \frac{-a\mu}{\pi(1-\nu)}\ D_z\ \frac{1}{x^2-a^2} \tag{A.25}$$
$$\sigma_{xz}(x,0) = \frac{-a\mu}{\pi(1-\nu)}\ D_x\ \frac{1}{x^2-a^2}\ . \tag{A.26}$$

Normal stresses σ_{xx} and σ_{zz} depend only on the normal component of the discontinuity displacement D_z, whereas the shear stress σ_{xz} is only connected with the transverse component D_x. Stresses are finite and continuous everywhere except for $x = \pm a$, where they are singular and discontinuous.

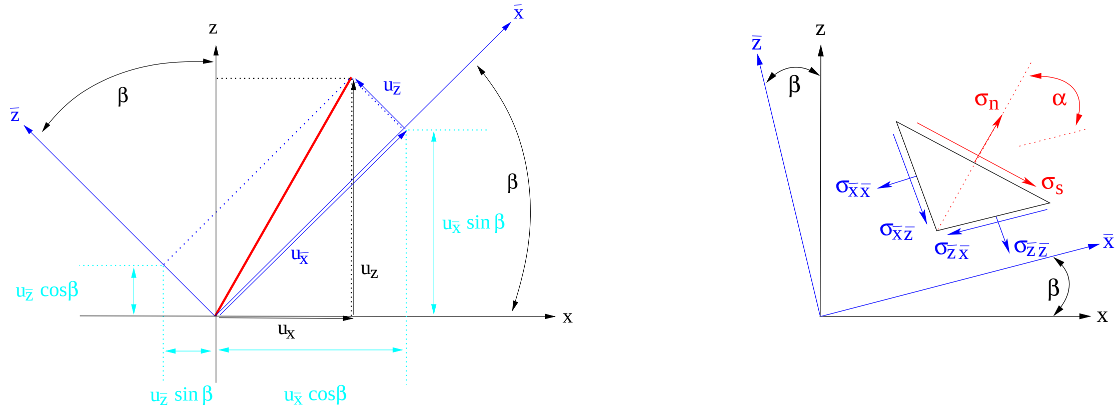

Figure A.4: Coordinate transformation of displacement and stresses; black: global coordinate system (x, z), dark blue: local coordinate system $(\bar{x}, \bar{z})$; left: coordinate transformation of displacements: red: displacement vector, light blue: distances required for transformation; right: coordinate transformation of stresses: red: normal and shear stress in local coordinate system; sketches after Crouch and Starfield (1983)

Coordinate transformations

Fig. A.4 describes the corresponding coordinate transformation of displacements on the left and stresses on the right. Displacements and stresses are transformed in the following way from global to local coordinates:

$$u_{\bar{x}} = u_x \ \cos\beta + u_z \ \sin\beta \tag{A.27}$$

$$u_{\bar{z}} = -u_x \ \sin\beta + u_z \ \cos\beta \tag{A.28}$$

and

$$\sigma_{\bar{x}\bar{x}} = \sigma_{xx}\cos^2\beta + 2\sigma_{xz}\sin\beta\cos\beta + \sigma_{zz}\sin^2\beta \tag{A.29}$$

$$\sigma_{\bar{z}\bar{z}} = \sigma_{xx}\sin^2\beta - 2\sigma_{xz}\sin\beta\cos\beta + \sigma_{zz}\cos^2\beta \tag{A.30}$$

$$\sigma_{\bar{x}\bar{z}} = -(\sigma_{xx} - \sigma_{zz})\sin\beta\cos\beta + \sigma_{xz}(cos^2\beta - \sin^2\beta) \quad , \tag{A.31}$$

where β is the angle between the global and the local coordinate system. The inverse transformation is for displacements

$$u_x = u_{\bar{x}} \ \cos\beta - u_{\bar{z}} \ \sin\beta \tag{A.32}$$

$$u_z = u_{\bar{x}} \ \sin\beta + u_{\bar{z}} \ \cos\beta \tag{A.33}$$

and for stresses

$$\sigma_{xx} = \sigma_{\bar{x}\bar{x}}\cos^2\beta - 2\sigma_{\bar{x}\bar{z}}\sin\beta\cos\beta + \sigma_{\bar{z}\bar{z}}sin^2\beta \tag{A.34}$$

$$\sigma_{zz} = \sigma_{\bar{x}\bar{x}}\sin^2\beta + 2\sigma_{\bar{x}\bar{z}}\sin\beta\cos\beta + \sigma_{\bar{z}\bar{z}} \ (cos^2\beta - sin^2\beta) \tag{A.35}$$

$$\sigma_{xz} = (\sigma_{\bar{x}\bar{x}} - \sigma_{\bar{z}\bar{z}}) \ \sin\beta\cos\beta + \sigma_{\bar{x}\bar{z}} \ (cos^2\beta - sin^2\beta) \quad . \tag{A.36}$$

A.3 Extensions on oceanic crust formation

Heat flow and solidification of a dyke

The governing equation is Eq. 5.1. The boundary conditions are

$$\begin{array}{lll} T = T_m & x = x_m(t) & t > 0 \\ T \rightarrow T_0 & x \rightarrow \infty & t > 0 \; . \end{array}$$

The introduction of the dimensionless temperature ratio Θ changes Eq. 5.1 to

$$\frac{\partial \Theta}{\partial t} = \kappa \frac{d^2 \Theta}{dx^2} \tag{A.37}$$

and the boundary conditions to

$$\begin{array}{rcl} \Theta(x_m, t) & = & 1 \\ \Theta(\infty, t) & \rightarrow & 0 \; . \end{array}$$

Eq. A.37 is transformed further with the help of the similarity variable $\lambda = \frac{x}{2\sqrt{\kappa t}}$ to be

$$\begin{array}{rcl} \dfrac{\partial \Theta}{\partial t} & = & \dfrac{d\Theta}{d\lambda} \cdot \dfrac{\partial \lambda}{\partial t} = \dfrac{d\Theta}{d\lambda} \left(-\dfrac{1}{4} \dfrac{x}{\sqrt{\kappa t}} \dfrac{1}{t} \right) = \dfrac{d\Theta}{d\lambda} \left(-\dfrac{1}{2} \dfrac{\lambda}{t} \right) \\ \dfrac{\partial \Theta}{\partial x} & = & \dfrac{d\Theta}{d\lambda} \cdot \dfrac{\partial \lambda}{\partial x} = \dfrac{d\Theta}{d\lambda} \dfrac{1}{2\sqrt{\kappa t}} \\ \dfrac{\partial^2 \Theta}{\partial x^2} & = & \dfrac{1}{2\sqrt{\kappa t}} \dfrac{d^2 \Theta}{d\lambda^2} \cdot \dfrac{\partial \lambda}{\partial x} = \dfrac{1}{4} \dfrac{1}{\kappa t} \dfrac{d^2 \Theta}{d\lambda^2} \end{array}$$

and finally becomes

$$\begin{array}{rcl} \dfrac{d\Theta}{d\lambda} \left(-\dfrac{1}{2} \dfrac{\lambda}{t} \right) & = & \kappa \dfrac{1}{4} \dfrac{1}{\kappa t} \dfrac{d^2 \Theta}{d\lambda^2} \\ -\lambda \dfrac{d\Theta}{d\lambda} & = & \dfrac{1}{2} \dfrac{d^2 \Theta}{d\lambda^2} \; . \end{array} \tag{A.38}$$

The boundary conditions are substituted by

$$\begin{array}{rcl} x = x_m(t) & \rightarrow & \lambda = -\lambda_2 \\ x \rightarrow \infty & \rightarrow & \lambda \rightarrow \infty \end{array}$$

to give the simplified conditions

$$\Theta(\lambda \rightarrow \infty) \rightarrow 0 \tag{A.39}$$

$$\Theta(\lambda = -\lambda_2) = 1 \; . \tag{A.40}$$

Hence, the similarity approach leads to the reduction of a partial differential equation to an ordinary differential equation as well as the transition of separate boundary conditions in t, x to consistent conditions involving only λ. The problem can be solved with the help of separation of variables by integration. Let ϕ be defined as $\phi \equiv \frac{d\Theta}{d\lambda}$ so that Eq. A.38 changes to

$$\begin{aligned} -\lambda\phi &= \frac{1}{2}\frac{d\phi}{d\lambda} \\ -\lambda d\lambda &= \frac{1}{2}\frac{d\phi}{\phi} \quad , \end{aligned} \tag{A.41}$$

which can be solved by integration to deliver

$$\begin{aligned} \phi &= c_1 e^{-\lambda^2} = \frac{d\Theta}{d\lambda} \\ \Theta &= c_1 \int_0^\lambda e^{-\lambda'^2} d\lambda' + c_2 \quad , \end{aligned} \tag{A.42}$$

where c_1, c_2 are constants of integration. Boundary condition A.39 leads to

$$0 = c_1 \int_0^\infty e^{-\lambda'^2} d\lambda' + c_2 \ . \tag{A.43}$$

Since the integral is well known

$$c_1 \int_0^\infty e^{-\lambda'^2} d\lambda' = \frac{\sqrt{\pi}}{2} \ , \tag{A.44}$$

it follows that

$$\begin{aligned} \Rightarrow c_1 &= -c_2 \frac{2}{\sqrt{\pi}} \\ \Theta &= c_2 \left(-\frac{2}{\sqrt{\pi}}\right) \int_0^\lambda e^{-\lambda'^2} d\lambda' + c_2 \\ &= \left(1 - \frac{2}{\sqrt{\pi}} \int_0^\lambda e^{-\lambda'^2} d\lambda'\right) c_2 \ . \end{aligned} \tag{A.45}$$

An errorfunction erf is defined

$$\mathrm{erf}(\lambda) \equiv \frac{2}{\sqrt{\pi}} \int_0^\lambda e^{-\lambda'^2} d\lambda' \tag{A.46}$$

leading to

$$\begin{aligned} \Theta &= [1 - \mathrm{erf}(\lambda)] \cdot c_2 \\ &= \mathrm{erfc}(\lambda) \cdot c_2 \ , \end{aligned} \tag{A.47}$$

where erfc(λ) is the complementary errorfunction. Boundary condition A.40 leads to

$$\begin{aligned} 1 &= \mathrm{erfc}(-\lambda_2) \cdot c_2 \\ \Rightarrow c_2 &= \mathrm{erfc}(-\lambda_2) \end{aligned} \tag{A.48}$$

and

$$\begin{aligned} \Theta &= \frac{\mathrm{erfc}(\lambda)}{\mathrm{erfc}(-\lambda_2)} \\ &= \frac{\mathrm{erfc}(\lambda)}{1 + \mathrm{erf}(\lambda_2)} \ . \end{aligned} \tag{A.49}$$

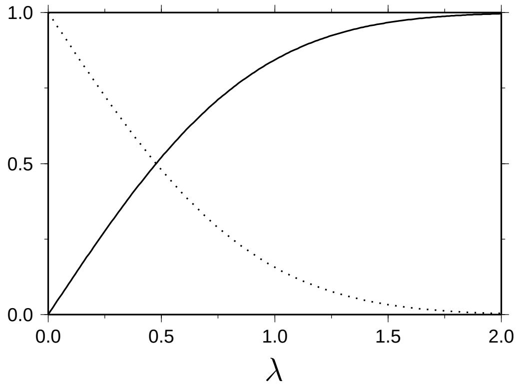

Figure A.5: Continuous line: errorfunction; dotted line: complementary errorfunction

Values of the errorfunction can only be calculated numerically. Both errorfunction and complementary errorfunction are displayed in Fig. A.5.
Calculations involving phase change lead to two additional aspects: First, the location of the phase change boundary shifts during the solidification process and has to be identified continuously. Second, a latent heat of fusion L is released during the crystallisation and has to be conducted away from the phase change boundary to ensure the conservation of energy (see Fig. A.6).

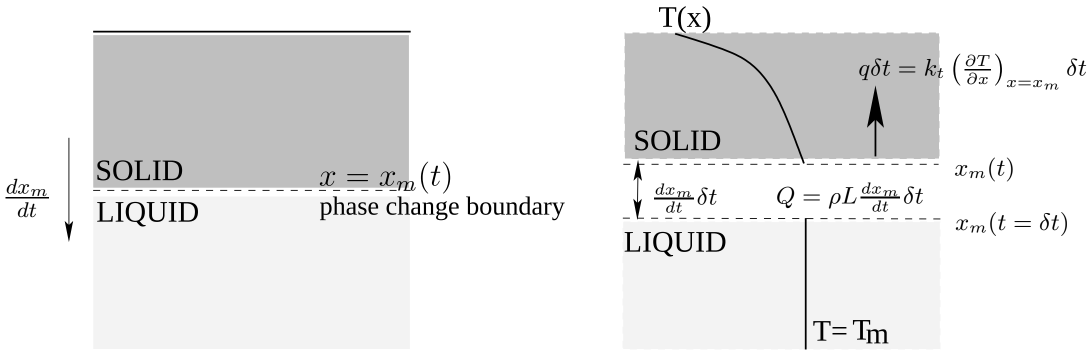

Figure A.6: Left: Phase change boundary between liquid and solid shifts in time with velocity $\frac{dx_m}{dt}$; right: generated latent heat of fusion has to be conducted away from phase change boundary

During the time span δt, the phase change boundary moves downwards by the amount $\frac{dx_m}{dt}\delta t$, equivalent to solidifying the mass per unit area $\rho\frac{dx_m}{dt}\delta t$, where ρ is the density of the magma. Thus, an amount of latent heat $Q = \rho L\frac{dx_m}{dt}\delta t$ is released which must be conducted away from the interface at the rate at which it is set free. The rate of heat flow is $q\delta t = k_t \left(\frac{dT}{dx}\right)_{x=x_m} \delta t = \kappa\rho c \left(\frac{dT}{dx}\right)_{x=x_m} \delta t$, when the heat flux q is conducted in direction of the positive x coordinate. This leads to

$$\rho L \frac{dx_m}{dt}\delta t = \kappa\rho c \left(\frac{dT}{dx}\right)_{x=x_m} \delta t \ . \tag{A.50}$$

Inserting

$$x_m \ = \ -2\lambda_2\sqrt{\kappa t}$$

$$\frac{dx_m}{dt} = -\lambda_2 \left(\frac{\kappa}{t}\right)^{1/2}$$

as well as

$$\begin{aligned}\left(\frac{dT}{dx}\right)_{x=x_m} &= \left(\frac{d\Theta}{d\lambda}\right)_{\lambda=-\lambda_2} \cdot \left(\frac{d\lambda}{dx}\right)(T_m - T_0) \\ &= \frac{-(T_m - T_0)}{\sqrt{\pi\kappa t}} \frac{e^{-\lambda_2{}^2}}{1+\mathrm{erf}(\lambda_2)}\end{aligned}$$

in Eq. A.50 finally yields

$$\frac{L\pi}{c(T_m - T_0)} = \frac{e^{-\lambda_2{}^2}}{\lambda_2(1+\mathrm{erf}(\lambda_2))} \quad , \tag{A.51}$$

which is a transcendental equation for the determination of λ_2. It is not directly solvable, only by iterative calculation or graphical determination as presented in Fig. A.7.

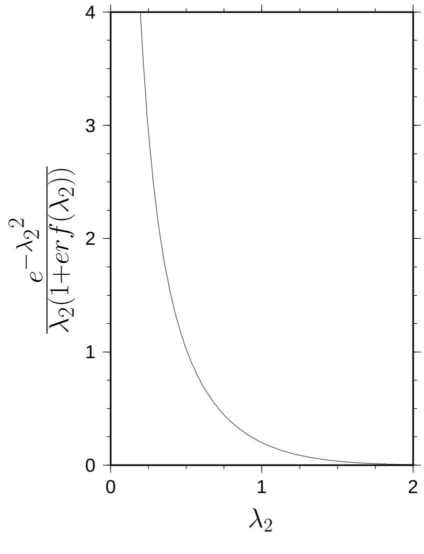

Figure A.7: Transcendental function for the determination of λ_2

Interaction between 2 dykes

The first model is chosen to be very simple and serves to highlight stress fields generated by dyke and sill openings. A large dyke is placed artificially at a certain depth. Small dykes are ascending and are interacting with the stress field of the large "test dyke", **but not among themselves**. At the top of Fig. A.8, the influence of a large vertical dyke on succeeding smaller dykes can be observed, whereas at the bottom the influence of a large horizontal sill is shown.

In the first case, succeeding dykes accumulate horizontally alongside the test dyke whereas in the second case, the smaller dykes are aligned vertically beneath the sill. In both instances, succeeding dykes try to follow the trajectories of maximum compression.

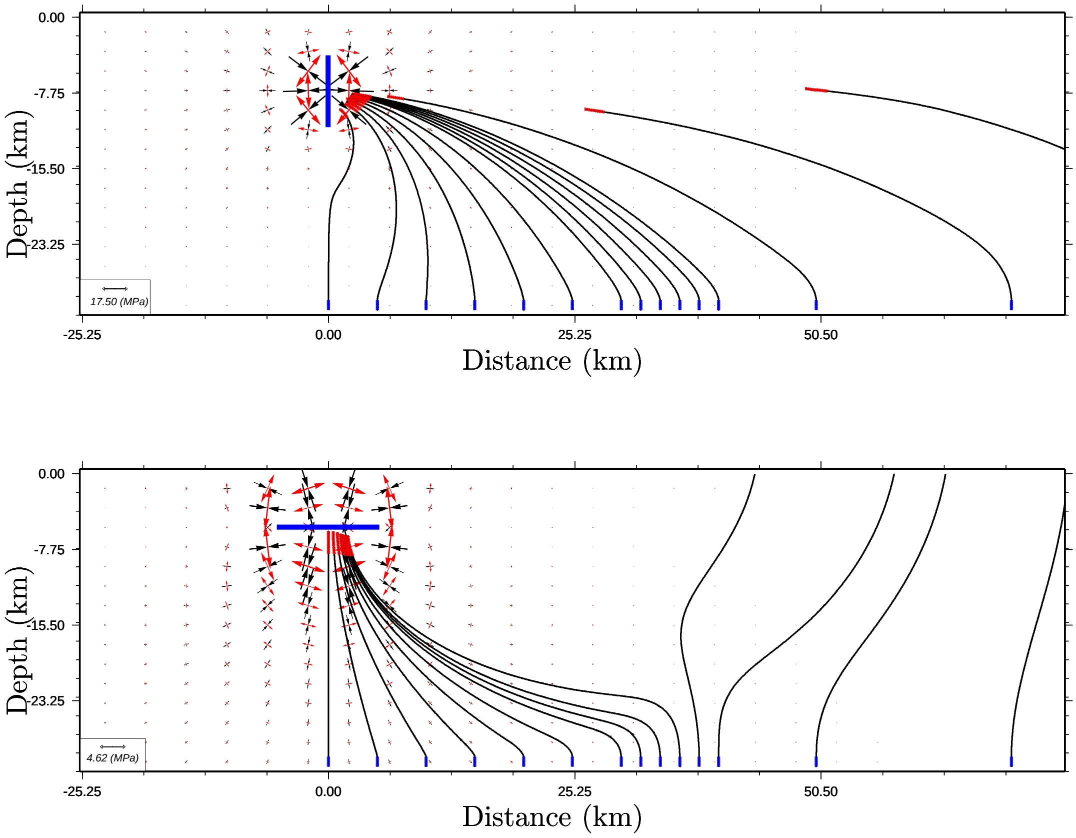

Figure A.8: Top: influence of a large, vertical dyke on succeeding, smaller dykes; bottom: influence of a large, horizontal sill on succeeding, smaller dykes; internal pressure of dyke chosen to be larger than in the case of the sill

The circle of influence depends on the internal pressure of the test dyke. For demonstration purposes, the internal pressure of the dyke was chosen to be higher than in the case of the sill. Thus, dykes at greater distances are influenced by its stress field.

This model can be made more realistic including the following.

- All dykes have the same length.
- All dykes ascend from beneath including the ”test dyke”.
- Dykes stop at a level of neutral buoyancy.

In Fig. A.9, the dyke furthest left (at zero distance) is ascended first and represents the test dyke. Its stress field is indicated by black (principal axis of maximum compression)

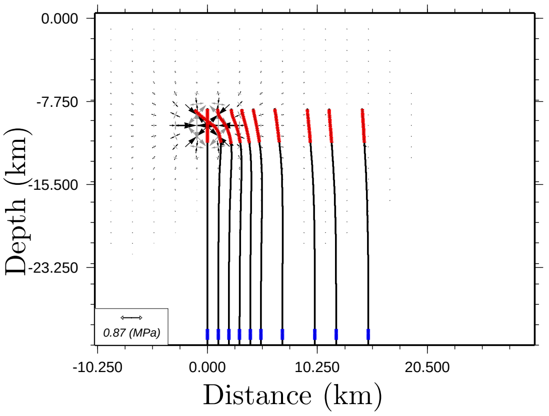

Figure A.9: More realistic model of dyke ascent: all dykes have the same length, test dyke ascended from beneath similar to succeeding dykes and dykes stop at a level of neutral buoyancy

and grey arrows (principal axis of maximum extension). The effect of the stress field of the test dyke decreases with increasing distance. The magnitude of the stress field is lower than in the previous model, since the internal pressure of the dyke matches its length and is no longer chosen arbitrarily. The circle of influence decreases compared with Fig. A.8 due to the similarity in dyke length and comparability of the stress fields. Dykes align vertically and not horizontally to the test dyke, since the ratio between stress field magnitude and dyke length prevents them of a quick adjustment to the trajectories of maximum compression.

Ascent paths chosen by succeeding dykes depend on their length. On the left of Fig. A.10, the interaction between long fractures is depicted, on the right, short fractures are displayed. Large fractures exhibit a strong preferred orientation in vertical direction. The

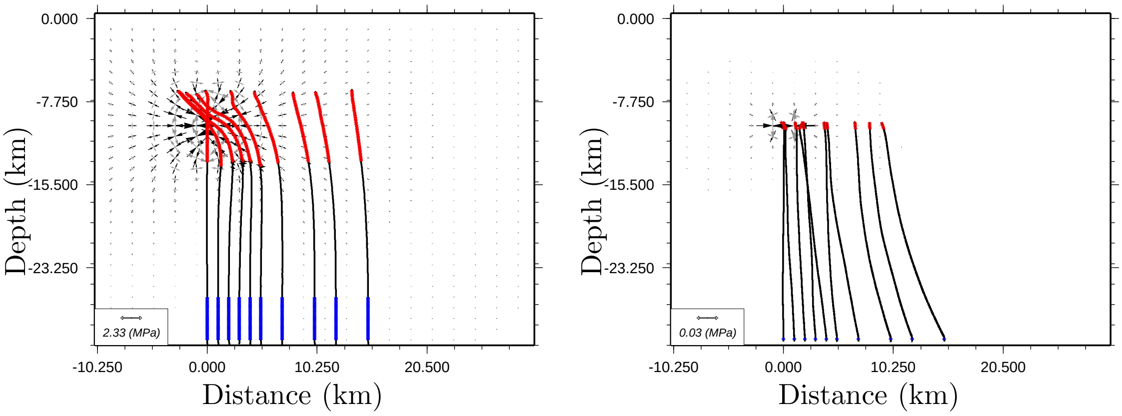

Figure A.10: Influence of dyke length on ascent paths

diversion from this orientation occurs only at depth of the test dyke and is largest for the close-up range. Short fractures are able to quickly adapt to stress fields. The deviation from a vertical path occurs near their initial positions and is largest for the middle range because of the orientation of the stress field.

More examples for distributed initial positions

Model runs with different sequences of dyke ascent are compared with show the similarity of results (see Fig. A.11). Whereas the initial distribution of fractures is the same for all models, namely a constant distance distribution, the order of ascent is random and different for all figures. Nevertheless, the result is similar: a dyke cluster is formed whose location is arbitrary. It is generated where two dykes incidentally are situated close-by. The first fracture ascended is recognisable by its straight propagation path and does not necessarily coincide with the position of the "focussing area".

Free surface effects

Another modification in dealing with models corresponding to the geological setting of a mid-ocean ridge is to include the effect of the free surface at the ocean bottom into the computation of stress and displacement fields. This is performed by using the method of images, where the actual discontinuities situated in the crust at $z > 0$ are mirrored to $z < 0$ and the results are superpositioned. Thus, shear and normal traction on $z = 0$ are bound to vanish. Equations are not given here, but can be found in Crouch and Starfield (1983). The influence on the dyke propagation paths is noticeable, but does not change the results substantially.

A comparison of dyke ascent paths ex- and including the free surface effect can be found in Fig. A.12. The free ocean bottom interface hinders slightly the focussing of fractures. Nevertheless, the formation of a dyke cluster is still clearly visible. If an extensional stress field is included in the model, the parallel alignment of dykes seems to be uninfluenced of the presence of a free surface.

In Fig. A.13, the displacement fields for the dyke distributions of Fig. A.12 are shown by arrows. Dyke end positions are indicated by red lines. Again, it is clearly visible that the influence of the free surface is stronger for models without regional stress field.

In Fig. A.14, the vertical displacement at the ocean bottom is displayed. In general, the displacement is increased by including free surface effects (Crouch and Starfield, 1983). Hence, the biggest amount of displacement is found in the model without regional stress field and a free ocean bottom interface. However, it differs not much from the model computed by the full space solutions. Models including an extensional stress field of 5 MPa exhibit scarcely a vertical displacement, since fractures are situated vertically and thus, the largest amount of displacement is parallel to the ocean bottom interface.

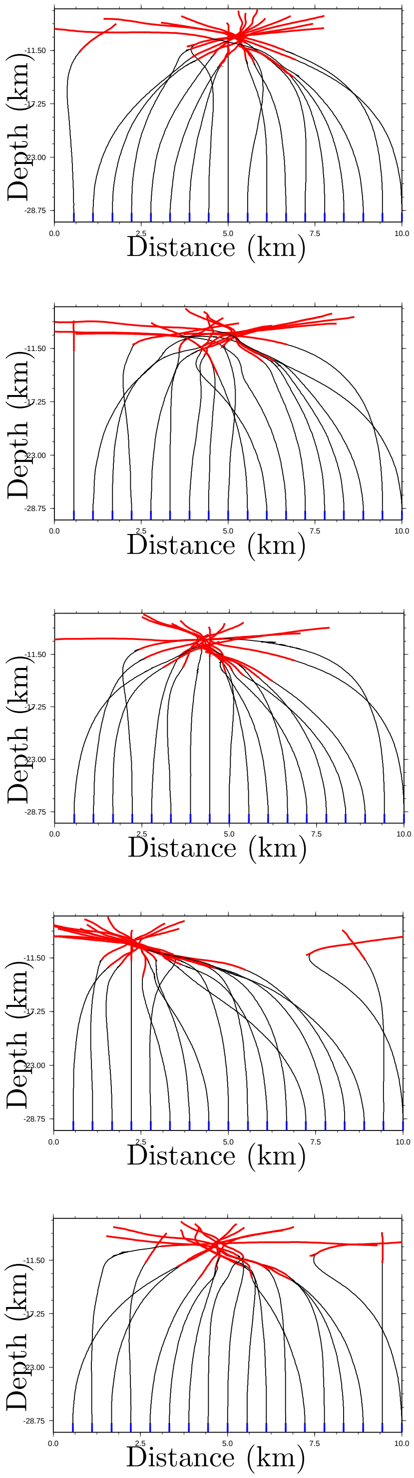

Figure A.11: Comparison of model runs with different sequences of dyke ascent; whereas the initial distribution of fractures is the same for all models, namely a constant-distance distribution, the order of ascent is random and different

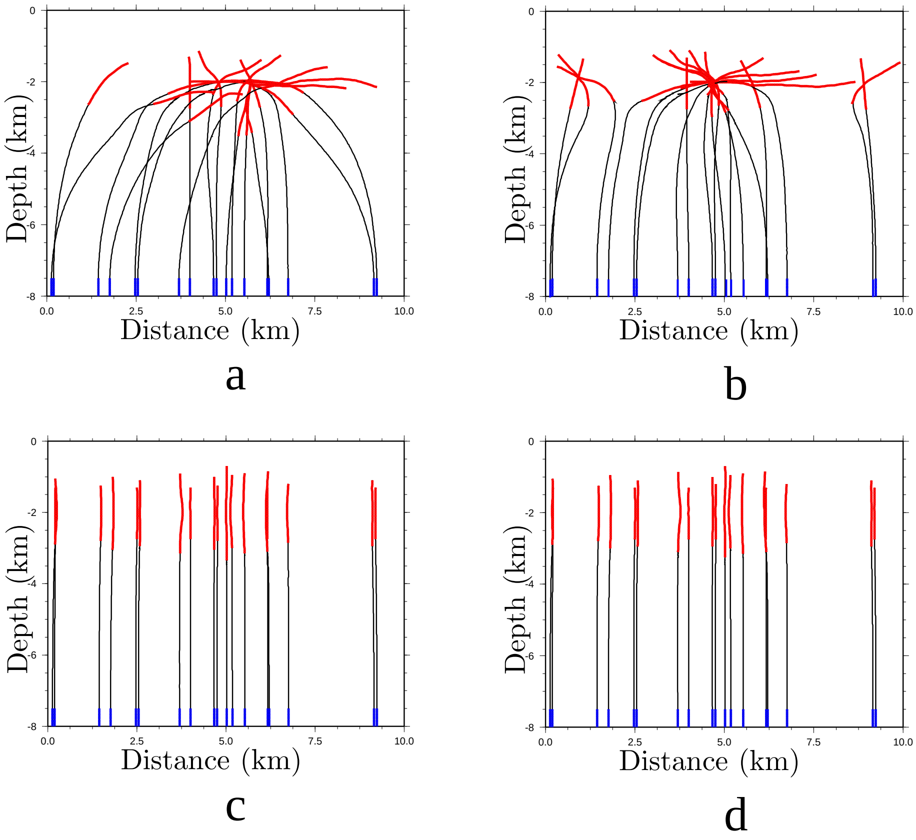

Figure A.12: Influence of free ocean bottom interface on dyke propagation paths; a) no regional stress field, no free surface effect, b) no regional stress field, free surface effect included, c) extensional stress field, no free surface effect, d) extensional stress field and free surface effect included

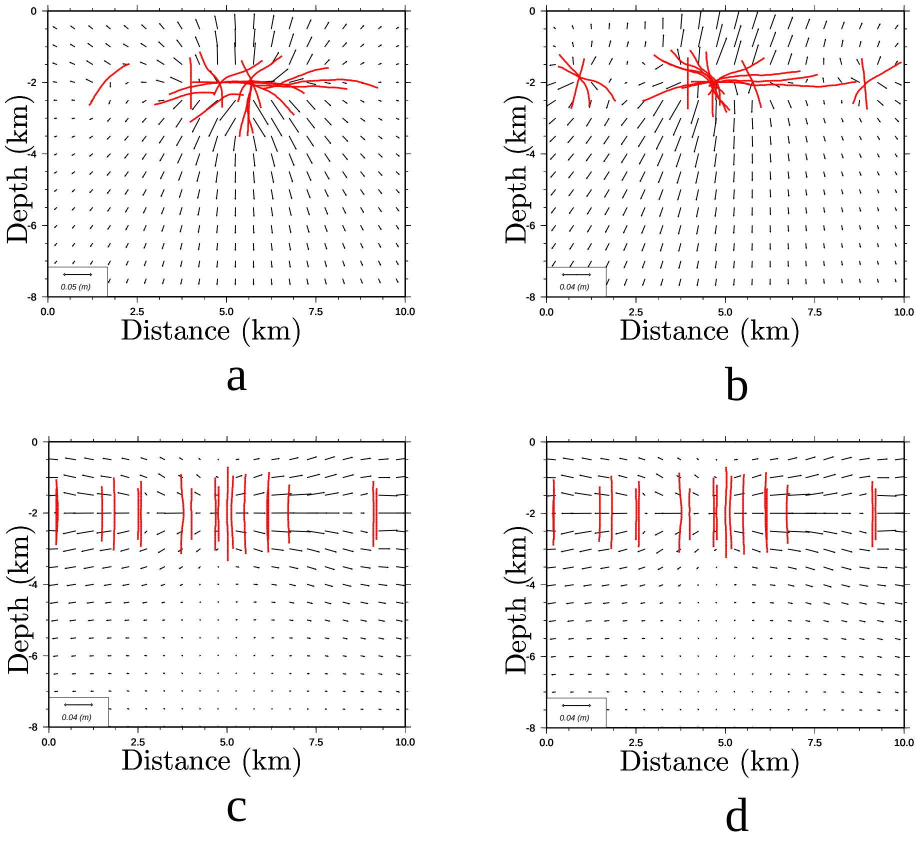

Figure A.13: Influence of free ocean bottom interface on displacement field; a) no regional stress field, no free surface effect, b) no regional stress field, free surface effect included, c) extensional stress field, no free surface effect, d) extensional stress field and free surface effect included; displacement indicated by arrows, end position of dykes marked by red lines

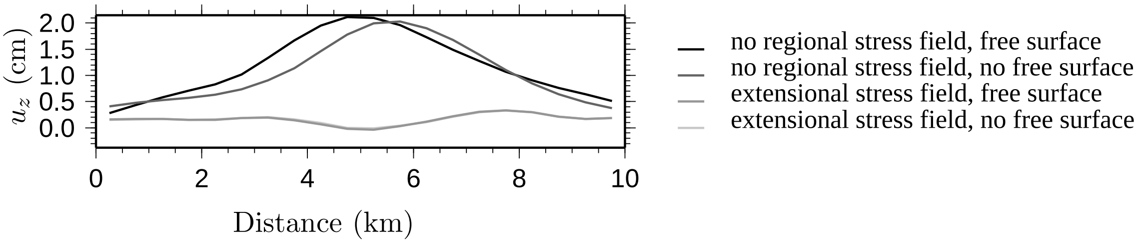

Figure A.14: Vertical displacement at ocean bottom

Appendix B

Fortran subroutines and input file

B.1 Program input file ”crouch.inp”

```
### TITEL
Dyke ascent from crust-mantle boundary, example file
### REGIONAL STRESS FIELD: S_ij = b_ij + a_ij*z + c_ij*x (in MPa and MPa/km)
### istress: How many different  stress layers (here: 2 stress layers with different density)
### Here: 2 layers, layer 1: 2400 kg/m3, layer 2: 3000 kg/m3, boundary at 2 km depth
#   istress,axx(1),azz(1),axz(1),bxx(1),bzz(1),bxz(1),fs2,cxx(1),czz(1),cxz(1)
2  0.23544E+02  0.23544E+02  0.00000E+00  0.00000E+00  0.00000E+00  0.00000E+00  0.50000E+00
&  0.00000E+00  0.00000E+00   0.00000E+00
   0.29430E+02  0.29430E+02  0.00000E+00 -0.11772E+02 -0.11772E+02  0.00000E+00  0.20000E+01
### MATRIX INVERSION
### linv=0: nonnegative least square
### other parameters required for visco-elastic version of program (not here)
#   linv,lw,deltat,t2,t1,intgl)
    0    0 0.000E+00 0.000E+00 0.000E+00    0
### LAYERS OF MODEL AND SYMMETRY
### nlay: number of layers defined by boundary elements
### Here: none
### nsym=1: no symmetry axes
#   nlay,nsym,cdis
    1    1 0.000E+00
### PROPERTIES OF LAST LAYER (FULL SPACE)
### lhalf=0: full space solutions applied; lhalf=1:  half space solutions applied
### pois: poisson’s ratio
### emodul: shear modulus (in GPa)
### area: area covered by fracture surfaces (in m**2)
### exdruck: bulk modulus (in MPa)
#   lhalf(nlay+1),pois(nlay+1),emodul(nlay+1),area,exdruck
              1       0.25E+00  0.30E+02            0.20E+02  0.10E+04
#############################################################################################
#               Layer  1
#############################################################################################
### PROPERTIES OF THE LAYER
### nlin: number of lines describing segments at layer boundaries (here: none)
### nsou: number of lines describing segments inside layer (here: 20)
#   nlin, nsou, lhalf(ilay), pois(ilay), emodul(ilay)
    0   20    1       0.25E+00  0.30E+02
### num: fragmentation of element in parts (here: none)
### kode: type of boundary conditions (here: kode=1, meaning that traction is defined)
### xb,zb: start coordinates of segment (in km)
### xe,ze: end coordinates of segment (in km)
### Here: vertical fracture at x=0
### tn, tne: normal traction on segment at segment start and segment end (in MPa)
### tt, tte: shear traction on segment at segment start and segment end (in MPa)
```

```
#   num, kode, xb, zb, xe, ze, tn, tt, tne, tte
    1    1        0.000        7.500        0.000        7.525          0.199E+03    0.000E+00
&    0.199E+03    0.000E+00
    1    1        0.000        7.525        0.000        7.550          0.199E+03    0.000E+00
&    0.200E+03    0.000E+00
    .    .         .            .            .            .              .            .
    .    .         .            .            .            .              .            .
    .    .         .            .            .            .              .            .
### (20 lines)
##############################################################################################
#               Next layer, if present (here: 1-layer model)
##############################################################################################
### Name of file containing arbitrary points, where stress and displacement field is to be
### plotted afterwards
# numos, cprofile
   -1     profile.dat_dy
### COORDINATES OF MODEL REGION (only for plotting)
# xleft, xright, zbot, zend
           -0.10E+02  0.30E+02  0.00E+00  0.30E+02
```

B.2 Fortran routine to compute background stress field including corner flow/dyke interaction

```
subroutine getpxx(z,x,pxx,pzz,pxz)

implicit none
integer mla,istress,i,idyke
parameter (mla=7)
double precision z,x,pxx,pzz,pxz
double precision pxz1,pxx1,pzz1,pyy1
real fs2
real*8 axx(mla),azz(mla),bxx(mla),bzz(mla),axz(mla),bxz(mla)
real*8 cxx(mla),czz(mla),cxz(mla)
real*8 zstress (mla)
double precision sigxx,sigzz,sigxz
COMMON /S5/ AXX,AZZ,AXZ,BXX,BZZ,BXZ,CXX,CZZ,CXZ,zstress,istress
COMMON /dy/ idyke
COMMON /pfeld/ pxz1,pxx1,pzz1,pyy1

###  Computation of background stress field (cp. ''crouch.inp'', line 7/8)
if(z.ge.zstress(istress))then
   write(*,*)'z.ge.zstress(istress)'
   stop
end if
if(z.lt.zstress(1))then
   PXX=BXX(1)+AXX(1)*Z+CXX(1)*X
   PZZ=BZZ(1)+AZZ(1)*Z+CZZ(1)*X
   PXZ=BXZ(1)+AXZ(1)*Z+CXZ(1)*X
else
   do i=2,istress
      if(z.ge.zstress(i-1) .and. z.lt.zstress(i))then
         PXX=BXX(i)+AXX(i)*Z+CXX(i)*X
         PZZ=BZZ(i)+AZZ(i)*Z+CZZ(i)*X
         PXZ=BXZ(i)+AXZ(i)*Z+CXZ(i)*X
      end if
   end do
end if

### POSSIBILITY 1: Calculation of dyke ascent in the mantle
### Background stress field influenced by corner flow
if(icorn.gt.0) then
   call cornerflow(icorn,x,z,vslab,dslab,etaslab,zasth,sigxx,sigzz,sigxz)
   .
```

```
   .
   .
   (onward as listed below)

### POSSIBILITY 2: Dyke ascent in the crust
### Background stress field influenced by preceding dykes
if(idyke.gt.0) then
   call dyke(x,z,sigxx,sigzz,sigxz)

### Save old background stress field to calculate lithostatic gradient
   pxx1=pxx
   pxz1=pxz
   pzz1=pzz

### Complete background stress field by summation
   PXX=PXX+sigxx
   PZZ=PZZ+sigzz
   PXZ=PXZ+sigxz

   fs2=0.5
   if(pxx1.gt.pzz1)then
      pyy1=pzz1+fs2*(pxx1-pzz1)
   else
      pyy1=pxx1+fs2*(pzz1-pxx1)
   end if

end if

return
END
```

B.3 Fortran routine computing corner flow

```
subroutine cornerflow(icorn,xi,zi,vslab,dipslab,eta,zasth,sigxx,sigzz,sigxz)

implicit none
integer i,j,k,m, icorn
real*8 beta(3,3),xm0(3,3),xm1(3,3)
real*8 xi,zi
real*8 pi,rad,deg
real*8 r,phi,phi1
real*8 sigrp,u,zasth
real*8 f0,e0,g,P
real*8 eta,vslab,dipslab

pi = 4.*datan(1.d0)
rad = pi/180.
deg = 180./pi
g=9.80665

sigzz = 0.
sigxx = 0.
sigxz = 0.

r = sqrt(xi**2 + zi**2)

### Computed only beneath crust
if(zi.gt.zasth)then

   phi = atan2(xi,zi)
### Formula by MacKenzie(1979)
   f0 = r*pi
   igrp = 4.*eta*vslab*sin(phi)/f0
   P = -4.*eta*vslab*cos(phi)/f0
```

```
### Different definitions of angles in MacKenzie(1979) and this thesis
   phi = atan2(zi,xi)
### Matrix definition and rotation by T. Dahm
   do i=1,3
      do j=1,3
         beta(i,j) = 0.d0
         xm0(i,j) = 0.d0
         xm1(i,j) = 0.d0
      end do
   end do
   xm0(1,3) = sigrp
   xm0(3,1) = xm0(1,3)
   xm0(1,1) = P
   xm0(2,2) = xm0(1,1)
   xm0(3,3) = xm0(1,1)
### Rotational matrix
   beta(1,1) = dcos(phi)
   beta(1,3) = -dsin(phi)
   beta(3,1) = +dsin(phi)
   beta(3,3) = dcos(phi)
   beta(2,2) = 1.d0

   do k=1,3
      do m=1,3
         xm1(k,m) = 0.d0
         do i=1,3
            do j=1,3
               xm1(k,m) = xm1(k,m) + xm0(i,j)*beta(k,i)*beta(m,j)
            end do
         end do
      end do
   end do

   sigzz = xm1(3,3)
   sigxx = xm1(1,1)
   sigxz = xm1(1,3)

end if

return
END
```

B.4 Fortran routine computing dyke interaction

```
subroutine dyke(xbla,zbla,sigxx_f,sigzz_f,sigxz_f)

implicit none
integer i,j,k,m,nlay,mla,ndim,nndim,numbd_old
parameter (mla=7,ndim=920,nndim=9999)
integer ilay,ibeg,layer(0:mla,2),lhalf(mla)
integer lay_old1,lay_old2,lay_old3,lay_old4
integer kode,ninf,nsym,KOD(ndim)
double precision A_old(nndim),X_old(nndim),Z_old(nndim),BETA_old(nndim)
double precision xi,zi,xj,zj,aj,betai,betaj,cdis,pr,emod
double precision xbla,zbla
double precision sigxz_f,sigxx_f,sigzz_f
double precision pois(mla),emodul(mla),fact
double precision vec_dn(nndim),vec_dt(nndim),vec_dnr(nndim),vec_dtr(nndim)
double precision DN_f,DT_f,DNR_f,DTR_f
double precision ats_f,atn_f,ans_f,ann_f,ass_f,asn_f
double precision bss_f,bsn_f,bns_f,bnn_f
COMMON /veccoeff/ vec_dn,vec_dt,vec_dnr,vec_dtr
COMMON /lay_old/ lay_old1,lay_old2,lay_old3,lay_old4
```

```
COMMON /S3/ pois,emodul,lhalf,layer,nlay
COMMON /pcoef/ xi,xj,zi,zj,aj,betai,betaj,cdis,pr,emod,kode,ninf,nsym
COMMON /S8_old/ X_old,Z_old,BETA_old,A_old,numbd_old

### Loop over layers
do 100 ilay=1,nlay+1
   pr=pois(ilay)
   emod=emodul(ilay)
   ninf=lhalf(ilay)
   kode=1
   fact=emod/(16*datan(1.D0)*(1.d0-pr*pr))
   if(ilay.eq.1)then
      ibeg=1
   else
      ibeg=lay_old1+1
   end if

   xi=xbla
   zi=zbla
   betai=0.d0
   sigxx_f=0.d0
   sigzz_f=0.d0
   sigxz_f=0.d0

### Loop over dislocation sources situated within layer
   do 830 j=lay_old3+1,lay_old2

      xj=0.d0
      zj=0.d0
      aj=0.d0
      betaj=0.d0
      DN_f=0.d0
      DT_f=0.d0
### Following vectors contain geometrical parameters for segments of fractures already
### arrested in the crust
      xj=X_old(J)
      zj=Z_old(J)
      aj=A_old(J)
      betaj = BETA_old(j)
### Subroutine initialises boundary coefficients
      call INIT_OLD(ats_f,atn_f,ass_f,asn_f,ans_f,ann_f,bss_f,bsn_f,bns_f,bnn_f)
### Subroutine calculates boundary coefficients
### depending among other things on problem geometry, i.e. position of point, where
### stress field is currently computed
      call COEFF(0,j,ats_f,atn_f,ass_f,asn_f,ans_f,ann_f,bss_f,bsn_f,bns_f,bnn_f)

### Dislocation sources of segments of fractures already arrested in the crust are
### stored in vectors vec_dn (normal dislocation) and vec_dt (shear dislocation)
      DN_f=vec_dn(j)
      DT_f=vec_dt(j)
### Compute stress field from boundary coefficients and current dislocation sources
      SIGXX_f=SIGXX_f+ATS_f*DT_f+ATN_f*DN_f
      SIGZZ_f=SIGZZ_f+ANS_f*DT_f+ANN_f*DN_f
      SIGXZ_f=SIGXZ_f+ASS_f*DT_f+ASN_f*DN_f

   830  continue

### fact is a multiplication factor comprising shear modulus and poisson's ratio
   sigxx_f=sigxx_f*fact
   sigzz_f=sigzz_f*fact
   sigxz_f=sigxz_f*fact

100 continue

return
END
```

Acknowledgments

Experience is the name everyone gives to their mistakes.
(Oscar Wilde, 1854-1900)

I would like to thank the following people for providing their assistance and sharing their experiences.

I gratefully acknowledge the enthusiastic supervision of Prof. Dr. Torsten Dahm. The topic of oceanic crust formation has been of interest to me already in the past, as my former fellow students from the University of Münster possibly remember, since I am to blame for them having to recite the geological layers of oceanic crust during their geophysical examination. This topic still is of interest to me, despite having worked on it for three years.
I would like to thank Prof. Dr. Frank Roth for being the second advisor.
My work was supported by the German Research Foundation (DFG) by means of the grants DA 478/3-1 and 3-2. Prof. Dr. Harro Schmeling did a good job in coordinating the bundle project and was always interested in discussions.
Many thanks to all my colleagues and friends at the Institute of Geophysics, University of Hamburg, for the pleasant working atmosphere. I thank Prof. Dr. Matthias Hort for advice. The helpfulness among fellow students was great; in particular, I would like to thank Tina Kaschwich and Gesa Netzeband for many good advices work related and more. Christel Mynarik supplied me with pencils, envelopes and everything else required over the years, including kindliness.
A big thank-you goes to my working group for a lot of stimulating discussions. I don't know how the thesis would look like now without the assistance of Dr. Carsten Riedel and Dr. Andrew Dobson and their constructive comments.
I was surprised about the support which was given from outside the institute, often from people who do not even know me personally: Dr. Andreas Klügel, Dr. Oliver Heidbach, Dr. Thomas Ruedas and Dr. Mark Behn. I met also other PhD students willing to provide their own results: Johan Lissenberg and Kristian Müller. Thanks to them, too. It was always fun to work on dyke ascent with Dr. Eleonora Rivalta.

I can always rely on the support and love from my family and my friends. Finally, I want to thank Manuel Beitz for his understanding, endless patience and encouragement when it was most required.

Declaration

I hereby declare that the work presented in this thesis is my own and has not been accepted in any previous application for a degree. The help given by others and all sources of information have been duly acknowledged.

Hamburg, den